Focal plane detectors of a Laue lens telescope for Nuclear Astrophysics

by
José Manuel Álvarez Pastor

degree of
Doctor of Philosophy

at
Department of Physics
Facultat de Ciències
Universitat Autònoma de Barcelona (UAB)
Bellaterra, Barcelona (Spain)

Advisor: Dr. Margarita Hernanz Carbó (ICE, CSIC-IEEC)
Tutor: Dr. Javier Rodríguez Viejo (UAB)

José Manuel Álvarez Pastor
Institut de Ciències de l Espai (ICE, CSIC-IEEC)
Universitat Autònoma de Barcelona
Facultat de Ciències
Torre C-5 -Parell- 2a Planta
E-08193 Bellaterra (BARCELONA)
alvarez@ieec.uab.es

To the memory of my father
Modesto Alvarez

Acknowledgements

I would like to express my deepest gratitude to all those who gave me the possibility to write this thesis, which arose out of years of research at the Institute of Space Sciences. At the Institute, I had the opportunity to meet leading researchers in workshops, meetings and conferences; whose expertise, understanding, and patience moved them to answer my inquires, adding considerably to my research experience, but nonetheless, it is not free of my own mistakes. There could not have been a better framework to acquire expertise in this exciting field.

All this would not have been possible without the support of my supervisor, Dr. Margarita Hernanz and the head of the Institute, Dr. Jordi Isern, to whom I would like to express my gratitude. I would also like to thank the members of my dissertation committee, Dr. Peter von Ballmoos, Dr. Carmen Baixeras Divar and Dr. Ezio Caroli, for the time they took out of their busy schedules to read through my dissertation and attend my defense presentation. I extend thanks to Dr. Javier Rodríguez, Dr. Carles Domingo Miralles, Dr. Pierre Jean and Dr. Rui Curado Da Silva.

I am very grateful to Dr. Elena Aprile and Dr. Karl L. Giboni for welcoming me at the Nevis Laboratory and giving me first hand experience on operating liquid Xenon chambers. I want to express my gratitude to Dr. Mokhtar Chmeissani, I appreciate his availability and willingness to share his knowledge. I also would like to thanks Dr. Manolo Lozano and Dr. Paul Seller for their technical support and Dr. Andreas Zoglauer for his advice to handle many simulation tools.

I thanks also all my colleagues and friends in the Institute, past and present, whom have all been a vital part of my live in Barcelona. There are so many people to thank that I cannot possibly list them all, but you all know who you are and I thank you each for all your friendship. All in all, I would like to thank the colleagues with whom I have worked more closely: Jose Galvez, Merce Llopis and Nil Garcia. I extend thanks to Alina Hirschman for unlimited friendship and kindness. In the same way, it is a pleasure to thank Josep Guerrero who has provided assistance in numerous ways.

Lastly, I would like to extend a special thanks to my entire family. I dedicate this thesis to my parents, Maria Luisa and Modesto, who taught me the value of education. My brothers, Joaquin and Luis, for his encouragement and support when I needed it most. I am eternally grateful to my beloved Maite and little Samuel, this thesis would have remained a dream had it not been for your patient love and unconditional support.

Thanks to you all.

Abstract

Gamma-ray astrophysics in the energy range of nuclear transitions (from a few hundred keV to a few MeV) has an extraordinary potential for understanding the evolving and violent Universe. In spite of the strong efforts accomplished by past and current instruments in order to perform observations in this energy range, an improvement in sensitivity over present technologies is needed to take full advantage of the scientific potential contained in this energy range. In response to this desire, the gamma-ray lens concept based on Laue diffraction was presented as a solid alternative. Its feasibility was demonstrated in the CLAIRE project, where ground and balloon-borne experiments with a Laue lens prototype were accomplished. The successful results of these and others R&D activities have pushed gamma-ray lens technology on the road towards a space mission. This work deals mainly with the focal plane detector of a Laue lens telescope, and the results of a long distance test performed with the gamma-ray lens CLAIRE are also presented. Our main research has evolved in the framework of two missions concept studies -GRI (2007) and DUAL (2010)- submitted to the ESA Calls for a Medium-size mission opportunity in the Cosmic Vision 2015-2025 programme. As far as the GRI mission is concerned, a focal plane detector configuration based on CdTe pixelated detectors is proposed, whilst development and testing of a detector prototype are accomplished. As for the DUAL mission, simulations of the expected space radiation environment and the resulting detector activation are carried out in order to estimate the performances of the mission. Beyond the detector technology proposed in GRI and DUAL, a wide variety of technologies could be explored for the focal plane of a gamma-ray lens mission as well as for a stand-alone detector; a focal plane detector based on liquid xenon is also considered.

Contents

List of Figures

List of Tables

Introduction

Gamma-rays in the MeV energy range is still one of the least known and less explored regions of the energy spectrum. However this energy range presents an extraordinary scientific potential for the study of the most powerful sources and most violent events in the Universe, such as *stellar explosions* and *cosmic acceleration processes*. During *supernova* and *nova explosions*, radioactive nuclei are synthesized and ejected to the interestellar medium, producing the elements in the Cosmos and filling the Galaxy with radioactivity. The observations of the photons emitted by the so created radioactive nuclei, with typical energies around 1 MeV, are highly relevant to give a direct insight on the synthesis of elements and the explosion processes themselves. Likewise, γ-ray observations might help to clarify how and where the cosmic acceleration processes operate. Cosmic acceleration manifests itself most prominently in γ-rays, and is hypothesized to take place in many different scenarios: locally in *solar flares*; within our Galaxy in *compact binary systems*, *pulsars* and *supernova remnants*; very distant objects in *active galactic nuclei* and *Gamma-Ray Bursts*.

Past and current γ-ray space missions have made strong efforts to detect the weak fluxes coming from cosmic sources compared to the high background noise at this energy range. COMPTEL provided the first all-sky survey in the MeV regime (0.75 - 30 MeV). SPI (20keV - 8 MeV) and IBIS (15keV - 10 MeV) on INTEGRAL followed. Despite the progress made by the γ-ray instrumentation, a big step forward is still needed to fulfill the scientific goals, where better sensitivity is the foremost requirement. For instance, the sensitivity required for the study of Type Ia supernovae (by observing the ^{56}Co line at 847keV) is in the range of $10^{-6} - 10^{-7}\gamma cm^{-2}s^{-1}$, within an observation time of $10^{6}s$. Thus, an improvement in sensitivity of at least an order of magnitude is required over present technologies for the next generation of γ-ray mission. This is not only required to study Type Ia supernovae, but for many other scientific objectives in the MeV range γ-ray astronomy. In order to achieve this sensitivity, γ-ray astronomy has been looking, over the last decade, for new ways to increase the efficiency of its instruments while reducing the background noise. With the intend that as much background as possible should be avoided and rejected (through shielding mechanisms and data analysis techniques), a strong effort on innovation and design (build-up of prototypes and numerical simulations studies) is being conducted by a community facing the challenge of preparing the next generation of γ-ray telescopes.
In particular, the progress achieved during the last years on focusing optics based on Laue

lenses is especially remarkable. Conceptually, a focusing telescope will reduce drastically the background noise by concentrating the γ-rays onto on a small size detector (the background noise is roughly proportional to the detector volume).
Focusing γ-rays with a Laue lens is not just a theoretical concept, but a reality, mainly thanks to the development of a first prototype of Laue lens for nuclear astrophysics accomplished by the CESR(Toulouse) collaboration (CLAIRE project). Moreover, the development of focusing optics during these years has also encouraged the development of new detector technologies. The focal plane detector of a focusing telescope should provide imaging capabilities, perform high resolution spectroscopy and measure the polarization of the incident photons in order to achieve the ambitious scientific goals in this energy range.
The research presented in this thesis covers both sides of a γ-rays telescope: lens and detector. As far as the optics is concerned, a test of the Laue lens CLAIRE was performed in order to confirm the prototype performance. Concerning the focal plane detector, theoretical and experimental studies with new detector technologies have been carried out. Our goal is to push the focusing technology on the road towards a future γ-ray space mission. In fact, during this work we have actively contributed to different high energy telescope concepts submitted for consideration to the European Space Agency, ESA, as well as the French Space Agency, CNES:

- The MAX mission was proposed in 2004 by a team led by P. von Ballmoos (CESR, Toulouse), in response to an announcement of opportunity for a technological mission by the French Space Agency (CNES) (von Ballmoos *et al.*, 2004c).

- The Gamma-Ray Imaging (GRI) mission was an initiative of the European Gamma-Ray Community submitted in 2007, in response to a Call for Medium-size mission within ESA s Cosmic Vision 2015-2025 program (Knodlseder, 2007).

- The DUAL mission was proposed in 2010 by an European consortium led by P. von Ballmoos (CESR, Toulouse), in response to a ESA s second Call for a Medium-size mission opportunity for a launch in 2022 (von Ballmoos *et al.*, 2010a).

In this framework, our research deals with the following aspects: development and test of a gamma-ray detector prototype based on *cadmium-telluride* as an option for the focal plane detector of the GRI mission, and estimation of the expected performances of the DUAL instrument based on *germanium*. Moreover, *liquid Xenon* detector technology is also considered in this thesis for the focal plane of a Laue lens mission. For this reason, performances of avalanche photodiodes immersed in *liquid Xenon* were measured.
This thesis is organised according to the outline detailed below:

- **Chapter 1** explains the enormous challenges posed by observation of cosmic sources in the energy range of nuclear transitions. After a brief overview of the astrophysical issues that are expected to be solved with the next generation of γ-ray telescopes, this chapter ends by describing the background conditions experienced by the instruments when performing an observation.

- **Chapter 2** presents the instrumentation for γ-ray astrophysics, from the interaction principles of γ-ray with matter, to design concepts for advanced γ-ray telescopes. A brief overview of past and current γ-ray detectors and telescopes is also presented.

- **Chapter 3** presents the ground test performed with the first Laue lens for nuclear astrophysics. This campaign of the CLAIRE s lens was carried out in Ordis (Girona, Spain) in collaboration with CESR (Centre d Etude Spatiale des Rayonnements, Toulouse). A stay of several months at the CESR was conducted in order to tune the Laue lens at the optical bench in preparation for this campaign.

- **Chapter 4** describes the Gamma-Ray Imager (GRI) mission proposed to the ESA s Call for Missions in the framework of the Cosmic Vision programme 2015-2025. After presenting an array detector configuration based on pixelated cadmium-telluride detectors, the development and tests of a CdTe detector prototype in our institute is presented.

- **Chapter 5** describes the DUAL mission proposed to the ESA s call for a Medium-size mission opportunity for a launch in 2022. The baseline detector is based on a compact array of cross-strip germanium detectors, with high spectral and 3D spatial resolution. The expected performance of the focal plane detector, obtained with the state-of-art Monte Carlo simulations packages, are presented.

- **Chapter 6** presents the measures performed with avalanche photodiodes immersed in liquid Xenon. This experimental work was conducted at Nevis Laboratory (NY) in collaboration with the astrophysics group at Columbia University, and its aim was to propose a focal plane instrument based on liquid Xenon technology.

In the last chapter conclusions are drawn from the experiments and simulations, and ideas on future work are presented.

Chapter 1

The observational challenges in nuclear astrophysics

The detection of photons in the MeV range from a cosmic source is particularly challenging:

- the opaqueness of the atmosphere to γ-rays obliges detection instruments to operate in space, onboard satellites or stratospheric balloons. This brings enormous restrictions on the instrumentation in terms of mass and power consumption.
- the radiation environment above the atmosphere causes a high instrumental background in this energy range.
- the flux weakness of astrophysical sources, coupled with the high background, causes a poor signal-to-noise ratio (typically, on the level of a few percent).

Despite all these handicaps, past and current γ-ray missions have made strong efforts to detect fluxes coming from cosmic sources in the MeV energy range, because of its great scientific interest (see section 1.1). However, there have been much less detections in this energy range than at higher or lower energies, which is also related to the low cross-section of the main interaction at this energy range, as will be explained in Chapter 2.
The challenge for future γ-ray mission is providing a significant increase in *sensitivity*, which is defined as the minimal flux a γ-ray detector can measure. For small count numbers, where Poisson statistics is applied, the sensitivity can be derived (see e.g., Shonfelder *et al.* (2001)) by:

$$F_{min}(E\ \Theta) = \frac{n_\sigma \quad \overline{N_S(E) + N_B(E)}}{A_{eff}(E\ \Theta)T_{obs}} \tag{1.1}$$

where $N_S(E)$ and $N_B(E)$ are the measured counts coming from the source and background respectively and, n_σ defines the number of standard deviations of the background fluctuations. It is usual to take $n_\sigma = 3$, i.e. the probability that the observed signal is due to a statistical fluctuations is $< 0\ 3\%$. $A_{eff}(E\ \Theta)$ is the effective area of the instrument which is related to the efficiency (as will be discussed in section 5.3.3) and depends on

energy and direction, and T_{obs} is the observation time. The factor $A_{eff}T_{obs}$ is also known as *exposure*.

Considering that $N_S(E)$, at the sensitivity limit, depends itself on the sensitivity ($N_S = F_{min}A_{eff}T_{obs}$), equation (1.1) can be expressed by the following expresion:

$$F_{min}(E\ \Theta) = \frac{n_\sigma^2 + n_\sigma \quad \overline{n_\sigma^2 + 4N_B(E)}}{2A_{eff}(E\ \Theta)T_{obs}} \tag{1.2}$$

The aim of any γ-ray telescope is to reduce F_{min} as much as possible in order to achieve the highest sensitivity, for which a *large exposure* ($E = A_{eff}T_{obs}$) and *low background* (N_B) are required.
In classical γ-ray telescope, where the aperture area of the system is coupled to the collecting area, an increase of A_{eff} is associated with an increase of the instrumental background (N_B). Thus, increasing *exposure* by increasing the *effective area* (A_{eff}) does not necessarily lead to an improvement in sensitivity. On the other hand, increasing T_{obs} could lead to an improvement in sensitivity as long as the instrumental background remains constant. However, a way to increase the observation time (within a given lifetime of a survey space mission) is increasing the field-of-view of the instrument, which might lead again to an increase of the instrumental background.
In order to increase the detection efficiency, two parallel (and complementary) approaches have been proposed during the last years:

- decoupling the collecting area from the detecting area, so that the enhancement of the collection area does not lead to an increase of the instrumental background. This is feasible by focusing γ-ray optics, what would provide unprecedented sensitivities (see section 2.3.3).

- improving the background rejection techniques through Compton scattering reconstruction (electron tracking, time-of-flight, etc) while increasing the efficiency through larger collection areas. This can be achieved by an advanced Compton telescope that would provide high sensitivity within a wide field-of-view (see section 2.3.2.1).

Feasibility studies of both approaches - focusing telescopes and advanced Compton telescopes - have been performed in the last years in order to improve the sensitivity. The accurate angular resolution of a focusing telescope, along with the wide field-of-view of a Compton detector, meet the observational requirements for both discrete and extended sources in gamma-ray astronomy.

1.1 Gamma-ray astronomy in the MeV region

The high penetration power of γ-rays provide a unique view into the most violent phenomena in the Universe, offering essential information to understand the nature of those extremely energetic phenomena, which are hidden at lower energies.

Observations at the typical energy of the photons emitted by radioactive nuclei, are of the highest relevance in providing a direct insight on the synthesis of elements. Moreover, detection of the characteristic γ-rays line signals emitted by objects (or regions) in the Universe allows the study of the physical processes in these objects (or regions), among others: Supernovae, Classical Novae, Gamma-Ray Bursts (GRBs), Supernova Remants (SNRs), Solar flares, Massive Stars, Active Galactic Nuclei (AGN) and Clusters of Galaxies.

In the exploration of the MeV energy range, the work performed by the instrument COMPTEL (Schonfelder *et al.*, 1993) aboard the NASA s Compton Gamma-ray Observatory (1991-2000) is especially remarkable. This exploration has been continued by the spectrometer SPI onboard the ESA s INTEGRAL mission (Winkler *et al.*, 2003) launched in 2002. Currently, SPI has been able to map antimatter in the Galaxy from the observation of the $e^{-}e^{+}$ annihilation emission (Knodlseder *et al.*, 2005), as well as to observe the red and blue shifts in the ^{26}Al line at 1.8MeV correlated to galactic rotation (Diehl, 2006), just to mention a couple of examples. Despite this enormous progress, a significant increase in sensitivity is essential for astronomy in the energy range from several keV up to a few MeV.

1.1.1 Nucleosynthesis

Nuclei synthesized during stellar explosions (novae and supernovae) are expelled to the interstellar medium, filling the Galaxy with radioactivity and explaining the origin of the elements in the Cosmos. The observation of γ-ray emissions from the decay of this radioactive isotopes, both at the stellar sources or along the Galaxy, shows the footprints of the explosions and give a direct insight on the nucleosysthesis.

Isotope	Decay chain	Lifetime	Line energy (keV)	Source Type
^{56}Ni	$^{56}Ni - {}^{56}Co$	8.8d	158,812	SN
^{56}Co	$^{56}Co - {}^{56}Fe$	111d	847,1238	SN
^{57}Ni	$^{57}Ni - {}^{57}Co - {}^{57}Fe$	(52h) 390d	122,136	SN
^{44}Ti	$^{44}Ti - {}^{44}Sc - {}^{44}Ca$	89yr (5.4h)	78,68,1157	SN
^{26}Al	$^{26}Al - {}^{26}Mg$	10^6 yr	1809	AGB Stars, Massive Stars Novae, SN
^{60}Fe	$^{60}Fe - {}^{60}Co - {}^{60}Ni$	2x10^6yr (7.6 yr)	1173,1332	SN, Massive Stars
^{7}Be	$^{7}Be - {}^{7}Li$	77d	478	Novae
^{22}Na	$^{22}Na - {}^{22}Ne$	3.8yr	1275	Novae

Table 1.1: Radioactive isotopes synthesized in explosive events.

Depending on their lifetime (see table 1.1) two types of isotopes can be distinguished:

- short-lived isotopes, that can be observed in individual objects, such as ^{56}Co or ^{57}Co detected in type II SN1987A, ^{44}Ti detected in Cas A, or ^{7}Be and ^{22}Na, not yet detected but expected from novae explosions.

- long-lived isotopes, that are undetectable in individual sources and only the accumulated emission in the Galaxy can be observed, such as ^{60}Fe and ^{26}Al (see figure 1.1).

Supernovae

Most of the isotopes listed in Table 1.1 are synthesized in supernovae events, either in core collapses (ccSNe) or in thermonuclear (SN Type Ia) explosions. Supernovae of Type II, Ib/c (core collapse supernovae) are exploding massive stars which leave either a black hole or a neutron star as a remnant after the explosion. On the other hand, thermonuclear supernovae (SN Type Ia) are exploding white dwarfs in close binary systems, which do not leave any remnant after the explosion.
The observation of Type Ia supernovae yields profound results for modern cosmology. The evidence of the accelerating expansion of the universe (Riess *et al.* (1998); Perlmutter *et al.* (1999)), is based on the use of these stellar explosions as standard candles to determine distances in the cosmos. This relies on an empirical relationship between the shape and the maximum of the light curve of a Type Ia supernovae (Phillips, 1993). Although this empirical rule has been proven to be very useful, it remains unclear how it works. However it is well known that the early evolution of the light curve of a Type Ia supernovae is powered by the decay of ^{56}Ni and its daughter ^{56}Co (see Table 1.1). The observation of this γ-ray emision, that appears several days after the explosion, is the most direct diagnostic tool to understand the explosion mechanism and distinguish between the several existing models of Type Ia supernovae (see e.g., Gómez-Gomar *et al.* (1998b); Isern *et al.* (2004)). The temporal evolution of radioactive lines, their relative ratios, widths and shapes, as well as the continuum component of the spectrum could be used for diagnostic purposes. However, since supernovae Type Ia are rare events, a γ-ray telescope needs an outstanding sensitivity to be able to gather adequate data. To date, only two Type Ia supernovae have been observed in γ-ray, in both cases with the instrument COMPTEL (Schonfelder *et al.*, 1993) onboard the Compton Gamma-Ray Observatory (CGRO): the exceptionally-bright SN1991T, that took place at a distance of 13Mpc and from which a marginal detection was obtained (Morris *et al.*, 1995a), the SN1998bu that exploded at a distance of $\sim 9Mpc$ from which only upper limits where obtained (Georgii *et al.*, 2002), and the current SN2011fe.

Novae

Novae are hydrogen thermonuclear explosions occurring on the surface of accreting white dwarfs in binary systems. These explosions are recurrent phenomena, i.e., an explosion is expected every time the critical accreted mass on top of the white dwarf is reached. The radioactive isotopes synthesized during novae explosions are listed in table 1.1. Gamma-ray emission is expected from the decay of these isotopes and from the annihilation of positrons produced by short-lived β^+-unstable elements such as ^{13}N and ^{18}F. A prompt emission of the $511keV$ positron-annihilation line, as well as a positronium continuum below this line, is expected even before the nova is visible in the optical. In addition, γ-ray lines at 478 keV (^{7}Be) and 1275keV (^{22}Na) are expected to last for a few months and

years respectively (Gómez-Gomar *et al.* (1998a);Hernanz *et al.* (1999);Hernanz & José (2004)).
Gamma-ray observations of novae, especially the prompt emission, offers a unique powerful diagnostic tool to understand the systems and physics therein. None of the γ-ray lines expected from a nova explosion have been observed yet.

1.1.2 Diffuse galactic nuclear lines

Diffuse line emission in the Galaxy is expected from the cumulative radioactive isotopes produced by a large number of sources. This diffuse emission is expected to be resolved, at least in part, by improving sensitivity and angular resolution of γ-ray instrumentation.

^{26}Al Decay

The decay line of ^{26}Al is the most intense radioactivity in the sky, showing a million years of nucleosynthesis activity in the Galaxy (Mahoney *et al.*, 1984). The ^{26}Al map obtained with COMPTEL (see figure 1.1) has posed interesting questions about the origin of the galactic ^{26}Al (e.g., Diehl (2011)), presumably produced by explosive nucleosynthesis in core-collapse Type II supernovae, in novae or by hidrostatic nuclear burning in the interior of massive stars (Wolf-Rayet massive stars and AGB stars).
Some high emission regions have been discovered (Cygnus, Carina, Vela), pointing to a link between ^{26}Al emission and massive star formation, as well as a relationship to the spiral structure of the Galaxy (see review by Diehl *et al.* (2005)).
Up to now, no ^{26}Al from individual Wolf-Rayet stars has been detected. Precise measurements from the nearby Wolf-Rayet star γ^2 Velorum, constrain models for the individual events and allows to use the global galaxy observations to understand the rates and distributions of these sources.

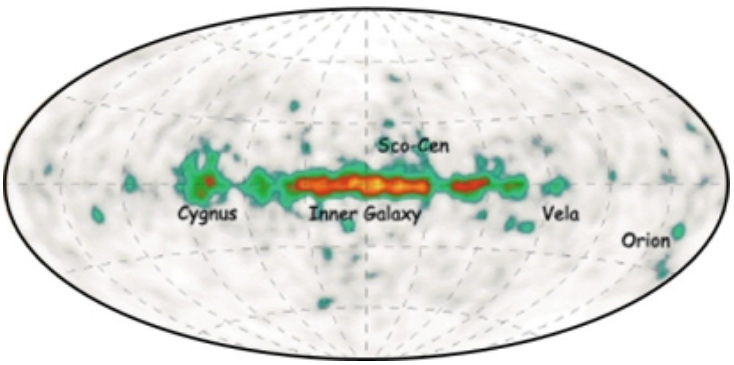

Figure 1.1: All-sky image of ^{26}Al γ-ray emission at 1809keV as mapped by COMPTEL s 9-year survey (Pluschke *et al.*, 2001)

^{60}Fe Decay

The ^{60}Fe isotope, whose decay results in 1.173 and 1.333 MeV γ-rays, is mainly ejected from core-collapse supernova although Wolf-Rayet contribution can not be excluded. The

ratio of ^{60}Fe to ^{26}Al should yield constraints to the overall amount of ^{26}Al, which is produced in massive stars (Prantzos, 2004). An all-sky ^{60}Fe map will be useful to trace core collapse supernovae.
The line emission from ^{60}Co (short-lived daughter of ^{60}Fe) has been detected by INTEGRAL (Harris *et al.* (2005); Wang *et al.* (2007)) and RHESSI (Smith *et al.* (2004); Caspi *et al.* (2006)), but current instrumentation is not sensitive enough to resolve individual supernova in the ^{60}Fe line.

^{44}Ti Decay

The 1 157MeV line from the decay chain of ^{44}Ti (see table 1.1), is a unique tracer of young supernova remnants (SNRs). The first detection of this decay line in Cas A with COMPTEL (Iyudin *et al.*, 1994) confirms the production of ^{44}Ti in core-collapse SNe. In addition, the small extinction of ^{44}Ti γ-ray line in our galaxy can be used to constrain the supernova rate in our galaxy from the number of SN remnants, which are hidden at lower energies.

Positron annihilation line

The 511keV line from positron-electron annihilation has been one of the most important features of high energy astrophysics (Leventhal *et al.*, 1978). Observations with SPI on INTEGRAL have revealed that a significant amount of the 511 keV annihilation radiation is consistent with emission from or near the galactic bulge (Knodlseder *et al.*, 2005) (see Figure 1.2). While the observed weak emission from the galactic disk can be explained by radioactive beta decay from ^{26}Al (and eventually ^{44}Ti), the origin of the positrons of our Galactic Center remains unknown.

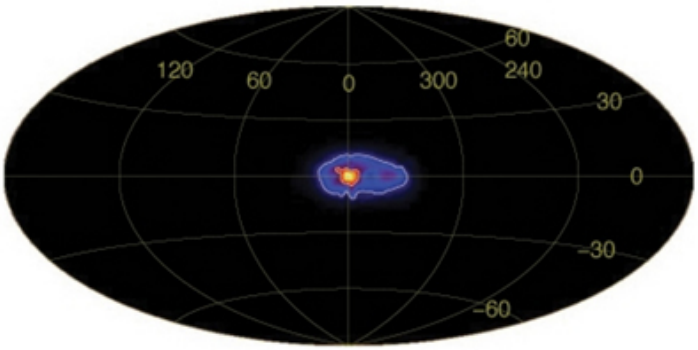

Figure 1.2: All-sky map of 511 keV positron-electron annihilation radiation line as mapped by INTEGRAL/SPI (Knodlseder *et al.*, 2005)

Compact objects, such as Type Ia supernovae, novae, or low mass X-ray binaries (LMXB), are believed to be positron production sites, leading to the 511keV emission, but also light dark matter (DM) annihilation has been proposed as a possible origin of the observed annihilation line.

1.1.3 Cosmic accelerators

Cosmic particles are accelerated to relativistic energies by diverse mechanisms. These particles are observed in nearby solar flares, or in more distance pulsars, X-ray binaries (XRBs) and super nova remnants (SNR), but also in cosmological distances accelerators, such as active galactic nuclei (AGN) and gamma-ray bursts (GRB).
Detailed emission scenarios are still unclear. How the acceleration process operates or what are the emitting geometries will be more clearly revealed through γ-ray observations. In particular, γ-ray timing and polarization measurements will provide important insights into the geometry and the physical processes that govern the acceleration sites.

Gamma-Ray Bursts (GRBs)

GRBs are the most luminous electromagnetic explosions in the universe. The central engines of GRBs drive highly relativistic jets (Mészáros *et al.*, 2006). Long-duration GRBs ($> 2sec$) are most likely signatures of the deaths of rapidly rotating massive stars (collapsars), connected to Type Ib/c supernovae. Short-duration GRBs ($< 2sec$) remain a mystery. Some theories suggest they might originate from mergers of two neutron stars. A small fraction of these short duration bursts could originate from soft γ-ray repeaters. Despite the significant progress in the understanding of their progenitors, the afterglows and host galaxies, a lot of mysteries remain around these phenomena since the discovery of GRB in the late 1960 s. Measuring the γ-ray polarization would greatly help to constrain the inner engines of GRBs. Up to now there has been a controversial claim of polarization in GRB021206, measured with the RHESSI satellite (Coburn & Boggs, 2003).

Active Galactic Nuclei (AGN)

The powerful and rapidly variable fluxes of γ-rays in some galaxies suggest that a supermassive black-hole engine is at their center. These black holes are surrounded by an accretion disk and, at least in blazars, exhibit relativistic jets where γ-rays are generated. The generation of the jets, its composition, its link to the accretion disk and the collimation process are still a matter of debate. The MeV energy range is crucial for undertanding the processes driving AGN.

Supernova Remnants

The remnants of stellar explosions are powerful particle acceleration sites. Soft γ-ray observations of supernova remnants prove that the low-energy end is produced by synchrotron mechanisms and are able to unveil the injection mechanism of particles into the shock front. On the other hand, GeV and TeV emission is produced by either inverse Compton or from secondary photons decayed from ψ^0.

Pulsars

Pulsars are rotating neutron stars with strong magnetic fields making them ideal accelerators for charged particles. However, particle acceleration and photon production mechanisms in pulsar magnetospheres are still unknown. The polarization of the emitted photons gives a clue on how to solve this issue, since polarization is inherently linked to the particle creation and emission region.

Solar flares

Gamma-ray lines are emitted in large solar flares from positron annihilation, secondary neutron capture and de-excitation of nuclei excited by interactions of flare-accelerated ions with the solar atmosphere. The bombardment of the solar atmosphere by flare-accelerated ions can also synthesize radioactive nuclei, whose decay can produce delayed γ-ray lines in the aftermath of large flares (Tatischeff et al. 2006). Gamma-ray astronomy is one of the best tools for studying the active Sun.

1.1.4 Cosmic γ-ray background

A large number of possible origins have been proposed to the cosmic γ-ray background. It has been attributed to either a diffuse origin or to the emission of unresolved point sources (or both). Over the years significant progress has been made in the determination of the energy spectrum. The components at low ($< 100keV$) and high ($> 10MeV$) energies are modeled assuming a relevant contribution from Seyfert galaxies and blazars, respectively. The situation between 0.1 and 10MeV is less clear and there is presently no accepted explanation for the origin of the MeV cosmic γ-ray background. It has to be determined how far the low and high energy sources reach into this regime and how considerable can the contribution be of other sources, e.g. Type Ia supernovae, AGN or more exotic ones like dark matter decay and annihilation.

1.2 The background of γ-ray telescopes

In space, the instrument and spacecraft materials are permanently irradiated by cosmic rays, diffuse cosmic X/γ-rays and there may be also an exposition to the trapped particles of the radiation belts of the Earth or secondary particles coming from the Earth s albedo. In this hostile radiation environment, gamma-ray detectors are subject to an intense and complex instrumental background noise. Each background component will become significant under different conditions, which are strongly influenced by the instrument design (i.e.,field-of-view, shielding, passive and active materials) and the space mission parameters (i.e., orbit, period of observation).
In this section we present the different background contributions which can affect a γ-ray telescope. Understanding the origin of each background component is crucial to properly implement rejection methods, and evaluate the capabilities of a γ-ray telescope. The study

of this background relies on Monte Carlo simulations, for which detailed computer models of the instruments (and spacecraft) are needed.
In the last part of this section, we describe the simulation tools used for predicting the instrumental background in a specific γ-ray space mission. These tools include packages to model space environment (SPENVIS, CREMA96) and a suite of Monte Carlo codes (MGGPOD) for simulating the physical processes relevant to the production of instrumental background.

1.2.1 The different sources of background

A description of the radiation environment is of great importance for instrumental background prediction. The different sources of background components in a space γ-ray telescope which has a clear dependence on the specific orbit for the mission, will be briefly presented here. A more detailed description can be found in Dean *et al.* (2003).

Galactic cosmic rays

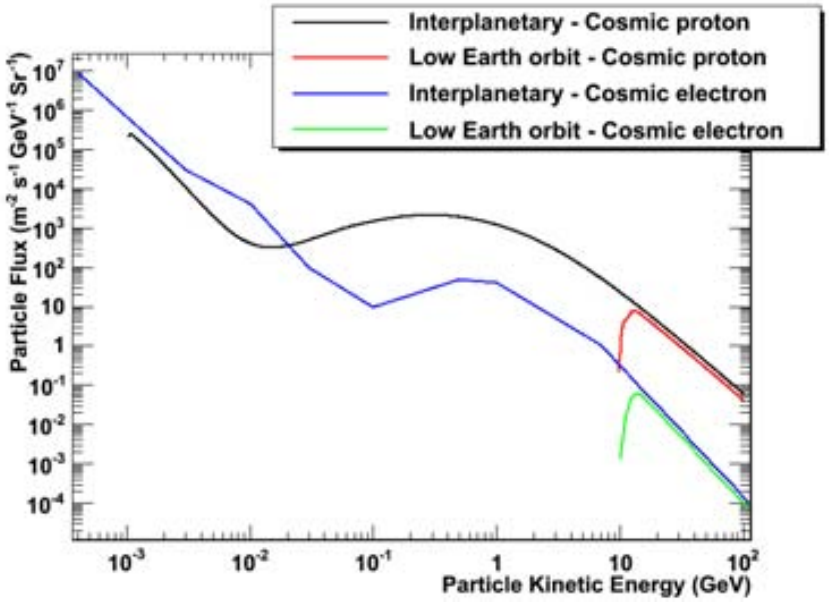

Figure 1.3: Spectra of galactic cosmic protons at low Earth orbit and interplanetary (CREME96).

Galactic cosmic rays are energetic charged particles, mainly protons ($\sim$ 90%), followed by α particles ($\sim$ 9%) and heavy ions, isotropically incident upon the Earth. In addition, electrons, positrons and antiprotons are also found in small quantities. The spectrum and intensity of Galactic cosmic-ray protons and electrons in the interplanetary space environment are shown in Figure 1.3. The proton spectrum is based on the cosmic-ray propagation models of Moskalenko *et al.* (2002). The spectrum of cosmic electrons is based on the description given by Ferreira *et al.* (2002).
Cosmic ray particles are affected by magnetic fields, either terrestrial or interplanetary, as they travel to Earth. At energies below a few GeV, the spectra of cosmic rays are affected

by solar modulation, i.e. Earth receives a maximum flux of galactic cosmic rays at the minimum solar activity and vice versa. This solar modulation is due to the propagation of the energetic particles in the dynamical environment of the Heliosphere.
Earth magnetosphere acts as a momentum filter, requiring a minimum kinetic energy per nucleon to cross it. To study this effect, the so-called *rigidity* concept is introduced. Every point in the Earth s magnetic field will have a minimum required rigidity for a charged particle. This parameter implies an energy cut-off in the cosmic ray spectrum, which can be defined (Gehrels, 1992) as:

$$E_c[MeV] = 10^3(-0\ 938 + (0\ 938^2 + R_c^2)^{0\ 5}) \tag{1.3}$$

where the rigidity, R_c, is defined as the momentum per unit charge of particle (see Dean *et al.* (2003)).
The minimum rigidity at a spacecraft position plays an important role in determining the cosmic ray spectrum incident on a spacecraft and the instruments onboard. In a low-Earth orbit mission (LEO) this source of background may be less significant, but will become dominant for missions that spend most of their time outside the Earth s magnetosphere, i.e., in a high-Earth orbits (HEOs). Figure 1.3 shows clearly the cut-off energy in the spectra of galactic cosmic protons and electrons in a low Earth orbit (550km altitude, 8° inclination), obtained with ACTtool/CREME96 (see section 1.2.2.1 and references therein).

Trapped particles

On Earth s magnetosphere there are charged particles, mainly protons and electrons, confined by the magnetic field in a structure known as *radiation belts*. The innermost belt, at an altitude of ~ 1 Earth radius, has a higher density of high energy protons. The energies extend up to several hundred MeV, and their angular distribution is highly anisotropic. On the other hand, the outer belt, at an altitude of $\sim (3-4)$ times Earth radius, contains mainly low energy electrons and is less stable than the inner one. Figure (1.4) shows the flux contour map at an altitude of 550km for trapped protons and electrons, obtained with SPENVIS (see section 1.2.2.1).

The radiation belt on the sourthern hemisphere extends to lower altitudes due to the diferences on the magnetic field at the Earth s centers. This area, known as the *South Atlantic Anomaly (SAA)*, can be a major source of background noise for instruments in low-Earth orbits. A gamma-ray mission in LEO should seek to avoid the SAA as much as possible, choosing wisely the orbit s altitude and inclination (see figure 1.5).

Solar Energetic Particles (SEPs)

SEPs are ejected from the Sun during flares or Coronal Mass Ejections (CME). Their flux can be much larger than other particle radiations, and it is highly variable and anisotropic. Their energies can reach several hundred MeV, which is not enough to penetrate the

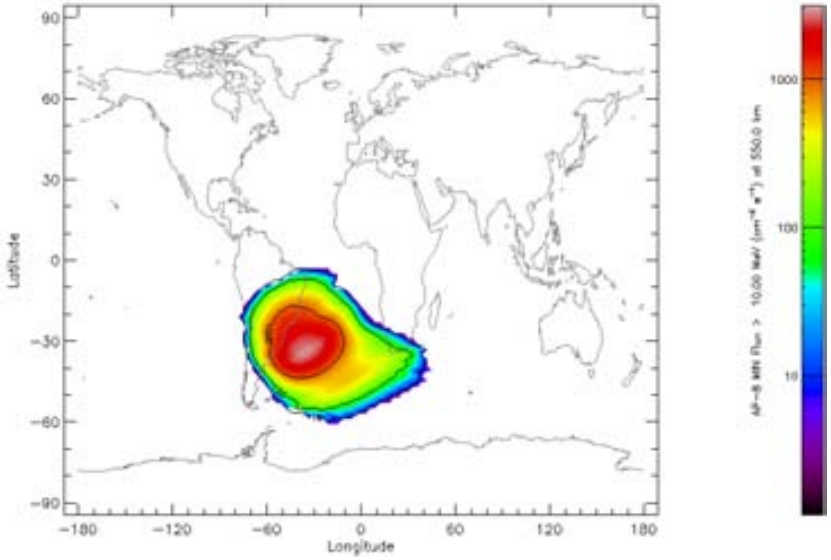

(a)

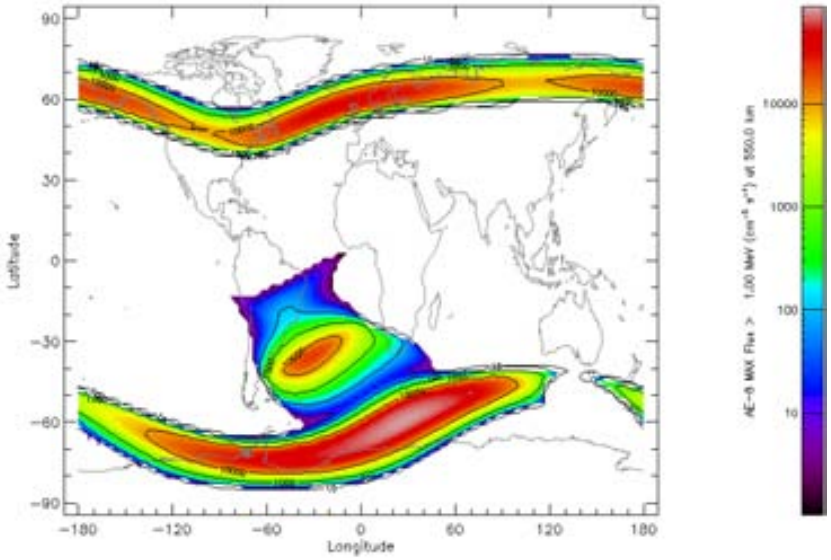

(b)

Figure 1.4: Trapped protons (a) and trapped electrons (b) flux contour map at an altitude of 550km obtained with SPENVIS. The SAA is clearly shown in both maps.

magnetosphere. Missions inside the magnetosphere (LEOs) are shielded from most of these particles.

Earth albedo radiation

The high energy particles of Cosmic rays interact violently with Earth s atmosphere, producing nuclear interaction cascades that finally result in the production of multitude

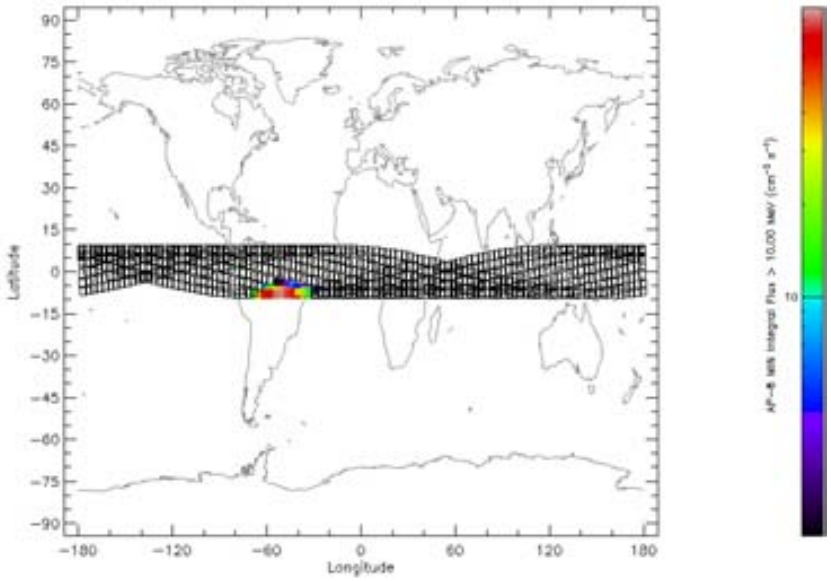

(a) AP-8 proton model in solar minimum conditions

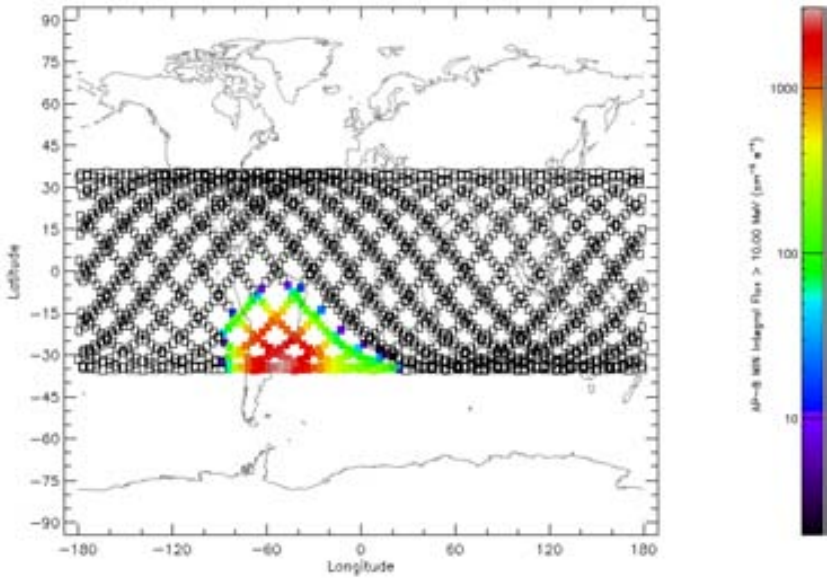

(b)

Figure 1.5: Trapped protons flux for a low Earth orbit (LEO), with an altitude of 550Km and orbital inclination of 8° (a) and 35° (b), obtained with SPENVIS.

of secondary particles. Among them, the most important ones for our study are photons and neutrons.

Figure (1.6) shows the spectra of both particle contributions for a low Earth orbit (LEO) with 550km altitude and 8^o inclination. Data are from the ACTtool/CREME96 enviroment tool (see section 1.2.2.1 and references therein). Earth albedo radiation can also be a strong and anisotropic source of background.

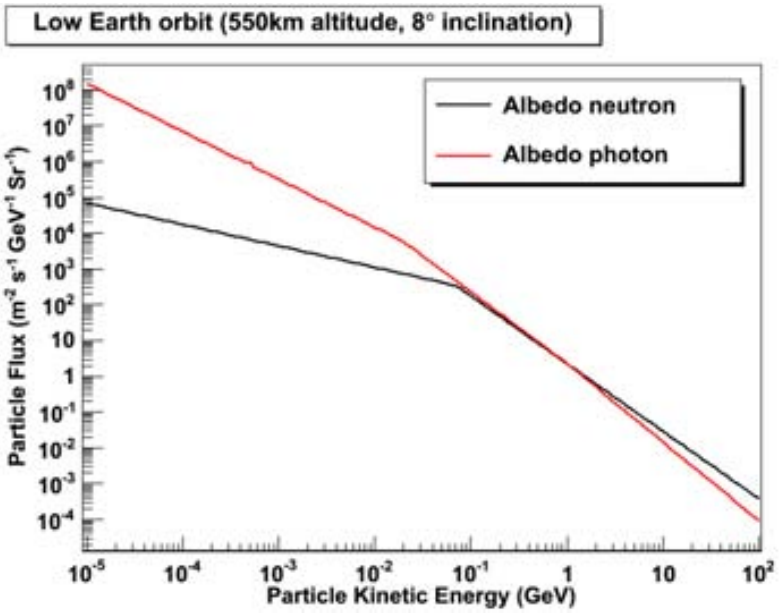

Figure 1.6: Spectra of albedo photons and neutrons at low Earth orbit, data from CREME96.

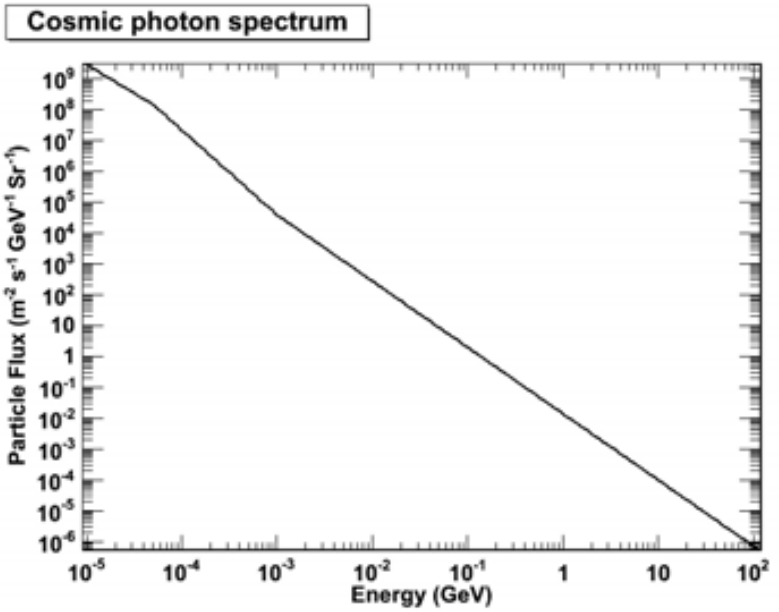

Figure 1.7: Cosmic photon spectrum, data from CREME96.

Cosmic diffuse γ-rays

As previously mentioned in section 1.1.4, the origin of diffuse cosmic γ-rays is a topic of great astrophysical interest but is also a source of background in any γ-ray astrophysical observation. Its contribution to instrumental background can be considered to be isotropic and obviously, it is unaffected by the geomagnetic field.

Cosmic diffuse γ-rays have been measured by many instruments, either in balloon flights or space missions. Their spectrum can be defined as a broken power law, following the

analytical description given by Gruber *et al.* (1999). The cosmic diffuse γ-ray spectrum shown in figure 1.7 was obtained from ACTtool/CREME96 (see section 1.2.2.1).

1.2.2 Modeling instrumental background

As a result of the interaction of particles and photons (from the different sources described above) with the material of the space-borne instrument, a large variety of processes take place that will produce the instrumental background. Among this diversity, two components of background can be differentiated, according to the timescales of the process:

- *prompt component*, such as prompt photon emission associated with the de-excitation of excited nuclei by neutron capture, inelastic neutron scattering, and spallation.
- *delayed component*, which is due to the decay of radioactive isotopes produced by nuclear interactions, or decay of natural radioactive elements.

The activation of the material, especially the activation caused by long term build-up of radioactive isotopes, is an important component of the background for γ-ray telescopes operating in the energy range of nuclear lines. As will be presented in the next section, detailed Monte Carlo simulations are a good approach to determine the instrumental background, which in turn is essential to estimate the instrument performance.

1.2.2.1 Space environment model

Accurate space environment models are essential inputs for background simulation and reliable prediction of γ-ray telescope performance. For a given orbit, each source of background discussed above should be modeled in order to obtain realistic initial conditions for background simulations. An integrated set of space radiation environment models can be found in some public available packages, such as SPENVIS[1] and CREME96[2]. Comparisons to on-orbit data have demonstrated the accuracy of the analytical models implemented in these suites, which have been improving for years.
The Cosmic Ray Effects on Micro-Electronics (CREME96) is a widely-used tool for determining satellite electronic design constraints, which has been shown to be accurate at predicting galactic cosmic rays, anomalous cosmic rays, and solar flare components on the near-Earth environment (Tylka *et al.*, 1997). The package also includes a well-tested geomagnetic transmission calculation algorithm, and uses the established AP8 models for predicting trapped proton flux. For the atmospheric neutron environment component, the models based on empirical data reported in Morris *et al.* (1995b) are used. For the electron/positron cosmic rays, the diffuse photon and the albedo photon components, the analytical models presented by Mizuno *et al.* (2004) are used convolved with the geomagnetic transmission function supplied by CREME96. The electron cosmic rays are extended to energies below 7 GeV based on data provided in Ferreira *et al.* (2002).

[1] http://www.spenvis.oma.be
[2] https://creme.isde.vanderbilt.edu

1.2.2.2 Monte Carlo simulation

The Monte Carlo suite *MGGPOD* is based on the Geant3 package from CERN (1993). It has been developed by Weidenspointner *et al.* (2005a) for simulating ab initio the physical processes relevant for the production of instrumental backgrounds. It is an ideal tool for simulations of γ-ray telescopes in a space radiation environment that includes the build-up and delayed decay of radioactive isotopes as well as the prompt de-excitation of nuclei. Therefore, it allows us to predict the production and decay of radioisotopes inside detector materials for a given radiation history.

	Step 1	Step 2	Step 3
Input	Mass model and radiation environment	Isotope production rates and radiation history	Mass model and activity per isotope and volume
Tool	MGEANT, GCALOR, PROMPT	ORIHET	MGEANT, GCALOR, DECAY
Output	Isotope prod. rates Prompt energy deposits	Activity per isotope and volume	Delayed energy deposit

Table 1.2: The sequence of simulation steps of MGGPOD (details are given in Appendix B.3).

MGGPOD comprises several closely integrated packages. The flow of the simulation can be divided into three steps listed in table 1.2. A necessary input for the Monte Carlo simulation is the so-called *mass model*, i.e. an accurate representation of the spacecraft and payload that includes the geometrical structures, the atomic and/or isotopic composition of materials, and any other parameters that may influence the transport of particles.
Once the mass model is obtained, the first step of MGGPOD is to simulate the isotope production and the prompt energy deposit. From these, the isotope production rates for a given radiation environment are calculated. Three individual packages, MGEANT, GCALOR and PROMPT take care of this first step. The second step, calculates the activation of each radio isotope in each detector volume with the ORIHET package, based on a given radiation history. Finally, in the third step, the delayed energy deposition by the combination of MGEANT, GCALOR and DECAY packages is simulated. For more details on the various simulation packages, input and output files, see Appendix B.1.2.
Currently MGGPOD provides the best agreement between measurements and simulations (Weidenspointner *et al.*, 2004), but since Geant3 is no longer supported and is being replaced by its successor Geant4 (Agnostelli *et al.*, 2003), also *MGGPOD* has a successor tool based on Geant4 named *Cosima* (Zoglauer *et al.*, 2009). This new tool to simulate instrumental background is part of the medium-energy gamma-ray astronomy library MEGAlib (Zoglauer *et al.*, 2006b). Its preliminary results are very promising although it is undergoing a verification phase and comparison with real measured data should be carried out.

Chapter 2

Instrumentation for astrophysics in the MeV energy range

Instrumentation for astrophysics in the MeV energy range is intended to measure the energy of the photons coming from a cosmic source, their incoming direction, flux and polarization. In other words, instrumentation for astrophysics should be able to perform spectroscopy, imaging, polarimetry and timing measurements.
In this chapter, the techniques used in γ-ray telescopes onboard past and current space missions will be briefy described, as well as new concepts under development for future missions. Firstly, γ-ray interactions processes with matter will be discussed, followed by a brief description of *gamma*-ray detectors. In particular we will focus on *Cadmiun-Telluride* and *liquid Xenon* detectors, which are relevant for the experimental development that will be presented in Chapter 4 and Chapter 6, respectively.

2.1 Basic principles of γ-ray detection

2.1.1 Interaction of γ-ray photons with matter

In the energy range from few hundred keV up to several tens of MeV, the interaction of radiation with matter takes place through one of these mechanisms: *Photoelectric Absorption*, *Coherent (Rayleigh) Scattering*, *Incoherent (Compton) Scattering* and *Pair Production*. A more detailed description on the interaction processes can be found, for example, in von Ballmoos (2005). In order to illustrate the energy domain of each one of these processes, the mass attenuation coefficient (as will be defined below) is plotted for the particular case of cadmium-telluride in Figure 2.1.

- *Photoelectric Absorption*. In this process the photon gives all of its energy to a bound atomic electron which is expelled from the atom. The kinetic energy carried away by the electron is the difference between the photon energy and the binding energy of the electron to the atom. The photoelectric effect dominates at low energies, from few keV to hundreds of keV, depending on the atomic number, Z (see Fig.2.1).

- *Rayleigh (coherent) scattering.* In this process, photons are scattered by bound atomic electrons, while the atom remains unexcited or ionized. It is often assumed that Rayleigh scattering is elastic. However, the scattering from a free atom is never strictly elastic because of the recoil energy of the atom. For a lattice of atoms, the scattering from the different atoms may add up coherently or incoherently depending on the atomic arrangement. The process of γ-rays scattering in a crystalline lattice is addressed in more detail in section 3.1.1.

- *Compton Scattering.* This is an inelastic process between the incident photons and the electrons in the material, i.e., the incident photon is deflected from its original direction while it transfers part of its energy to the bound electron. The process becomes elastic in the case of scattering with free (unbound) electrons in which case it is known as *Thomson scattering.*

  Compton scattering, as the dominant process in the MeV energy region (see Fig.2.1), will be discussed in more detail in section 2.1.2.

- *Pair production.* When the photon energy is greater than twice the electron rest mass (511keV), the creation of an electron-positron pair becomes possible in the vicinity of a nucleus. This process is called pair production and dominates above 5MeV.

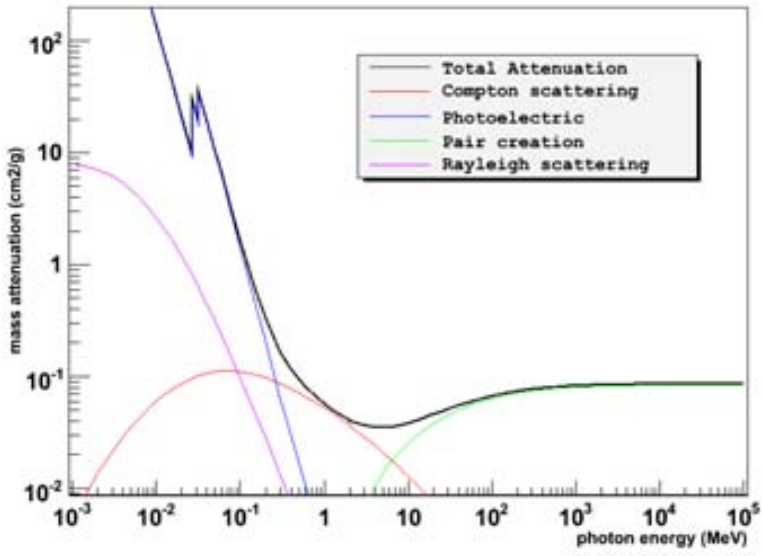

Figure 2.1: Mass attenuation coefficients (μ ρ) for the case of cadmium-telluride. Data are from the Photon Cross Sections Database (Berger *et al.*, 2009).

γ-ray attenuation

Let s consider a γ-ray beam going through a material. Each one of the interaction processes described above could remove a γ-ray photon from the incoming beam according to the

cross-section of the interaction process. The intensity of the incoming beam follows a exponential extinction:

$$I = I_0 e^{-\mu t} \tag{2.1}$$

where I_0 is the initial intensity of the beam, t the path length in the material, and σ the so-called *linear attenuation coefficient*. This coefficient adds the cross-section of each interaction process (consider only the relevant processes around the MeV):

$$\sigma = \sigma_\tau + \sigma_\sigma + \sigma_\kappa \tag{2.2}$$

where σ_τ, σ_σ and σ_κ are the linear attenuation coefficient related to the cross-sections of photoelectric, compton and pair processes respectively. Usually they are expressed independently of the density of the material, and are called *mass attenuation coefficient* $\sigma\ \chi$. A rough description of the dependence of the attenuation coefficient on the atomic number of the material (Z) and the energy of the incoming γ-ray photon is given for the main interaction processes (see e.g. von Ballmoos (2005)):

- $\sigma_\tau\ \chi$: there is not a single analytic expression of the photoabsortion cross-section over all range of Z and E, but a rough approximation is given by:

$$\sigma_\tau\ \chi = (N_0\ A)\tau_\tau \quad \tau_\tau \sim \frac{Z^n}{E_\gamma^{3\ 5}}\ per\ atom \tag{2.3}$$

  where n is in the range [4 5], the exact value depending on the initial photon energy (Knoll, 1999).

- $\sigma_\sigma\ \chi$: the mass attenuation coefficient due to the Compton scattering is given by:

$$\sigma_\sigma\ \chi = (N_0\ A)Z\tau_\sigma \tag{2.4}$$

  where the cross-section τ_σ is derived from the Klein-Nishina expression (see next section)

- $\sigma_\kappa\ \chi$: the attenuation due to pair production is given by:

$$\sigma_\kappa\ \chi = (N_0\ A)\tau_\kappa \quad \tau_\kappa \sim Z^2 ln(2E_\gamma\ mc^2)\ per\ atom \tag{2.5}$$

  where the cross-section τ_κ is given for low energy photons by Bethe & Heitler (1934).

From the above expressions, it is clear that each process dominates for a range Z and E, as illustrated in Figure (2.2).

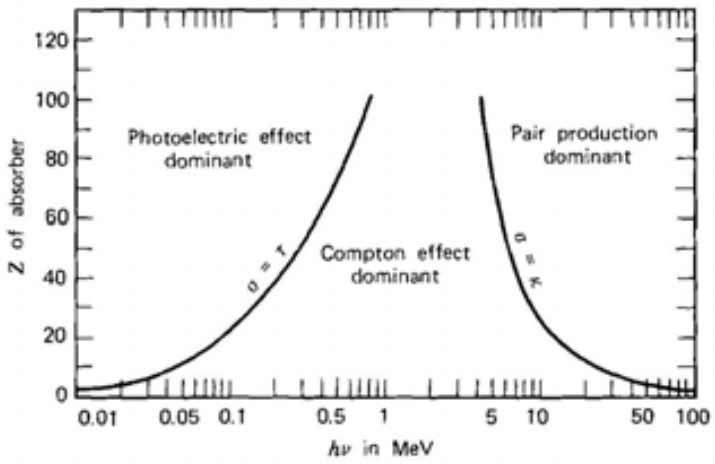

Figure 2.2: Regions where one of the three γ-ray interactions dominates over the other two as a function of the atomic number (Z) and energy (E) (Evans, 1955).

2.1.2 Compton scattering

In order to describe Compton scattering, two aspects should be considered: kinematics and cross-section of the interaction. The first one is related to the energies and directions of the particles involved in the scattering. The second aspect is related to the probability that a Compton interaccion takes place.

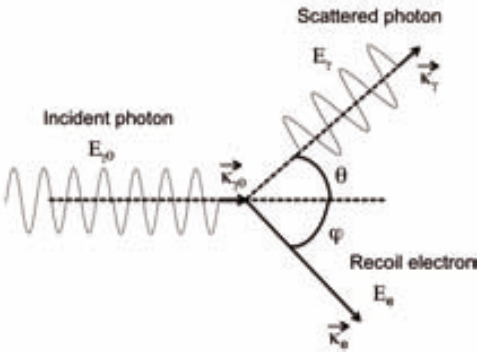

Figure 2.3: Schematic representation of the Compton scattering kinematics

Figure (2.3) schematically shows the interaction process between an incident γ-ray photon and an electron. The incident γ-ray is scattered at an angle θ with respect to its initial direction, and transfers part of its energy to the recoil electron.
Using the following notation:

- E_{γ_0} and $\vec{k}_{\gamma_0}$: Energy and momentum of the initial gamma-ray.
- E_γ and $\vec{k}_\gamma$: Energy and momentum of the scattered gamma-ray.
- E_e and $\vec{k}_e$: Energy and momentum of the recoil electron.
- θ: Scatter angle of the gamma-ray (*Compton scatter angle*).

- : Scatter angle of the recoil electron.

the interaction process can be described in terms of conservation of energy and momentum of photon and electron:

$$\begin{aligned} k_{\gamma_0} + k_{e_0} &= k_e + k_\gamma \\ E_{\gamma_0} + E_{e_0} &= E_e + E_\gamma \end{aligned} \tag{2.6}$$

The initial energy and momentum of an atomic bound electron are unknown. In the following it is assumed that the electron is at rest and its momentum is zero. As will be explained later, this approximation has a consequence, the so-called Doppler-broadening limit to a Compton telescope angular resolution.
Application of the relativistic energy-momentum-relation and the relation between energy and momentum of photons leads to the Compton equation:

$$E_\gamma = \frac{E_{\gamma_0}}{1 + \alpha\,(1 - cos\theta)} \tag{2.7}$$

where $\alpha = \dfrac{E_{\gamma_0}}{m_e c^2}$ is the initial photon energy in units of electron rest mass (0.511MeV).
As it was pointed out in the previous section, in the limit α 0, the process goes from being inelastic (Compton scattering) to being elastic (Thomson Scattering).
It is important to remember that this equation only states how the various parameters must be related to each other if a Compton interaction takes place, but it tells us nothing about the probability of a photon (or electron) being scattered in any particular direction.

Thomson and Klein-Nishina cross sections

The first expression of the Compton cross-section for unpolarized radiation and free electron was derived by Klein & Nishina (1929) from quantum electrodynamics:

$$\left(\frac{d\tau}{d\Omega}\right)_{KN} = \frac{r_0^2}{2}\left(\frac{E_\gamma}{E_{\gamma_0}}\right)^2\left(\frac{E_\gamma}{E_{\gamma_0}} + \frac{E_{\gamma_0}}{E_\gamma} - sin^2\theta\right) \tag{2.8}$$

with r_0 the classical electron radius (e^2 m_0c^2= 2.818 x 10^{-13} cm).
Figure 2.4 (a) shows the Klein-Nishina Compton scattering differential cross-section, as a function of the scattering angle θ for several energies of the incident γ-ray. The backward scattering ($\theta > 90$) probability is lower for an incident photon with larger energies. A representation in polar coordinates for the same distribution is also shown in Figure 2.4 (b).
Equation (2.8) was derived on the assumption that the scattering electron is unbound and at rest. On the limit $E_{\gamma_0} << m_e c^2$, the KleinNishina equation reduces to the Thomson scattering equation:

$$\left(\frac{d\tau}{d\Omega}\right)_{Th} = \frac{1}{2} r_0^2\left(1 + cos^2\theta\right) \tag{2.9}$$

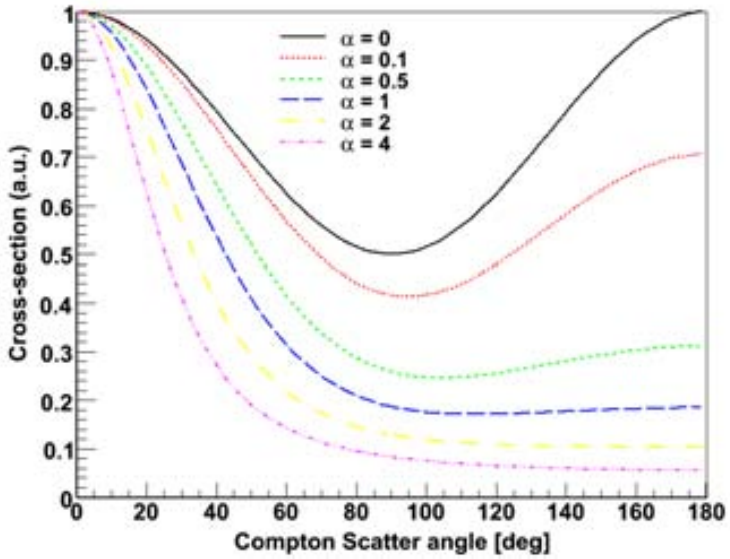

(a) Angular distribution of Klein-Nishina cross section for several incident γ-ray energies, represented as a function of $\alpha = E_{\gamma_0}\ 511keV$. All curves are normalized at $\theta = 0°$.

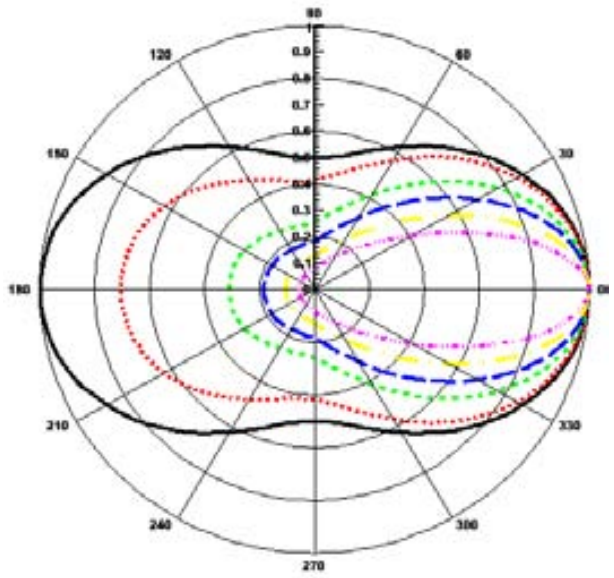

(b) Polar representation of the Klein-Nishina cross section. We clearly see that the higher the energy, the stronger is the forward scattering. Uses the same color code than figure (a).

Figure 2.4: Klein-Nishina cross section as a function of the Compton scatter angle θ for different energies.

This equation is also called elastic or coherent scattering equation. Note that the low-energy limit given by the Thomson scattering equation (α 0), is also represented in the uppermost curve in Figure 2.4.

Bound Compton cross section

Equation (2.8) is also known as unbound Compton cross-section, since the electron is assumed to be unbound to a nucleus. In reality, electrons are bound to a nucleus and with a given momentum. Although the equation is a good approximation for many applications, in the case of low energy photons or small scatter angles this approximation is not valid, since the recoil energy of the electron would be comparable (or smaller) to the electron binding energy.
In order to take into acount the binding of the electrons to the atom and its momentum distribution, the Klein-Nishina differential cross-section is multiplied by the so-called *incoherent scatter function*:

$$\left(\frac{d\tau}{d\Omega}\right)_{Bound} = \left(\frac{d\tau}{d\Omega}\right)_{KN} S(E_\gamma\ \theta\ Z) \tag{2.10}$$

where the incoherent scattering factor, $S(E_\gamma\ \theta\ Z)$, is a function of the energy of the incident photon, E_γ, the scattering angle, θ, and the atomic number of the scattering material, Z.

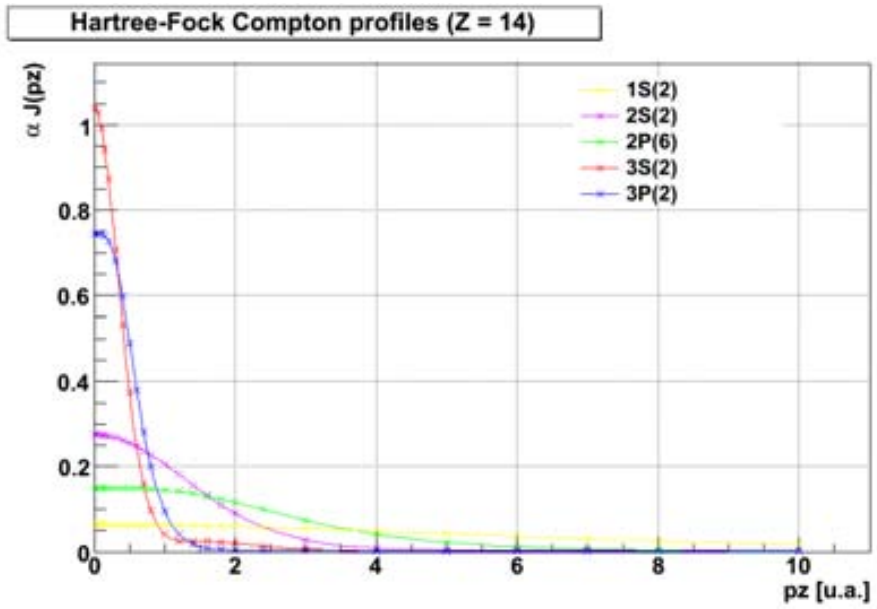

Figure 2.5: Shellwise Compton profile data for silicon from Biggs *et al.* (1975)

The Klein-Nishina cross-section and angular distribution is slightly modulated by $S(E_\gamma\ \theta\ Z)$, specially at low energies. Another important effect, not predicted by the unbound scattering model, is the broadening of the energy distribution of Compton scattered photons known as Doppler broadening.

Doppler broadening

The observed broadening in the Compton spectra was interpreted by DuMond (1929), as a Doppler broadening caused by the momentum distribution of the scattering electrons.

Instead of a fixed energy for a given scattering angle, scattered photons show an energy distribution around the predicted energy given by equation 2.7. These distributions (known as *Compton profiles*) for each atomic electron sub-shell can be obtained based on the Hartee-Fock calculations.
Figure 2.5 shows the shell-wise Compton profiles for the case of silicon. These Hartree-Fock Compton profiles, $J(pz)$, are a collection of orbital atom data as a function of the projected momentum of the electron, pz. Inner shells having a larger pz result in a greater broadening. Values of the Compton profiles for the elements $1 < Z < 102$ were published by Biggs *et al.* (1975).

2.1.3 Polarization of γ-ray photons

The interactions of γ-ray with matter discussed in section 2.1.1 (photoelectrons, scattering photons and electron-positron pairs) depend on the polarization of the incident photons. This dependence can be the basis of the polarization measurement in different energy ranges. Regarding the MeV range, when a polarized γ-ray photon undergoes a Compton scatter, the probability for the photon to be scattered at a given angle depends on the *azimuthal angle*, i.e. the angle between the polarized vector of the incident γ-ray and the scattering plane.
For linearly polarized γ-ray, the Klein-Nishina cross-section (equation (2.8)) becomes:

$$\left(\frac{d\tau}{d\Omega}\right)_{KN} = \frac{r_0^2}{2}\left(\frac{E_\gamma}{E_{\gamma_0}}\right)^2\left(\frac{E_\gamma}{E_{\gamma_0}} + \frac{E_{\gamma_0}}{E_\gamma} - sin^2\theta cos^2\theta\right) \tag{2.11}$$

where θ is the azimuthal angle, while the other variables are defined such as in equation (2.8). For any specific scattering angle, the scattering probability is maximized when $\theta = 90°$, i.e., it is more likely that the photon will be scattered at directions perpendicular to the polarization plane of the incident photon. By measuring the azimuthal angular distribution of the scattered photons, the polarization information of the incident photons can be deduced. The probability distribution of the azimuthal scatter angle, derived from equation 2.11, is:
In order to quantify the polarization information, a modulation factor (σ) is defined:

$$\sigma = \frac{N(\quad) - N(\quad + \psi\ 2)}{N(\quad) + N(\quad + \psi\ 2)} \tag{2.12}$$

where is an arbitrary angle in a plane perpendicular to the incident direction, and N is the measured number of events about that angle (Δ). The azimuthal angle in equation (2.11) is given by $\theta =$ $-$ $_0$, considering that the polarization direction of the incident γ-rays is at $_0$. From the above definition of the modulation factor, considering equation (2.11), the following expression can be derived:

$$\sigma = \frac{-sin^2\theta}{\frac{E_{\gamma_0}}{E_\gamma} + \frac{E_\gamma}{E_{\gamma_0}} - sin^2\theta} cos(2(\quad - \quad_0)) = M(E\ \theta)\cdot cos(2(\quad - \quad_0)) \tag{2.13}$$

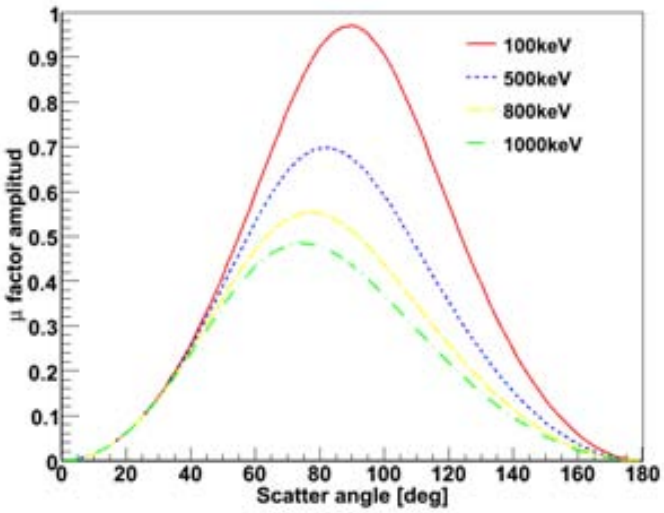

Figure 2.6: Amplitude of the μ-factor versus the scattering angle for different energies of the incident photon.

At each Compton scattering angle θ, the function $cos(2(\quad - \quad_0)$ has a period ψ. The σ factor is maximized when is perpendicular to the polarization plane of the incident photon. The amplitude of the σ factor ($M(E\ \theta)$), versus the scattering angle at a given incident energy, is shown in Fig. 2.6. The maximum value is obtained when the scattering angle is slightly less than $\theta = 90°$, and this maximum value is enhanced for lower γ-ray energies.

2.2 γ-ray detectors

In general terms, a γ-ray detector can be defined as a device that registers the presence of γ radiation. It may only count the number of γ-rays hitting the detector (Geiger-Mueller counter), or also determine the energy (spectrometer), or even measure the direction of the incoming γ-ray (imaging detector). In any case, whatever is the complexity of the measure performed, a γ-ray detector must be able to register in some way the interaction process of γ-ray photons with matter. That is to say, the detector must be *sensitive* to the energy transfer from the photon to the matter through any of the interaction processes described in section 2.1.1. A detailed discussion on the operational principles of γ-ray detectors can be found in Knoll (1999).
The characteristics and operational principles of semiconductor (e.g., Si, Ge, CdTe) and scintillator (e.g., NaI, $LaBr_3$, liquid Xenon) γ-ray detectors are described in the following paragraph, focusing our description on *cadmiun-telluride* and *liquid Xenon* detectors.

2.2.1 Basic properties of γ-ray detectors

There are many *figures of merit* that describe the properties of a γ-ray detector: sensitivity, detector efficiency, energy resolution, response function, spatial resolution, response time

and so on. A detailed description of all of them can be found in Leo (1994). Here, the efficiency and energy resolution is discussed.

Efficiency The *absolute or total efficiency* of a detector is defined as the ratio between the number of photons emitted by the source and the number of photons actually detected. On the other hand, the ratio between the number of photons incident on the detector and the number that are actually detected is defined as the *intrinsic efficiency*. In both cases, the energy of the incident photons is not taken into account. The *full energy peak efficiency* (or *photopeak efficiency*), that takes into account the energy of the incident photons, is defined as the ratio of photons detected within a specific energy range divided by the number of incident photons.

Energy resolution The capability of a detector to resolve two close lying energies is known as the energy resolution. In γ-ray astronomy the resolution, R, at the energy, E_0, is defined as:

$$R = \frac{\Delta E}{E_0} \tag{2.14}$$

where ΔE is the width of the peak in the measured spectrum, that is usually given in terms of the *full-width-half-maximum* (FWHM). Assuming a Gaussian distribution centered on the energy peak (E_0) the FWHM correspond to 2 35 times the standard deviation (τ) of the distribution.
The width of the measured energy peak with any γ-ray detector has three different contributions:

$$(\Delta E)^2 = (\Delta E_{Fano})^2 + (\Delta E_{elec})^2 + (\Delta E_{collect})^2 \tag{2.15}$$

where:
ΔE_{Fano} is the statistics limit contribution, ΔE_{elec} is the electronic noise contribution, and $\Delta E_{collect}$ is the contribution due to charge collection. The last two contributions will be discussed in section 2.2.2 and section 4.3.3.2 respectively. Regarding the statistics contribution, it provides the lower limit to the energy resolution. This limit comes from the fact that charge carriers are generated within the detector by a quantum of radiation. Assuming that the formation of charge carriers is a Poisson process, the standard deviation (τ) of the statistical noise is proportional to $\overline{N}$, with N the average number of charge carriers created in the detector. In this case, the limiting resolution due to statistical fluctuations is: $R_{Poisson} = \frac{2\,35}{\overline{N}}$ (see e.g. Knoll (1999)).
It was demostrated by Fano (1947) that the variance in the fluctuation of electron-ion pairs produced by an ionizing particle, when all its energy is absorbed by a stopping material, is not given by Poisson statistics. This indicates that the formation of individual charges carriers is not independent. The ratio between observed statistical fluctuations and the ones predicted from Poisson statistics is called *Fano factor*:

$$F = \frac{observed\ variance}{Poisson\ predicted\ variance (= N)} \tag{2.16}$$

The statistical limit to the resolution becomes:

$$R_{statistical} = 2\ 35 \quad \sqrt{\frac{F}{N}} \tag{2.17}$$

where F is a positive constant less or equal to one. For instance, the Fano factor in semiconductors is in the range (0.06-0.14) (Devanathan *et al.*, 2006).

2.2.2 Semiconductor detectors: Cadmium-Telluride

Semiconductor detectors are based on the collection of charges (electrons-holes) by the application of an external electric field to the material. After the interaction of a γ-ray photon in the semiconductor, electrons are raised to the conduction band leaving an equal number of positive holes in the valence band. Then, a strong electric field is applied across the device in order to separate the pairs (before they recombine) and drift them to the electrodes. The movement of electrons and holes induces a charge in the electrodes (anode and cathode) which can be calculated by the Shockley-Ramo theorem (see review by He (2001)). The energy of the incident γ-ray photons can be measured from the induced charge on the electrodes.

The spectroscopic performance of a semiconductor detector is affected by the so-called *charge collection efficiency* which relates the induced charge in the detector electrodes with the total generated charge (electrons-holes) in the semiconductor. The physical properties of the semiconductor (density, electron and hole mobility, etc) as well as the external conditions (temperature, electric field intensity, etc) will determine the charge collection efficiency. Table 2.1 lists the main physical characteristics at room temperature of some semiconductors. Data are taken from Owens & Peacock (2004) and Devanathan *et al.* (2006).

Mobility (σ) and lifetime (λ) of a charge carrier are intrinsic transport properties of a semiconductor, that depend on processes such as recombination and trapping which take place in the crystal as a result of its internal structure (e.g., impurities and defects in the crystalline lattice). The product $\sigma\lambda$ is an important figure of merit to determine the charge-transport properties of a semiconductor. As listed in table 2.1, Si and Ge have a high $\sigma\lambda$ factor, therefore, excellent charge-transport properties. In fact, Ge detectors have the best energy resolution available for γ-ray spectrometry.

The strong electric field required to efficiently collect the charges, can induce a current in the semiconductor even without the interaction of a γ-ray photon. This is the so-called *leakage current* whose origin lies in the carriers generated by thermal excitation.

	Si	Ge	CdTe	GaAs	CdZnTe
Density $[g\ cm^3]$	2.33	5.33	5.85	5.32	5.78
Z	14	32	48,52	31,33	48,30,52
E_{gap} [eV]	1.12	0.67	1.44	1.43	1.57
E_{e-h} [eV]	3.62	2.96	4.43	4.2	4.64
μ_e $[cm^2V^{-1}s^{-1}]$	1400	3900	1100	-	1000
μ_h $[cm^2V^{-1}s^{-1}]$	1900	1900	100	-	120
τ_e [s]	10^{-3}	10^{-3}	3×10^{-6}	-	3×10^{-6}
τ_h [s]	10^{-3}	2×10^{-3}	2×10^{-6}	-	10^{-6}
Fano Factor	0.06	0.06	0.06	0.14	0.10

Table 2.1: Physical properties at room temperature of CdTe, CdZnTe, Si, and Ge.

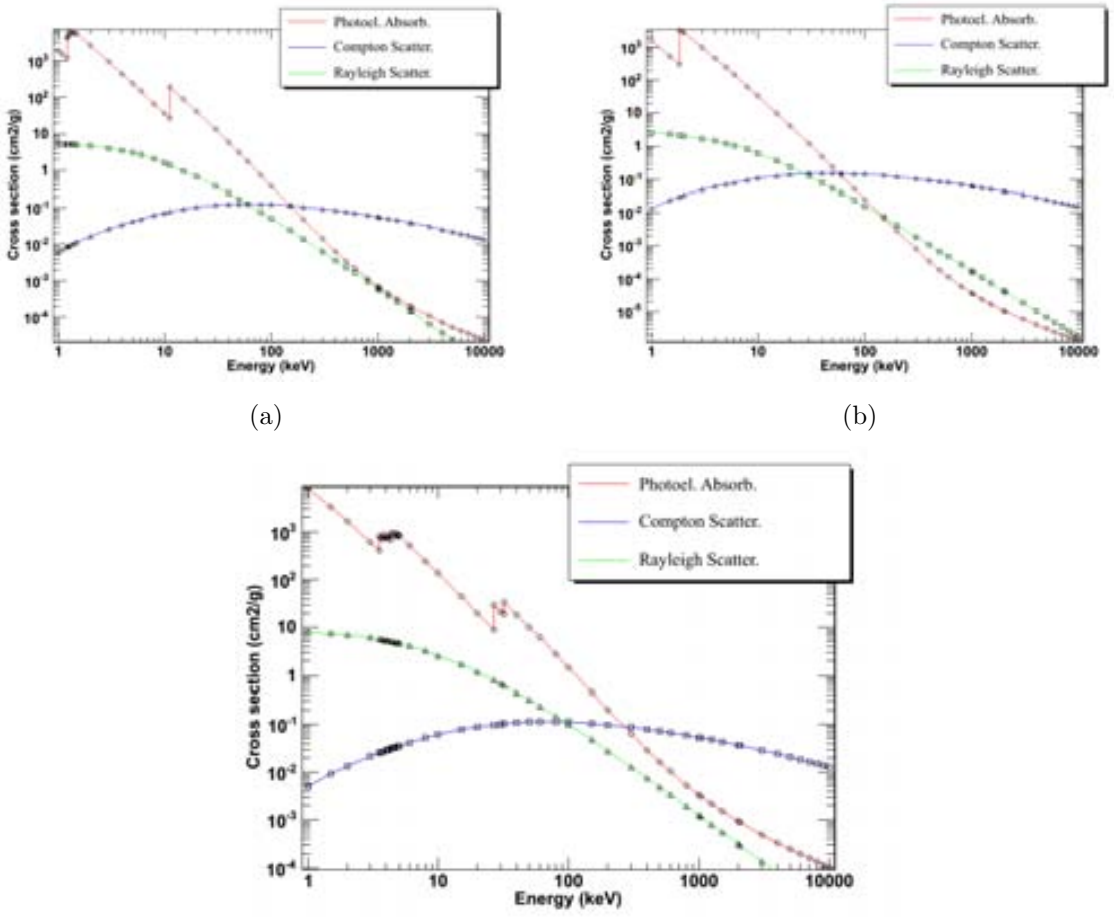

(a)

(b)

(c)

Figure 2.7: Compton, Rayleigh and photoelectric cross section for (a) gemanium, (b) silicon and (c) cadmium-telluride. Data are taken from NIST-XCOM, (Berger *et al.*, 2009).

This current arises when the thermal energy exceeds the energy bandgap (E_{gap}) of the semiconductor. Regarding the bandgap energy (E_{gap}) listed in table 2.1, there are two categories of semiconductor detectors: those which have a narrow bandgap, and therefore need to be cooled to avoid a large leakage current (e.g., Ge requires cryogenic tempera-

tures ∼77K), and those which have a wide bandgap and can operate at room temperature (e.g., CdTe).

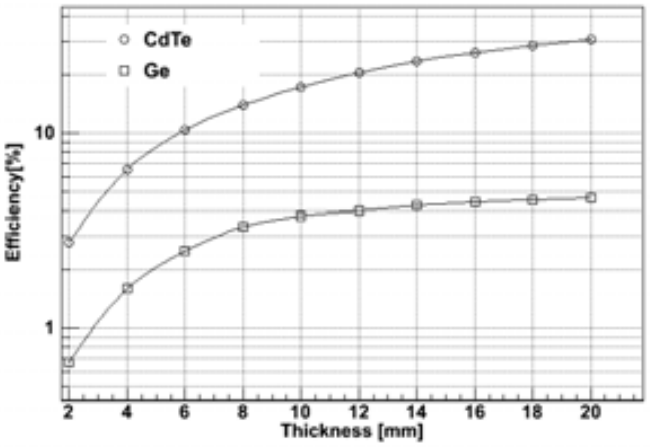

Figure 2.8: Photopeak detection efficiency versus thickness of CdTe (circles) and Ge (square), for 511keV γ-ray photon.

Concerning the detection efficiency of semiconductor detectors, as discussed in section 2.1.1, high atomic number and density will enhance the linear attenuation coefficient in the material. Therefore, a high efficiency is expected with CdTe and CdZnTe detectors. The cross-section of the main interaction processes for silicon (Si), germanium (Ge) and cadmium-telluride (CdTe) are shown in Figure 2.7. As shown, the energy where Compton scattering becomes the dominant interaction is different for each semiconductor.
Simulations with the Geant4 Monte Carlo code (see Appendix B.1.1) were performed in order to calculate the *detection efficiency* of CdTe and Ge. Figure 2.8 shows the *photopeak detection efficiency* of 511keV γ-rays for various thicknesses of CdTe and Ge. An efficiency of 15% is obtained for a 10mm thick CdTe semiconductor, while an efficiency below 4% is obtained for a Ge semiconductor with the same thickness and incident photon energy. Figure 2.9 shows the photopeak detection efficiency of CdTe at different energies for a thickness of 10mm and 5mm. In order to obtain an efficiency of ∼10% at 1MeV energy, thicknesses above 10mm of CdTe are needed. These efficiencies assume that γ-ray photons deposit all their energy in the detector volume and that all electron-hole pairs generated in the detector can be collected, i.e., full charge collection. However, the charge collection efficiency in CdTe is far from 100%. In fact, the considerable amount of charge loss in CdTe due to the low mobility (σ) and short lifetime (λ) of holes, degrades the energy resolution achieved with this material (see e.g. Siffert (1994)).

In order to illustrate the impact of incomplete charge collection on the spectroscopic performance of a CdTe detector, we considered the charge collection efficiency given by the Hecht equation (Hecht, 1932):

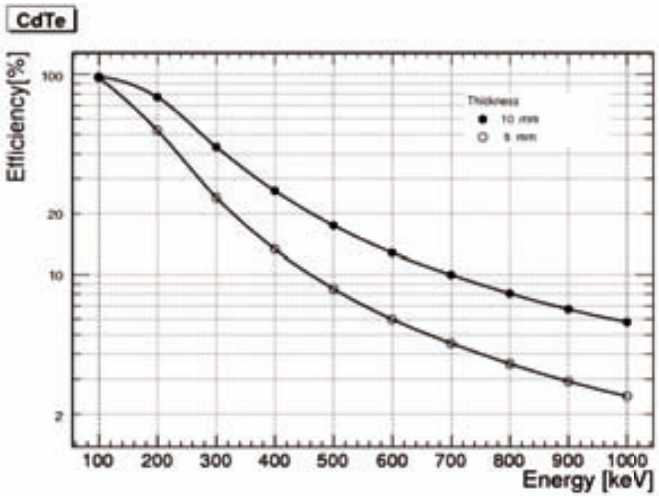

Figure 2.9: Photopeak detection efficiency of CdTe at different energies for a detector of 10mm (closed circles) and 5mm (open circles) thickness.

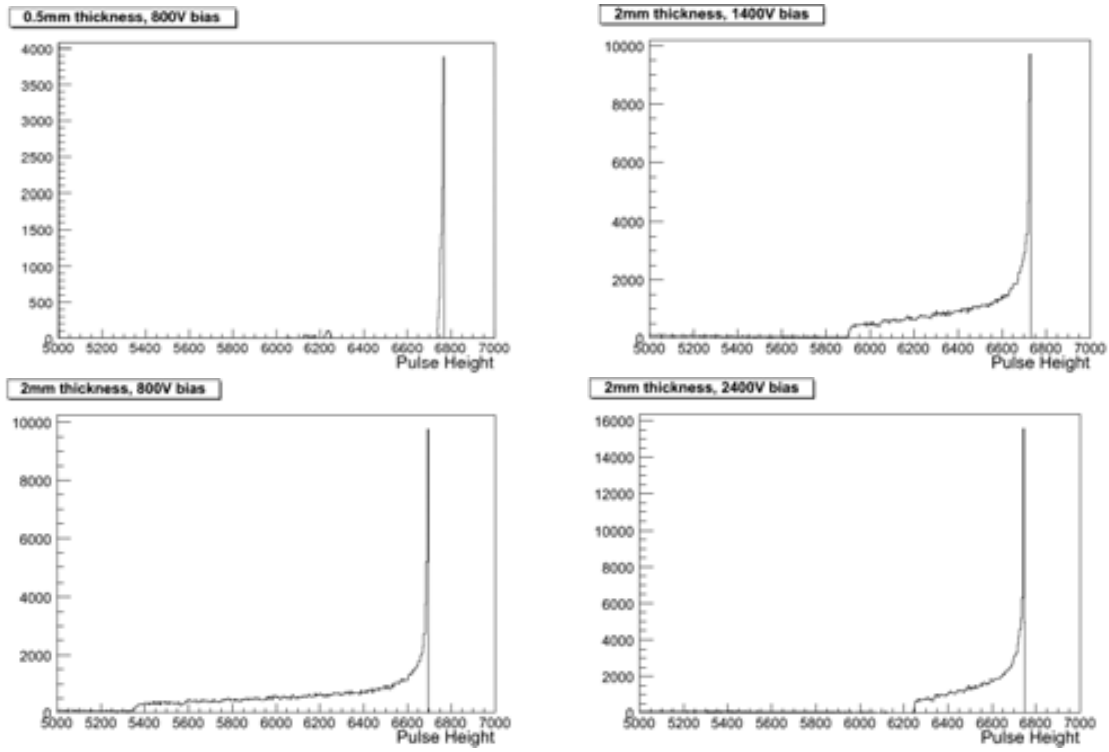

Figure 2.10: Pulse Height spectra simulated with the Geant4 Monte Carlo code and the Hecht equation. Details are given on the test.

$$\frac{Q}{Q_0} = \left[\frac{\lambda_h}{d}\left(1 - exp\Big(-\frac{z}{\lambda_h}\Big)\right) + \frac{\lambda_e}{d}\left(1 - exp\Big(-\frac{d-z}{\lambda_e}\Big)\right)\right] \tag{2.18}$$

where $\lambda_e = \mu_e \tau_e E$ and $\lambda_h = \mu_h \tau_h E$ is the mean drift path of electrons and holes respectively, d is the detector thickness and z the depth of interaction in the semiconductor.

From Hecht equation and with the Geant4 Monte Carlo code, the pulse height spectra for various thicknesses and bias voltages were computed (Álvarez & Hernanz, 2006). Figure (2.10) (left hand) shows the pulse-height spectra when γ-rays with energy of 300 keV irradiate the CdTe detector with a thickness of 0 $5mm$ and $2mm$. The applied electric field is assumed uniform ($E = \frac{V}{d}$), and a constant voltage bias of 800V is applied. Right hand of figure (2.10) shows the pulse-height spectra of CdTe with a constant thickness of $2mm$ and bias voltage of 1400V and 2400V.
A large tail appears on the spectra as the thickness of the detector increases. This tailing effect, caused by the charge loss in the CdTe semiconductor, is characteristic of semiconductor detectors with low mobility of carriers. The tail can be reduced by increasing the bias voltage. However, a high bias voltage could also increase the leakage current. In order to overcome this problem, a high resistivity semiconductor such as CdZnTe ($10^{10}\Omega\ cm$) would be desirable over CdTe ($10^{9}\Omega\ cm$). Moreover, CdTe detectors with a Schottky contact (Matsumoto *et al.*, 1997) withstand much higher bias voltages than ohmic connections, while at the same time their leakage current is lowered by several orders of magnitude. However, a critical issue of these detectors are their time instability under high bias voltages, the so-called *polarization effect* (Sato *et al.*, 2011).

Advances on CdTe/CdZnTe detectors

g the use of these detectors for years. This situation has changed during the last decade thanks to advances in different growth techniques (see review by (Sordo, 2009)).
Among other semiconductors, CdTe and CdZnTe are very attractive materials for γ-ray detection. The high density and atomic number of their components provide a high detection efficiency medium (see figure 2.9) while the wide band gap guarantees room temperature operation. However the considerable amount of charge loss in CdTe/CdZnTe, due to poor hole transport properties, limits their spectral properties.
In the last years, there have been significant advances to overcome the so-called *incomplete charge collection problem*. For instance, *unipolar electrode geometries*, *electronic corrections methods* and *specific detector configuration* that are sumarized in the following paragraph:

Unipolar electrode geometries. - Since electrons have better transport properties than holes (see table 2.1), some techniques to overcome the poor hole transport properties are based on collecting nothing but electron induced charges. This technique was implemented for first time in gas detectors (Frisch, 1944).
Specific electrode design provides single charge collection capabilities to CdTe/CdZnTe detectors. Among the broad variety of designs, we highlight the following configurations:

- Frisch grid semiconductor detector, where parallel metal strips are built on opposite faces of the detector, see McGregor *et al.* (1998).
- Coplanar grid structure, where a series of narrow strip electrodes are formed on the detector surface, see Luke (1995) and He *et al.* (1997).

- Pixels on the anode electrode, in which unipolar properties are presented if the pixel size is smaller than the detector thickness, see Barrett *et al.* (1995).

These detectors are shielded from the effect of the moving holes and thus their output signal due to the moving electrons. Although electron transport properties are much better than those of holes, there is still a significant amount of electrons that could be trapped, especially in a thick CdTe/CdZnTe detector. Other techniques, in combination with the above mentioned design, are used for further improvement. For instance, a method to correct for electron trapping was proposed by He *et al.* (1996), using a *depth sensing* technique. The depth of the γ-ray interaction in a semiconductor can be obtained by the correlated signal from anode and cathode. This depth sensing technique was applied to pixellated anode detectors to compensate for electron trapping by He *et al.* (1999).

Electronic corrections methods. - Since the mobility of electrons is much higher than hole s mobility, the contribution of each carrier can be separated by their respective *rise-time*, i.e. the time required for a signal to change from a specified value to a higher value. Rise-time discrimination (RTD) is based on the selection of preamplifier pulses with a short rise-time, which are mainly due to electrons. This technique improves the energy resolution but leads to significantly reduced sensitivity, since many pulses are rejected (Jordanov *et al.*, 1996).
Another electronic method is based on the analysis of the correlations between the amplitude (pulse height) and the rise time of the signals, the so-called *bi-parametric analysis*, see for example Richter & Siffert (1992).

Specific detector configuration.- Last, but not the least, we refer to some techniques to overcome the charge collection problem related to detector configurations. This technique is particularly useful for high energy detectors, where thick detectors are needed to reach high detection efficiency.

The idea of stacking together several thin CdTe devices and operating them as a single thick detector, was adopted by Takahashi & Watanabe (2001). A *stacked device* will reach high detection efficiency with good energy resolution, since high bias voltages for full charge collection can be easily applied in thin CdTe devices.

Another technique concerns the specific configuration of the electric field in the detector. In the so-called *planar transverse field* (PTF) configuration (Auricchio *et al.*, 1999), the direction of incoming gamma-rays is transverse (orthogonal) to the electric field applied in the detector. Therefore, the path length of the gamma-ray photon can be increased while the inter-electrode distance remains short. This technique, proposed for the baseline detector of the GRI mission, is discussed in Chapter 4.

2.2.3 Scintillation detectors: liquid Xenon

A scintillation detector is a luminescent material (either solid, liquid or gas) in which γ-rays induce the emission of light. Afterwards, light is collected by photodetectors and converted into an electric pulse by a photosensor (see section 6.1.1). The scintillator is typically surrounded with photodetectors in order to minimize loss of the isotropically emitted light and enhance detection efficiency.
A fundamental property of a scintillator is the linear conversion of the γ-ray energy into scintillation light. This allows to derive the energy of the incident γ-ray by adding up the energy collected by the surrounding photosensors. The number of photons emitted per unit of energy transferred to the medium is known as the *light yield*.

	(1/e) Decay time [ns]	ϵ_{max} of max emission [nm]	Density [$g\ cm^3$]	Total Light Yield [photons/keV]	Refractive index at ϵ_{max}
NaI(Tl)	250	415	3.67	38	1.85
BGO	300	480	7.13	9	2.15
BaF_2	0.7	$\sim$ 210	4.88	1.8	1.54
$LaBr_3$:Ce	16	380	5.08	63	$\sim$1.9
LXe (see Table 2.3)	4.3 , 22.0	178	3 (@1 atm and $T_{boiling}$)	72 ($\frac{1}{W_{ph}}$)	1.54-1.69
Plastic (NE 102A)	2.4	423	1.03	10000	1.58

Table 2.2: Properties of some inorganic scintillators and a typical organic plastic scintillator. Data are primarily taken from Saint (2009)

Table 2.2 lists some properties of a scintillator medium. The scintillation material can be classified in *organics* (e.g., Anthracene, Stylbene, plastics and some liquids) or *inorganics* (e.g., Bismuth Germanate (BGO), Cerium activated Lanthanum Bromide ($LaBr_3$:Ce), liquid Xenon (LXe), Sodium Iodide doped with Thallium (NaI(Tl)). As shown in the table, scintillator light yield is higher in organic materials, while inorganic materials have a higher stopping power.

Liquid xenon

Liquid xenon (LXe) is a very efficient medium to stop penetrating radiation due to its high atomic number (Z=54) and density ($3g\ cm^3$). Moreover, the production of both charge carriers and scintillation photons with high ionization and scintillation yields, along with fast time responses, makes liquid xenon an excellent medium for radiation detection. In addition, large and homogeneous volume detectors can be provided without passive material in between. Table 2.3 lists some important physical and operational properties of LXe taken from Aprile & Doke (2010) and references therein.

Parameter	Value	Parameter	Value
Atomic Number Z	54	Dielectric Constant	1.95
Mean atomic weight A	131.30	Temperature Range (K)	165-180
Density @ 1 atm and $T_{boiling}$ ($g\ cm^3$)	3	Wavelength of scintillation light (nm)	175
Fano Factor	0.059	Decay time constant (ns)	4.3 , 22.0
Drift Velocity (mm/ms) @ 1kV/cm	2.2	Ionization Potential (eV)	13.8
W-value (ionization) (eV)	15.6	Gap energy (eV)	9.28
W-value (scintillation) (eV)	14.7	Boiling point (K) @ 1atm	165.05

Table 2.3: List of some physical and operational properties of liquid Xenon.

Ionization

Liquid xenon has a band structure like a semiconductor, with a band gap energy, $E_g = 9\ 28eV$. Due to this large gap, LXe is an excellent insulator where high electric fields can be applied in order to drive the charge produced by ionization.
The average energy required to produce one electron-ion pair, know as *W-value*, is smaller (15.6 eV) than for other liquid rare gases (23.6eV for liquid argon and 18.4eV for liquid krypton).

Scintillation

The luminescence emission of LXe is attributed to the decay of excited dimers (or excimers) to ground state. This excimers are formed by direct excitation of atoms from the ionization process, but also from the recombination of electron-ion pair (Doke *et al.*, 2002). The scintillation light is centered at 177.6 nm, in the vacuum ultra-violet region (VUV), and has two characteristics times (4.3 ns and 22.0 ns), corresponding to the decay of two different excited molecular states (Hitachi *et al.*, 1983). The average energy required to produce a single photon is known as *Wph-value* and the maximum scintillation yield is given by $\frac{E}{Wph}$, where E is the energy deposited by the ionizing radiation.

Anti-correlation of ionization and scintillation

The charge and light signals produced in LXe in response to radiation interaction are anti-correlated: charge yield increases with increasing drift field but light yield is decreasing (see Figure 2.11). This anti-correlation was originally reported by Kubota *et al.* (1978) and the combination of both signals can be used to improve the energy resolution of a LXe detector.

Energy resolution

The moderate energy resolution achieved with a liquid Xenon detector is a significant drawback for γ-ray line spectroscopy. The best measured energy resolution is far from what is expected by the Fano factor. For instance, the Fano factor value shown in Table (2.3) predicts an energy resolution of about 0.1% at 1 MeV for electrons in liquid Xenon, while the experimental measured resolution is much worse (Ichinose *et al.*, 1992).

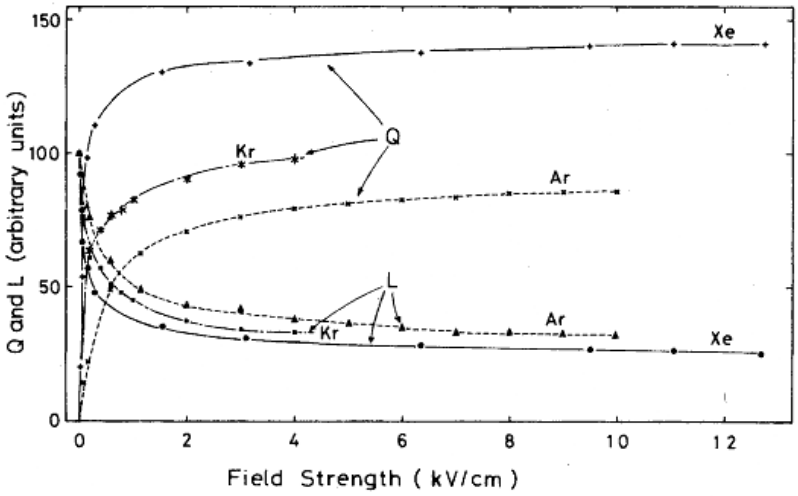

Figure 2.11: Variation of relative luminescence intensity L and collected charge Q in liquid argon, krypton and xenon for electrons vs. applied electric-field (Kubota *et al.*, 1978).

The large discrepancy between experimental and theoretical values is not yet fully understood, but fluctuations in electron-ion pair recombination rate are known to play a dominant role (see, for example, Aprile *et al.* (2006a)). In any case, this theoretical prediction points to the possibility of further improvements in energy resolution.
In this direction, the anti-correlation between ionization and scintillation signals produced by MeV γ-ray in liquid xenon has been used to improve the energy resolution. A measure of 1.7% (τ) at 662keV, with a drift field of 1kV/cm, was reported by Aprile *et al.* (2007) combining the ionization and scintillation signals.

2.2.4 Astrophysical applications

The great potential of semiconductor detectors has already been demostrated in astrophysics for imaging and spectroscopy applications (see e.g. Lebrun (2006)). In particular, room temperature semiconductor detectors, such as CdTe and CdZnTe, have shown their capability in the instrument IBIS onboard the European astronomical satellite INTEGRAL, (INTErnational Gamma-Ray Astrophysics Laboratory) (Winkler *et al.*, 2003) or the BAT instrument onboard the NASA mission SWIFT (Gehrels *et al.*, 2004), just to mention two examples.

Germanium detectors have been widely used in past and current γ-ray mission, such as SPI/INTEGRAL (Vedrenne *et al.*, 2003), Wind/TGRS (Owens *et al.*, 1995) and RHESSI (Lin *et al.*, 2002). Cooled high-purity Ge detectors offer the best energy resolution available, but this implies a complex cooling system and requires periodic annealing cycles to maintain its spectroscopic performance.

Classical scintillators, such as NaI or CsI, are being used in γ-ray astrophysics for quite a long time. The instrument COMPTEL (Schonfelder *et al.*, 1993) onboard the Comp-

ton Gamma-Ray Observatory (CGRO), used a liquid scintillator (NE213A) in the upper detector plane and an inorganic scintillator (NaI(Tl) on the bottom detector plane. Moreover, most of the instruments for γ-ray astrophysics are surrounded by an active shield made of scintillation detectors, in order to reject part of the cosmic and atmospheric background radiation (see section 1.2).

As far as liquid Xenon is concerned, this medium is being used in the development of a Compton telescope based on a Liquid Xenon Time Projection Chamber (LXeTPC) -the operational principles of a LXeTPC are discussed in section 6.1-. A liquid xenon gamma-ray imaging telescope prototype (LXeGRIT) was flown successfully in balloon-borne experiments (Aprile *et al.*, 2004). However, the modest energy resolution measured has been a major limitation of the LXe time projection chamber (TPC) technology for astrophysics applications.

2.3 γ-ray telescopes

In the previous section we described briefly how different detector devices measure the energy of γ-ray photons. However, a γ-ray telescope is not only a spectrometer but also it must be able to locate the position of the source in the sky, i.e., must be able to map the sky. Other important features of a γ-ray telescope are the capability of measuring the *arrival time* and *polarization* of photons from a cosmic source.
The different techniques to determine the position of a cosmic γ-ray source are briefly discussed in this section. More detailed descriptions can be found, for example, in von Ballmoos (2005).

2.3.1 Coded mask telescope

One way of obtaining the position of a γ-ray source is by modulating the signal from the source in a characteristic way. This modulation is performed by blocking part of the field-of-view of the detector with an absorber material. From the detected modulated signal and the knowledge of the blocking scheme, the position of the γ-ray source can be derived. The source signal can be modulated either *spatially* (e.g. coded mask telescopes) or *temporally* (e.g occultations, rotating modulation collimators).

A coded mask telescope typically consists of a planar array of opaque and transparent elements located in front of a position sensitive detection plane (see Figure 2.12). Thus, the source will project the shadow of the mask on the detection plane. The spatial distribution of γ-ray interactions in the detector plane, known as *shadowgram*, is registered by the position-sensitive detector. From the shadowgram, an image representative of the observed sky can be reconstructed (see, e.g Skinner (1984)).
Several instruments using the modulation principle, either *spatially* or *temporally*, have been built and succesfully applied to γ-ray astronomy:

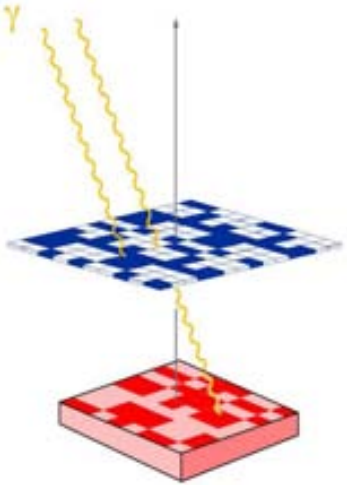

Figure 2.12: The basic design of a coded mask telescope (figure from von Ballmoos (2005)).

- The earth occultation technique was applied by the instrument BATSE (Harmon, 1992) onboard CGRO (Compton Gamma-ray Observatory).
- The rotating modulation approach is used by the solar spectroscopic imager RHESSI (Lin *et al.*, 2002).
- The coded mask technique was first applied by the instrument SIGMA on GRANAT satellite (Paul *et al.*, 1991). This system is currently wide-spread in γ-ray astronomy since it allows a high angular resolution with a relatively simple detection technique. At the present time three coded mask instruments (SPI, IBIS and JEM-X) operate onboard INTEGRAL (INTErnational Gamma-Ray Astrophysics Laboratory) (Winkler *et al.*, 2003).

2.3.2 Compton telescope

The measurement principle of a Compton telescope was first described by Schonfelder *et al.* (1973). The direction of the incoming photons is obtained through the dominant interaction between photons and matter in the MeV energy range (see 2.1.2). The principle of a Compton telescope is illustrated in Figure 2.13. An incoming γ-ray, with energy E_γ, interacts in the detector D1 transfering an energy E_1 and being deflected by an angle θ. The scattered photon is then absorbed in the detector D2.
In order to favor the scattering in D1, low Z materials are chosen, while high Z materials are needed in D2 to absorb the scattered photon.
The energy deposited (E_1, E_2) and interaction position (r_1, r_2) are measured in both detectors (D1 and D2). From them, the energy and direction of the incoming photon can be constrained. As far as the energy is concerned, the total energy can be obtained by :

$$E_{tot} = E_1 + E_2 \tag{2.19}$$

as long as the photon deposits the total energy in the detector D1 and D2. Concerning the direction of the incoming photon, it can be restricted to lie on a cone around the scatter direction (χ, ψ) with a half opening angle ϕ (see Figure 2.13(a)). The angle ϕ can be obtained from the Compton equation (2.7):

$$cos\ \phi = 1 - \frac{m_e c^2}{E_2} + \frac{m_e c^2}{E_1 + E_2} \tag{2.20}$$

but, it also can be derived by the direction of the incident ($\vec{r_1}$) and scattered ($\vec{r_2}$) photons:

$$cos\ \bar{\phi} = \frac{\vec{r_1}\ \vec{r_2}}{r_1\ r_2} \tag{2.21}$$

The uncertainties in the determination of the scattering angle are discussed in section (5.3.2), where the *angular resolution measure* of a Compton telescope is introduced.

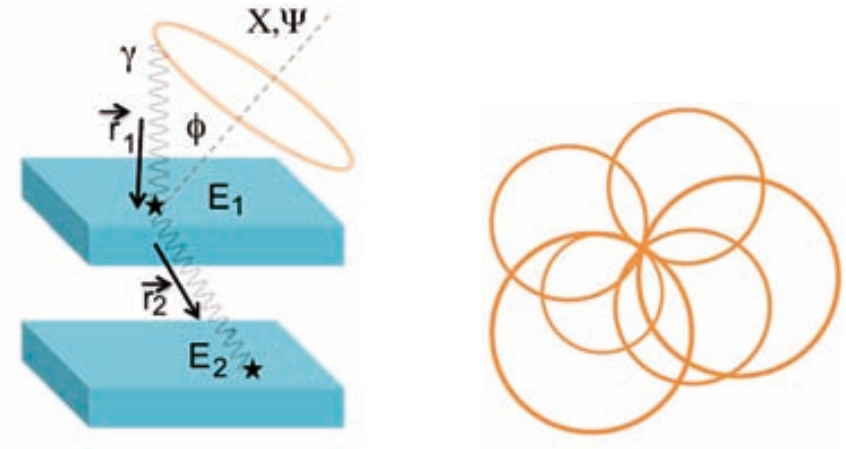

(a) Schematic illustration of a classical Compton telescope design consisting of two detectors (D1) and (D2)

(b) Projection of the Compton cone on the celestial sphere defining the so-called event circle

Figure 2.13: The principle of measurement of a Compton telescope.

Once the angle ϕ is derived and the scatter cone is defined, the projection on the celestial sphere of this cone will define the so-called event circle. The source position on the sky measured with a Compton telescope is the common intersection of many event circles, as is shown in Figure 2.13(b).

The Compton reconstruction technique was first applied by the instrument COMPTEL (Schönfelder *et al.*, 1993) onboard the Compton Gamma-Ray Observatory (CGRO) launched in 1991. Since then, there has not been another Compton telescope for γ-ray astronomy in space. However, there have been numerous designs and prototypes of *advanced Compton telescope* that have successfully flown in balloon experiments. Some of them will be mentioned in the following paragraphs.

2.3.2.1 Advanced Compton telescope

The Compton telescope described above can be considered as the classic design, where two detectors (D1 and D2) are arranged at a given distance. If the separation distance is large enough, the *time-of-flight* can be defined, i.e. time spent by photon to go from D1 to D2. For the COMPTEL telescope, a distance of $1.5m$ allows to define a $40ns$ time-of-flight. On one hand, a time window is a great advantage for background reduction but on the other hand, a large detector separation reduces the detection efficiency and the field-of-view of the instrument (see figure (2.14)). For instance, the efficiency of COMPTEL was about 1% (Schönfelder, 2003).

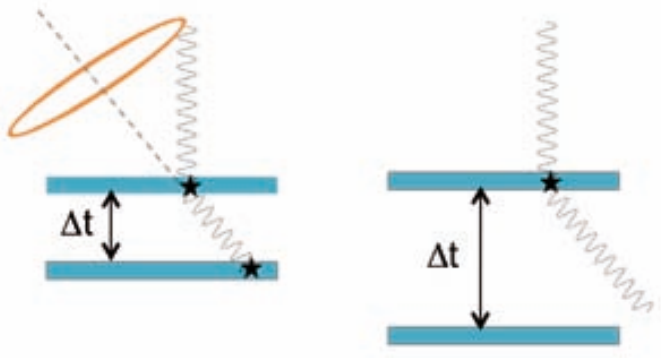

Figure 2.14: Schematic illustration of the reducing detection efficiency for a classical Compton telescope design with time-of-flight capability described in the text.

An advanced Compton telescope design aims to obtain high efficiency instruments with wide field-of-view and high background rejection capability. Therefore, advanced designs are compact instruments with many detectors arranged nearby, as close as a few centimeters. With such a short distance, time-of-flight (in the ns range) becomes technically difficult or impossible to measure. Hence, other background rejection techniques should be implemented.

Unlike the classic design where a photon is scattered in D1 and then absorbed in D2 (see figure 2.13), in an advanced design a single event may involve multiple interactions in many detectors (see figure 2.15).

Figure 2.15 (a), shows a Compton telescope configuration based on two different materials: a low Z medium where the Compton interaction takes place (the so-called tracker), and a high Z medium where the scattered photon is absorbed (the so-called calorimeter). The large number of detectors in the *tracker* and the geometric arrangement of the *calorimeter* increases considerably the efficiency of this Compton telescope. Single and multi-Compton events will take place in this configuration. In addition, the tracker may be able to track the recoil electron (illustrated as a red track in figure 2.15). This capability could be used to restrict the direction of the incident γ-ray to a small segment on

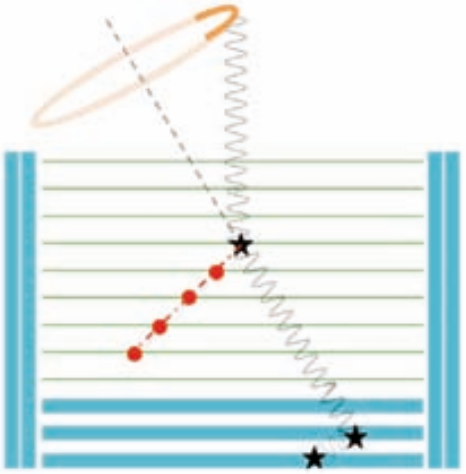

(a) Advanced Compton telescope design based on two detectors types: a low Z scatterer and a high Z absorber.

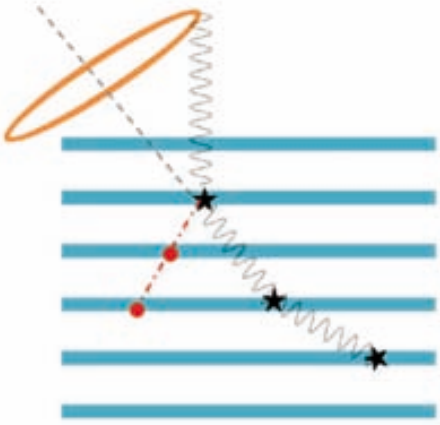

(b) Advanced Compton telescope design based on a single detector type.

Figure 2.15: Advanced Compton telescope design.

the event circle (see detailed discussion in Zoglauer (2005)). Several Compton telescope concepts are being studied using this configuration, e.g., MEGA (Kanbach *et al.*, 2004), TIGRE (Bhattacharya *et al.*, 2004) and SMILE (Kubo *et al.*, 2006), based on thin silicon, cadmium-zinc-telluride and gaseous xenon detectors, respectively.

Figure 2.15 (b), shows an advanced Compton Telescope configuration based on a single material where multi-Compton interactions take place. An event may consist of multiple interactions in which finally the photon is either absorbed or escapes. If the sequence has at least three Compton scatter interactions, the energy of the incident photon is uniquely determined by measuring the energies of the first two interactions, and the position of the first three interactions (Kurfess *et al.*, 2000). This technique will enhance efficiency, since the energy and direction of the primary γ-ray can be determined without the full energy of the photon being absorbed. Moreover, the capability of tracking the recoil electron (for high energy photons) could also be implemented. Compton telescope concepts based on this configuration are, for instance: NCT based on germanium detectors (Boggs *et al.*, 2004), LXeGRIT based on liquid xenon (Aprile *et al.*, 2004), or the thick silicon concept described by Kurfess *et al.* (2004).

2.3.2.2 Event reconstruction

Regardless of the Compton telescope design, the acquisition of a Compton telescope consists of a set of energy and position data without any temporal order (unless ToF measurement becomes feasible), from which the interaction sequence must be reconstructed in order to obtain the incident photon direction.
To illustrate this task, three interactions are drawn in Figure 2.16. In principle 3! possi-

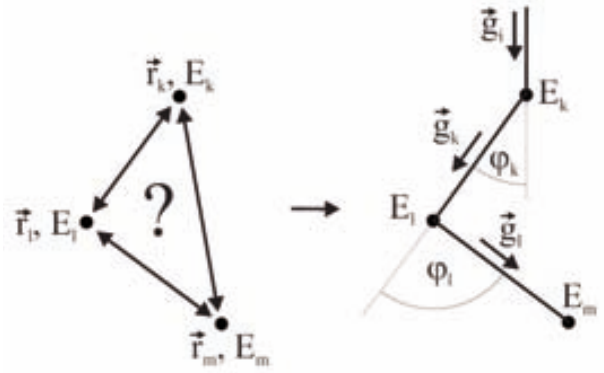

Figure 2.16: Schematic illustration of the reconstruction of a Compton interaction sequence with three hits.

bilities exist for the ordering of these hits, each with a different outcome of the incident photon direction. For n interactions, $n!$ possibilities have to be considered.
The main task of a reconstruction algorithm is to identify the interaction sequence of a γ-ray photon. For events with three or more interactions, redundant information is available to infer the most likely sequence. But in case of only two interactions, it is almost impossible to discriminate between both possible secuences except in rare cases.
Different approaches can be implemented to perform this ordering. In the so-called classic approach, the scatter angle ϕ is obtained from the measured energy (see equation 2.20) and compared with the angle inferred from the geometry (see equation 2.21). In case of a correct sequence ordering, the two evaluations of ϕ must show a certain agreement. A test statistic can be defined as indicator of the goodness of the reconstructed sequence.
Event reconstruction can be performed using the MEGAlib package (see Appendice B.2). The results based on this library have been successfully tested with experimental data from the MEGA prototype (Zoglauer, 2005).

2.3.2.3 Angular resolution

The angular resolution of a Compton telescope is usually described in terms of the *angular resolution measure* (ARM). This figure of merit is defined as the difference between the initial photon scatter angle, $\bar{\phi}$ (see eq. 2.21), and the scatter angle reconstructed from the Compton equation ϕ (see eq. 2.20).

$$ARM = \phi - \bar{\phi} \tag{2.22}$$

As pointed out before, since those angles are obtained from measurement of energy and position, the uncertainties in these measurements limit the accuracy when determining the origin of the photons. But even an ideal instrument with infinite energy and position resolution, has an angular resolution limited by the *Doppler broadening* effect (see section 2.1.2).

The uncertainty on the measure of the Compton scatter angle has three contributions:

- The energy uncertainty contribution, given by the energy resolution of the detector.
- The spatial uncertainty contribution, given by the accuracy on the interaccion location, i.e., the detector spatial resolution.
- The Doppler broadening contribution, which is a fundamental limit for the angular resolution. This contribution is more important for low energies, large scattering angles and a high atomic number of the scatter detector (Zoglauer & Kanbach, 2003).

2.3.2.4 Imaging response

The measurement performed with any γ-ray telescope can be expressed as:

$$D = R \cdot I + B \tag{2.23}$$

with D being the measured data, R the instrument-response matrix, I the celestial source intensity and B the instrumental background.
The goal of any image reconstruction algorithm is to invert the measurement process and determine the source image I from the measured data D. Since many parameters may be measured per γ-ray photon (even more in an advanced telecope as discussed in section (2.3.2.1)) the response R is a multi-dimensional matrix and the inversion of equation 2.23 becomes a difficult problem that can only be performed using statistical estimation theory methods. Among these methods, *list-mode maximum-likelihood expectation-maximization* algorithm (LM-ML-EM)[1] is an iterative statistical algorithm that makes successive approximations to the most probable source distribution that would have led to the observed data.

2.3.2.5 Polarization sensitivity

An important feature of a Compton telescope is its capability for measuring polarization. Polarized γ-rays lead to modulation of the azimuthal scatter angle of Compton events (see section 2.1.3), from which the degree of polarization of the photons can be determined (Lei *et al.*, 1997).
A figure of merit to quantify the polarimetry capability of an instrument is the minimum detectable polarization (MDP), which is defined as:

$$MDP = \frac{n_\sigma}{\sigma_{100} N_S} \sqrt{\frac{2(N_S + N_B)}{T}} \tag{2.24}$$

[1]The list-mode maximum-likelihood expectation-maximization algorithm, originally developed for medical imaging (Wilderman *et al.*, 1998), is wide-spread in the field of Compton imaging telescopes. In order to obtain an image, this algorithm maximizes the expectation of the underlying likelihood function. A detailed discussion about the operational principles of the this algorithm can be found in Lange & Carson (1984) and Zoglauer (2005).

where n_σ is the significance level, N_S is the source count rate, and N_B is the background count rate in the time T. Finally, σ_{100} is the detected modulation (see equation 2.12) for an 100% linearly polarized beam.

2.3.3 Focusing γ-ray telescopes

Compared to the previously presented concepts (Compton and coded mask Telescope), focusing γ-ray telescopes allow to reach unprecedented sensitivities and angular resolution, thanks to the decoupling of collecting area and detector volume, i.e. the photon collecting area can increase without a parallel increase of the detector volume, thus improving the signal without increasing substantially the background noise (see figure 2.17). With focusing telescopes, a drastic improvement in both sensitivity and angular resolution are expected with respect to the best nonfocusing instruments of the current generation.

A focusing telescope is made of two parts: the focusing optics and the focal plane detector.

Figure 2.17: The principle of a focusing system for high energy photons. Gamma-rays are concentrated in a focal point behind the collecting area where a small detector is located (figure from von Ballmoos (2005)).

2.3.3.1 Focusing optics

In the MeV energy range, *Laue* and *Fresnel* lenses are the proposed systems to focus γ-rays. For an overview of focusing telescopes in nuclear astrophysics see von Ballmoos (2006).

Diffraction lenses

Gamma-rays can be focused via crystal diffraction lenses. An incoming gamma-ray must satisfy the Bragg-relationship in order to be diffracted. This relationship relates the energy

of the incident photons, the incident angle and some parameters of the crystalline structure (see section 3.1.1). A Laue lens is made of a large number of crystals which allows to concentrate the incident radiation onto a focal spot (see figure 2.17). As a consequence of the small Bragg angle at the MeV energy range, the focal length of a Laue lens telescope is relatively long, in the range of tens to hundreds of meters. Large deployable structures or formation flying of two spacecrafts have been proposed for space missions involving Laue lenses (see section 2.4).

Fresnel lenses

Fresnel lenses can focus γ-rays by using a combination of diffraction and refraction. Because the wavelengths of γ-rays are so short, and the penetrating power is high, a phase shift can be achieved in a highly transparent thickness of material. This type of γ-ray lens was proposed by Skinner (2001). A telescope based on these principles can have an angular resolution better than a micro arcsecond, and efficiency close to 100%. Despite this outstanding characteristics, an important drawback to its implementation is the long focal lengths (up to a million kilometers). On the other hand, development of *formation flying* spacecraft make possible a mission in which the lens and detector are on two separate spacecrafts, separated by this huge distance.

2.3.3.2 Focal plane detector

A focusing γ-ray telescope configuration working at the MeV energy range will require a focal plane detector able to fulfill the following requirements:

- *high stopping power*: the detector has to be composed of a high-Z and high density material in order to provide significant stopping power at energies up to the MeV range and, therefore, a high detection efficiency over the entire operating range of the focusing lens.
- *high spatial resolution*: a spatial resolution of the order of $1mm$ (or better) is required to sample the PSF of a Laue lens.
- *high energy resolution*: the energy resolution is a critical parameter to reach the scientific requirements. A resolution of 1% at 1MeV (or better) is required;
- *small detector volume*: the field-of-view (FoV) of the instrument depends on the area of the detector. A trade off between low background and large FoV should be considered.
- *polarimetry capability*: sensitivity to the photon linear polarization is a scientific requiriment for the observation of several astrophysical emission processes. This capability is strictly related to the spatial resolution of the detector.

2.4 A Laue lens Gamma-ray telescope

The principles of a gamma-ray lens for nuclear astrophysics were successfully proven with the R&D project CLAIRE (von Ballmoos *et al.*, 2005) (see section 3.2). Once the objectives of the first prototype of Laue lens for nuclear astrophysics were achieved, the next natural step was to study and develop this technology towards a future space mission. In the last years, different mission concepts have been proposed. In 2004, the MAX mission was proposed to the French Space Agency (CNES). In 2007, an initiative of the European Gamma-Ray Community proposed the GRI mission to the ESA s Cosmic Vision 2015-2025 program. Finally, in 2010 the DUAL mission was proposed to the call of the European Space Agency for a M3 mission in the framework of the Cosmic Vision 2015-2025 program. Table 2.4 lists some benchmarks of the proposed Laue lens missions.

Mission [$Year$]	Laue Lens Mass [kg]	Laue Lens Energy range [keV]	Focal lengh [m]	Detector Mass [kg]	Num. spacecraft Technology
MAX [2004]	150	$[847 \pm 50]$ $[511 \pm 50]$	84	30	2 SC (formation flying)
GRI [2007]	523	[200-1300]	100	100	2 SC (formation flying)
DUAL [2010]	80	[800-900]	30	112	1 SC (deployable mast)

Table 2.4: Some benchmark of the proposed Laue lens missions.

The key technology required to accomplish a Gamma Ray Lens space mission was deeply studied by a Technological Reference Study conducted by ESA (Brown *et al.*, 2005). The proposed missions listed in table (2.4) (GRI and DUAL) have benefited from the results of this study to ensure their feasibility.

2.4.1 MAX

MAX was proposed by a consortium led by Peter von Ballmoos (CESR, Toulouse) to the French Space Agency (CNES) in response to an anouncement of opportunity for a formation flight demonstration mission (von Ballmoos *et al.*, 2004b). MAX consists of a Laue lens mounted on a spacecraft where photons are collected and focused onto a detector placed on a second spacecraft. Both spacecrafts are *flying in formation* (Duchon, 2005), to form a gamma-ray telescope of $86m$ focal length (see figure 2.18).
The MAX γ-ray Laue lens is made of copper and germanium crystals (about 8000) arranged on concentric rings. It was designed to simultaneously focus two energy bands (100keV wide) centered on two lines: the broadened 847keV line from the decay of ^{56}Co produced in Type Ia supernovae, and the 511keV positron annihilation line from the Galactic centre region.
The base line focal plane instrument of MAX is a stack of planar Ge detectors using orthogonal strips, cooled by a passive radiator and actively shielded by BGO scintillators. A Monte Carlo study of the detector concepts for MAX can be found in Weidenspointner *et al.* (2005b).
A feasibility study of the MAX mission was conducted by the French Space Agency (CNES). Further information can be found in Barriere *et al.* (2005) and Barriere *et al.*

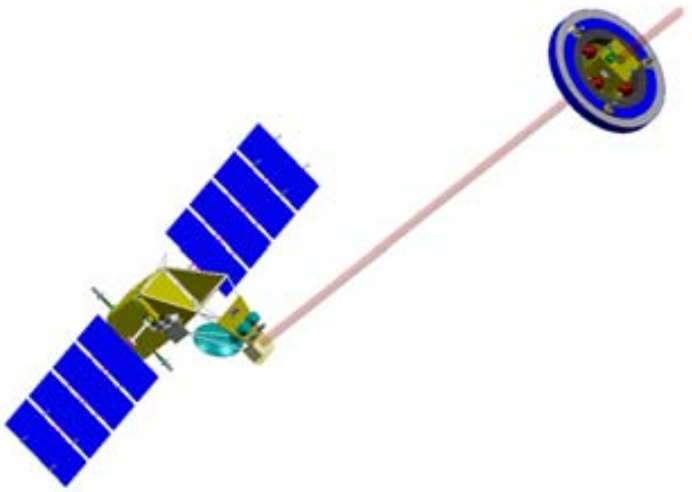

Figure 2.18: A possible design of a focusing space mission based on the formation flying concept. The imaginary optical axis from the lens to the detector is illustrated (figure from MAX collaboration).

(2006) (*including Alvarez J.* in both cases).

2.4.2 GRI

The Gamma-Ray Imaging (GRI) mission was an initiative of the European Gamma-Ray Community in 2007, aiming to the definition of an European Gamma-Ray mission within ESA s Cosmic Vision 2015-2025 program (Knodlseder, 2007). The GRI telescope is composed of two satellites that are actively keeping in formation flying at $100m$ distance (see figure 2.18). One spacecraft carries the focusing optics while the other spacecraft carries the detector. The GRI proposal benefited from the results of the MAX project study.
The Laue lens of GRI consists of copper and germanium crystals (about 28.000) arranged on concentric rings. It was designed to cover the energy range from $200keV$ up to 1 $3MeV$, with an angular resolution of $30arcsec$ and a narrow field-of-view of $300arcsec$.
The focal plane instrument of GRI is a stack of semiconductor detectors (CdZnTe/CdTe), actively shielded by BGO scintillators. The focal plane instrument is discussed in more detail in Chapter 4.

2.4.3 DUAL

The DUAL mission was proposed in 2010 by a consortium led by Peter von Ballmoos (CESR, Toulouse), in response to a ESA s call for a Medium-size mission opportunity for a launch in 2022 (von Ballmoos *et al.*, 2010a). The DUAL mission is composed of a single spacecraft. The optical modules are located on the main satellite while the detector module is situated on a deployable structure at a distance of $30m$ from the lens (see figure 2.19).

Figure 2.19: A possible design for a space-borne γ-ray telescope base on Laue lens (figure from DUAL collaboration)

The Laue lens of DUAL consists mainly of Cu and Ge crystals (about 5800) arranged on concentric rings. It was designed to cover the energy band $800keV - 900keV$, with an angular resolution of $1arcsec$ and a narrow field-of-view of $300arcsec$.
A Compton camera, based on a compact array of cross-strip germanium detectors with passive shielding, was proposed for the focal plane of DUAL.
In addition to the concept of focusing γ-ray telescopes, DUAL was also proposed as a survey mission. The Laue lens focuses gamma-ray photons onto the Compton telescope, while the wide-field of the instrument catches γ-ray photons from the full sky in the energy range from $100keV$ to $10MeV$. A more detailed study of the Compton camera of DUAL is presented in Chapter 5.

Chapter 3

A Laue lens for nuclear astrophysics

A Laue lens telescope is intended to overcome the lack of sensitivity for nuclear astrophysics γ-ray lines by focusing the cosmic γ-rays onto a small detector, and thus, reducing drastically the effective background volume noise.
The concept of a Laue lens telescope has been developed at *Centre d Étude Spatiale des Rayonnements*, Toulouse, for a number of years (von Ballmoos & Smither, 1994).
In the framework of the R&D project CLAIRE, a Laue lens prototype was built and extensively tested in the laboratory, in stratospheric balloon flight campaigns (Halloin, 2003), and in a ground campaign (Álvarez *et al.*, 2004a). This last campaign, the long distance test of the CLAIRE lens, is presented and discussed here.

3.1 Principles of a Laue diffraction lens

The basic principles of a Laue lens design, along with basic crystallographic concepts, are described in this section. A detailed introduction to the crystallographic theory can be found in Zachariasen (1945) or more recently and more specifically related to Laue lenses in the work presented by Halloin & Bastie (2005).

3.1.1 Scattering in a crystal

In order to explain the scattering process of γ-ray photons in a crystal lattice, we must first model the intensity scattered by free electron, then the scattering by a set of electrons bound in an atom, and finally the scattering by an atomic cristal lattice.
In section 2.1.2, the incoherent scattering (Compton scattering) of a photon with a free electron was discussed. As mentioned there, a more realistic description of photon scattering should include the effects of the binding energy of the electron, taking into account the full distribution of electrons in the atom. However, the intensity of the radiation scattered from an atom is obtained by squaring the sum of the amplitudes of the scattered radiation by each atomic electron, where two possible cases should be considered: *coherent* and *incoherent* scattering. In the coherent scattering, the amplitudes of the scattered radiation by each electron are added and the sum is squared. For incoherent scattering, there is no

relationship between the radiation of the different electrons, and thus, the total scattered intensity is obtained by adding the individual intensities scattered from each electron. An extensive discussion of atomic scattering is given in Davisson (1966).
The amplitude of scattering from a single atom is called *atomic scattering factor* or *form factor* (**f**), and depends on the atomic electron charge density distribution. The exact computation of this factor is a difficult task, since it requires considering the coherent diffusion by each electron, taking into account screening factors. Theoretical results are obtained within the framework of quantum theory, e.g the Hartree-Fock method (see Figure 2.5) and Thomas-Fermi method.
Once the radiation scattered from one atom is known, the scattering from a crystal can be obtained by adding the radiation scattered by each atom, from which the so-called *structure factor* (**F**) is defined. This coefficient quantifies the scattering efficiency of an elementary cell. The difference in path length from the scattering centers is translated into a phase difference, leading to a constructive or destructive interference in the scattered intensity by the crystal. As will be shown next, maximum interference takes place when the Bragg relation is satisfied.

3.1.2 Bragg diffraction

The notation system in crystallography for planes and directions in crystal lattices is based on the Miller indices. A family of lattice planes is determined by three integers (hkl). Each index denotes a plane orthogonal to a direction (hkl) in the basis of the reciprocal lattice vectors (see e.g. Kittel (2005)). For the special case of simple cubic crystalline lattice, the spacing ($d_{(hkl)}$) of planes (hkl) is given by:

$$d \;=\; \frac{a}{\sqrt{h^2+k^2+l^2}} \tag{3.1}$$

The Bragg law provides a relationship between the spacing of atomic planes ($d_{(hkl)}$), the energy (E) and angle (θ) of the incident radiation:

$$2d_{(hkl)}sin\theta \;=\; n\epsilon \;=\; n\frac{hc}{E} \tag{3.2}$$

This relationship can be easily derived from the von Laue formulation of difraction. Figure 3.1 shows schematically the geometric condition for diffraction, where k_0 and k are the incident and diffracted wave respectively. The Laue condition states that in order to obtain constructive interference, the direction given by $q \;=\; k - k_0$ should be perpendicular to the plane described by the Miller indices.
From the definition of q, it follows that:

$$q \;= q = 2k_0 \sin\theta_i = 2\;\frac{2\psi}{\epsilon_{\,0}} \sin\theta_i \tag{3.3}$$

where $\epsilon_{\,0}$ is the wavelength of the incident beam, and θ_i is the angle of k_0 with respect to the plane orthogonal to q. Since the reciprocal lattice vector q can be expressed as:

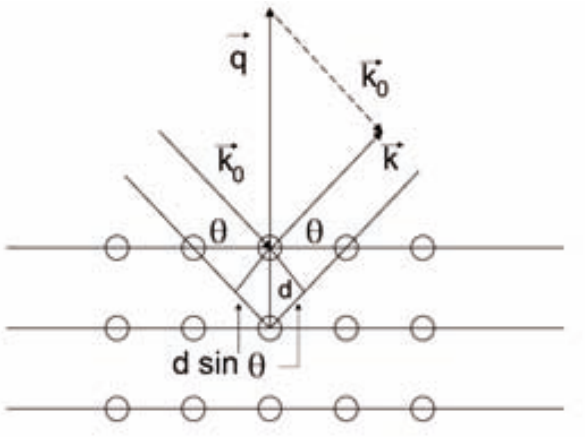

Figure 3.1: Schematic representation of diffraction in a crystal according to Laue's formulation.

$$q = \frac{2\pi}{d_{hkl}}, \tag{3.4}$$

From (3.3) and (3.4), the Bragg's equation (3.2) is immediately derived.
This relation is valid for an ideally perfect crystal. Actually, even for very good monocrystals, the relation is not purely monochromatic and the diffraction has a very small angular width of the order of few arcseconds (Halloin & Bastie, 2005).

3.1.3 Darwin mosaic model

In order to study the diffraction in a crystal, a first approximation is to assume that the interaction of the propagating waves inside the crystal medium is negligible. This theory is known as *kinematical or geometrical*. A more general theory, commonly referred to as *dynamical theory of diffraction*, takes into account the interaction between incident and scattered radiation inside the crystal medium (Zachariasen, 1945). However, neither of both theories explain the measurements performed on macroscopic crystals. The angular (or energy) acceptance of a real crystal can be relatively large (up to few degrees) and the diffraction efficiency is much higher than expected from a perfect crystal (Halloin & Bastie, 2005).
A description of a macroscopic crystal was proposed by Darwin (1941) as an agglomerate of perfect crystals blocks. Structural defects on a real crystal (e.g., impurities, dislocations, inhomogeneous strains) are expressed by perfect *crystallites* which are slightly offset in angle (see Figure 3.2). This model (known as Darwin or mosaic model) is defined through an angular distribution of the crystallites (a continuous function of the orientation of the blocks) and their mean thickness. Usually, it is assumed that this function is a Gaussian distribution with a FWHM called the *mosaicity or mosaic width*.
Each single perfect crystal shown in figure 3.2, only diffracts an energy band over an angular range called the *Darwin width* (see e.g. Authier & Malgrange (1998)). Another assumption of the mosaic model is that the mosaicity is much bigger than the Darwin width, which is usally valid for mosaicities above ten arcseconds. In this case, the beam

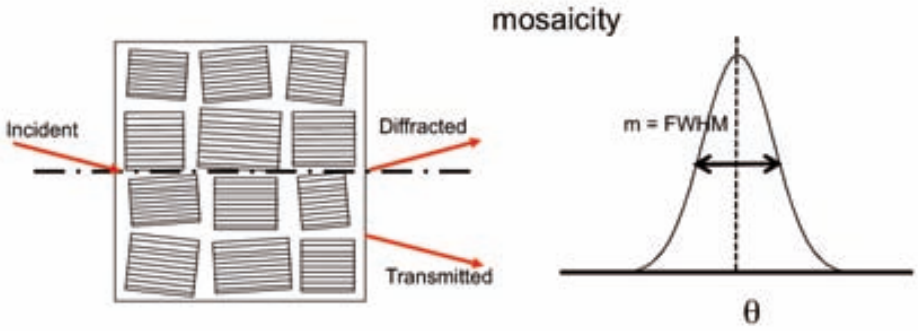

Figure 3.2: Schematic representation of a mosaic crystal. The orientation of perfect crystallites is assumed to be a Gaussian distribution, whose FWHM is called the mosaicity.

diffracted from the individual crystals blocks does not interfere. The diffracted intensity can be expressed by the following equation (see e.g. Halloin & Bastie (2005)):

$$\frac{I}{I_0} = \frac{1}{2}\left[1 - e^{-2\sigma T}\right] e^{-\mu T} \tag{3.5}$$

where I_0 is the incident intensity, T is the crystal thickness, μ is the linear attenuation coefficient, and σ is the *diffraction coefficient*, whose definition is analogous to the attenuation coefficient (see section 2.1.1):

$$\sigma = m\frac{R}{t_0} \tag{3.6}$$

where m is the distribution of the crystallite orientation, t_0 the size of the cristallite and R is the integrated intensity diffracted by a single perfect crystal (given by the dynamical theory of diffraction).
Equation 3.5, along with equation 3.6, is used to estimate the diffraction efficiency of a mosaic crystal and by extension, the efficiency of a Laue lens (see e.g. Naya (1995) and Halloin (2003)).

3.1.4 Lens design in Laue geometry

The diffraction in a crystal can either occur near the surface (i.e. beam penetrates and exits through the same surface in the crystal) or while the beam is propagating through the crystal (i.e. beam penetrates through a surface and exits through the opposite surface in the crystal). Both geometric configurations, named *Bragg geometry* and *Laue geometry* respectively, are shown in figure 3.3.
For γ-ray energies above one hundred keV, the diffracted angle given by the Bragg's law (eq. 3.2) is so small that extremely long crystals are needed in the Bragg geometry configuration, e.g. a diffraction angle of $1degree$ for a $1cm$ beam would require a crystal length of $L = A/sin\theta \sim 57cm$ (Naya, 1995). Therefore, Bragg geometry is not suitable for a lens in the MeV energy range and Laue geometry should be used. Moreover, Laue lens design fits well in the MeV range due to the low attenuation of γ-ray photons going through a crystal at these energies.

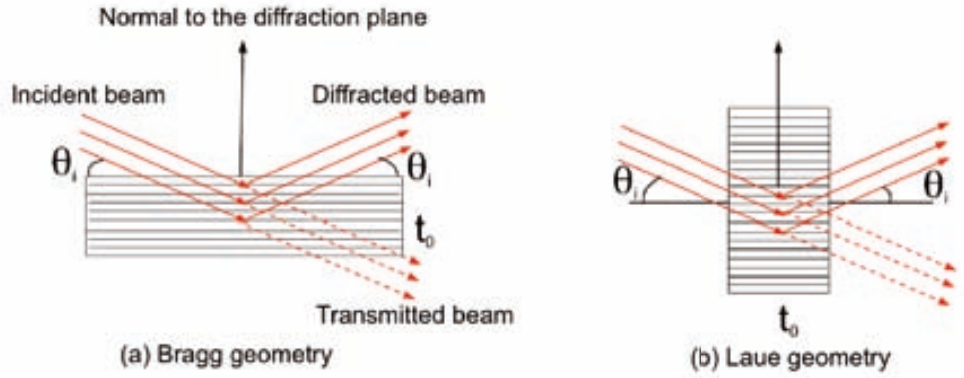

Figure 3.3: Diffraction in Bragg and Laue geometry.

Geometric description

A γ-ray lens in Laue geometry is shown schematically in Figure 3.4. Assuming that the radiation source is located at an infinite distance from the lens (i.e. γ-rays come parallel to the optic axis of the lens), an incoming γ-ray must satisfy the Bragg relation (eq. 3.2) in order to be diffracted to the focal plane. This means that a crystal placed at a distance r_1 from the optical axis, must be oriented so that the angle between the incident beam and the crystalline plane is just the Bragg angle θ. This can be done for a given energy E_∞ and constant $d_{1(hkl)}$ of the crystal. Crystals are placed at the distance r_1 from the optical axis in a ring structure, so that all of them diffract the incident radiation E_∞ onto a common focal spot. Similarly, crystals placed at distance (r_2) are able to diffract the same energy (E_∞) onto the same focal spot when the new difraction angle (given by the Bragg law) is suited geometrically. This can be obtained by using other materials for the cristal with different constant $d_{(hkl)}$. For a given focal distance F_∞, the relationship between the radius of the ring r_i and the crystalline plane distance d_i is given by:

$$r_i = F_\infty tan(2\theta_\infty) \;=\; F_\infty \frac{n\lambda}{d_i} \;=\; F_\infty \frac{nhc}{d_i E_\infty} \tag{3.7}$$

where n is the diffraction order and λ is the wavelength of the incident photon.

In order to build a Laue lens and diffract a monochromatic beam onto a common focal spot, the product $r_i d_i$ must be constant.
Let's consider now the case of a source located at a distance D of the Lens' center (see figure 3.4). In this case, for the same energy of the incident photons and the same orientation of the crystals, a different focal distance is obtained. The following geometrical relationship between angles and distances in both cases can be easily obtained:

$$\tan(\theta - \theta_\infty) \;=\; \frac{r}{D} \;\;,\;\; \tan(\theta + \theta_\infty) \;=\; \frac{r}{F} \tag{3.8}$$

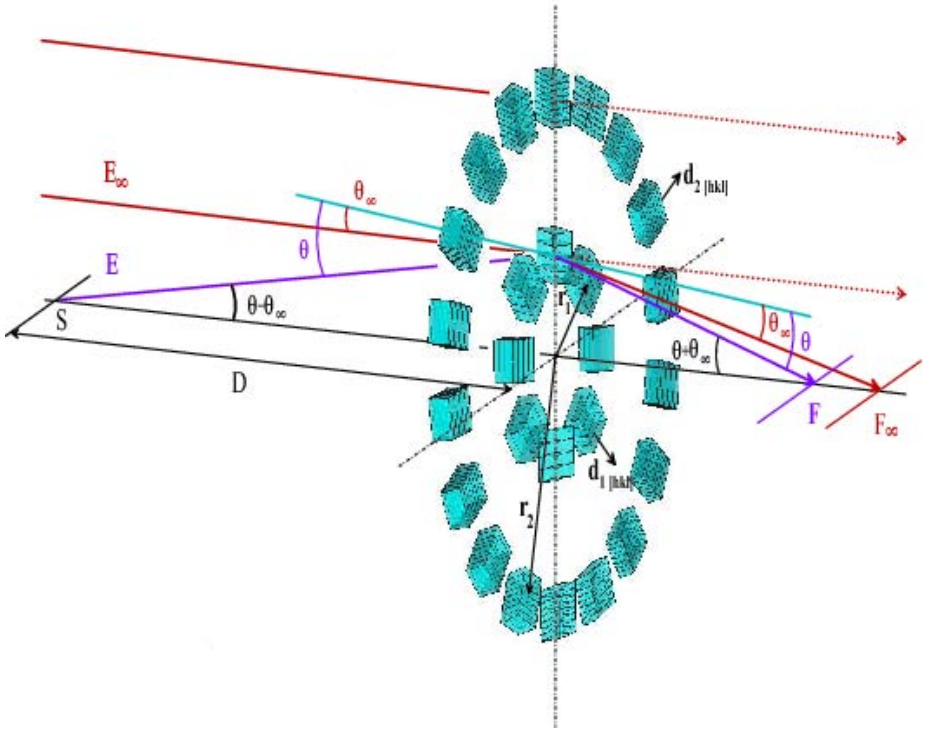

Figure 3.4: Diffraction process is displayed schematically through a crystal placed in a concentric ring of a Laue lens. E and E_∞ are the diffracted energies from a source at distances D and infinity, respectively; r is the radius of the ring and d is the distance between diffraction planes ($[hkl]$ are the Miller indices).

For small diffracted angles (high energy photons) the Bragg s relationship can be approximated by:

$$2\ d_{(hkl)}\ sin\theta\ =\ \frac{hc}{E} \qquad \theta \sim \frac{hc}{2d_{hkl}E} \tag{3.9}$$

Similarly, the geometric relationship (eq. 3.8) can be approximated by:

$$\theta \sim \theta\ \ + \frac{r}{D} \tag{3.10}$$

From eq 3.9 and eq 3.10 the following expression is obtained:

$$\frac{1}{E} \approx \frac{1}{E} + \frac{2\ d_{(hkl)}}{hc}\frac{r}{D} \tag{3.11}$$

This equation shows a relationship between the energies of a source located a distance D and a source located at infinity from the lens. This equation is very useful when tuning a Laue lens in the laboratory where the distance from the source to the lens is quite limited.

Similarly, performing the linear approximation in equation (3.8):

$$F \approx \frac{r}{\theta + \theta} \qquad F\ \ \approx \frac{r}{2\theta} \qquad D \approx \frac{r}{\theta - \theta} \tag{3.12}$$

a relationship between focal lengths F and F can be obtained.

$$\frac{1}{F} - \frac{1}{D} \approx \frac{1}{F} \tag{3.13}$$

which is analogous to the equation of a classical optical lens.
Finally, from equation (3.7) the following relationship is obtained (for n=1):

$$F \approx \frac{rE \; d_{[hkl]}}{hc} \tag{3.14}$$

This expression allows to distinguish two types of lenses in order to define the focal spot of a Laue lens:

- The first type uses various crystalline materials (or diffraction planes), in order to keep the product $rd_{[hkl]}$ constant for each ring of the lens. Thus, all crystals diffract the same energy value on the same focal spot. This allows the design of a *narrow bandpass Laue lens*, like the one of the CLAIRE prototype.
- In the second type of lens, the same diffraction planes are used on many consecutive rings so that the diffracted energy is slightly shifted from one ring to the next. If each individual crystal diffracts a large enough bandpass energy, the contributions of the neighbouring rings overlap and the result is a broadband continuous energy coverage. An example of a *broad bandpass Laue lens* is the Laue lens proposed for the GRI mission (see Chapter 4).

Energy bandwidth of a Laue lens

The energy bandpass of a Laue lens is given by its design (either narrow or broad bandpass), but the energy bandpass of a single crystal is also a fundamental parameter for the design of a lens. As pointed out in section 3.1.2, an ideally perfect crystal has an angular range (Darwin width) over which the Bragg relationship is verified. This angular range is very narrow and leads to an energy band of a few eV. The Darwin model of a crystal assumes that the mosaicity is much bigger than the Darwin width, in which case, the energy bandwidth of a single crystal increases with mosaicity. The relationship between mosaicity and energy bandpass can be estimated by differentiating the Bragg s relationship (3.2) in the small angle approximation:

$$\Delta E \approx \frac{2d \; E^2 \; \Delta\theta}{hc} \tag{3.15}$$

where $\Delta\theta$ is any angular deviation (either the mosaicity or source s depointing) and ΔE is the energy bandpass. Therefore, the energy bandpass of a mosaic crystal grows with the square of the energy. On the other hand, the reflectivity efficiency of a mosaic crystal decreases with the crystal mosaic width, although it also depends on the thickness of the crystal.
In the particular case of the CLAIRE lens, relation (3.15) becomes:

$$\Delta E \approx 40(\frac{d}{dGe_{[111]}})(\frac{E}{511keV})^2(\frac{\Delta\theta}{1arcmin})keV \tag{3.16}$$

An extensive study of the efficiency of mosaic crystals and the optimization for the Laue lens CLAIRE design can be found in Halloin (2003).

From the mosaicity of the individual crystals, a Laue lens can be designed with a certain spectral range, either narrow or broad energy bandpass, as long as the crystal alignment is kept with great precision. The energy bandwidth of a *narrow band lens* is given by equation (3.15). On the other hand, for a *broad band lens*, the diffracted energy depends on the radius. From one ring to another, the diffracted energies differ by:

$$\Delta E \approx \frac{d}{hc}\frac{E^2}{F}\Delta r \tag{3.17}$$

where Δr is the radio difference between rings ($r_2 - r_1$ in Figure 3.4).
From equations 3.17 and 3.15, there is an energy overlap between two identical crystals at different radii only if:

$$\Delta r < 2F \ \ \Delta\theta \tag{3.18}$$

In order to have a smooth energy distribution in a broad band lens, this relationship between the mosaicity of the crystals (or accuracy on the crystals positioning), $\Delta\theta$, the focal lengh of the lens, F , and the distance between rings, Δr, and therefore the size of the crystals, must be satisfied.
Instead of following a ring-shaped distribution, the crystals can be distributed according to an Archimedes spiral, where the crystal radius changes with its azimuth angle. This distribution, proposed by Lund (1992), would ensure a smooth energy distribution.

3.2 First prototype of a Laue lens for γ-ray astrophysics: CLAIRE

The CLAIRE project was a stratospheric balloon flight experiment aimed to prove the principle of a Laue diffraction lens for nuclear astrophysics (von Ballmoos *et al.*, 2004a) *(including J. Alvarez)*. The instrument payload consists of three instruments: a Laue diffraction lens, an array of HPGe detectors and a balloon gondola capable of stabilizing the γ-ray lens with pointing accuracy of a few arcseconds.
On June 2001, CLAIRE was launched by the French Space Agency (CNES) from its balloon base at Gap, in the French Alps, and was recovered after 5 hours at float altitude. During this stratospheric flight, the instrument was pointed to the Crab nebula during 3.5h with a fine pointing quality. An extensive discussion on this flight can be found in (Halloin, 2003).
On May 2003, the CLAIRE lens was tested on a $205m$ long set-up in an aerodrome near Figueres (Girona) (Álvarez *et al.*, 2004a). The measurements of this long distance test confirmed the results of the stratospheric balloon flight experiment and were a crucial contribution to CLAIRE s concept proof (von Ballmoos *et al.*, 2005) *(including J. Alvarez)*.

CLAIRE's gamma-ray lens

A Laue lens system was built and successfully tested by Naya *et al.* (1996). Moreover, the efficiency of Germanium crystals was tested experimentally and a good agreement with the Darwin model was obtained (Kohnle, 1998). As a consequence of this experiment and in order to demonstrate the diffraction lens principe under space conditions, a Laue lens for nuclear astrophysics has been developed at CESR (Toulouse) during these last years.

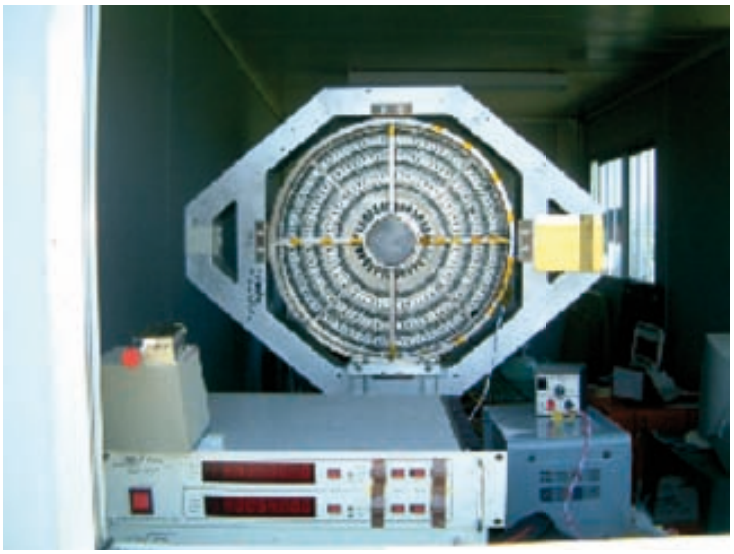

Figure 3.5: Photography of the CLAIRE's lens during the long distance test in Ordis

The lens consists of 556 Ge(Si) crystals mounted on eight concentric rings of a $45cm$ diameter titanium frame (see figure 3.5). The total geometric area of the lens is about 511 cm^2. The structure was designed and manufactured at the Argonne National Laboratory (USA) and the crystals were produced at the Institut fur Kristallzuchtung (IKZ) in Berlin. The crystals were glued on a flexible aluminium support and then they were mounted on the lens frame at the CESR in Toulouse.
Table 3.1 lists the main design parameters of the lens: dimensions and crystal planes of each ring of CLAIRE's gamma-ray lens. The Miller indices [hkl] correspond to the germanium crystals (lattice constant $a = 5.56\mathring{A}$) with a small amount of silicon, added to obtain the required mosaicity. The crystals ($Ge_{1-x}Si_x$) were grown through a modified Czochralski technique described by Abrosimov *et al.* (2005). Basically, in this method of producing large single crystals, a small seed crystal of semiconductor material is inserted into a crucible filled with similar molten material, then slowly pulling the seed up from the melt while rotating it.
As mentioned previously, in order to test the application of a γ-ray lens for astrophysics, CLAIRE's lens was designed to observe a celestial source during a stratospheric balloon flight. This means that the focal length of the lens should fit on a balloon instrument. Taking the continuum energy emission from the Crab Nebula at $170keV$, a feasible focal distance of $279cm$ was obtained. At the focal plane, the diffracted photons were concentrating onto a common focal spot of about $1.5cm$ in diameter. This size is basically

Ring	Plane [hkl]	d[hkl] [A]	Number of Crystals	Crystal size [mm]	Mean radius [mm]
0	111	3.27	28	10x10	61.7
1	220	2.00	52	10x10	100.8
2	311	1.71	56	10x10	118.2
3	400	1.41	72	10x10	142.6
4	331	1.30	80	10x7	156.2
5	422	1.15	96	10x10	174.7
6	333	1.09	96	10x7	188.1
7	440	1	104	10x10	201.7

Table 3.1: Germanium crystal's parameters and dimensions of CLAIRE's γ-ray lens.

determined by the size and shape of the crystal ($\sim 1cm^2$) projected onto the focal plane. As described in section 3.1.4, the CLAIRE's lens is a *narrow bandpass Laue lens*. The mosaicity of the crystals ranges from 30 arcsec up to 2 arcmin, leading to a diffracted energy bandwidth of about 3keV at 170keV (eq. 3.15).

Tuning the Laue lens

Figure 3.6: Optical bench for tuning the Laue lens at the CESR (Toulouse).

Tuning the lens means tilting each crystal to the appropriate Bragg angle so that the diffracting energy is $170keV$ for a source at infinity. Instead of using a parallel beam of 170 keV photons, the lens was tuned in an optical bench at CESR (see Figure 3.6) with the beam of an X-ray generator placed at a distance of $14.16m$ from the lens. Applying equation (3.11) to the CLAIRE's lens, the following relation is obtained:

$$\frac{100keV}{E} \approx \frac{100keV}{E_\infty} + 0.3251\frac{10m}{D} \tag{3.19}$$

where the multiplying constant is slightly different for each ring, since the spacing $d_{(h,k,l)}$ of the crystal depends on the ring (see table 3.1).
The graph in Figure (3.7) shows the relationship between source distance and diffracted energy. At the available distance at the CESR's laboratory ($14.16m$) the corresponding tuning energy is $122keV$.
Each crystal was mounted on an aluminum plate and tilted with a screw (see Figure 3.8) so that the diffraction peak was measured at the corresponding energy ($122.28keV$) on

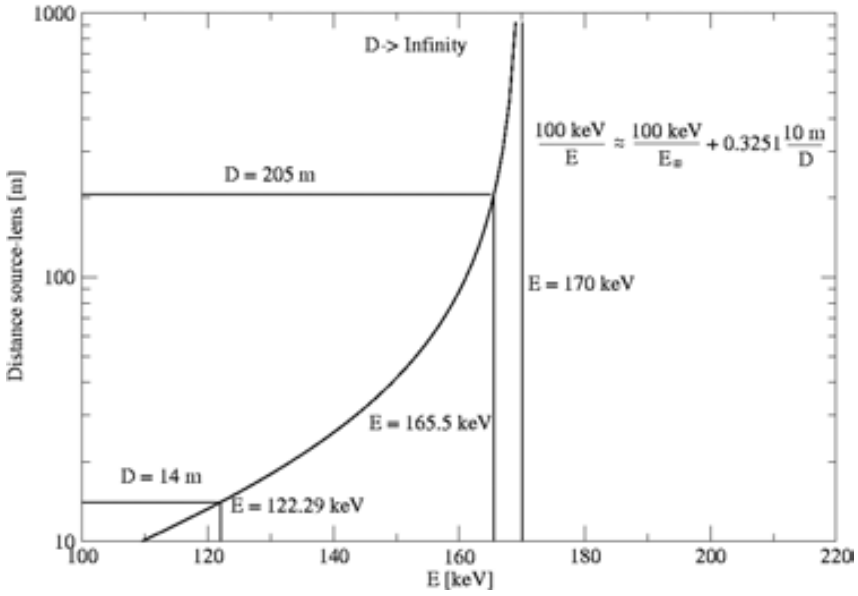

Figure 3.7: The graph shows the relationship between source distance and diffracted energy, according to equation 3.19 applied to the CLAIRE γ-ray lens.

(a) Tuning a the γ-ray lens at the CESR.

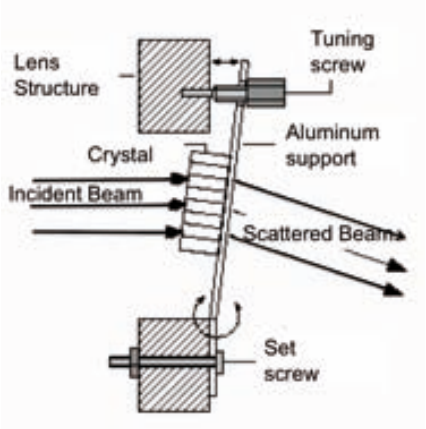

(b) Schematic of tilting process of the crystals in the lens's frame.

Figure 3.8: Photograph of the CLAIRE's lens and crystal mounting detail.

the focal plane where the detector was placed. This process was done with the 556 crystals as preparation of the lens for the balloon campaign as well as the ground test.

3.3 The Long Distance Test of CLAIRE

In order to measure the diffraction efficiency of the lens, several laboratory tests were performed using an X-ray generator source and different isotopes sources. However, at the laboratory distance the angular size of the crystal is about a few arcmin, which is larger than the mosaicity. Therefore, only a small fraction of each crystal contributes to the diffraction.

To measure the total lens response, a distance larger than a hundred meters between lens and source is needed. For this long distance the angular size of each crystal (1 cm height at 205m) becomes small enough in comparison to the mosaicity. In addition, the diffraction energy is very close to the one corresponding to a source at infinity (see Figure 3.7).

Figure 3.9: Photograph of the long distance test setup along one of the tracks of an aerodrome in Ordis (May 2003).

For this purpose, a ground test was arranged with the CLAIRE s lens pointed to an X-ray generator (300-kV tube) placed at a distance of $205m$ from the lens (Álvarez *et al.*, 2004a). The test aimed not only to calculate the lens efficiency but also to validate the energy-distance relationship, verify the pointing system and measure the lens response to depointing.

3.3.1 Test preparation

Experimental setup

In order to prepare the experiment, three mobile cabins were placed along one of the tracks of an aerodrome in Ordis (Girona) (see Figure 3.9). The lens and HPGe detector were housed in one of the cabins. At 205 m, the X-ray generator was placed inside another cabin. A lead panel was installed 10 m away from the X-ray tube, in order to collimate the beam. The third cabin, used as a control room for data acquisition, was located tens of meters away from the detector s cabin. The general layout of the test is shown in Figure 3.10.

Radiation source In order to have enough flux to obtain a measurement in a reasonable exposure time (no more than 10-15 minutes for each run) an industrial X-ray generator tube was used for the test.
An X-ray tube mainly consists of a solid target on the anode, and a filament on the cathode. When an intense current passes through the filament, electrons are emitted from the cathode and are accelerated towards the anode by a potential of hundreds of kVolts.

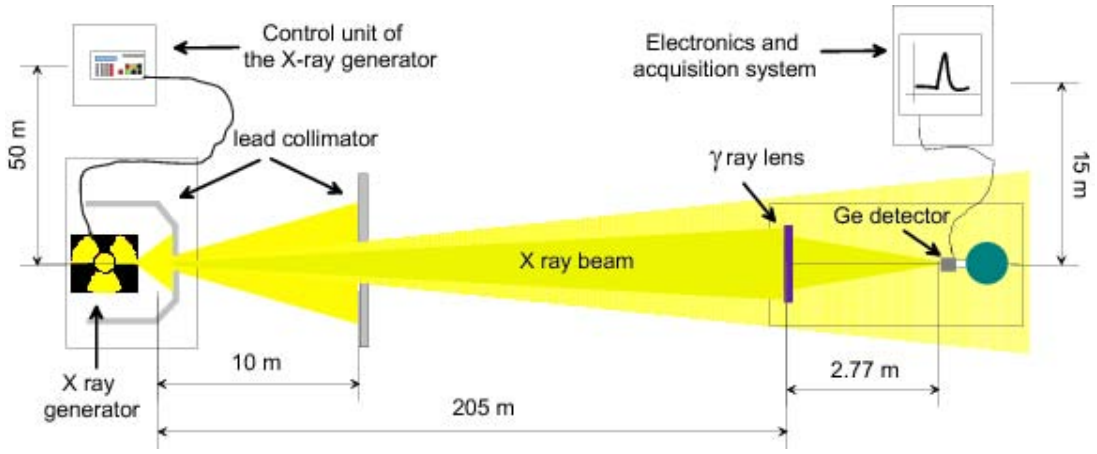

Figure 3.10: General setting of the long distance test assembly in May 2003 along one track of an aerodrome in Ordis.

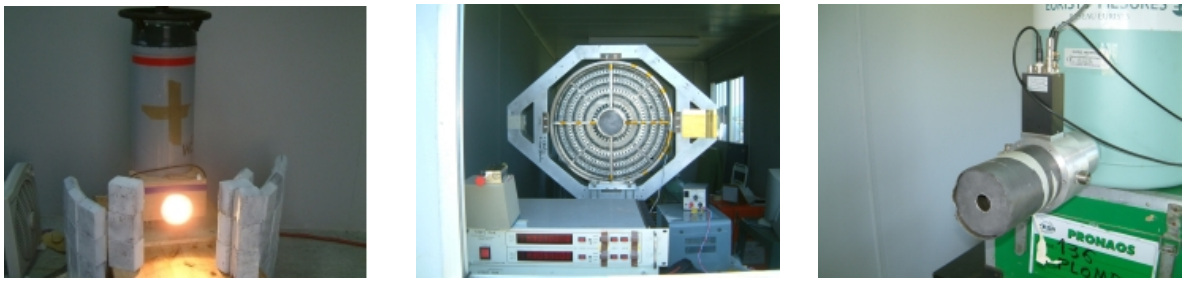

(a) (b) (c)

Figure 3.11: Photograph of the X-ray generator (a), γ-ray lens (b) and HPGe detector (c) used in the long distance test (detailed description on the text).

The radiation emitted has a spectrum characterized by a continuous bremsstrahlung and characteristic fluorescent lines of the target material. Figure 3.12 shows a calculated spectrum of an X-ray tube with a Tungsten anode, absorbed by air along 200m (Poludniowski *et al.*, 2009).
An industrial X-ray tube (Model-ICM D3006) [1] was used in the test. Its main characteristics are listed in table 3.2. With the purpose of reducing the large aperture angle of the beam to about ± 5 deg, a lead screen with a $20cm$ diameter hole in the center was placed $10m$ away from the source (see Figure 3.13). In addition, some blocks of lead were also placed around the X-ray tube (see in Figure 3.11 (a)).
The voltage and current of the X-ray tube were set to $250kV$ and $1mA$. As will be discussed later, this voltage and current yield a high enough flux in the energy range $[160 - 170]keV$, after absorption by 205m of moist air. Due to the small size of the source ($2\ 5x2\ 5mm$) and the long distance, the source can be considered to be point-like.

Alignment A first alignment was performed with topographic techniques, for positioning of the lens and the generator. Then, the alignment method for the test was similar to

[1] http://www.icmxray.com/

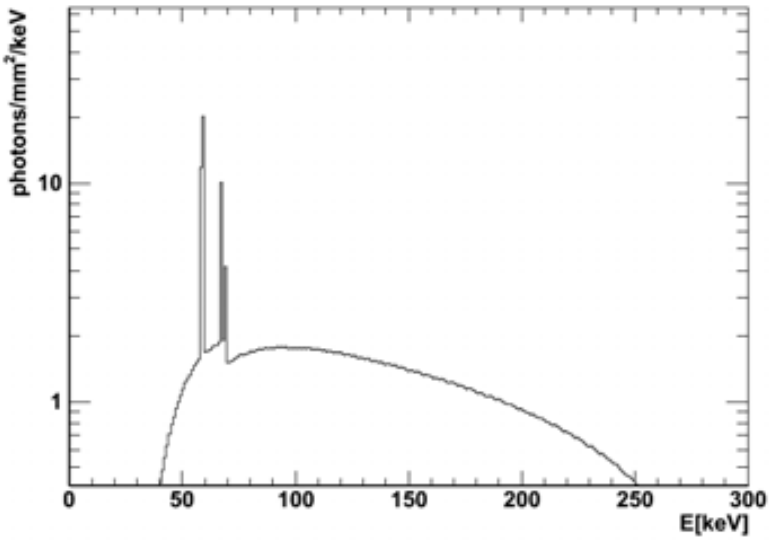

Figure 3.12: Calculated spectrum of an X-ray tube with a Tungsten anode after 200m of air absorption.

Figure 3.13: Photograph of the lead diaphragm (front) and the X-ray tube (back) used in the test.

the one used in the laboratory and the stratospheric-balloon flight.
As described in von Ballmoos *et al.* (2005), a small optical telescope equipped with a CCD camera was mounted in the centre of the lens frame with a special rotating system that allows to define the lens s optical axis when the telescope turns around. Observing a light source (while this small telescope is rotated) allows to observe a circle on the CCD image whose centre gives the direction of the rotation axis. This invariant pixel is then used to represent the γ-ray lens optical axis.
As shown in Figure (3.11) (a), a lamp was mounted just in front of the X-ray source in order to obtain the location of the invariant pixel and point the lens. A black screen with

Characteristic	Value
Model	ICM SITE-X D3006
Voltage	130 to 300 kV
Current	1 to 6 mA
Anode material	W
Inherent attenuation	4mm (Al)
Spot size	2.5 x 2.5 mm
Operating temperature range	25 to 70 ^{0}C
Aperture angle of the emission	60 x 40

Table 3.2: Main characteristics of the X-ray tube used on the long distance test.

a hole was placed a few meters away from the lens to reduce the effect of the ambient light on the CCD.

HPGe detector The detector consists of a matrix of 3×3 Ge detectors housed in a single cylindrical aluminum cryostat. Each one of the single Ge bars is an n-type coaxial detector of 1 5×1 5×4 cm with an internal electrode hole of 4mm diameter and energy resolution about 1% (FWHM). The thermal control for the detectors is provided by a liquid-nitrogen dewar with a capacity of 30l, which ensures a cooling lifetime of about 2 weeks. This detector array, used in the CLAIRE project, is described in detail in Naya (1995). As shown in Figure 3.11 (c), a lead cylinder of $2mm$ thickness and $70mm$ height was used to shield the HPGe detector during the test.

3.3.2 Measurements

The recorded beam spectrum from the X-ray tube at the distance of $\sim 200m$, when the γ-ray lens was removed from its position, is shown in Figure 3.14 (curve named Beam ON). The continuous shape of the spectrum is produced by the bremstralung radiation emitted by the X-ray tube, while the different peaks are produced by the characteristic emission lines of the anode (see Figure 3.12). The emission lines from the abundant lead used in the test are also shown in the spectra, even in the background spectrum recorded when the X-ray tube was turned off (named as Beam OFF in Figure 3.14).

The spectrum of the incident beam also shows a contribution due to the Compton scattered photons that reach the detector, i.e., the flux detected by the detector is not only the direct beam from the source but also part of the scattered beam on the 200m air column. In order to determine this contribution (see next section), the so-called *chopper technique* was used. It consists of suppressing the direct beam by blocking the detector field of view with an occulter (see e.g., Shonfelder *et al.* (2001)). In this case, the occulter was a block of lead ($10 \times 10 \times 5cm$) placed between the source and the detector, $100m$ away from the source. The recorded spectrum is shown in figure 3.14 (Beam Blocked).

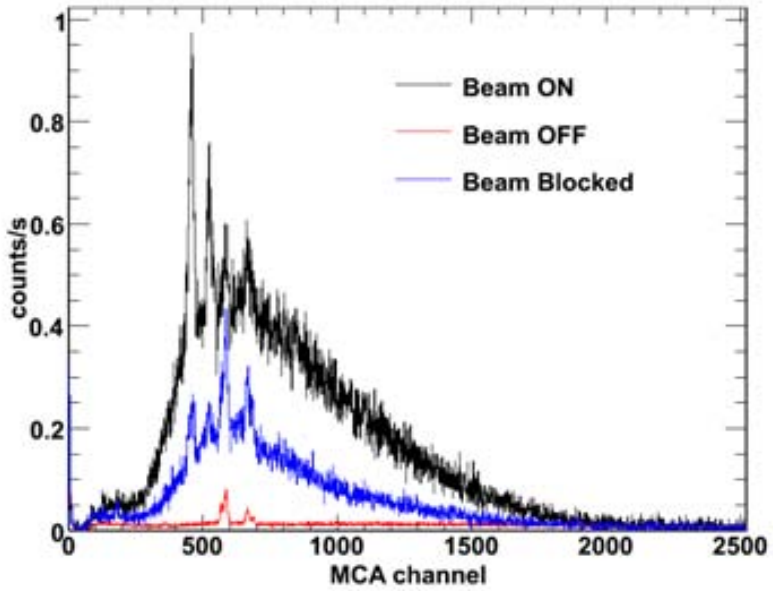

Figure 3.14: Recorded beam spectrum without the CLAIRE s lens (details in the text)

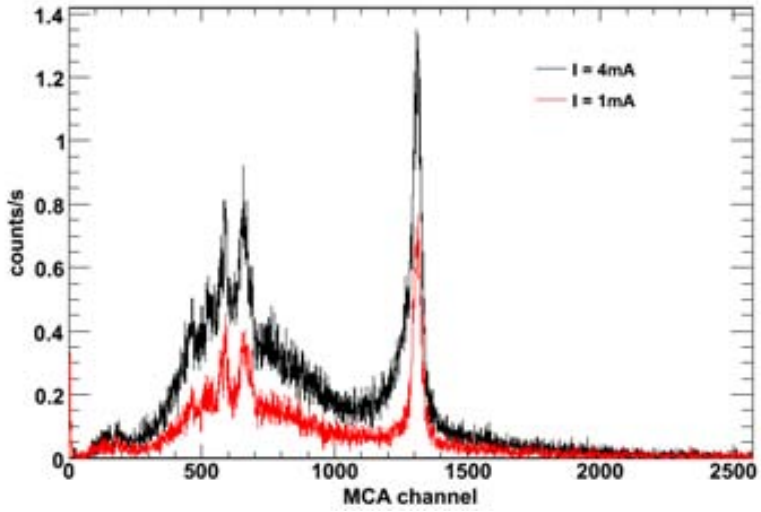

Figure 3.15: Diffracted peak of the CLAIRE s lens for two incident beam fluxes.

First measurements of the γ-ray lens diffraction peak are shown in 3.15. The flux of the incident beam was reduced by decreasing the current on the X-ray tube, from $4mA$ to $1mA$. Since the diffracted peak is more symmetrical at lower fluxes, and the exposure time required for the acquisition was about 10 minutes, the value of $1mA$ (and $250kV$) was used to perform the test.

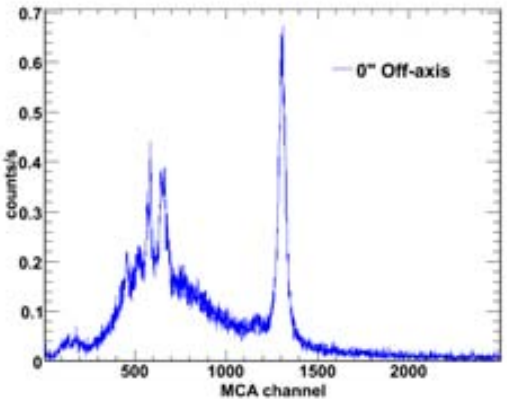

(a) on-axis

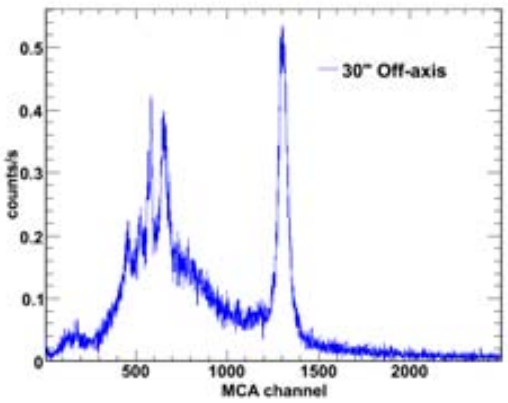

(b) 30 off-axis

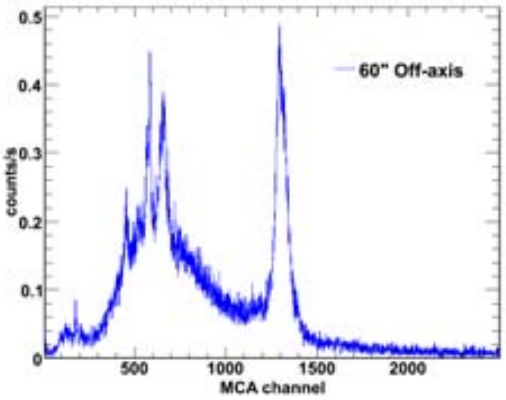

(c) 60 off-axis

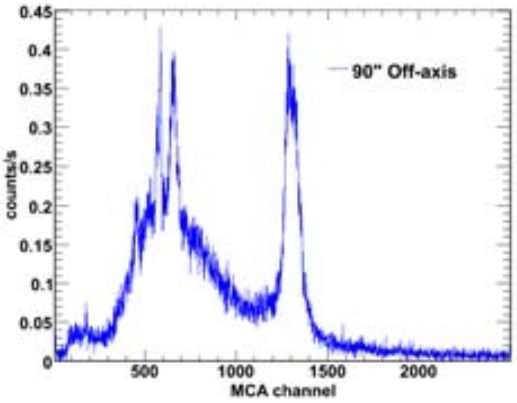

(d) 90 off-axis

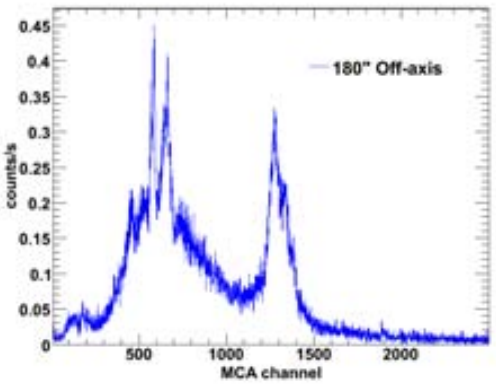

(e) 180 off-axis

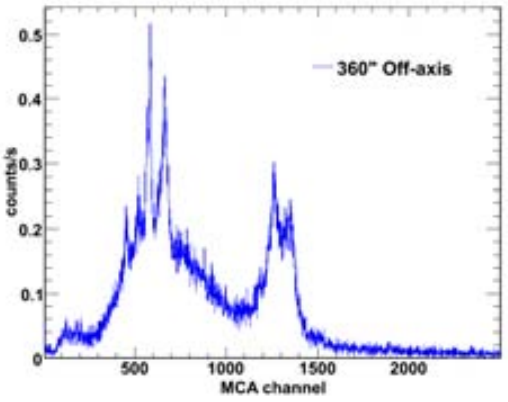

(f) 360 off-axis

Figure 3.16: Recorded spectra with a source on and off-axis. As the off-axis angle increases the FWHM of the diffraction peak also increases.

Figure 3.16 shows the recorded spectra with the source on-axis ($\theta = 0$) and for various off-axis angles. As the angle increases, the FWHM of the diffraction peak also increases. The off-axis angle was measured accurately using the autocollimation technique that was performed with a theodolite pointed to a small mirror located on the lens frame.

Calibration

The energy calibration of the HPGe detector was performed several times during the test. For this purpose the spectra of two radiactive isotopes (^{152}Eu and ^{57}Co) were recorded. Figure (3.17) shows two of these recorded spectra. A gaussian distribution was fitted to the main peaks of the ^{57}Co (122keV, 136keV) and ^{152}Eu sources (121keV, 244keV, 344keV, 778keV), and a linear regression curve was fitted and used for the calibration. From here on, spectra are represented in [keV] instead of channels.

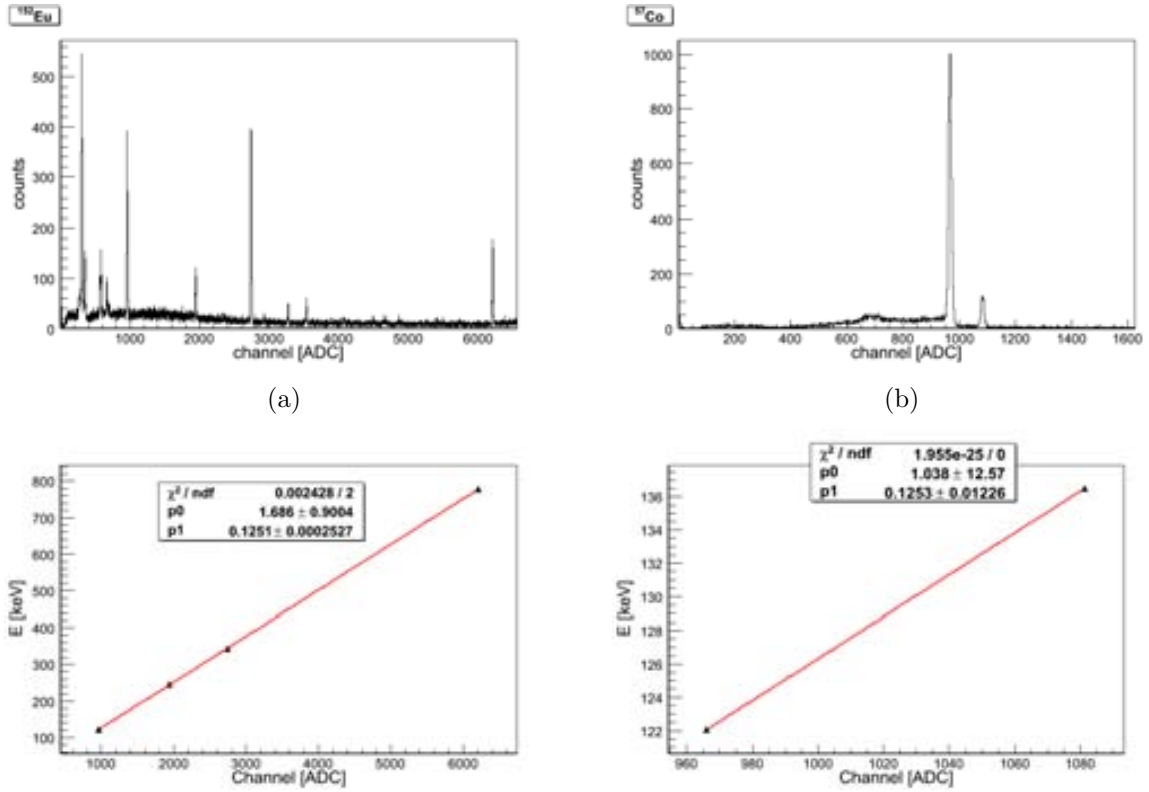

(a) (b)

Figure 3.17: Measured spectrum of ^{152}Eu (a) and ^{57}Co (b) and calibration curves.

3.3.3 Analysis and Results

Incident beam

The beam incident on the lens is estimated by means of the *chopper technique* discussed in section 3.3.2. The occulter (a lead brick) blocks the photons emitted by the source within the solid angle of the detector. However, there is a fraction of photons that have suffered Compton scattering in the air and reach the detector without crossing the lens.

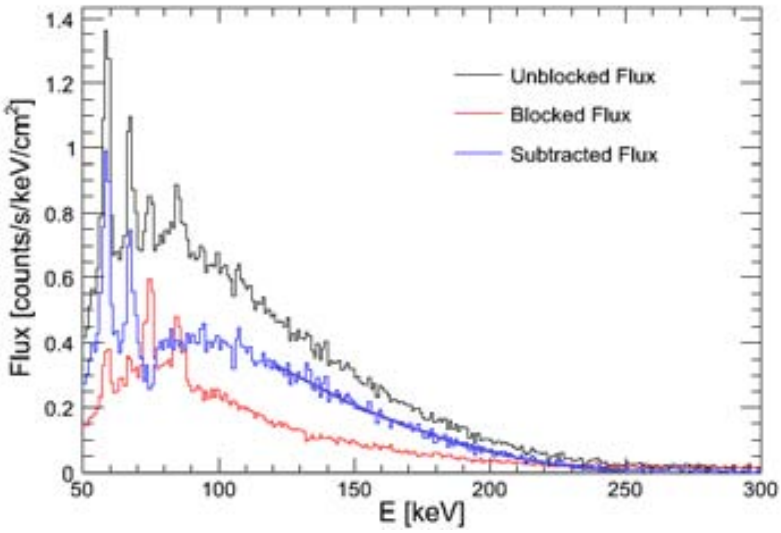

Figure 3.18: Estimation of the incident beam on the lens from the so-called chopper technique (see text for details).

In the *blocked mode* the recorded spectrum is produced by photons that have undergone at least one Compton scattering along their track to the detector, while in the *unblocked mode*, when the occulter is removed, both direct and scattered photons are recorded. An estimation of the incident beam on the lens can be obtained by subtracting the spectrum measured in the blocked mode from the spectrum measured in the unblocked mode, as shown in Figure (3.18). A quadratic fit of the subtracted flux was performed in the energy range [120-250]keV. Hence, the flux incident on the lens is given by the following expression:

$$\begin{aligned} F[E] &= p_2(E - 165\ 5)^2 + p_1(E - 165\ 5) + p_0 \\ p_2 &= (1\ 714 \pm 1\ 74)10^{-5} \quad [counts\ \ s\ \ keV^3\ \ cm^2] \\ p_1 &= -(3\ 231 \pm 1\ 434)10^{-3} \quad [counts\ \ s\ \ keV^2\ \ cm^2] \\ p_0 &= (0\ 155 \pm 0\ 04) \quad [counts\ \ s\ \ keV\ \ cm^2] \end{aligned} \tag{3.20}$$

A particularity of the *chopper technique* is that the geometrical arrangement of the setup is not the same with and without the occulter. Therefore, the recorded spectrum in the blocked mode has an additional contribution that is not present in the unblocked mode: the scattered photons coming from the occulter itself. This effect is usually studied by means of Monte Carlo simulations. In our experiment, this additional contribution is negligible (see Halloin (2003)).

Diffraction peak

Figure 3.19 shows the spectrum of the diffracted peak with the source on-axis. The peak is fitted to a Lorentzian distribution plus a linear part:

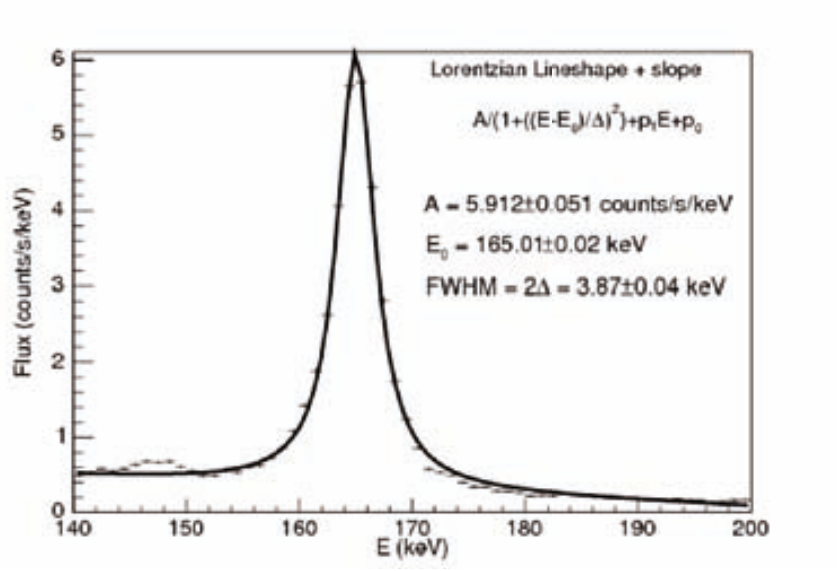

Figure 3.19: Spectrum of the diffracted peak with the source on-axis.

$$\begin{aligned} P(E) &= \frac{A}{(1+(\frac{E-E_0}{\Delta})^2)} + p_1 E + p_0 \\ A &= 5.912 \pm 0.051 \quad [counts/s/keV] \\ E_0 &= 165.01 \pm 0.02 \quad [keV] \\ FWHM &= 2\Delta = 3.87 \pm 0.04 \quad [keV] \end{aligned} \tag{3.21}$$

According to equation (3.11), the diffracted peak for a source at $205m$ is expected at $165.5keV$. However the measured peak is slightly lower (165.01 ± 0.02keV) probably because of detector calibration shifts.
In addition, the width of the peak is wider than expected, (3.87 ± 0.04keV) instead of 3keV (FWHM). This is most probably due to the effect of the strong wind during the test that caused oscillations of the experimental setup during acquisition (i.e., off-axis pointing).

Lens efficiency

The efficiency of the lens can be derived by the following expression (Naya, 1995):

$$\epsilon_{diff} = \frac{A_D N_L D_S^2 \epsilon_{nc}}{n\ s\ N_D (D_I + D_S)^2 \epsilon_c} \tag{3.22}$$

where:

N_L count rate diffracted by the lens and seen by the detector
N_D count rate measured by the detector when the lens is removed from the system
$D_S = 205m$ distance from the lens to the source

$D_I = 2.77m$ distance from the lens to the detector
$A_D = 4.9\ cm^2$ area of the detector
$n = 556$ number of diffracting crystals in the lens
$s = 1\ cm^2$ average surface area of the front side of a single crystal
ϵ_{nc} detector efficiency for a non concentrated beam
ϵ_c detector efficiency for a lens concentrated beam

Using the incident flux from equation 3.20 and the diffracted flux from equation 3.21 we are able to determine the lens efficiency. Considering that the detector efficiency for a concentrated and non concentrated beam is the same ($\epsilon_{nc} = \epsilon_c$), the peak efficiency at quasi infinite distance is $7.3 \pm 0.7\%$ at 165.5 keV. Assuming a width of 3 keV, the obtained peak efficiency is $8.5 \pm 0.7\%$.

Source off axis

Figure 3.20 shows the energy response of the lens for various depointing angles, from 30 to 300 arcseconds (successive plots have been shifted down for clarity). The raw data of these spectra were displayed individually in figure 3.16.

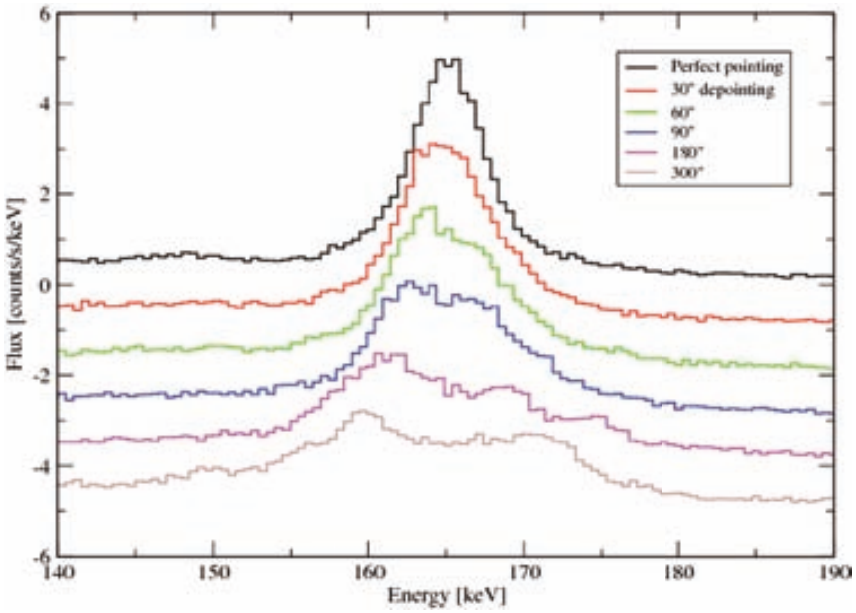

Figure 3.20: Energy response of the lens for various depointing angles, from 30 to 300 arcseconds. Successive plots have been shifted down for clarity.

These accurate measurements were compared with the results of a Monte-Carlo simulation of the CLAIRE's lens, reported in (Halloin *et al.*, 2004) *-including J. Alvarez-*. The shape and deformation of the energy response are well reproduced by the realistic model that includes the parameters (mosaicity, mean length of the crystallites,...) obtained during the lens tuning Halloin (2003). This Laue lens model has been included in a software package (Halloin, 2005b) that is used to calculate the point-spread-function of a Laue lens in the following section.

3.3.4 Conclusions

Within the experimental margins, the *long distance test* confirms the relationship between distance and diffracted energy for the energy chosen for the CLAIRE s stratospheric balloon flight ($170keV$).
The measured efficiency of the lens was $8\,5 \pm 0\,7\%$, assuming a width of 3 keV (FWHM), which is in good agreement with the peak efficiency deduced from the balloon flight (von Ballmoos *et al.*, 2005). Data obtained during tuning shows that some crystals are much more efficient than others, therefore the efficiency calculated from the experiment is limited by the quality of the crystals used in the CLAIRE s lens (von Ballmoos *et al.*, 2004b).
In recent years, a great effort has been made to develop more efficient diffracting crystals, such as mosaicity copper and gradient silicon-germanium (Barriere *et al.*, 2007), which can increase significantly the efficiency of a Laue lens telescope.
Another important result of the test was to study the effect of lens depointing. The broadening of the spectrum with increasing off-axis angle matches very well the prediction of a theoretical model of the instrumental response of the lens developed by Halloin (2003). In this sense, this experiment validated the Monte-Carlo simulation code of a Laue lens, which has been crucial to predict the point-spread-function (see below) of a Laue lens for a future space mission.
Results of CLAIREs Long Distance Test along with those from the balloon flight, have successfully demonstrated the feasibility of a γ-ray lens telescope based on a Laue lens. Therefore, the Laue lens is a very promising instrument concept for astrophysics, offering the possibility to increase the sensitivity by more than an order of magnitude with respect to existing instruments.

3.4 Point Spread Function of a Laue lens

The Point Spread Function (PSF) of the Laue lens describes the two-dimensional distribution of photons in the focal plane of the lens for a point source at infinity. As far as the capability of concentrating an on-axis source is concerned, the Laue lens is similar to a classical optical lens. However, the observation of an off-axis source induces deformation of the PSF associated with the modification of the diffracted spectrum shown in Figure 3.20. In order to define the optimal detector for the focal plane of a Laue lens telescope, it is essential to know the *point-spread-function* (PSF) of the lens.
The imaging response of the Laue lens has been simulated using a Monte Carlo software, specifically developed for Laue lenses simulations (Halloin, 2005b). The simulations have been performed for an on-axis source and for various off-axis angles with two different lenses. The results are illustrated on Figures (3.21) -CLAIRE Laue lens- and Figure (3.22) -MAX Laue lens-.

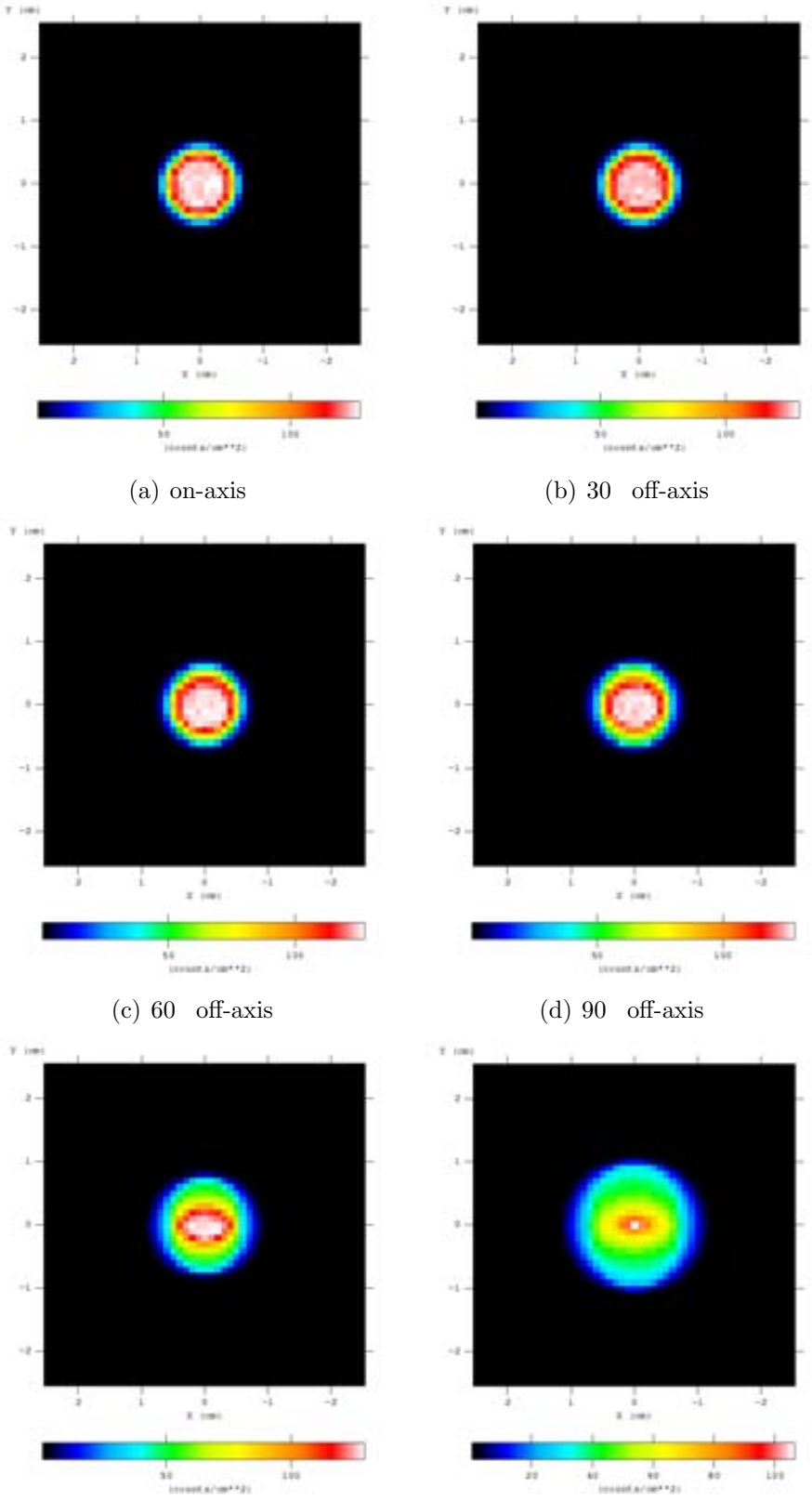

(a) on-axis (b) 30 off-axis

(c) 60 off-axis (d) 90 off-axis

(e) 180 off-axis (f) 360 off-axis

Figure 3.21: Focal spot of the CLAIRE lens for various depointing angles (based on Halloin (2005b)).

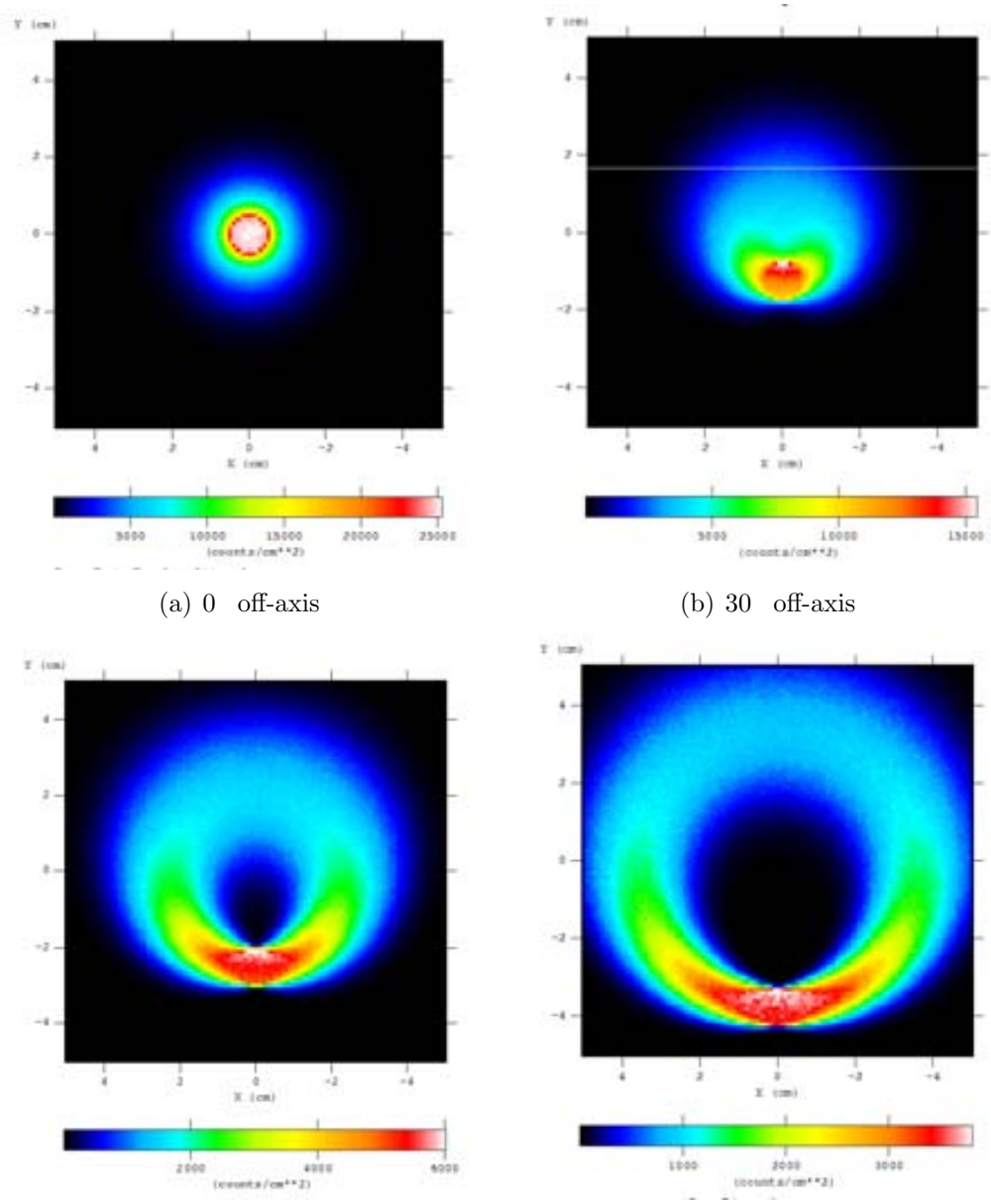

(a) 0 off-axis

(b) 30 off-axis

(c) 60 off-axis

(d) 90 off-axis

Figure 3.22: Focal spot of the Laue lens configuration proposed for the MAX mission for various depointing angles in the energy band 790-910 keV (based on Halloin (2005b)).

In order to obtain the results show in Figure 3.21, the design of the narrow band CLAIRE lens was used (see table 3.1), considering an energy of 170keV and focal length of 2.76m. Figure 3.22 shows the results for the broad band lens proposed for the MAX mission. For this simulation a lens made of concentric rings of germanium and copper was considered, with an energy range from 400keV to 950keV and focal length of 80m (see description of the MAX Laue lens in Barriere *et al.* (2005)).

The Monte Carlo simulations show the imaging properties of a Laue lens for two cases: narrow band Laue lens with short focal length and broad band lens with a long focal length. The PSF of a narrow band lens is only slightly modified by the off-axis angle. On

the contrary, the focal spot of a broad band lens is very sensitive to the depointing. As shown in figure 3.22, the PSF becomes a ring-like structure with a dependence on the azimuthal angle.
Although the Laue lens behaves basically as a radiation concentrator, this azimuthal modulation of the *point-spread-function* (PSF) allows to determine the position of the source within its field-of-view, giving a certain imaging capability to the lens.

Simulations performed with the Monte Carlo code (Halloin, 2005b), based on the principles and equations of the Darwin model, confirm the imaging properties of a Laue lens as discussed in Halloin (2005a). Regarding the spectral properties, the energy response of a narrow band lens is very sensitive to the depointing (see Figure 3.20), while the spectral shape of a broad band lens is only slightly affected (see Halloin (2005a)).

3.5 Gamma-ray beam line facility for the development of Laue lenses

The optical bench at CESR (see figure 3.6) allowed the tuning of the first prototype of a Laue lens for nuclear astrophysics at the energy of 170keV. Likewise, the Ferrara (Italy) X-ray facility with a tunnel of 100m long, is being used to perform studies of mosaic crystals at hundred keV (Loffrendo *et al.*, 2005). However, a beam line for higher energy γ-rays is needed for the development of a Laue lens telescope, both for testing and calibration.
The possibility to produce an energetic and highly polarized γ-ray beam through Compton scattering of polarized laser light with high energetic electrons beam was pointed out in 1963 (Arutyunian & Tumanian, 1963). The characteristics of the γ-ray beam (energy range, energy resolution, intensity, polarization,...) will depend on the characteristics of the electron and laser beam. The maximum achievable gamma-ray energy is a function solely of the laser photon energy and the electron energy. For a given laser photon wavelength the spectrum of energies extends from zero to this maximum. For (linear or circular) polarized laser photons, the gamma rays are also polarized, being the polarization transfer maximum at the top of the energy range. Most of the gamma-rays are emitted in a very narrow cone, providing a naturally collimated beam. The total gamma-ray intensity depends on the overlap of laser and electron density distributions and the Compton cross-section. A detailed description of the characteristics of a laser backscattering γ-ray sources can be found in Tain *et al.* (2004). Table 3.3 lists several of such facilities existing worldwide.
After our experience at the long distance test of CLAIRE, we participated in a collaboration aimed at the construction of a backscattering γ-ray beam-line (Tain *et al.*, 2004) at the synchrotron radiation facility ALBA [2] located in Cerdanyola del Vallés (Barcelona), that was constructed and is operated by the CELLS (Consortium for the Exploitation of the Synchrotron Light Laboratory) consortium. The laboratory was officially opened for experiments on seven beamlines in 2010. We submitted a proposal of a gamma-ray beam

[2] http://www.cells.es/

Name	Energy [MeV]	Intensity $[s^{-1}MeV^{-1}]$	Resolution [FWHM]
ETL-LCS [Tsukuba]	1-40	10^6-10^4	2.7-5%
NewSUBARU [Himeiji]	1-40	10^4	-
HIGS [Durham]	1-20	$5x10^7$-10^4	1%
LEGS [Brookhaven]	110-330	$2x10^4$	6MeV
ROKK [Novosibirsk]	100-1600	10^3	1-3%
GRAAL [Grenoble]	400-1500	1 $5x10^3$	16MeV
LEPS [Harima]	1500-3500	2 $5x10^3$	35MeV

Table 3.3: Facilities with laser backscattering γ-ray sources, data from Tain *et al.* (2004).

line (Tain *et al.*, 2004) in response to a Call issued in 2004.

Laser Source	Energy [MeV]	Intensity $[s^{-1}MeV^{-1}]$	Energy Resolution	Polarization [%]
$CO_2[10.6\sigma m]$	0.5-16	$3x10^8$	-	Lin(0-100) - Cir(0-100)
OPO $[1.5\text{-}12\sigma m]$	16-110	$4x10^6 - 4x10^5$	$\frac{\Delta E}{E} = 1\ 5\%$	Lin(100) Cir(100)
Nd:YAG $[1.06\sigma m]$	110-153	$2x10^5$	$\Delta E = 7MeV$	Lin(85-100) Cir(75-100)
Nd:YAG $[0.530\sigma m]$	153-290	$1x10^5$	$\Delta E = 7MeV$	Lin(50-100) Cir(0-100)
Nd:YAG $[0.353\sigma m]$	290-417	$7x10^4$	$\Delta E = 7MeV$	Lin(80-99) Cir(60-100)
Nd:YAG $[0.265\sigma m]$	417-531	$5x10^4$	$\Delta E = 7MeV$	Lin(90-98) Cir(80-100)

Table 3.4: Parameters of the gamma-ray beams at ALBA, data from Tain *et al.* (2004).

This line would extend the energy photon sources of ALBA into the hard γ-ray energy range. Gamma-rays up to hundreds of MeV would be produced by Compton backscattering of laser photons on the electrons circulating in the synchrotron ring. In such a line, high intensities could be achieved with energy resolutions of 1.5% and a high degree (80%-100%) of linear or circular polarization (see Table 3.4). As discussed in Álvarez *et al.* (2004b), such a line would be very well suited for the test and calibration of Laue lens telescopes not only in the field of crystallography but also for the focal plane instrument.

Chapter 4

The focal plane detector of GRI

The base-line detector proposed for the focal plane of the Gamma-Ray Imager mission (GRI) was based on a highly efficient and fine spatial resolution Cd(Zn)Te detector. In the framework of the GRI mission study, research and development of Cd(Zn)Te detectors have been done by several groups in the collaboration team. In particular, a R&D project at the *Institute of Space Science (IEEC-CSIC)* was conducted in order to find out an optimal detector configuration. Monte Carlo simulation studies as well as build-up of a prototype were acomplished in collaboration with *National Microelectronics Centre (IMB-CNM-CSIC)* and *Institute for High Energy Physics (IFAE).*

4.1 The GRI mission concept

The Gamma-Ray Imager mission, as described in 2.4.2, was proposed to ESA in June 2007 by a large international consortium (see Appendix A). GRI is a focusing telescope mission based on a formation flight architecture to be launched into a highly elliptical orbit (HEO). The telescope is composed of two satellites that are kept actively in formation flying at $100m$ distance (see figure 2.18). One spacecraft carries a Laue diffraction lens while the other spacecraft carries a detector, that must be placed at the focal plane of the gamma-ray lens.

4.1.1 Scientific requirements

The GRI mission is focused on performing detailed studies of cosmic explosions and cosmic accelerators (e.g., Supernovae, Classical Novae, Supernova Remants (SNRs), Gamma-Ray Bursts (GRBs), Pulsars, Active Galactic Nuclei (AGN)) and specially *Type Ia supernovae* (see section 1.1.1), which is one of its main observation targets. An overview of the GRI scientific objectives can be found in Knodlseder *et al.* (2009).
Table 4.1 lists the mission requirements in order to achieve the scientific goals of GRI. An improvement in the sensitivity by a factor $30 - 50$ compared with past and current γ-ray missions, was the major requirement. This unprecedented sensitivity allows deep observations, up to a distance of $\sim 30Mpc$. Moreover, the relatively modest energy res-

Parameter	Requirement	Goal
Energy coverage (keV)	20-900	10-1300
Continuum sensitivity ($\Delta E\ E = 1\ 2\ 3\tau\ 100ks$)	10^{-7} $ph\ cm^{-2}s^{-1}keV^{-1}$	$3x10^{-8}$ $ph\ cm^{-2}s^{-1}keV^{-1}$
Line sensitivity ($\Delta E\ E = 3\%\ 3\tau\ 100ks$)	$3x10^{-6}$ $ph\ cm^{-2}s^{-1}$	10^{-6} $ph\ cm^{-2}s^{-1}$
Energy resolution (FWHM)	3%	0 5%
FoV (arcmin)	5	10
Angular resolution (arcsec)	60	30
Timing	$100\sigma s$	$100\sigma s$
Polarimetry (MDP [1] , 3τ)	5% for 100 mCrab	1% for 100 mCrab
Observing constraints	ToO response < 1 day 50% sky coverage	ToO response < few hours all-sky coverage

Table 4.1: GRI mission requirements (Knodlseder, 2007).

olution (3% FWHM) would be enough to cover most of the science goals of the mission, although a goal of 0.5% (FWHM) was established. An angular resolution of $60arcsec$ was required in order to avoid confusion in regions with high density of sources. The narrow field-of-view, $5 - 10arcmin$, was appropriate for deep observations of individual objects. In addition, within this field-of-view, the lens can be used as an imaging device due to its off-axis response (see discussion in section 3.4).

4.1.2 Laue lens

The gamma-ray optics of GRI comprises a broad-band Laue lens (see section 3.1.4), covering the energy range from $200keV$ to $1300keV$, complemented by a single reflection multilayer coated mirror to cover the low energy range (30keV up to 300keV).
The development of the lens was based on the experience acquired from the CLAIRE project (discussed in Chapter 3). It consists of about 28.000 crystals of copper, germanium and silicon-germanium, arranged in concentric rings with an inner radius of $65cm$ and outer radius of 180 $5cm$. The angular resolution and field-of-view of the Laue lens is mainly determined by crystal mosaicity and focal length, repectively. Table 4.2 list the main characteristics of the crystals considered for the GRI Laue lens. An extensive discussion on the crystals for the Laue lens of GRI can be found in Barriere *et al.* (2007).

Crystal	Size [mm]	Mosaicity [arcsec]	Number	$Radius_{min-max}$ [mm]
Cu[111]	10x10	30	3204	650-754.5
Cu[200]	10x10	30	3688	755.5-859.5
Cu[111]	15x15	40	10769	992.5-1805.5
Cu[220]	15x15	40	1167	1046.5-1201.0
SiGe[111]	15x15	32	7167	1201.5-1805.5
Ge[311]	15x15	40	1331	1434-1666
Ge[400]	15x15	40	755	1666.5-1805.5

Table 4.2: Characteristics of the GRI Laue lens.

4.1.3 Focal plane detector

The detector for the GRI focal plane should fulfill the following requirements: high detection efficiency, highly position sensitivity to sample the point-spread-function (PSF) of the Laue lens (see section 3.4), good energy resolution to provide the required spectroscopic performance and polarimetric capability. As presented in section (2.2.2), room temperature semiconductor detectors (CdZnTe/CdTe) are well suited to all these requirements; thus, a position sensitive spectrometer of CdZnTe was chosen as baseline detector for the focal plane of GRI.
The detector configuration included in the GRI proposal is made of four stacked CdZnTe layers, with octogonal shapes, surrounded by CdZnTe side walls (see Figure 4.1). The top layer, with a thickness of $5mm$, was optimized for photoelectric absorption in the low energy range. It has a spatial resolution of $0.8mm$ and detection area of $210cm^2$. Under this top layer, three identical layers of $20mm$ thickness were arranged in the so-called *Planar Transverse Field (PTF) configuration* (see section 4.3.1), with a spatial resolution of $1.6mm$ and detection area of $214.6cm^2$. A detection efficiency better than 70%, up to energies of $\sim 1MeV$, is reached thanks to the total thickness of the instrument ($65mm$).

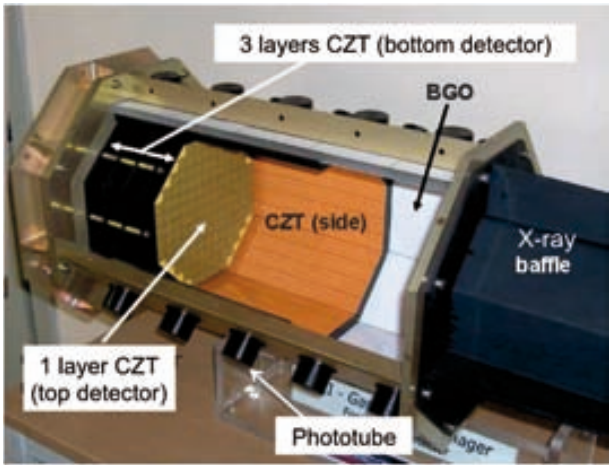

Figure 4.1: Model of the GRI detector at the *Istituto di Astrofisica Spaziale e Fisica Cosmica* (INAF) - Roma, adapted from *L. Natalucci, J. Álvarez et al., (2008)*

The multiple layers of CdZnTe detectors are surrounded by a side detector of $10mm$ thickness and $27cm$ length (see figure 4.1) in order to enhance γ-ray absorption in the Compton regime. The stacked detector is directly exposed to the focused photons from the Laue lens, while the side wall detector collects the scattered photons from the primary beam in order to maximize the detection efficiency (see section 4.2.1).
The side CdZnTe detectors are, in turn, surrounded by Bismuth Germanate (BGO) modules which are read out through coupled photomultiplier tubes (which are described in section 6.1.1). This provides an active veto shield against charged particles and diffuse gamma-ray photons. In addition, a collimator of $\sim 100cm$ length made of various materials (e.g. W, Sn, Cu), is placed on top of the instrument in order to provide a passive shield against the diffuse cosmic γ-ray background.

Further details on the baseline focal plane instrument of GRI can be found in Natalucci *et al.* (2008). It should be pointed out here the large number of channels needed in this baseline configuration.
Alternatively to the baseline instrument, a cooled high-purity germanium (HPGe) strip detector was proposed (Wunderer *et al.*, 2005). This detector would improve the spectroscopic performance while reducing the number of channels, but it would also increase the instrument complexity because the related cooling and annealing requirements are very demanding.

4.2 Basic properties of the GRI base line detector

The mass model of the CdZnTe detector used in the Monte Carlo simulations is shown in Figure 4.2. This model uses a simplified geometry of the baseline detector described above, with square based detector elements.

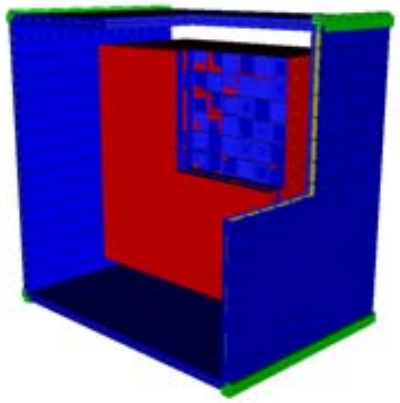

Figure 4.2: Mass model of the GRI detector.

Only detector performances achieved in the laboratory were included in the model for the simulation study. An energy resolution of 4.125 keV (FHWM) at 662keV (which worsens from top to bottom), a depth resolution of 2mm (FWHM) and a trigger threshold of 10keV were assumed. The state-of-the-art CdZnTe detectors proposed for GRI are described in Caroli *et al.* (2005).

4.2.1 Efficiency

Figure (4.3) shows the photopeak efficiency as a function of the incident energy for the baseline detector configuration (displayed with dots) and for a reduced configuration with no side detector (displayed with squares). It is worth noting that the CdZnTe side detector increases the efficiency significantly (5%-12% depending on energy).
The high stopping power of CdZnTe provides a high photopeak efficiency up to 1.2MeV. However, figure (4.3) shows an ideal case in which all the charge generated in the detector is collected. As described in section (2.2.2), the incomplete charge collection degrades the energy resolution while reducing the photopeak detection efficiency.

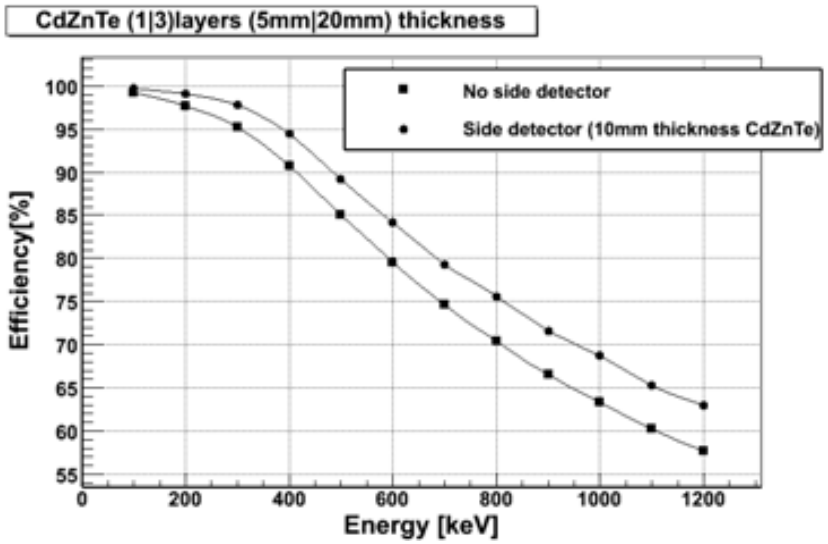

Figure 4.3: Peak efficiency of the focal plane detector of GRI as a function of energy for the baseline configuration (circles) and a reduced configuration with no side CdZnTe detector.

4.2.2 Angular resolution

Figure 4.4 shows the Angular Resolution Measure (ARM) (see section 5.3.2) for energies greater than 500keV. In order to obtain these results none event selection has been applied.

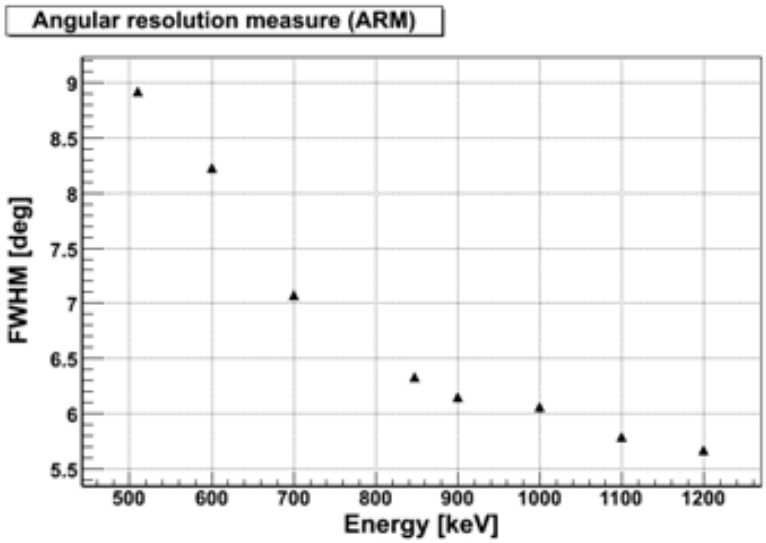

Figure 4.4: FHWM of the angular Resolution Measure (ARM) distribution of the GRI detector as a function of energy, for an on-axis source.

The poor angular resolution is mainly due to the short distance between two hits in an event. It can be improved by means of event selection but reducing the efficiency. In addition, a detector with better position and energy resolution would contribute to this improvement. During the last years a great effort has been done to develop a 3D-CZT detector prototype for Laue Lens telescope with millimeter and submillimeter position resolution (see e.g.Caroli *et al.* (2010)). Although the improvement of the resolution would

improve the angular resolution, it should be pointed out that the limit imposed by the Doppler Broadening in the case of CZT is relatively high (Zoglauer & Kanbach, 2003). Thus, alternative materials were proposed for the focal plane detector of GRI, such a Germanium detector or a detector configuration with Silicon layers on top of the CZT layers. A Monte Carlo simulation study was performed by Zoglauer *et al.* (2006a) with these detector configurations. Results of this study point out that using an additional Silicon detector on top of the CZT detector is advantage in terms of reached sensitivity.

4.2.3 Imaging capability

Monte Carlo simulations, aimed at testing the imaging capability of the GRI base line detector, were performed with the point-spread-function of a Laue lens. Firstly, the PSF of the Laue lens should be computed (for example, through the code developed by Halloin (2005b) and discussed in section 3.4). Then, the impact distribution given by the PSF is used as input of the Geant4 simulation carried out with the GRI mass model shown in Figure 4.2. Once the Monte Carlo simulation is completed, Compton event reconstruction is performed with the MEGAlib package (see Appendix B.2). Finally, the image deconvolution is done with the method LM-EM-ML (see section 2.3.2.4) also implemented in MEGAlib.

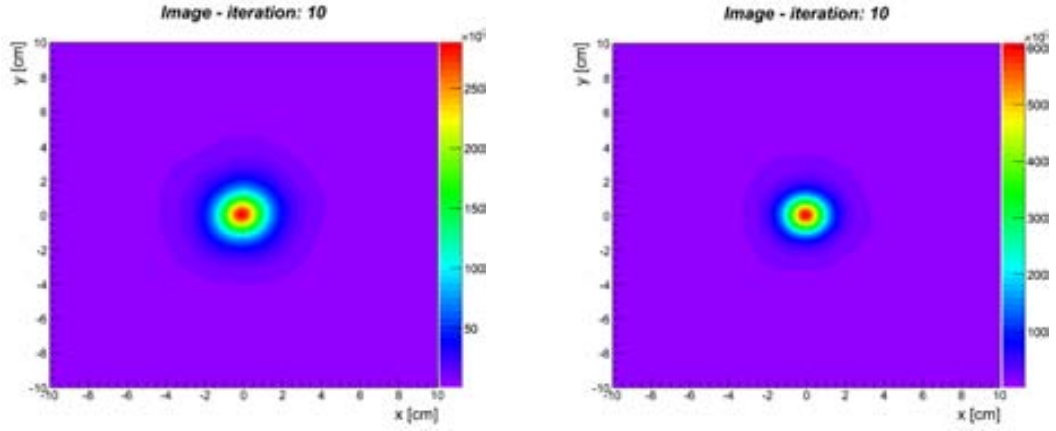

(a) (b)

Figure 4.5: Simulated images of the focal spots for monochromatic on-axis sources at 511 keV (a) and 847 keV (b).

The simulations have been performed for an on-axis source with two different energies (511keV and 847keV). The point-spread-function of the Laue lens study for the GRI mission, reported in Natalucci *et al.* (2008) *-including J.Alvarez-*, was used. The quality of the simulation results, illustrated in Figure 4.5, is a hint to the good performance of the base line instrument in terms of imaging capability. However, it would be necessary to simulate the off-axis response (the ring-like structure of the PSF shown in Figure 3.22) to draw a conclusion of the imaging capability of the GRI instrument.

4.3 A detector concept based on CdTe pixel detectors

A specific configuration based on CdTe/CdZnTe detector is proposed here for the focal plane of a Laue lens. Moreover a detector suitable as an element of this configuration is being developed in the framework of a research and development project at the *Institute of Space Science (IEEC-CSIC)*. Design, fabrication and test of a CdTe detector prototype is presented in this section.

4.3.1 Detector configuration

The underlying idea of the GRI baseline detector is the use of CdZnTe sensors in the so-called *Planar Transverse Field (PTF)* configuration (Auricchio *et al.*, 1999). In this geometrical configuration the irradiation direction is transverse (perpendicular) to the applied electric field. Figure 4.6 shows the schematic representation of the pixelated detector mounted in PTF and in standard configuration. The PTF configuration allows us to increase the length of the CdZnTe detector while minimizing the charge collection distance (Caroli *et al.*, 2005). As discussed in section 2.2.2, this has a huge impact on the energy resolution of the detector.

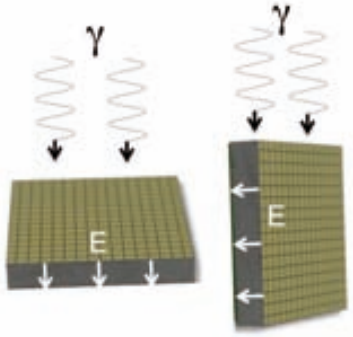

Figure 4.6: Schematic representation of an irradiated pixelated detector parallel (left) and perpendicular to the electric field (right).

Using the PTF configuration, we propose a detector configuration based on an array of CdTe pixel detectors as is shown in figure 4.7. Several CdTe pixel detectors are stacked as displayed in figure 4.7 (a). Various of such stacks are arranged together to build a detector plane (figure 4.7(b)). Finally several detector planes are stacked together to build the device (figure 4.7 (c)).
Such configuration of CdTe/CZT detectors has been presented as a very well suited arrangement for devices seeking high detection efficiency of γ-ray photons, leading to an European Patent (Chmeissani *et al.* (2008) *including J.Alvarez and C. Sánchez*). Beyond the astrophysics field, this detector configuration has shown great advantages in the field of medical applications (Chmeissani *et al.*, 2009).
A focal plane detector built under this configuration would have 3D position capability and could be used as a polarimeter (Álvarez *et al.*, 2011). The spatial resolution of such

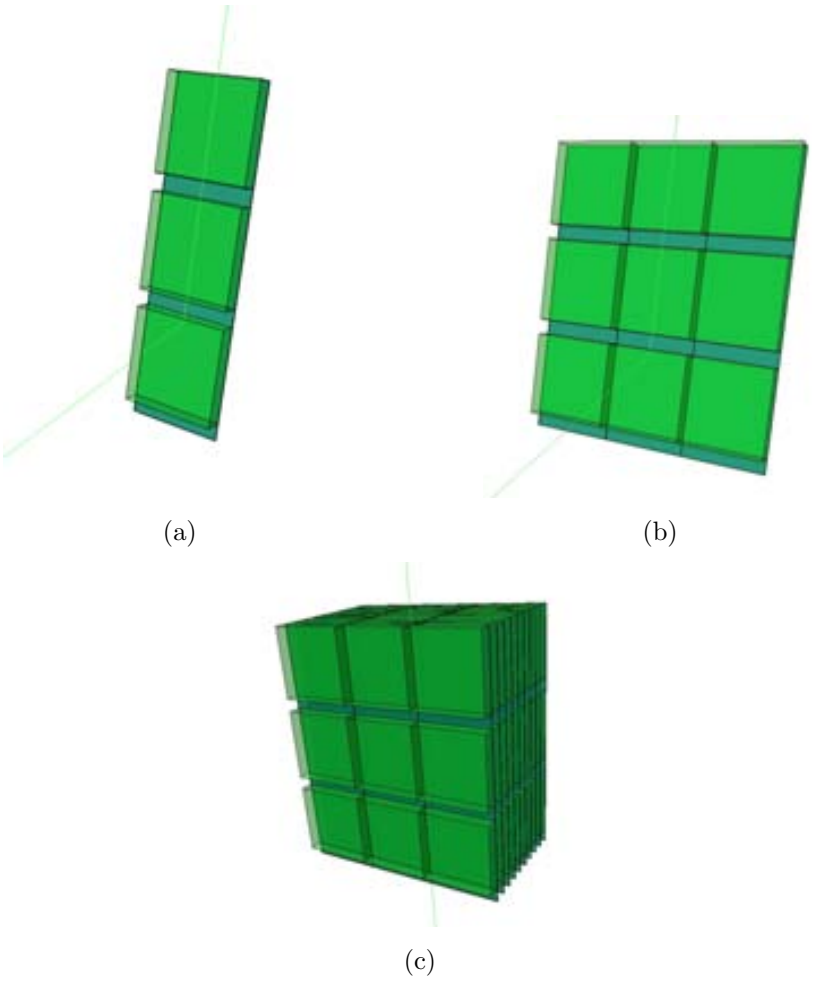

(a) (b)

(c)

Figure 4.7: Proposed configuration for the focal plane detector of a Laue lens based on a CdTe pixel detector.

a detector will be determined by the pixel size and thickness of the detector unit, where charge sharing is playing a fundamental role that should be taken into account. In the following section, our research to optimize the pixel size and energy resolution of a CdTe detector is presented.

4.3.2 Development of a CdTe detector prototype

4.3.2.1 Optimizing pixel size

In order to optimize the pixel size for a given CdTe detector thickness, it is necessary to estimate the size of the electron cloud that drifts to the anode and compare this size with the pixel pitch. Charge sharing between neighboring pixels needs to be considered in order to determine its effect on the energy resolution.
Our first step in this optimization, is to study the multiple-pixel events due to Compton scattering, e.g., analyzing the fraction of full energy peak events as a function of the number of pixel hits. Our simulations, based on the Geant4 code (Agnostelli *et al.*, 2003), include particle tracking (photons, photoelectrons and scatter electrons) as well as Cd and

(a) (b)

Figure 4.8: Schematics of the CdTe crystal geometry used in the simulations.

Te X-ray K_{alpha} fluorescence, regardless of diffusion of charge carriers during their drift towards the anode.

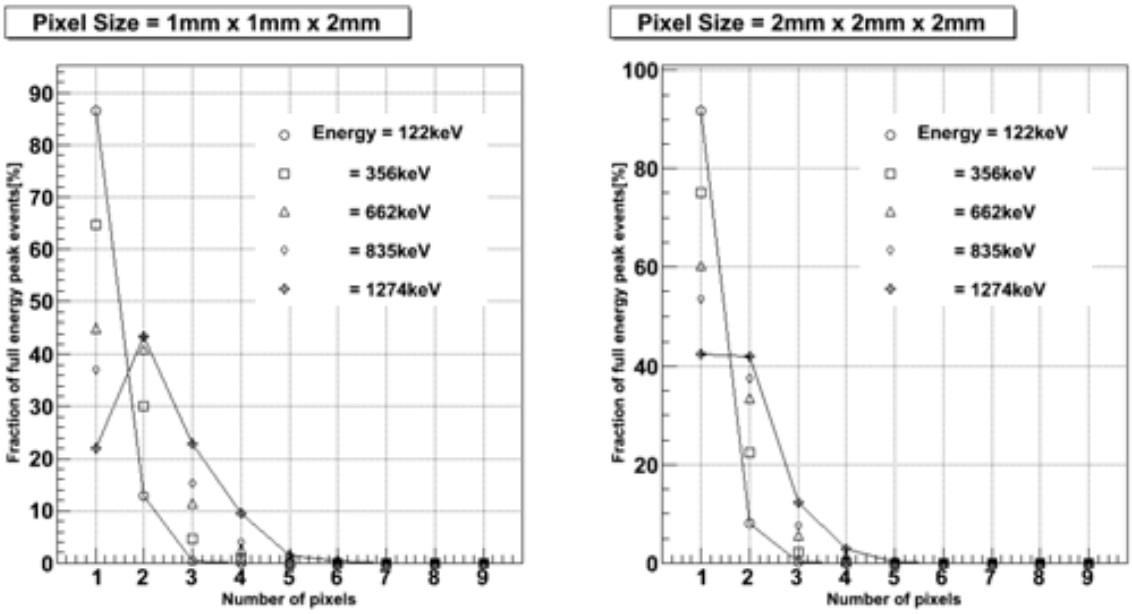

Figure 4.9: Simulation results of the fraction of multiple-pixel photopeak events as a function of the number of pixels hits in a CdTe array detector. Two different pixel sizes (thickness 2mm) for several energies of incident gamma-rays are shown.

In our model, a CdTe crystal ($10 \times 10mm$) is divided either in a (10×10) or (5×5) array (see figure 4.8). Since we do not deal with charge transport in this first step of the optimization process, the gap between pixels is ignored and it is assumed that the electrons created within one pixel are collected in that pixel. That is, the deposited energy is discretized according to the size of the pixel, either (1×1 mm) or (2×2 mm).
This simple model allows us to calculate the fraction of multiple-pixel photopeak events versus the incident photon energy (see figure 4.9 and 4.11) or versus the thickness of the detector (see figure 4.10). As expected, the simulations show that the fraction of multiple-pixel photopeak events increases as the gamma-ray energy increases (for a given thickness). It also shows that the fraction of multiple-pixel photopeak events increases as the thickness of the detector increases (for a given energy). When the electron cloud diffusion is taken into account, a decrease in the fraction of single-pixel photopeaks is

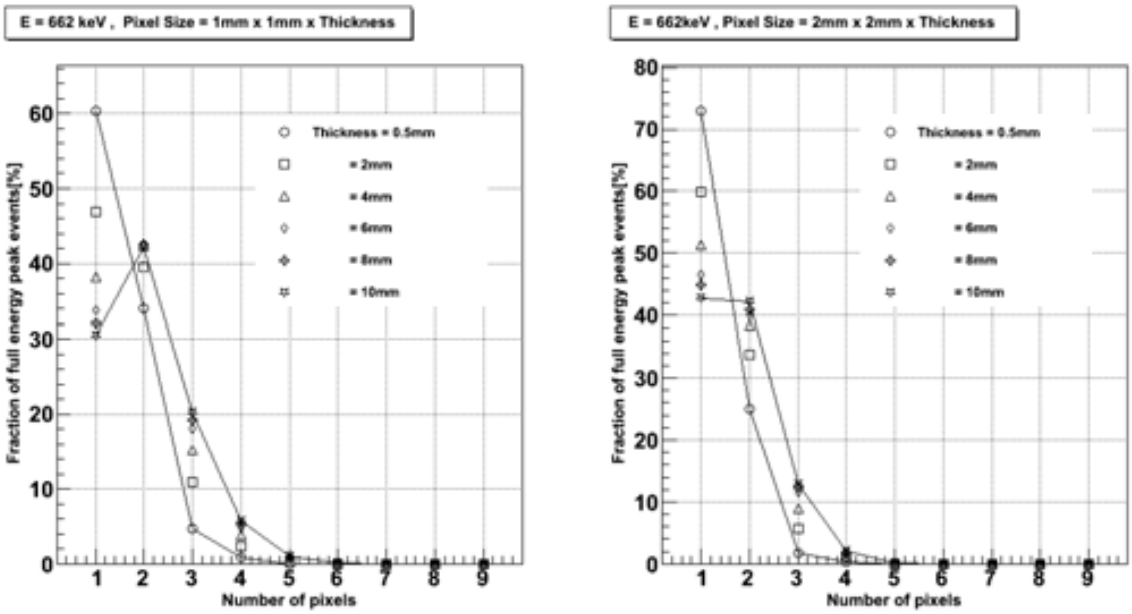

Figure 4.10: Simulation results of the fraction of multiple-pixel photopeak events as a function of the number of pixels hits in a CdTe array detector. Two different pixel sizes with several thicknesses are plotted. The energy of incident gamma-rays is 662keV.

expected, while the fraction of multiple-pixel increases due to the phenomenon of charge sharing (see the study reported by Du *et al.* (1999)).

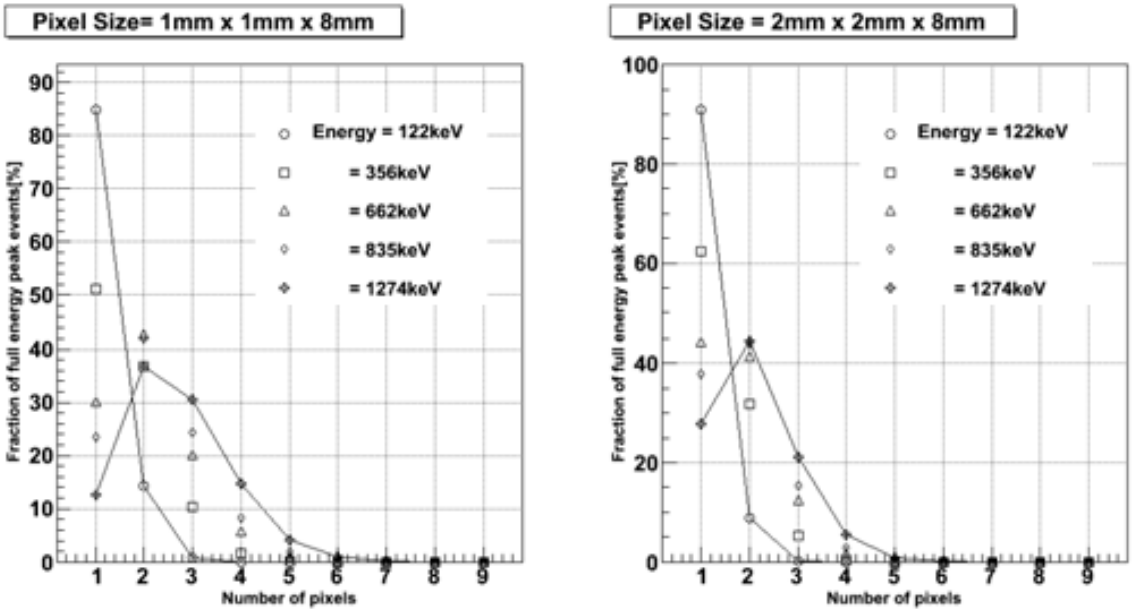

Figure 4.11: Simulation results of the fraction of multiple-pixel photopeak events as a function of the number of pixels hits in a CdTe array detector. Two different pixel sizes (thickness 8mm) for several energies of incident gamma-rays are shown.

In order to obtain high detection efficiency, proper reconstruction of multiple events is required as the fraction of multiple-pixel photopeak events increases. As shown in figure

(4.9) and (4.10), increasing the size of the pixel can be used to reduce the fraction of multiple-pixel events and improve the spectrometric capability but reducing the spatial resolution at the same time. This trade-off was considered in order to design a detector prototype. In addition, the capacity of the readout electronics should be kept in mind.

4.3.2.2 Design and structure

A CdTe pixel detector was manufactured by *Acrorad* (Japan), following the design shown in Figure 4.12. The anode was an array of 11×11 pixels, with a pixel pitch of $1\ 05mm$ and a pixel size of $1 \times 1\ mm$. A $0\ 1mm$ width guard ring surrounds the pixels in order to reduce the leakage current, caused mainly by the detector edge effects. The structure of the detector is: Platinum/CdTe/Platinum, with a thin layer of Ni/Au/Ni deposited above the Platinum (on the pixels side of the detector) in order to ensure a good bonding connectivity. The structure metal-semiconductor-metal, provides an ohmic contact to the CdTe detector.

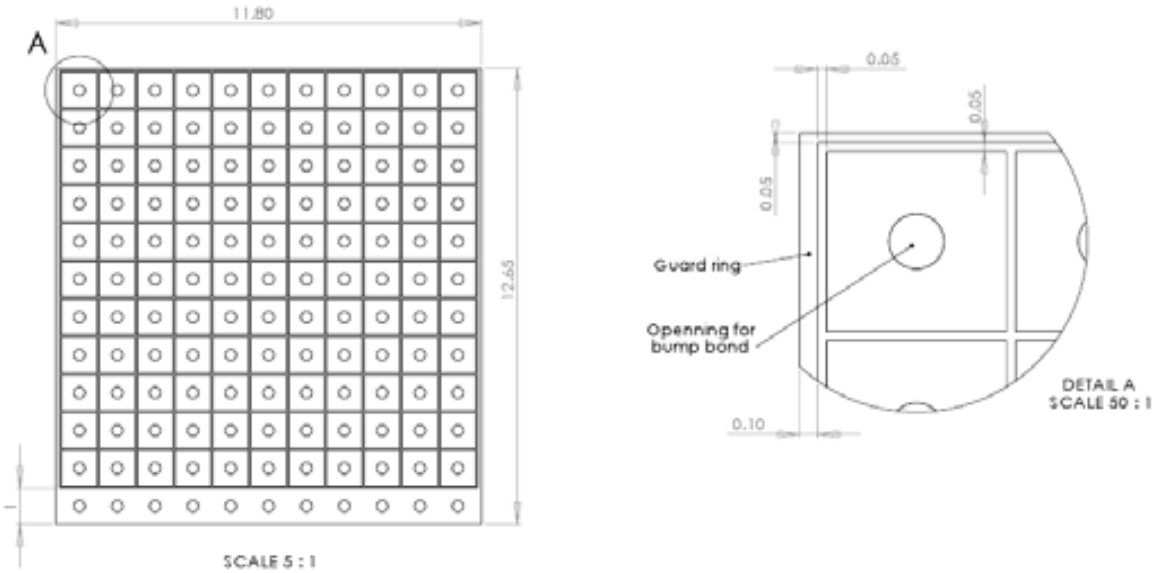

Figure 4.12: Design of the pixelated CdTe detector manufactured by Acrorad (courtesy M. Chmeissani, IFAE).

As pointed out in section 2.2.2, a Schottky contact (Matsumoto *et al.*, 1997) withstands much higher bias voltages than ohmic connections, and therefore would allow to reduce the tailing effect caused by the charge loss in the CdTe semiconductor. However, an ohmic contact CdTe detector was chossen in order to avoid the *polarization effect* (Sato *et al.*, 2011).

4.3.2.3 Readout electronics

The readout electronics used for the prototype is based on an Application Specific Integrated Circuit (ASIC), named NUCAM, developed by Seller *et al.* (2006) at the Rutherford Appleton Laboratory (RAL).

This low-noise ASIC, powered by a single 3 3V supply, is primarily intended for readout of CdTe/CZT detectors. It carries out the measure of pulse-height and rise-time for 128 channels. Data conversion is managed by a 12bit ADC integrated in the chip. The ADC has two ranges in order to trace resolution against maximum measurable signal. Table 4.3 lists the main programmable functions of this NUCAM ASIC.

Function	Control range	Used for test with ^{133}Ba	Used for test with ^{241}Am
Leakage current compensation	0.25nA - 4nA	2nA	2nA
Shaping time	0 5μs-7 5μs	7 5μs	7 5μs
ADC amplitude	0 (900mV) or 1 (1600mV)	1	1
Collection-time clock	5μs - 12μs	12μs	12μs
Threshold input	0V - 3.3 V	2.4V	1.8V

Table 4.3: Main programmable functions of the NUCAM ASIC from Seller *et al.* (2006), and values used in the test with each radioactive isotope.

The *NUCAM evaluation board* (see figure 4.15) was used as an interface with a National Instruments card for data acquisition. A program based on LabVIEW [2] was used to control the NUCAM ASIC and store the data in the computer.

4.3.2.4 Fanout fabrication and test card assembly

Due to the pitch difference between the pixels of the CdTe detector and the channels of the NUCAM ASIC, a pitch adapter or fanout board is required. This connection is carried out by an insulating glass substrate, with metal tracks to route the signal of each pixel to the front end ASIC. In addition, the fanout also provides mechanical support for the detector on the electronics board, while maintaining an effective insulation from the high bias voltage applied to the detector between these parts.

The fanout board was manufactured in the clean room facilities of the CSIC s National Microelectronics Centre (IMB-CNM-CSIC). Two masks were designed for the manufacturing, as shown in figure 4.13. A thin layer of Ni/Au was deposited in the bump pads of the fanout, in order to ensure good stud bonding connectivity to the pixels. Figure 4.14(a) shows the final result of the fanout. An optical examination of the paths was also done in the laboratory, as shown in figure 4.14(b). Further information on the manufacturing process can be found in Álvarez *et al.* (2010b) and references therein.
Once the detector is attached to the fanout board, the pads are wirebonded to the input channels of the NUCAM. The final results, after the assembly of the fanout with the CdTe and the NUCAM test card, are shown in figure (4.15).

[2] http://www.ni.com/labview/

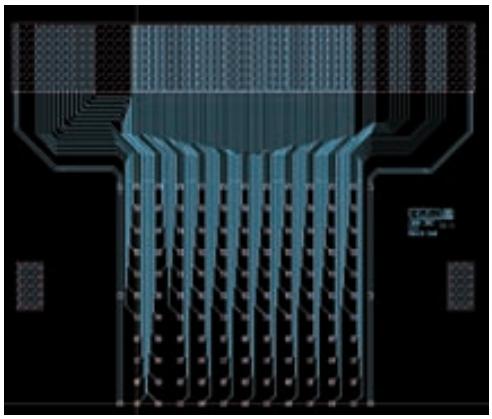

Figure 4.13: Masks of the fanout board for the pixel detector. 121 bump pads are used for pixels and 6 bump pads are used for the guard ring (courtesy J. L. Gálvez and CNM).

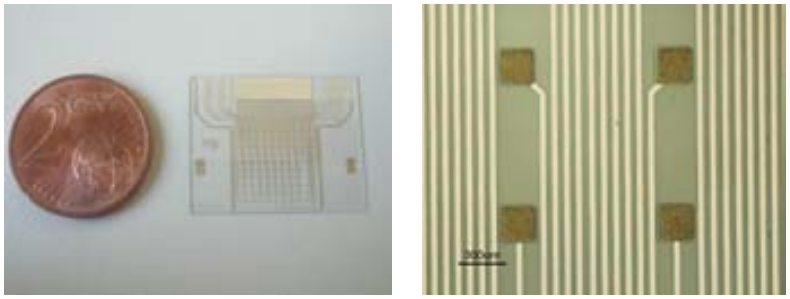

(a) (b)

Figure 4.14: (a) View of the fanout board. (b) Zoom of the fanout pads. The bump pad dimension is $200\mu m$ x $200\mu m$. The width and pitch of the metal tracks shown in the picture are $40\mu m$ and $80\mu m$, respectively (courtesy J. L. Gálvez and CNM).

4.3.3 Test of the prototype

The CdTe ohmic detector prototype was tested in the laboratory with uncollimated sources (Álvarez *et al.*, 2010a). Experimental set-up, and first measurement results are presented in this section.

4.3.3.1 Experimental set-up

The 11×11 array CdTe detector was mounted inside a customized aluminum chamber with the required input and output connections (see right panel in figure 4.16). Air was pumped out of the chamber to reach a moderate vacuum. This was done to avoid any potentially damaging condensation during the cooling process. Then, the detector was cooled down in order to decrease the leakage current and apply much higher bias voltage to the common cathode.

The measurements were performed with two γ-ray sources, ^{133}Ba and ^{241}Am, with activities 1μCi and 10μCi, respectively. The isotopes were placed at a distance of $\sim 15mm$ from the center of the detector, in the cathode side (see left panel in figure 4.16). Due to the low activity of the sources, an exposure time of $\sim$5 hours was needed. The programmable parameters of the NUCAM ASIC implemented to carry out these measurements, are those

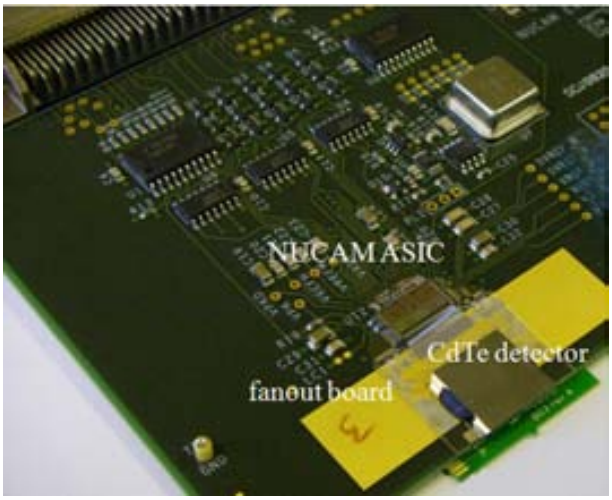

Figure 4.15: Picture of the CdTe pixel detector and readout chip within the evaluation board (or test card). The pixels of the CdTe are stud bonded to the fanout board. At the upper end of the fanout board we can see the paths that have been wired bonded to 121 input channels of the readout electronics NUCAM ASIC.

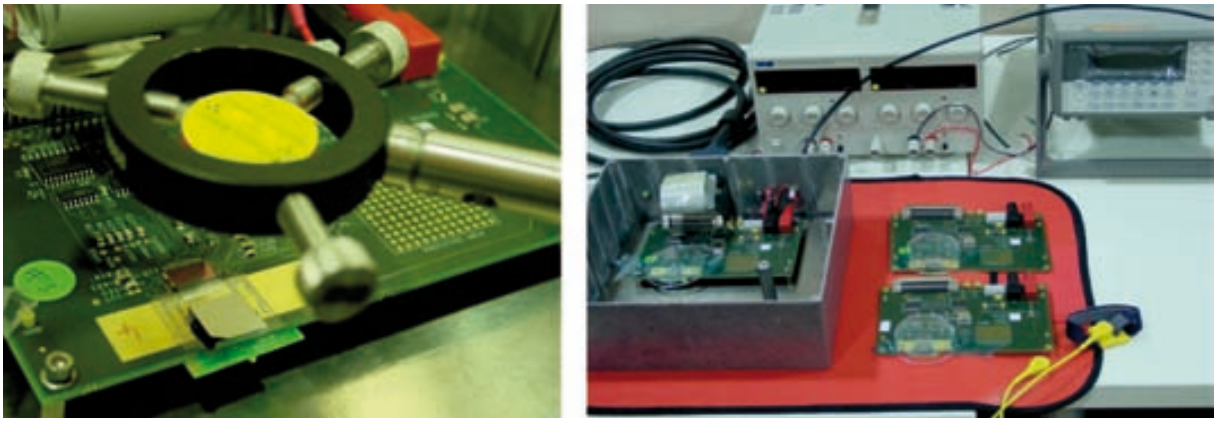

Figure 4.16: Uncollimated source placed in front of the detector, in the cathode side (left panel). NUCAM test board mounted in a customized aluminum box next to other two test boards (right panel).

shown in table 4.3.

4.3.3.2 Measurements and discussion

The objective of the initial measurements was to test the correct operation of the prototype as well as studying its spectroscopic performance. As shown in the right panel of Figure 4.16, three identical prototypes were built. The measurements and results corresponding to the prototype with the largest number of working pixels are presented here.

Electronic board test

Firstly, the NUCAM ASIC was evaluated using the test board and the Labview system. A pulse generator (33250A Agilent[3]) was used to apply a $100ns$ linear fall-time step to the calibration capacitor of $8fF$. This is the total capacitance seen at the entrance of each channel of the NUCAM ASIC when it operates in test mode.

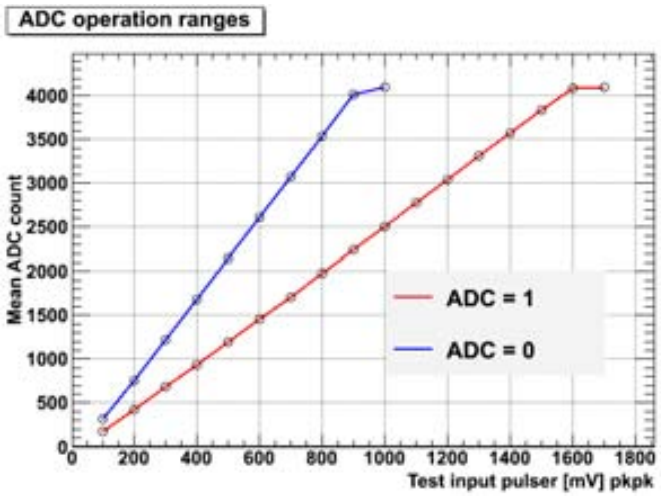

Figure 4.17: Signal conversion range of the NUCAM ASIC for both operation ranges of the ADC (Gálvez, private communication).

Figure 4.17 (Gálvez, private communication) shows the ADC values, for a channel, against the input pulse amplitude, for both operation modes of the NUCAM ASIC (listed in table 4.3). A linear behavior up to $900mV$ (operation mode ADC=0) and up to $1600mV$ (operation mode ADC=1) is obtained. These numbers are ideally equivalent to a 250keV and 350keV γ-ray interaction in CdTe, respectively (using the ionisation energy listed in table 2.1). This is consistent with the expected operation ranges of the NUCAM ASIC described by Seller *et al.* (2006). The lower signal input that was measured, with the threshold set at its minimum operable level, was $100mV$ (corresponding to 22keV in CdTe). Below this value, the existing noise did not allow us to measure a clear signal.

For each of the 128 NUCAM s channels, the ADC values were measured in both ADC operation ranges while a test pulse amplitude was applied. From these measurements, gain and offset of each channel were obtained for later correction. Figure 4.18 (a) shows the ADC values obtained with a test pulse amplitude in the range $800 - 1600mV$ for a few channels. Figure 4.18 (b) shows the gain distribution measured for all channels of the NUCAM ASIC in the operation mode ADC=1. The low dispersion of the gain, $\tau = 0\ 06$, indicates a quite similar response for all channels.

[3]www.agilent.com

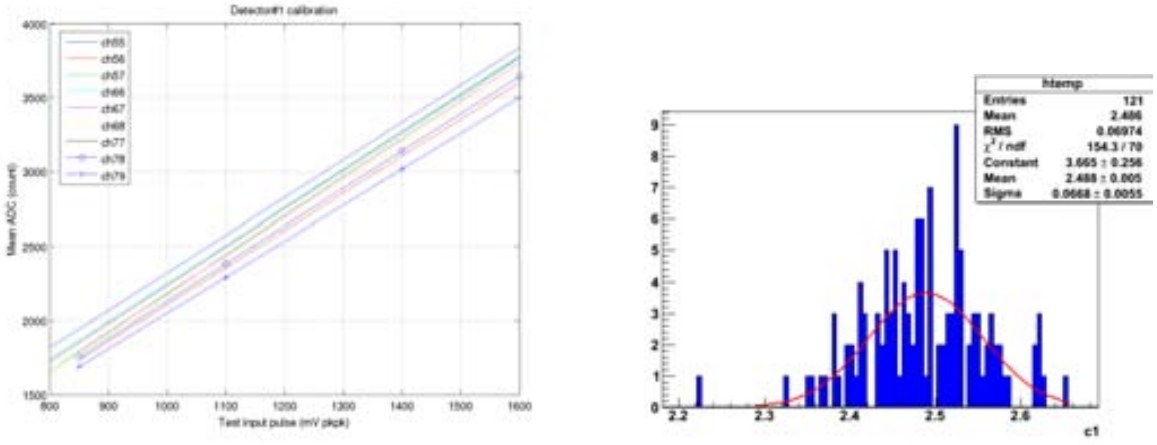

(a) (b)

Figure 4.18: (a) ADC values measured for some channels with a test pulse amplitude in the range 800-1600mV (Gálvez, private communication). (b) Gain distribution obtained for all channels of the NUCAM ASIC.

Electronic noise measurements

In order to estimate the best spectral resolution achievable with the NUCAM ASIC coupled to the CdTe detector, the electronic contribution to the energy resolution (see equation 2.15) needs to be studied.

The electronic noise of a bare NUCAM channel is measured using an external pulse as described above. Figure 4.19 shows two measurements, one for each ADC operation range. Considering the FWHM ($= 2\,35\tau$) of the gaussian fit in each case, the signal conversion of the NUCAM ASIC shown in Figure 4.17 and the ionization energy in CdTe ($E_{e-h} = 4\,43eV$), a noise of 1.3keV and 1.1keV FWHM was obtained for each operation mode of the NUCAM ASIC (ADC=1 and ADC=0 respectively).

It should be kept in mind that this electronic noise was measured without anything connected but the test capacitance ($8fF$). Connecting the $2mm$ CdTe detector to the NUCAM ASIC will add the capacitance of the CdTe ($\sim 32fF$), bonding and pads. Taking into account the NUCAM ASIC simulation presented in Seller *et al.* (2006) (which predicts a slope of $80eV\ pF$ for added detector capacitance), we do not expect a high contribution to the electronic noise because of the additional capacitance.

The leakage current will be another source of noise at the input of the NUCAM ASIC channel, presumably of great relevance because of the ohmic contact of the CdTe prototype (see section 4.3.2.2). However, the guard ring designed in the prototype (see figure 4.12), as well as the low temperature at which measurements were carried out, should reduce the effect of the leakage current. For instance, when a bias voltage of $-400V$ was applied at room temperature (23°C) an average input current of $330nA$ was meassured in the device, while at -10°C and same bias voltage, this current dropped to $0\,6nA$. In order to perform our measurements, the leakage current compensation of the NUCAM ASIC was set to $2nA$, after several tests in the operating range of the NUCAM ASIC (0.25nA - 4nA).

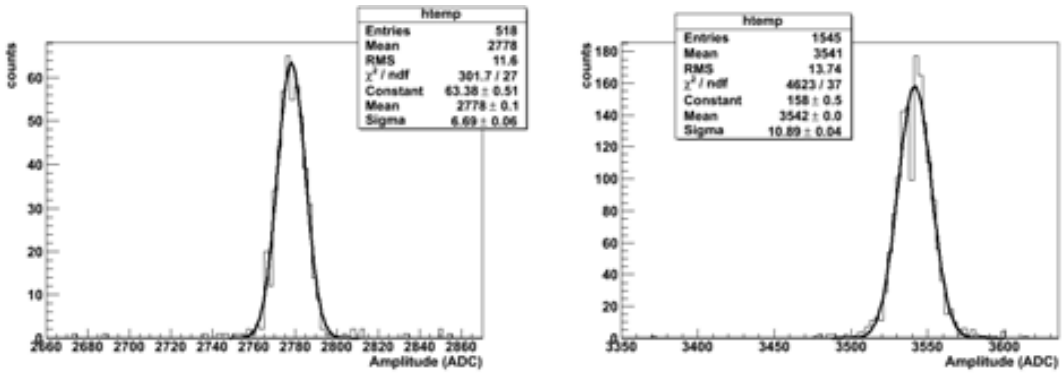

(a) (b)

Figure 4.19: Electronic noise measurements for a bare channel of the NUCAM ASIC, operating in the range ADC=1 (a) and ADC=0 (b).

Gamma radiation sources and raw spectra

The radioactive isotope, ^{133}Ba (1σCi) and ^{241}Am (10σCi), was placed in front of the CdTe detector without collimation (see figure 4.16). Several measurements with different values for the parameters (bias voltage, shaping time, temperature) were carried out. The most promising results were obtained for a temperature of -10 °C, bias voltage of $-400V$, and the selected functions for the NUCAM ASIC given in table 4.3.
Figure 4.20 shows raw data spectra obtained with the 121 pixels of the CdTe prototype when it was irradiated with photons from the ^{133}Ba source. Almost all pixels were conected properly -since we get a spectrum for each pixel- but we found some differences between their responses. It can be seen that pixels framed in red have a less defined distribution than those framed in green (in the central part). In this measurement, the different gain for each channel (see figure 4.18) was not taken into account.

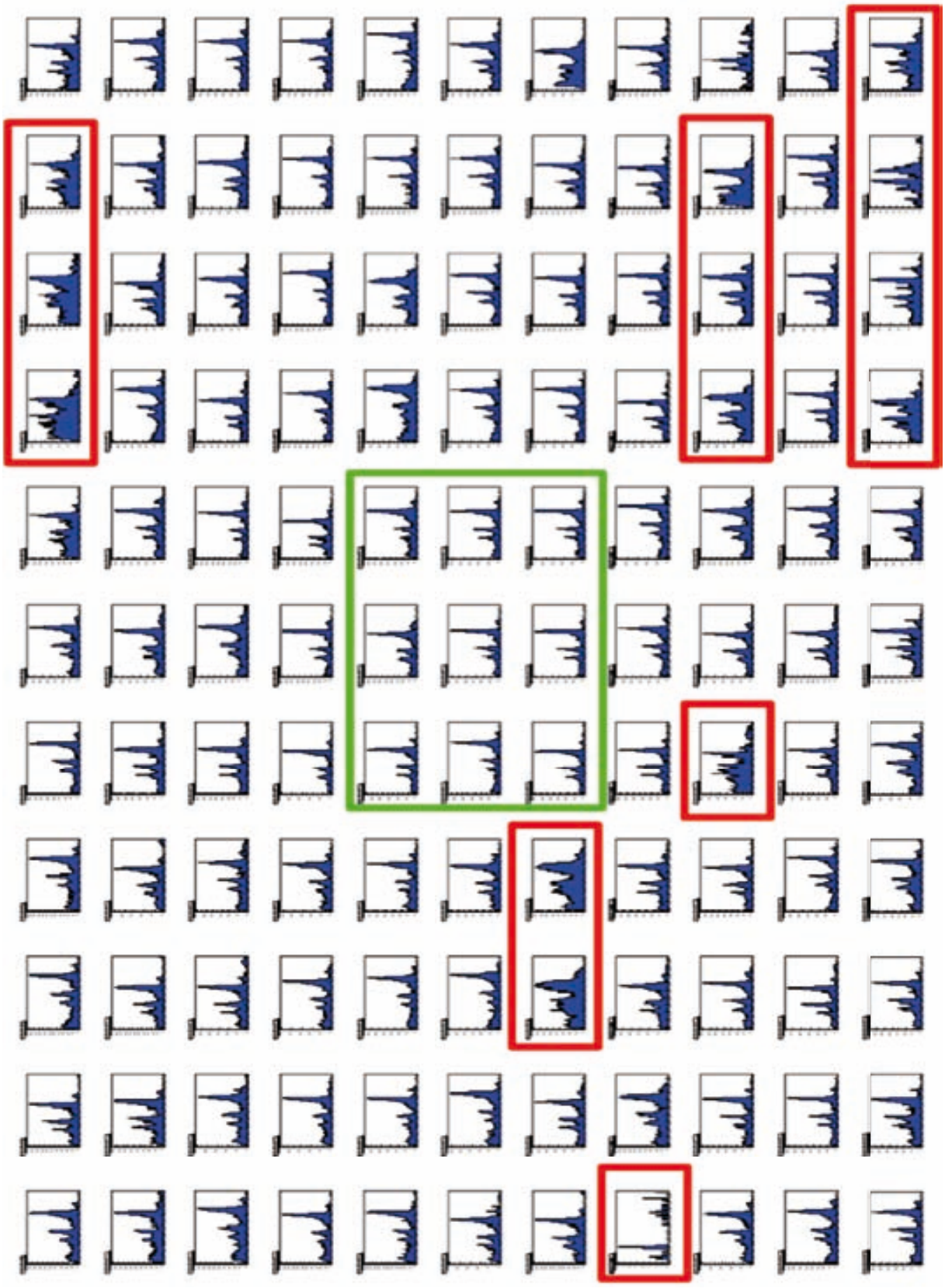

Figure 4.20: Spectrum of the ^{133}Ba source obtained in each of the 121 pixels of the CdTe prototype (raw data).

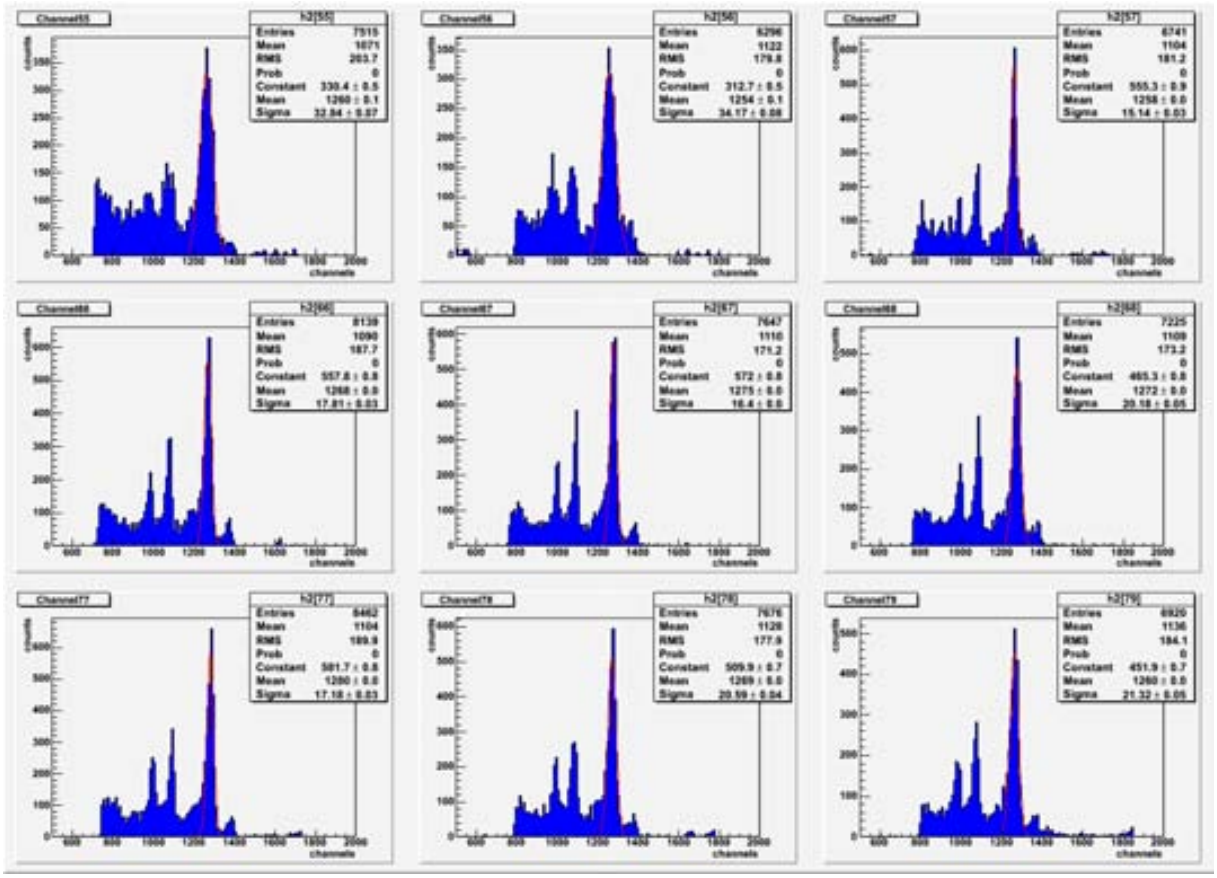

Figure 4.21: Spectra of the ^{133}Ba source obtained by 3x3 central pixels of the CdTe detector after gain correction of the channels.

The ^{133}Ba spectra, obtained in the 3x3 central pixels of the CdTe detector (framed in green in figure 4.20) after gain and offset correction for each channel are shown in Figure 4.21. Although some degree of homogeneity was observed, we found important differences even after gain and offset correction. Thus, for example, the FWHM of the 356keV peak, in the first two panels of figure 4.21 almost doubles that of the others peaks. For this reason we have not added the contribution of each pixel to obtain a combined spectrum.

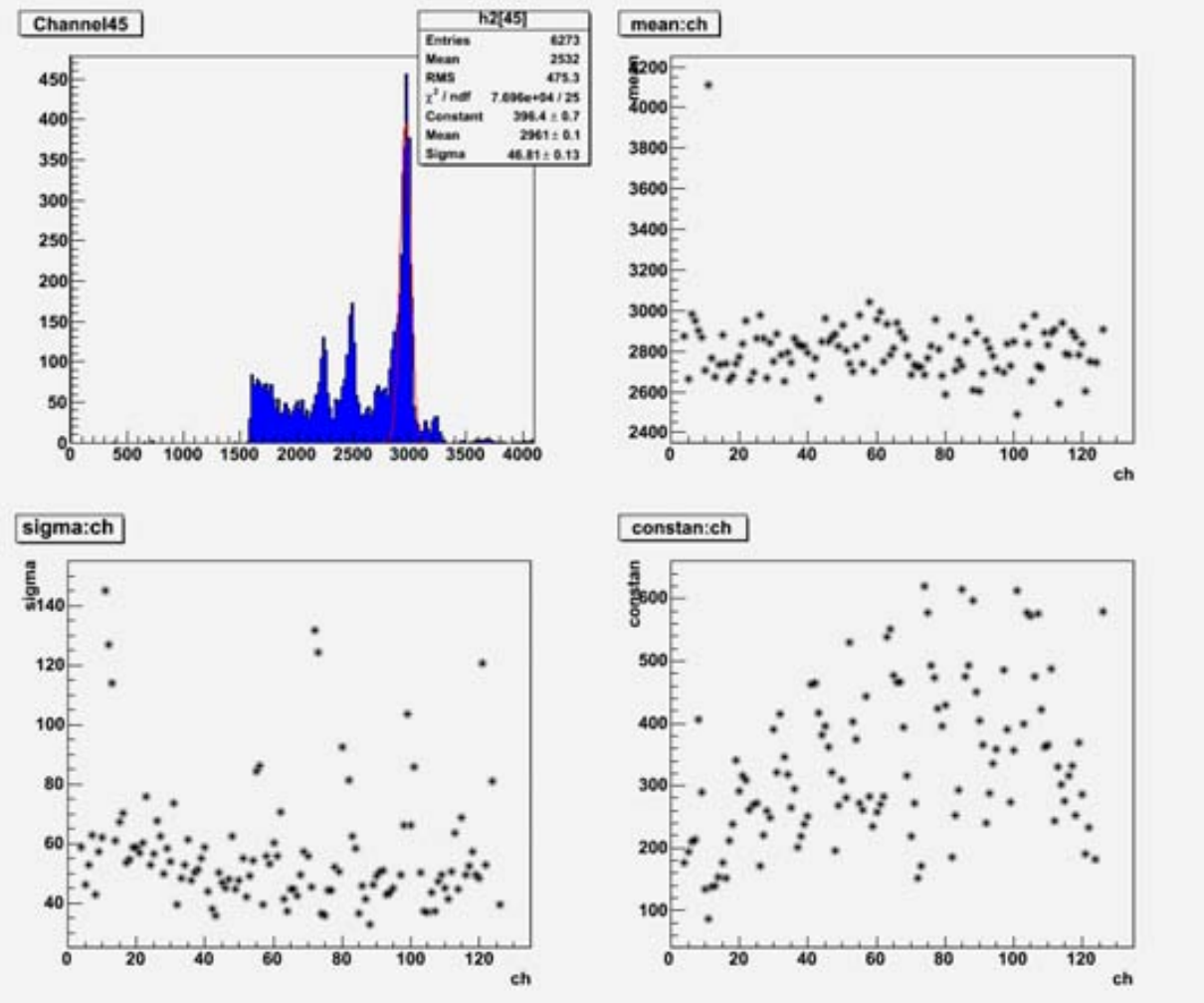

Figure 4.22: The upper left panel shows the raw data spectrum of the ^{133}Ba source obtained with a single pixel. The other panels show the gaussian fit parameters (mean, sigma, constant) obtained for the 121 pixels of the CdTe prototype.

The ^{133}Ba spectrum obtained with a single pixel (corresponding to the channel 45) is shown in the upper left panel in Figure 4.22. The gaussian fit parameters (mean, sigma, constant) performed on the higher peak of the measured spectrum in the 121 pixels, are shown in the other panels. The dispersion on the data caused by the different responses of the 121 pixels is clearly shown. Likewise, the non-homogeneous illumination of the detector by the uncollimated source is clearly visible in the lower right panel which shows the number of photopeak counts in each pixel.

Analogously to the previous measurement, figure 4.23 shows the measurements with the ^{241}Am source.

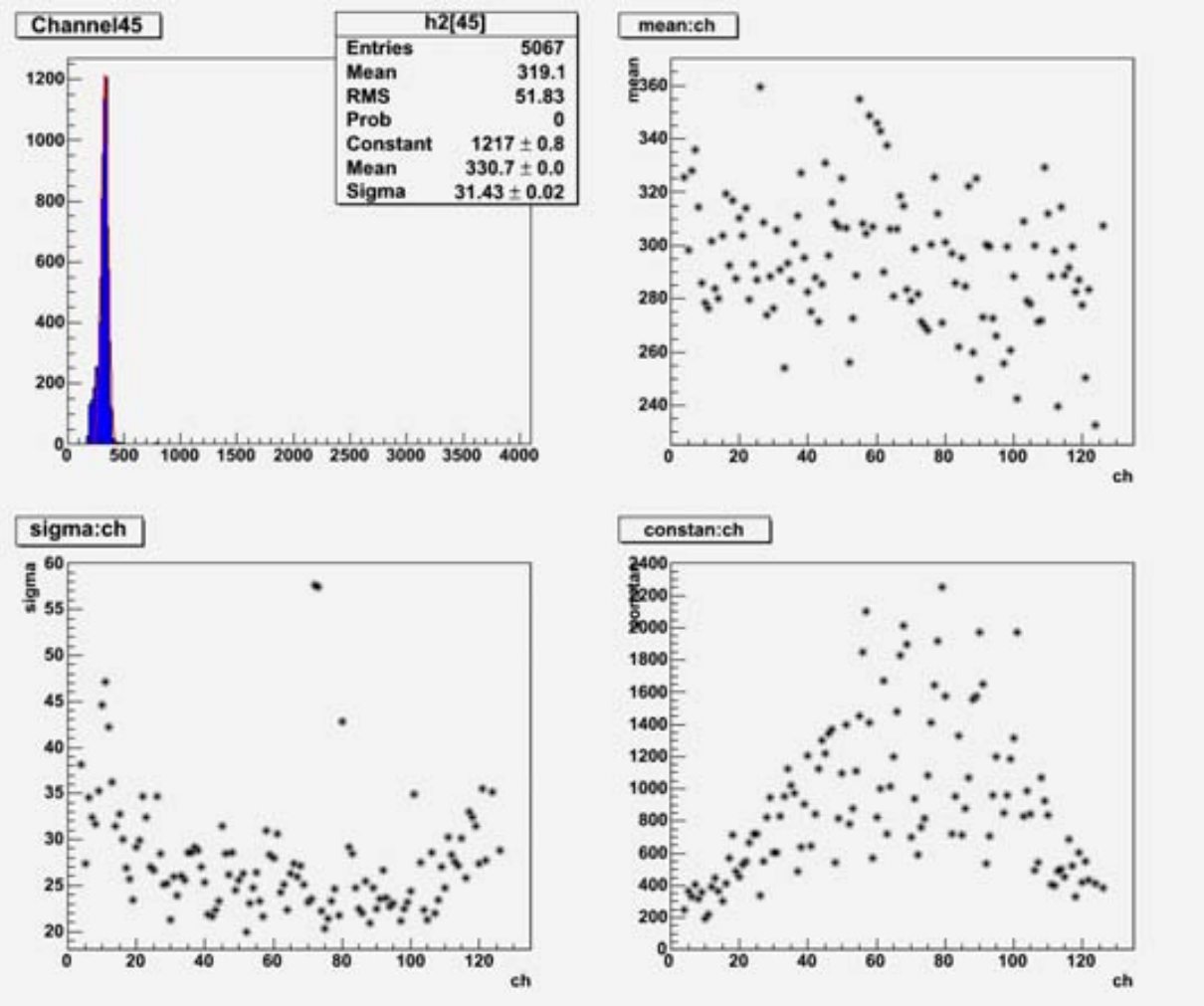

Figure 4.23: The upper left panel shows the raw data spectrum of the ^{241}Am source obtained with a single pixel. The other panels show the gaussian fit parameters (mean, sigma, constant) obtained for the 121 pixels of the CdTe prototype.

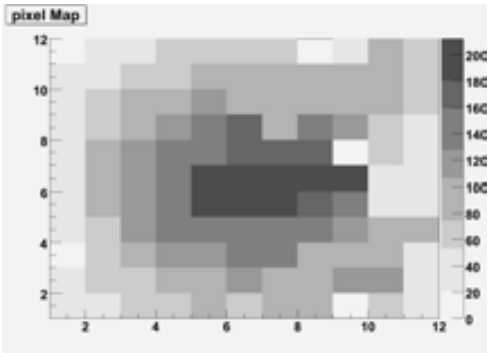

Figure 4.24: Pixels map of the CdTe detector prototype when it is irradiated with photons from the uncollimated ^{241}Am source.

The pixels map shown in Figure 4.24 was obtained by illuminating the detector with the uncollimated ^{241}Am source. It represents the number of counts in the photopeak for the spectrum measured with each pixel of the detector (see lower right panel of figure 4.23). The non-homogeneous illumination of the detector by the uncollimated source is clearly visible in this map.

Calibrated spectra

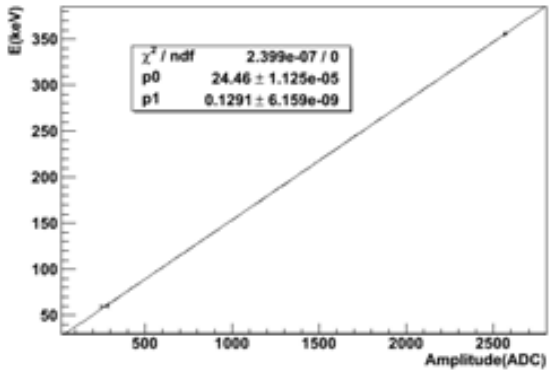

Figure 4.25: Calibration curve obtained with X- and γ-rays from ^{133}Ba and ^{241}Am.

For calibration purposes, measurements with both radioactive sources, ^{133}Ba and ^{241}Am, were carried out with the NUCAM ASIC in the same operation mode. The high energy operation mode of the NUCAM ASIC (ADC=1) was chossen in order to measure the 356 keV energy peak of ^{133}Ba. As described above, the higher energy achievable with the mode ADC=0 is 250keV (see figure 4.17 and the text explanation).

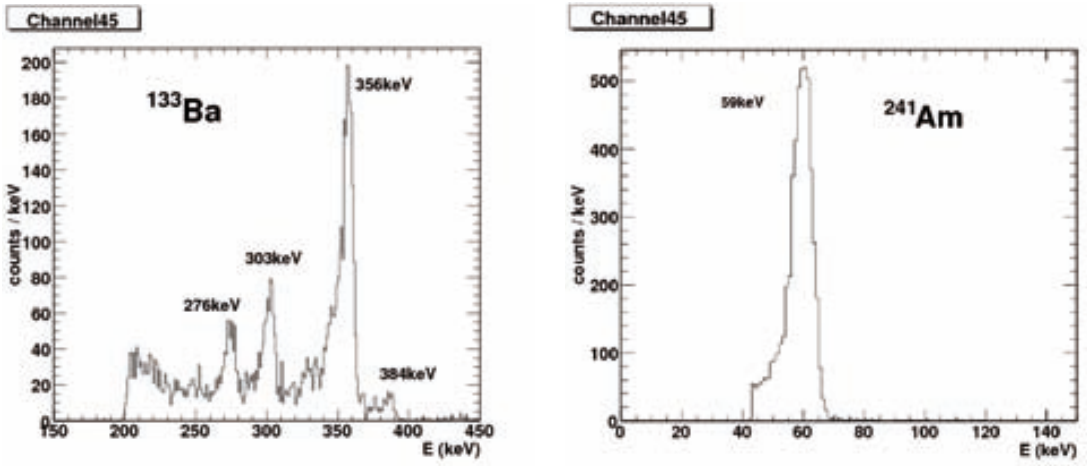

(a) (b)

Figure 4.26: Spectra of ^{133}Ba and ^{241}Am obtained with a single pixel of the 2mm thickness CdTe prototype. The measured energy resolutions (FWHM) are 5.47keV and 9.2keV at 59.5keV and 356 keV, respectively.

The calibration curve is shown in figure 4.25, after fitting the 59.5keV energy peak (^{241}Am) and 356keV energy peak (^{133}Ba). A simple gaussian fit was used, without taking into account the tail of the peaks shown in the upper left panel of figures 4.23 and 4.22. The origin of the tail was discussed in section 2.2.2.

The spectra of ^{133}Ba and ^{241}Am obtained for one pixel (channel 45) after calibration are shown in Figure 4.26. A different threshold level was set in both cases, depending on the energy range (listed in table 4.3). The cut in the ^{241}Am spectra is clearly seen at $\sim 42keV$. The measured energy resolution (FWHM), for this particular pixel, is listed in table 4.4.

Energy [keV]	ΔE (FWHM) [keV]
59.5	5.47
356	9.2

Table 4.4: Measured energy resolution in one pixel of the CdTe prototype.

It should be pointed out that this energy resolution was obtained with one of the best performance pixels. As shown in the lower left panel of Figures 4.23 and 4.22, there is a wide dispersion on the FWHM measured throughout the pixels.
There are various possible explanations for the heterogeneous response of the 121 pixels after correction of the channels, e.g. imperfections in the CdTe crystal, defect in the electric contact or temperature fluctuations. In any case, stabilities issues related with the long acquisition time (about 5 hours) is the more likely cause of those variations. Further measurements are needed in order to draw a conclusion.
Regarding the energy resolution measured in one pixel, let us consider the three different contributions given by equation (2.15):

- ΔE_{Fano}

  The statistic limit to the energy resolution (Fano-limit) is calculated from equation (2.17), taking $\epsilon = 4\ 43eV$ and $F = 0\ 15$ (data from Takahashi *et al.* (2001)).

Energy [keV]	ΔE_{Fano} (FWHM) [keV]
59.5	0.467
356	1.143

Table 4.5: Fano limit of the energy resolution.

- ΔE_{elec}

  The measured electronic contribution for the ADC=1 mode is $\Delta E_{elec} = 1\ 3keV$ (discussed above), to which the leakage contribution has to be added. In addition, temperature fluctuations during the long acquisition times (over 5 hours), could produce significant variations of the electronic noise. It should be pointed out here that the leakage current compensation of the NUCAM ASIC is the same in each channel.

- $\Delta E_{collect}$

  With a bias voltage of $-400V$ and a thickness of 2mm, the effects of incomplete charge collection should be taken into account as a major cause of energy resolution degradation. As seen in Figure 4.26, the characteristic energy tail below photopeak energies appears in both measurements: 59.5 keV (^{241}Am) and 356keV (^{133}Ba).

4.3.4 Summary and Outlook

The undergoing development of a detector array concept based on CdTe pixel detector in planar-transverse-field (PTF) configuration is presented. A CdTe pixel detector prototype has been succesfully designed and implemented. First measurements with a ^{133}Ba and an ^{241}Am source have been carried out in order to test the prototype. All 11×11 pixels of the prototype were properly connected to the NUCAM ASIC channels but a heterogeneous response was observed even after correction for gain and offset of each ASIC channel. Further measurements with shorter exposure time (i.e., with more active sources) are needed in order to draw a conclusion about the origin of this heterogeneity.
The measured energy resolution is far above the Fano-limit, due to the electronic noise and incomplete charge collection in CdTe. In order to determine the importance of each contribution, a measurement method to estimate the leakage current is needed. On the other hand, the NUCAM ASIC provides a measure of the collection time, that can be used to perform a rise-time discrimination (see section 2.2.2). Although this technique would improve the energy resolution, it would also lead to a significant reduction of the sensitivity.
In order to perform all these new measures, a customized vacuum chamber with a cooling system that allows an accurate control on the temperature (down to -30C), is being set up in the laboratory of the *Institute of Space Sciences (CSIC-IEEC)*. In addition, a radiation laboratory has been defined at the ICE, in order to perform measurements with more active sources.
Among the prospects, our undergoing detector design (Álvarez *et al.*, 2011) is proposed as a payload options for a balloon-borne experiment dedicated to hard X- and soft gamma-ray polarimetry currently under study (Caroli *et al.* (2011) *-including Alvarez J.M-*). On the last years, the capabilities of Cd(Zn)Te pixel detectors as hard X- and soft gamma-ray polarimeter have been studied in the framework of the POLCA (POLarisation with Cd(Zn)Te Array) experiment (see e.g. Caroli *et al.* (2009) and da Silva *et al.* (2008)) or in the recently experiment reported by Limousin *et al.* (2011).

Chapter 5

An all-sky Compton telescope of DUAL

In contrast to the proposed missions MAX and GRI (see section 2.4), the DUAL mission combines a Compton telescope with a Laue lens in order to meet the broad variety of requirements that a future γ-ray mission must face. While the Compton telescope performs large-scale exposures, the Laue lens will simultaneously perform very deep pointed observations (see DUAL mission concept in von Ballmoos *et al.* (2011)).
The DUAL Compton detector, which is also the focal plane detector of the Laue lens, is based on cross-strip germanium detectors. This chapter describes the Monte Carlo simulations performed in order to estimate the DUAL mission performances.

5.1 DUAL mission concept

The DUAL mission (introduced in section 2.4.3) was proposed to the ESA Call for a Medium-size mission [1]. The proposal was prepared in the framework of a large international collaboration (see Appendix A) and submitted in December 2010 (von Ballmoos *et al.*, 2010b).
The DUAL mission is composed of a single spacecraft that carries the gamma-ray optics (Laue Lens and Coded Mask) and a Compton detector. The optics is located on the main satellite while the detector is at the end of a 30 meters-long mast at the focal plane (see artistic view in Appendix A). This configuration is particularly advantageous for a γ-ray Compton instrument since it provides an all-sky field-of-view while the background induced by the spacecraft is reduced (see section 1.2.2). In order to take advantage from these properties, DUAL was proposed to operate in the second Lagrange point (L2) where background radiation from the earth s albedo can be avoided and the entire sky (4ψ steradians viewing) is available. The L2 orbit provides more than four times exposure time for every source in the sky than a low Earth orbit, while simplifying the pointing of its $30m$ long configuration.

[1] http://sci.esa.int/science-e/www/object/index.cfm?fobjectid=47570

In contrast to the previously discussed GRI mission, DUAL is not a focusing mission but a survey mission with a focusing Laue lens. Hence, the Compton detector is a key payload of the mission that performs a *DUAL* function: as a focal plane detector for the optics and a sensitive wide-field monitor for an all-sky survey.

5.1.1 Scientific requirements

The DUAL mission aims to address many of the astrophysical issues discussed in section 1.1. Among them, primary scientific objectives of the mission are: *Type Ia supernovae* that will be targeted by the Laue lens (see section 1.1.1), *Gamma-Ray Burts (GRB)* that will be detected on the entire sky with the Compton instrument (see section 1.1.3), and *Galactic Cosmic positrons* (see section 1.1.2) that will be targeted by the Coded Mask. Table 5.1 lists the mission requirements in order to reach these scientific goals. An overview of the DUAL scientific objectives can be found in von Ballmoos *et al.* (2010a).

Parameter/Objective	GC positrons	SN Ia	GRB
Energy coverage	$0\,2 - 0\,6\ MeV$	$800 - 900\ keV$	$20\ keV - 10\ MeV$
Narrow line sensitivity ($ph\ cm^{-2}s^{-1}$)	$3x10^{-6}$ in 3 y	10^{-6} in 10^6 s	-
Energy resolution (FWHM)	0 5%	1%	0 5%
FoV	4ψ steradian	10 arcmin	4ψ steradian
Angular resolution	1 degree	-	1 degree
Timing	-	-	$100\sigma s$
Polarimetry (MDP [2], 3τ)	-	-	5% for 100 mCrab

Table 5.1: DUAL mission requirements from von Ballmoos *et al.* (2010b).

5.1.2 Laue lens

The Laue lens of DUAL is of a broad-band gamma-ray lens designed to be efficient in the energy range from $800keV$ to $900keV$ and aimed to detect the ^{56}Co line of SN Type Ia. The lens is composed of 5800 crystals of different materials that are arranged in 32 concentric rings. Each ring is populated by identical crystals and glued onto a CeSiC monolithic substrate. The main characteristics of the Laue lens are listed in Table 5.2. Further information about the crystals proposed for the DUAL lens can be found in Barriere *et al.* (2007).
The Laue lens of DUAL has an angular resolution of 1 *arcmin* and a field-of-view of 5 *arcmin* derived from the focal length and detector size. The effective area of the Laue lens peaks at $340cm^2$ for 847keV and has about 62% of the signal concentrated in a disc of 7mm radius (von Ballmoos *et al.*, 2010b).

5.2 Baseline instrument of the DUAL mission

The baseline detector proposed for the DUAL mission is based on a compact array of cross-strip germanium detectors with high spectral and 3-D spatial resolution. A total number of 45 highly segmented germanium detectors (HPGe) are arranged in a 3x3 matrix. A

Parameter	Value [units]	Parameter	Value [units]
Focal length	30 [m]	Mass of crystals	61 [kg]
Inner radius	12.85 [cm]	Total number of crystals	5800
Outer radius	48.50 [cm]	Crystals size	10×10 $[mm^2]$
Crystal Number (material)	3193 (Rh), 1662 (Ag), 521 (Pb)	Crystals thickness	5.1 - 12 [mm]
Crystal Number (material)	348 (Cu), 76 (Ge)	Crystal mosaicity	45 [arcsec]

Table 5.2: Characteristics of the Laue lens of the DUAL mission.

total of five layers are stacked together and mounted on a light structure designed to be compact and maximize the instrument detection efficiency (see Figure 5.1). The device is operated at cryogenic temperatures in a common vacuum cryostat.

5.2.1 3-D Ge strip detectors

Each one of the 45 HPGe detectors has an active area of $10 \times 10cm^2$ and a thickness of $15mm$. Anode and cathode are segmented into $2mm$ pitch strips, where the strips along one side are orthogonal to the ones on the other side. The electrodes are surrounded by a $1mm$ thick guard ring.

Parameter	Value	Parameter	Value
Strip pitch & gap	$2mm$ & 0 $5mm$	Guard ring thickness	$1mm$
Size	$10 \times 10cm^2$	Thickness	$15mm$
Depth res. (FWHM)	0 $4mm$	Depth threshold	$25keV$
Position resolution	1 $6mm^3$	Spectroscopy threshold	$10keV$
Spectral resolution (FWHM)@662keV	2 $1keV$	Spectral resolution $<$ 0 $1MeV$ (noise limit)	1 $6keV$

Table 5.3: Main performance parameters for the 3-D Ge strip detectors proposed for the base line detector of the DUAL mission (von Ballmoos *et al.*, 2010b).

When an interaction takes place in the germanium detector, the X-Y positioning is obtained through identification of the active anode and cathode, while the Z positioning is achieved through the time difference between the electron and hole collection on opposite faces of the detector. The expected position resolution for a γ-ray interaction within the HPGe detector is 1 $6mm^3$.
The 3-D Ge strip detector technology has been developed during the last years in the framework of the *Nuclear Compton Telescope* (NCT) project at the University of California (Berkeley) and has been validated in a successful balloon experiment (Boggs *et al.*, 2004).
The main performance parameters of the 3-D Ge strip detectors, assumed for the base line instrument, are summarized in Table 5.3. The main differences between the NCT prototype and the based line instrument of DUAL are the total number of channels (4500 of DUAL vs. 912 of NCT) and the volume ($6750cm^3$ of DUAL vs. $972cm^3$ of NCT).

5.2.2 Mass model

In order to estimate the background and obtain reliable performances for DUAL s instrument, it is crucial devising an accurate model of the detectors and its surroundings (see discussion in section 1.2.2.2). Figure 5.1 (a) shows the mass model of a 3-D Ge strip detector. All passive materials are included in detail (e.g. cold finger made of aluminum, $400nm$ thick aluminum strips, passive Germanium, $1mm$ Al guard rings, circuit boards, thermal junctions and screws). This model of the detector unit is based on the NCT Ge detector design. Likewise, the detector characteristics listed in table 5.3 were used in the simulation.

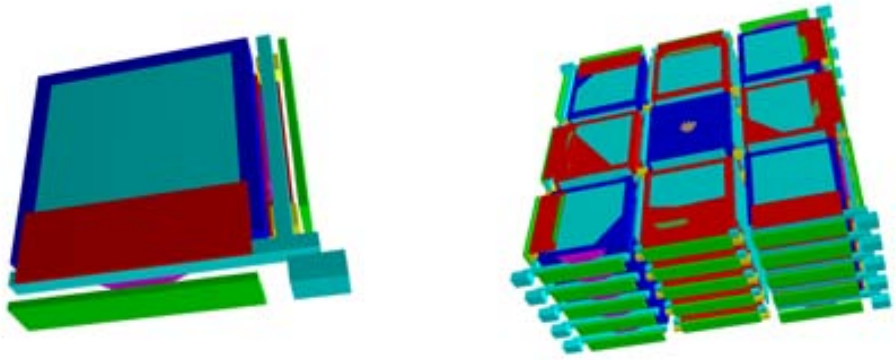

(a) (b)

Figure 5.1: View of a 3-D Ge strip detector (a) and the 45 detectors stacked in five layers (b) as used for simulations.

The 45 Ge-strip detectors of DUAL, stacked in five layers with 25mm gaps, are shown in figure 5.1 (b). The inner hole bored on the central detector of the front layer (seen in the image) was included in order to allow γ-rays from the lens to hit directly the second layer, so that backscattering photons can be captured on the first layer detectors.
The Ge-strip detectors are housed in a single vacuum cryostat where they are cooled down to 85K. The passive material of the cooling system was roughly modeled and placed on the equatorial plane outside the detector (see figure 5.2). The front-end electronics, to read out the 4500 signal channels, are located in boxes mounted on the sides of the cryostat. The entire structure is surrounded by a plastic anticoincidence shield which provides veto signals for charged particles entering the detector from any direction. The scintillation light is read out with photosensors coupled to the plastic shield (see section 6.1.1).
The Compton instrument of DUAL, with a total mass of about 96Kg (36Kg of Germanium), is placed on top of a carbon fiber structure 1cm thick and is located at the end of the 30m mast. Due to this long distance, the effect of the radiation coming from activation of the spacecraft material is neglected in our analysis.
The model used for the simulation study presented in the following section, is depicted in Figure 5.2. The DUAL detector mass model is a modified version of the *Galactic RadioActivity Survey Probe (GRASP)* mass model (Boggs *et al.*, 2008), proposed in response to NASA SMEX AO Call.

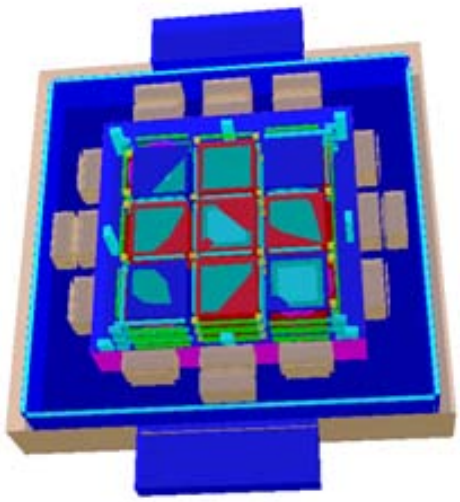

Figure 5.2: Cross-sectional view of the detector mass model of DUAL, as used for simulations.

5.3 Expected performance of DUAL

Estimating the performance of the γ-ray telescope is a quite complex process. Any simulation system used for this purpose must necessarily include many different components to address a multi-step process:

- describe astrophysical sources and the background environment in a given orbit.
- describe the detailed geometry and mass of the instrument and spacecraft.
- perform Monte Carlo simulations to estimate the response of the instrument to sources and backgrounds.
- analyze the resulting data taking into account a realistic operational capacity for the instruments.

The basic performance of the DUAL instrument has been calculated in the framework of the Medium Energy Gamma-ray Astronomy Library (see Appendix B.2). Moreover, the instrumental background was computed using the ACTtool (see Appendix B.3).

5.3.1 Spectral resolution

The main limiting factor of the spectral resolution of a γ-ray telescope is given by the energy resolution of its detectors (see section 2.2.1). However, other factors (such as the electronic noise for multiple detector interaction) should be added in order to estimate the spectral response of the instrument.
The expected photo-peak energy resolution of DUAL, in terms of the full-width-at-half-maximum, is shown in Figure 5.3. The assumed energy resolution for one 3-D Ge strip detector is also shown for comparation purposes. The photopeak at 1MeV, after event

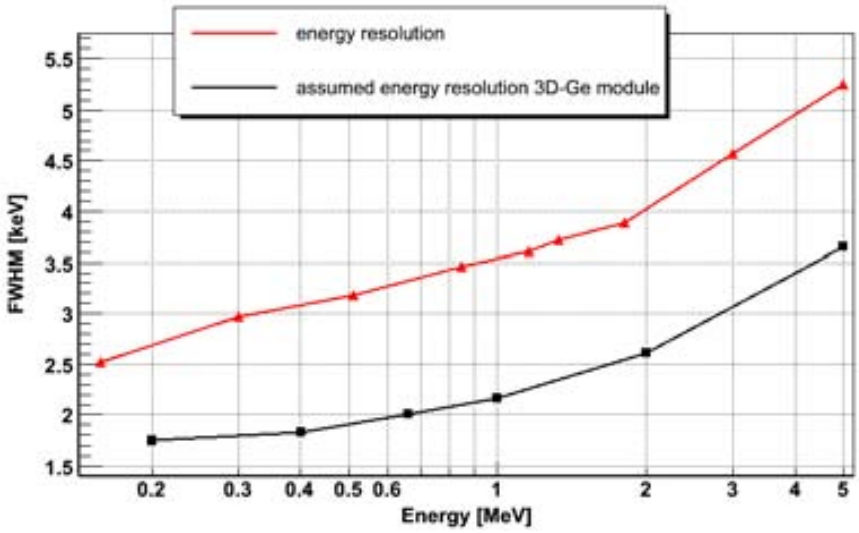

Figure 5.3: Spectral resolution of DUAL and assumed resolution for a 3-D Ge strip detector.

reconstruction, corresponds to a 3.5keV (FWHM) over the 2.1keV for a single detector. The focal plane detector of DUAL, as expected in a Germanium instrument, will achieve a very high spectral resolution ($< 1\%$ at 1MeV).

5.3.2 Angular resolution

The angular resolution of DUAL is presented here by adopting the ARM described in section 2.3.2.3. The uncertainty of the Compton scatter angle has differents contributions that cause a non-Gaussian profile of the ARM distribution. The distribution has a sharp central peak and broad wings which are dominated by the momentum distribution of bound electrons in the atoms (see figure 2.5). Figure 5.4 (a) shows the ARM distribution for an on-axis source at 847keV. The distribution due to the Doppler broadening effect is shown in figure 5.4 (b).

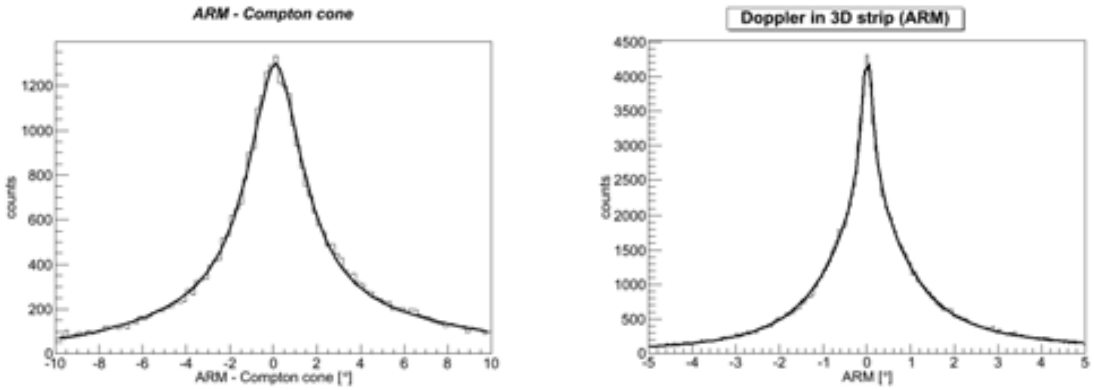

(a) (b)

Figure 5.4: ARM distribution for a narrow line on-axis source at 847keV.

The on-axis ARM distribution (FWHM) as a function of the energy is shown in figure

5.5, as well as the limits imposed by Doppler broadening. Only events within a $\pm 1\ 4\tau$ energy-resolution window around the simulated narrow-line energy have been selected. No other selection criteria have been applied.

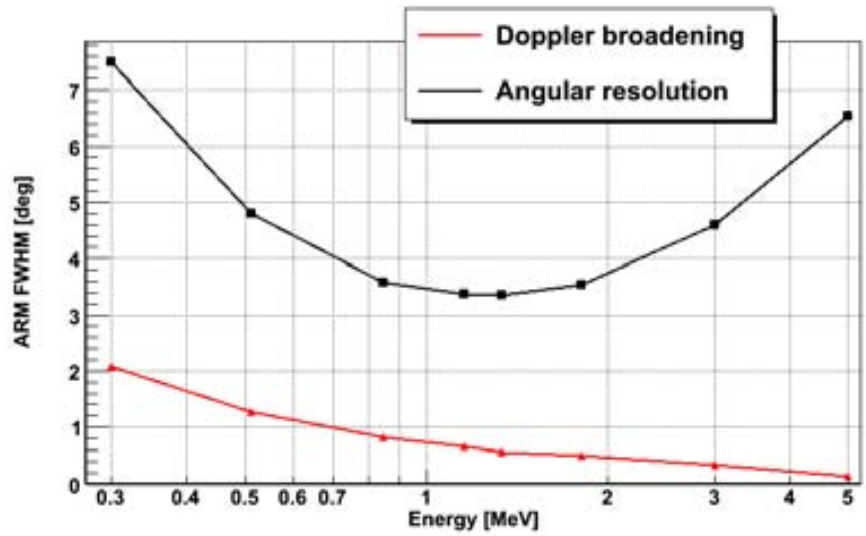

Figure 5.5: FWHM of the angular resolution measure (ARM) distribution of DUAL, for an on-axis source.

The influence of the broadening effect is higher at low energies, as expected, but the computed angular resolution is far above this limit (about a factor 4 at 1MeV), mainly due to the spatial uncertainty and the short distance between interactions. This ARM can be improved by event selection (imposing a long distance between hits) but this selection significantly reduces the efficiency.
In general, the larger the distance between Compton interactions the better the angular resolution. A stacked germanium detector with a larger distance between layers would have an angular resolution up to 1MeV only limited by Doppler broadening (Boggs & Jean, 2001).

5.3.3 Effective area

The *effective area* presented here is defined as the ratio of photons detected within the instruments angular and energy resolution multiplied by the collecting area of the instrument to the number of simulated photons. This effective area is the corresponding area of an ideal telescope which would measure the full energy of all photons passing through its geometric area. This figure-of-merit is a function of the energy and the incidence angle of photons.
The effective area of DUAL was computed based on Geant4 simulations according to the following equation:

$$A_{eff} = A_{start} \frac{N_{Photons\ within\ energy\ and\ ARM\ selection}}{N_{Simulated\ photons}} \tag{5.1}$$

Figure 5.6 shows the effective area as a function of energy for all events within a $\pm 1\ 4\tau$ energy-resolution window around the simulated narrow line energy and compatible with the position of the point source, according to the angular resolution of the instrument shown in figure (5.5) (i.e. which lie within the selected ARM window). Event selection is very important since the effective area has a strong dependence on this issue.

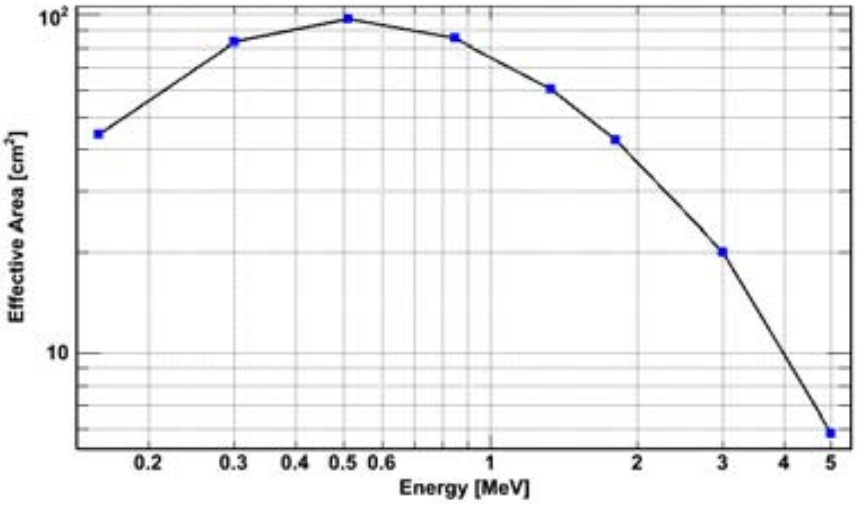

Figure 5.6: Photopeak effective area for on-axis sources.

The effective area of DUAL is maximum around 0.5MeV and has a significant efficiency down to 0.15MeV. The effective area at low energies decreases because the photoelectric effect becomes the dominating interaction process (see Figure 2.7). At high energies, the effective area decreases slowly with energy as a result of the incomplete photon absorption.

5.3.4 Field-of-View

DUAL is intended to perform an all-sky survey and monitoring together with deep observations with the Laue lens. For this reason the field-of-view is a key parameter of the mission to perform continuous sensitive γ-ray spectroscopy and polarimetry observations of the complete sky.
Figure 5.7 shows the field-of-view and polar representation of the effective area for the 511keV energy line. Events within a window of $\pm 1\ 4\tau$ energy-resolution and $\pm 2\ 5deg$ angular-resolution were selected.
As expected, the effective area has an off-axis peak since the Klein-Nishina cross section is not an isotropic function of the Compton scatter angle (see figure 2.4). Photons at 511keV have higher probability of being scattered at $\approx 35deg$.
The different effective area at cenit ($\theta = 0deg$) and nadir ($\theta = 360deg$) is due to the passive material included at the bottom of the mass model in order to support the structure.
The large field of view of DUAL improves the *exposure* (see equation (1.2)) due to the large observation time. Every source in the sky will be observed during the entire mission

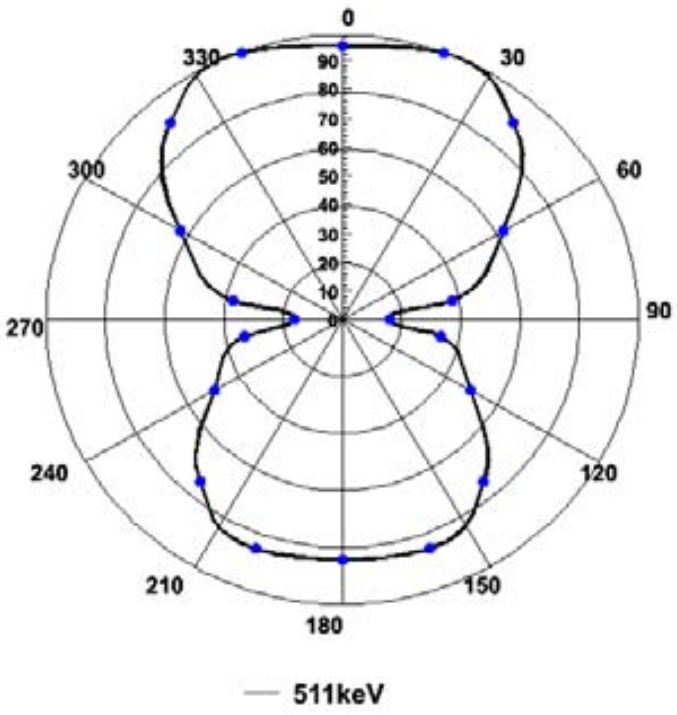

Figure 5.7: Field-of-view and polar representation of the effective area for 511keV energy photons.

lifetime, leading to a sensitivity improvement of at least an order of magnitude compared to SPI/INTEGRAL.

5.3.5 Modeling instrumental background

In order to predict the sensitivity of the instrument, it is necesary to estimate the background due to the space radiation environment. The study presented here, carried out with the ACTtool, follows the approach discussed in section 1.2.2.

5.3.5.1 Environment models

DUAL would be best operated at the second Lagrangian point (L2) to perform an all-sky survey and monitoring. This orbit has the advantage of avoiding near-Earth radiation background (see section 1.2.1). However, the shielding from charged cosmic-ray particles provided by the Earth s magnetosphere is missing in a L2 orbit. Therefore, DUAL would have to undergo the full intensity of protons, electrons, positrons, and ions in interplanetary space.
Figure 5.8 shows the spectra of these radiation fields, assumed to be isotropically incident on the instrument. The cosmic electron spectrum is based on the models of Schlickeiser & Thielheim (1977), while the other components are derived from the environmental model of the ACTtool/CREME96 (see section 1.2.2.1).

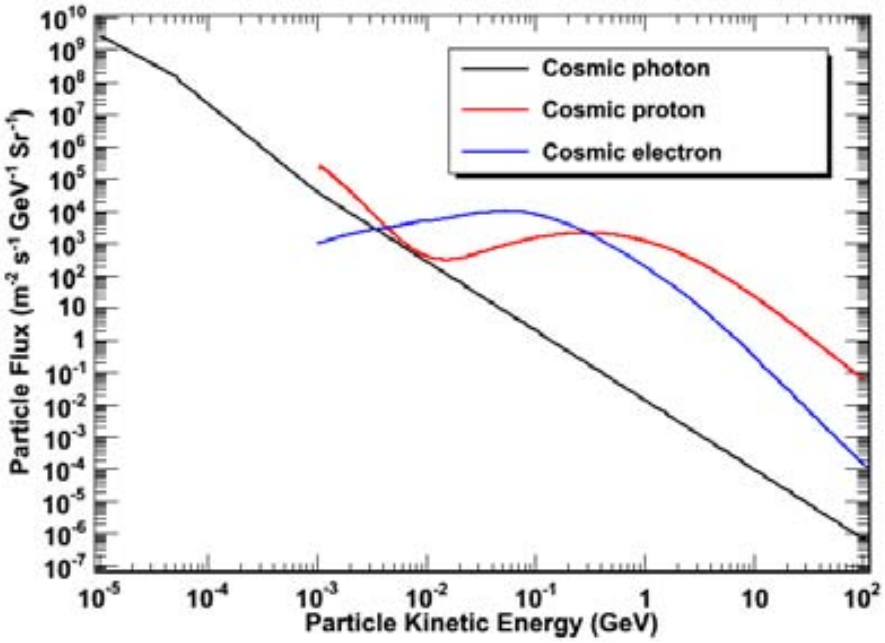

Figure 5.8: Integrated input spectra used for the background simulations of DUAL.

5.3.5.2 Active shielding

As pointed out in section 5.2.2, the DUAL mass model has thin plastic scintillators to suppress the background induced by charged cosmic-ray particles.

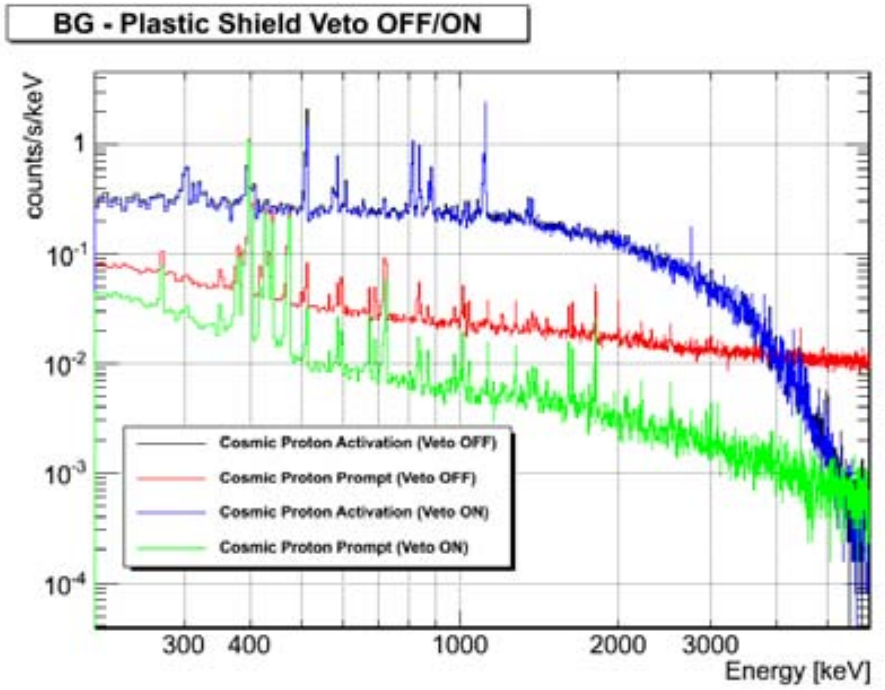

Figure 5.9: Effect of a veto shield on the background rate due to cosmic protons. The mass model used for this simulations is not the base line detector of DUAL.

In order to illustrate this background reduction, figure 5.9 shows the background rate induced by cosmic-ray protons in a given mass model, with and without veto signal from a plastic scintillator shield. The mass model used for this study is analogous to the one described in section 5.2.2 but with higher size (50cm x50cm). The *prompt component* is clearly reduced when the veto signal is taken into account, while the *delayed component* (due to the radioactive isotopes production) remains unchanged.
The passive material of the spacecraft is an important source of secondary particles that increase the background in the detector. The large distance between detector and spacecraft in the DUAL mission will minimize this internal background, avoiding heavy shields and allowing a 4ψ field-of-view.

5.3.5.3 Background estimation

Figure 5.10 shows the background spectrum induced in the instrument by the different components of the radiation environment in the energy range from 100keV up to 10MeV. All events with at least two interactions (not simultaneous) have been included in the spectrum as long as there had not been any veto signal from the plastic acticoincidence shield. We have assumed that the instrument was isotropically radiated during one year by the cosmic-ray proton spectrum shown in figure 5.8.
The major contribution to the instrumental background at low energies (below 300keV) are cosmic photons, while at high energies the activation from cosmic protons dominates all other components.

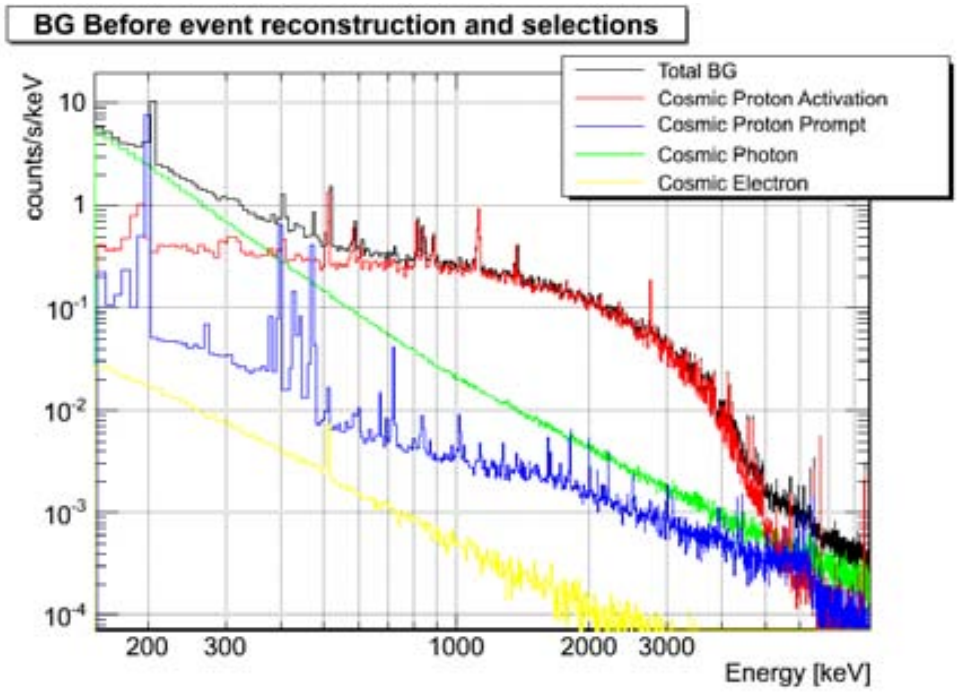

Figure 5.10: Background in the DUAL baseline detector induced by the different components of the radiation environment before event reconstruction and selection.

Figure 5.11 shows the predicted background after event reconstruction and selection. Only

those events that meet a specific selection criteria (i.e., statistic test, Compton scatter angle, number of interactions, angular resolution measure, total deposited energy) have been included. Using the MEGAlib tool, the sensitivity to an on-axis narrow line source at 847keV was optimized, finding the following set of parameters: angular deviation from source 0 to 1.1 degrees, Compton scatter angles 0-130 degrees, events with 3-7 interactions and minimum distance between interactions 1.6cm. This set of selection parametres has been applied in the energy range from 100keV up to 10MeV, in order to obtain the spectrum shown in figure 5.11. By comparing the spectra after and before event selection, it is clear that event selections reduces drastically the background (up to two orders of magnitude). Therefore, kinematic Compton sequence reconstruction is a key tecnique for background reduction and sensitivity improvement.

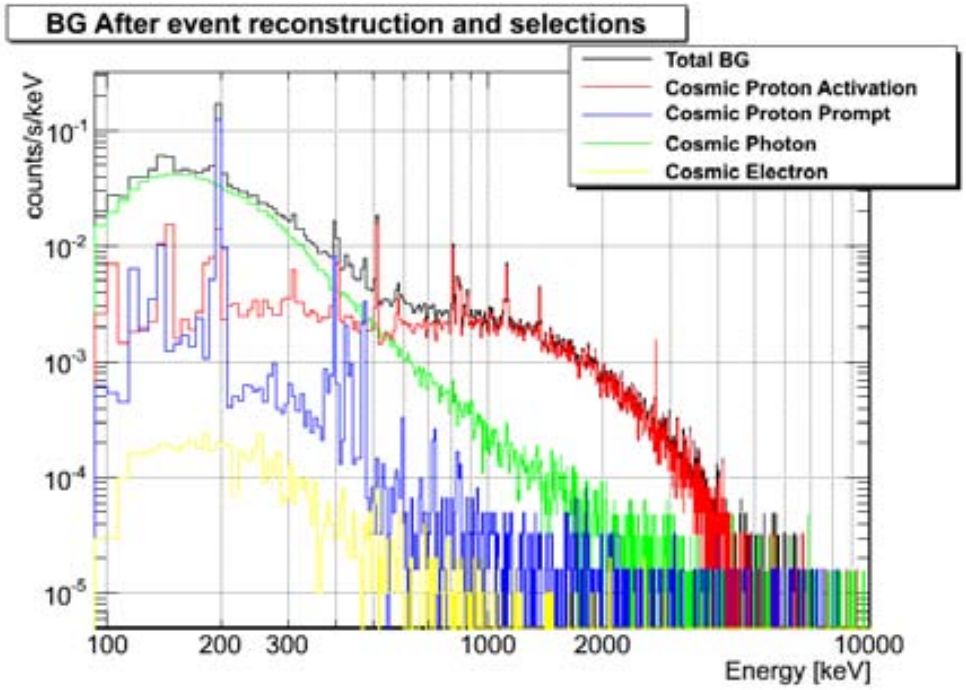

Figure 5.11: Background in the DUAL baseline detector induced by the different components of the radiation environment after event reconstruction and selection.

5.3.6 Sensitivity

Sensitivity is certainly the most important parameter for any γ-ray telescope. The sensitivity for point sources has been computed using equation (1.1) and from the estimated background shown above.

The sensitivity of DUAL, for an exposure time of 10^6s and 3τ limit, is listed in table 5.4 for two relevant astrophysical lines: positron annihilation line (511keV) and decay line at 847keV from ^{56}Co in supernovae. The Laue lens sensitivity has been computed for two cases (narrow and 3% FWHM broad line) considering a lens effective area of $340cm^2$ (von Ballmoos *et al.*, 2010b).

Laue lens (Effective Area $340cm^2$)	
Energy [keV]	Sensitivity [$ph\ cm^{-2}s^{-1}$] ($T = 10^6s$, 3τ)
847 (narrow)	10^{-6}
847 (3% FWHM broad)	$1\ 86\ 10^{-6}$
All-sky Compton Telescope	
Energy [keV]	Sensitivity [$ph\ cm^{-2}s^{-1}$] ($T = 10^6s$, 3τ)
511	$1\ 47\ 10^{-5}$
847 (narrow)	$7\ 27\ 10^{-6}$

Table 5.4: Narrow and broad line sensitivity at 847keV (and narrow line at 511keV) achieved by Laue lens and All-Sky Compton telescope.

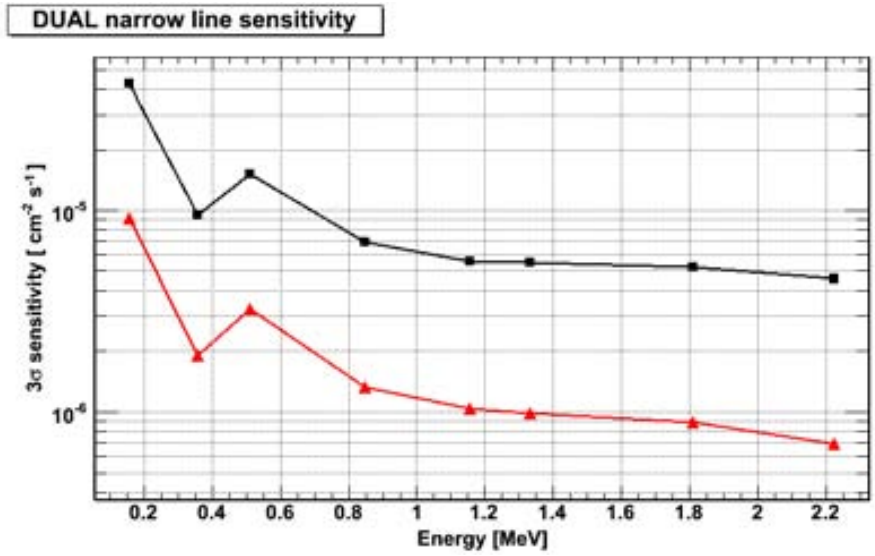

Figure 5.12: Narrow line sensitivity (3σ sensitivity limit) achieved by the All-Sky Compton instrument for any source on the sky for an observing time of 10^6s (black curve) and after two years of continuous sky survey (red curve).

The Compton detector of DUAL is intended for an all-sky monitoring. Thus, in order to determine the sensitivity for an all-sky survey, the angular dependence of the effective area should be taken into account (see Figure 5.6). The average exposure in the source element can be retrieved from an integration over the sphere and total observation time. Figure 5.12 shows the 3τ narrow-line sensitivities of an on-axis pointing source for an exposure time of 10^6s (black curve) and after two years of continuous sky survey (red curve).
Even with the relatively small effective area of the Compton detector (see figure 5.6) the long observation time of a given source, due to the large FoV, leads to an effective increase in sensitivity.
Figure 5.13 shows DUAL s average continuum sensitivity for point sources after two years of all-sky survey, considering a $\Delta E = E$ window.
After two years of continuous sky survey, the sensitivity achieved by the Compton detector for any source on the sky is an improvement by at least an order of magnitude with respect to existing and previous missions. The Laue lens reaches a sensitivity of

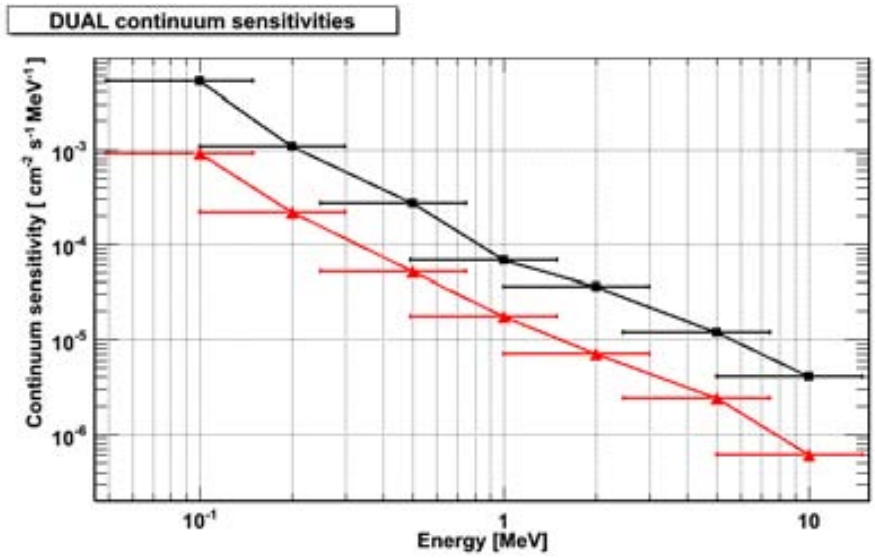

Figure 5.13: Continuum sensitivities achieved by the All-Sky Compton instrument for any source on the sky after two years of continuous sky survey.

1 86 10^{-6} $[ph\ cm^{-2}s^{-1}]$ for the 847keV broad line (3% FWHM) in a relatively short exposure time (10^6 s). An extensive comparison between the sensitivity of DUAL in the energy band from 100 keV to 10 MeV and previous instruments (e.g., COMPTEL, SPI) can be found in von Ballmoos *et al.* (2010b).

Chapter 6

Detector based on liquid Xenon TPC

During these last years, the application of liquid Xenon (LXe) detectors has been extended from high energy experiments to astrophysics, astroparticle physics and medical imaging (see, for example, review by Aprile & Doke (2010)). In particular, a Liquid Xenon Time Projection Chamber (LXeTPC) for γ-ray astronomy has been developed at Columbia University for a number of years (Aprile & Suzuki, 1989).

The low energy resolution obtained with LXe detectors has been a significant drawback for γ-ray line spectroscopy, and the major limitation for their application in astrophysics. This situation has been changing and the possibility of achieving energy resolutions below 1% FWHM at $1MeV$ is expected by using the strong anti-correlation of ionization and scintillation in LXe (see section 2.2.3). Nevertheless, intensive research on improving light and charge readout is required in order to develop this potential of liquid Xenon in a detector prototype. In this direction, the improvement of vacuum ultraviolet (VUV) photosensors technology is spectacular for the efficient and fast readout of LXe scintillation light.

In this chapter, we present the study of alternative photosensors for a compact detector based on LXeTPC. The operational characteristics of Large Area Avalanche Photodiodes (LAAPDs) and Silicon PhotoMultiplier (SiPM) directly immersed into LXe, have been investigated in a test chamber at the Columbia Astrophysics Laboratory (NY). Results of the measured quantum efficiency and gain are presented here. In addition, the operational principles of a liquid Xenon TPC as well as the photosensors technology are briefly discussed beforehand.

6.1 Liquid Xenon Time-Projection Chamber (LXeTPC)

An important feature of liquid Xenon, discussed in section 2.2.3, is the good ionization and scintillation yields it has in response to a γ-ray interaction. In a time projection chamber, both the charge carriers and scintillation light signals are detected. This enables measuring the energy and three spatial coordinates of each interaction and therefore

to operate the device as a Compton telescope, where Compton kinematics is used to reconstruct the direction of the incoming γ-ray. The operation principle of a LXeTPC, described in Aprile *et al.* (2001), is shown schematically in Figure 6.1.

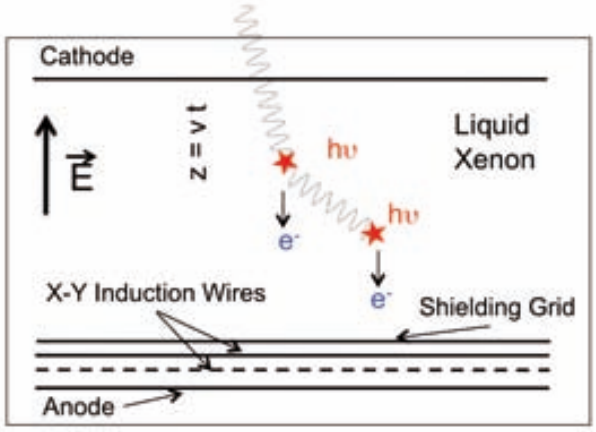

Figure 6.1: Principle of operation of a liquid xenon TPC.

An incoming γ-ray enters the LXeTPC and loses energy in a Compton scattering. The ionizing event creates free electrons (as well as ion pairs) and scintillation photons. Under an applied electric field the electrons drift to the anode. The contribution to the signals of the positive ions is neglected since their drift velocity is orders of magnitude slower. With a very small diffusion, the drifting electron cloud is well localized, and the signal induced in one coordinate wire mesh provides not only the pulse height, but the strip number position. An orthogonal wire mesh, in front of the first one, is used to determine the second coordinate. The third coordinate is measured with the drift time at a constant drift velocity of $2.2 mm/msec$ (see Table 2.3). The prompt Xe-scintillation light detected by photo sensors in the vacuum ultraviolet (VUV) region, triggers the drift time measurement. The drift time is also used to improve the spectral performance, by removing the dependence of the signal amplitude on the distance from the anode.
The amount of scintillation light is also an additional measurement of the event energy, while the light intensity distribution can be used for the 3D interaction location.

In the Liquid Xenon Gamma-Ray Imaging Telescope (LXeGRIT) (Aprile *et al.*, 2001), both ionization and scintillation were detected as described above. The fast scintillation signal was only used as the event trigger, while the ionization signal provided the energy measurement. An energy resolution of 4.2% (σ) at 1 MeV was obtained with this prototype (Aprile *et al.*, 2004). This poor energy resolution can be improved by combining the ionization and scintillation signals (see section 2.2.3).

The detection of VUV scintillation light was hard to perform efficiently in liquid Xenon at the time of the development of the LXeGRIT prototype. However, the technology of vacuum ultraviolet photo sensors for efficient and fast readout has improved dramatically over the last few years, and new developments are in progress. For instance, Hamamatsu

Photonics Co.[1] has developed compact photomultiplier tubes (PMTs), in compact stainless steel enclosures that can be mounted directly into the liquid, avoiding significant light losses through quartz windows. A measure of 1.7% (σ) at 662keV (with a drift field of 1kV/cm) was reported by Aprile *et al.* (2007) with these PMTs, by combining the ionization and scintillation signals. These improved PMTs, along with other VUV sensor technologies such as Large Area Avalanche Photodiodes (LAAPDs) and Si photomultipliers (SiPMs) promise further energy resolution improvement. An energy resolution below 1% FWHM at 1 MeV is expected by more efficient measurement of both ionization and scintillation signals.

6.1.1 Photosensor technologies

The use of scintillation detectors for radiation detection would be impossible without devices to convert the scintillation light into a measurable electrical current. Sensors such as photomultiplier tubes (PMTs) or photodiodes are used for this purpose. Despite PMTs being the most widely used devices, the requirements of certain instruments may be satisfied by photodiodes, either conventional (PIN) or avalanche photodiodes. A brief description of these photosensors is given in the following paragraphs.

6.1.1.1 Photomultipliers

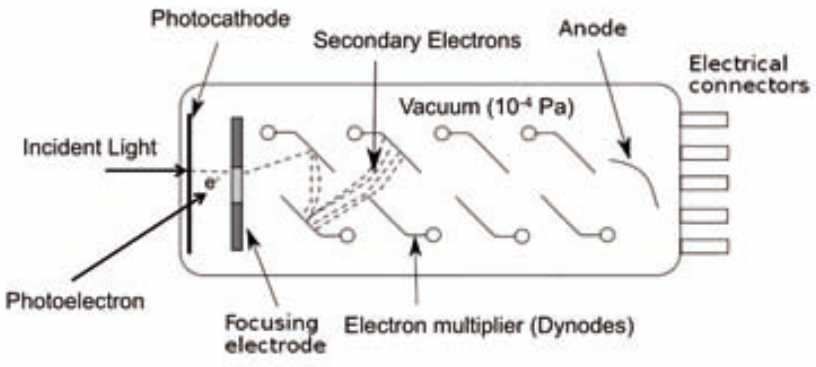

Figure 6.2: Basic elements of a photomultiplier tube (PMT) (adapted from Hamamatsu Photonics Co.).

Photomultiplier tubes (PMTs) are vacuum operated light detectors extremely sensitive to the ultraviolet, visible, and near-infrared ranges. As illustrated in figure 6.2, photons enter the tube through a window and are absorbed by the photocathode, producing an electron (photoelectron). This electron is accelerated towards a dynode, i.e. an electrode with a positive electric potential relatively to the photocathode. The electron energy is high enough to produce an average of more than one secondary electron by collision with the dynode. This process is repeated through a number of dynodes, typically 12 or 14,

[1] http://www.hamamatsu.com/

producing a gain factor in the final electrode (the anode), that can be as high as 10^7. (It must be pointed out here that photomultipliers for liquid xenon application usually have 10 dynodes and therefore the gain is a little lower, about 10^6). Due to this high gain, PMTs are the preferred detector for applications with very low light levels, providing single photon detections. An extensive study of PMTs can be found in Knoll (1999).

6.1.1.2 PIN photodiodes

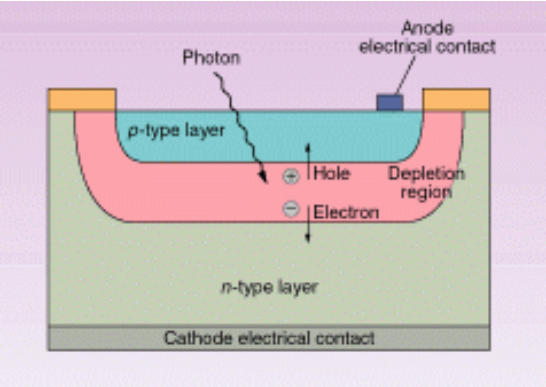

Figure 6.3: Working principle of the PIN diode (Koren & Szawlowski, 1998).

The PIN (positive-intrinsic-negative) photodiode, is a device made of silicon with a large depletion region which consists of a neutrally doped intrinsic zone between two semiconductor regions, with p and n-type doping, composed of an acceptor and a donor of electrons, respectively (see figure 6.3). In the PIN diode, the photon absorption in the depletion region creates a number of electron-hole pairs that depends on the diode quantum efficiency and on the incident radiation energy. A low intensity electric field in the photodiode leads to the migration of the produced charge carriers (electrons and holes) in opposite directions, towards two external electrodes. The PIN photodiode is a monolithic and compact device, much smaller than the PMT. Although lacking internal gain, the PIN diode constitutes a low cost detector for applications with high light levels. The electronic noise level in the photodiode is typically three orders of magnitude higher than in the PMT (Koren & Szawlowski, 1998) limiting the detector capability at low light levels.

6.1.1.3 Avalanche photodiodes

An avalanche photodiode (APD) tries to combine the benefits of both previous photosensors. It consists of a silicon photodiode that internally amplifies the current through an avalanche process, although the internal gain is considerable lower than the one obtained with the PMT, reaching less than 10^3. The gain is obtained applying a high reverse bias voltage to the photodiode, which establishes an intense electric field inside the APD, accelerating the electrons. The collision of these electrons with silicon atoms produces secondary electrons, and the produced electronic avalanche constitutes the APD gain.

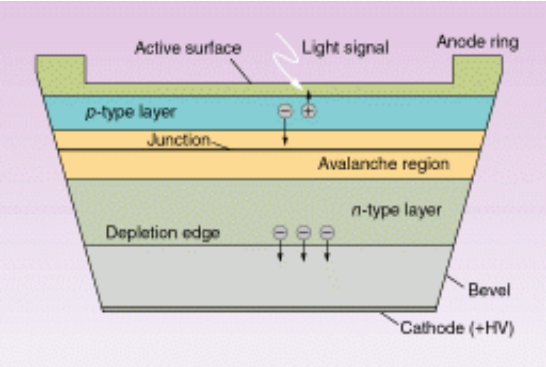

Figure 6.4: Working principle of an avalanche photodiode (Koren & Szawlowski, 1998).

Figure (6.4) shows the structure and working principle of an avalanche photodiode. A detailed discussion about their operational parameters can be found in Fernandes (2005).

6.2 Detector concept

6.2.1 LXeTPC configuration

Figure 6.5 (a) shows a detector concept based on the liquid Xenon Time Projection Chambers (LXeTPC) proposed by Rice and Columbia University for the Advanced Compton Telescope (Boggs, 2006). This detector consists of two LXeTPC (shown in blue) separated by a distance of $10cm$. The upper TPC contains $3cm$ of LXe while the lower TPC has $7cm$. Each TPC is viewed by an array of photo sensors (see figure 6.7). This detector can be considered for the focal plane of a Laue lens telescope.
Fast timing photosensors would allow to measure the fast xenon scintillation light and open up the possibility for time-of-flight (ToF) measurements between the detector modules in such a compact geometry (see section 2.3.2.1). Thus, for instance, Giboni *et al.* (2005) reported excellent timing capabilities of PMTs optimized for xenon scintillation light.

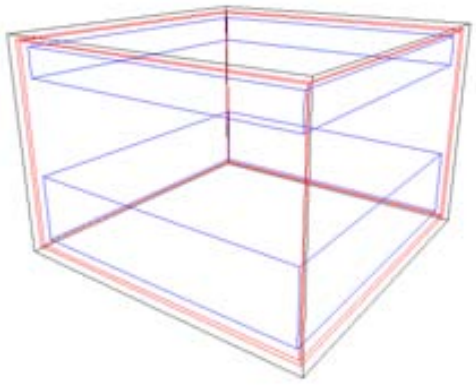

Figure 6.5: Liquid Xe TPC with time-of-flight (ToF) between detector modules.

A detector composed of two LXeTPC $30x30cm^2$ size chambers will be comparable (dimensionally speaking) to the focal plane detector proposed for the DUAL mission (see section 5.1). This detector has a low number of electronic channels and moderate cooling requirements, implying a low power. In addition, and opposite to the Ge-detectors proposed as baseline detector for DUAL, a design based on liquid Xenon could decrease significantly the amount of passive mass. However, the energy resolution of such a liquid Xenon detector should be improved in order to approach the results obtained with semiconductor detectors. Thus, for instance, the energy resolution obtained at 847keV (see Figure 6.6 (a)) is 24.96 keV (one τ). This result is based on a Monte Carlo simulation performed with Geant4/MEGAlib (see Appendix B.3) and using the mass model shown in figure 6.5.
Table 6.1 lists the energy and position resolution assumed for the simulation, where a conservative energy resolution of 5% at 1MeV has been considered.

	ΔE at 1MeV (1σ) [keV]	$\Delta x = \Delta y$,Δz [mm]	Threshold [keV]
$LXeTPC_{top}$	21.38	0.44,0.1	30
$LXeTPC_{bottom}$	21.38	0.44,0.1	30

Table 6.1: Detector performances assumed for the simulation.

Adopting the angular resolution described in section 2.3.2.3, figure 6.6(b) shows the ARM distribution for a 847keV on-axis source when a minimum distance between the first interactions are applied in order to consider only the Compton event that has a first scatter on the top TPC followed by an interaction on the bottom TPC. Despite this event selection, an angular resolution no better than 5deg (FWHM) is obtained. We should point out that the MEGAlib package is not optimized for the Compton reconstruction in this type of detector and further improvements are needed.

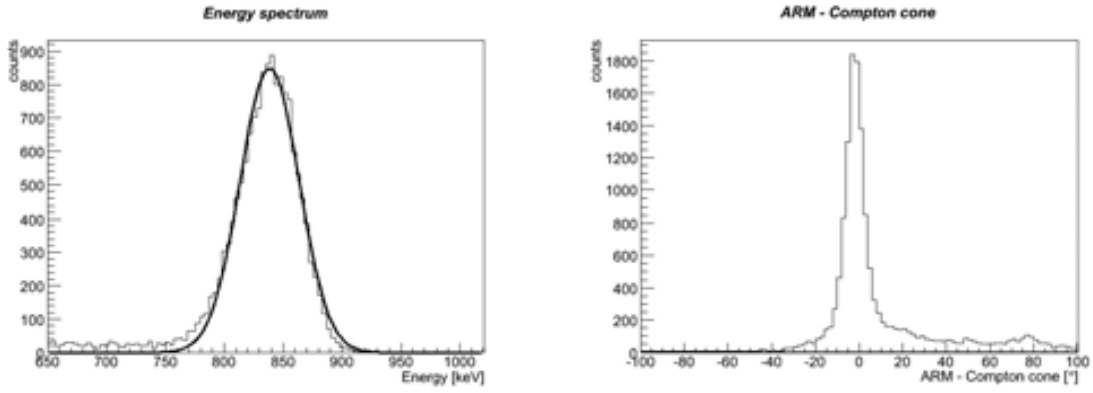

(a) (b)

Figure 6.6: Energy spectrum (a) and ARM distribution (b) for a 847keV on-axis source.

An improvement in the spectral response of LXe detector would significantly increase the potential of this detector concept.

6.2.2 Scintillation light readout

Figure 6.7 shows an array of photosensors on one side of a liquid Xenon TPC, collecting Xenon scintillation light produced by a interacting particle.

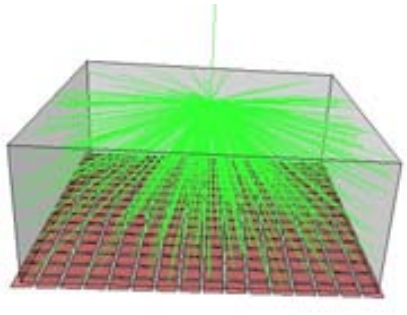

Figure 6.7: Array of photosensors on one side of a liquid Xenon TPC collecting Xenon scintillation light.

Using photosensors on both sides of the TPC, the light collection will be enhanced and the energy resolution can be improved. However, this implies the introduction of passive material in a Compton telescope configuration such as the one shown in Figure 6.5. This passive material can be minimized by using solid state photosensors, such as Avalanche Photodiodes (APDs) and Si photomultipliers (SiPMs), which are compact devices with little amount of passive material. The study of such solid-state photosensors are presented in the following section.

6.3 Test of semiconductor photodiodes immersed in LXe

The results of the experiments carried out at the Nevis Laboratory (NY), within the framework of a collaboration with the astrophysics group at the Columbia University, are presented here. We tested the operational characteristics of two types of semiconductor photodiodes directly immersed into LXe: a large area avalanche photodiode (LAAPD) from Advanced Photonix, Inc.(API) [2] and a silicon photomultiplier (SiPM) from MEPhI-PULSAR [3]. These photodetectors are designed to operate within liquid (i.e., they have to be compatible with high-purity LXe environment) and to efficiently detect the scintillation light from LXe.

Figure 6.8 shows a picture of the experimental area where the tests were carried out. The xenon gas filling and purification system is described in Aprile *et al.* (2002). For these tests we used a high temperature SAES getter [4] without continuous recirculation.

[2] http://www.advancedphotonix.com/
[3] http://www.mephi.ru/
[4] http://www.saesgetters.com/

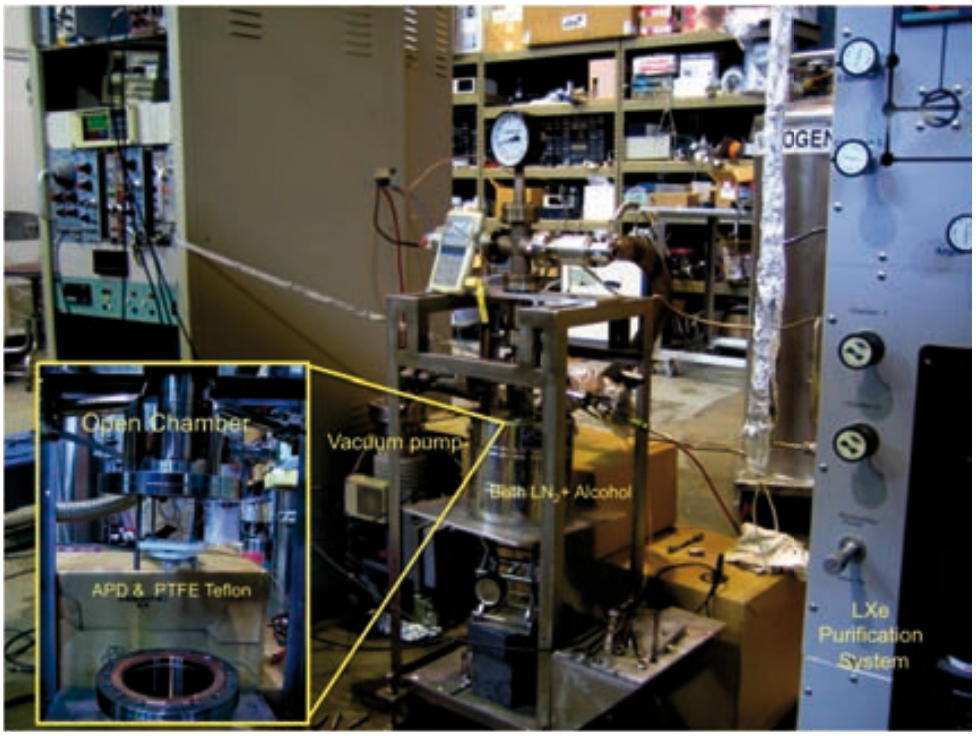

Figure 6.8: Picture of the experimental area at the **Nevis Laboratory**, Columbia University where tests were carried out. The stainless-steel chamber where the photodetector is enclosed and filled with purified LXe is shown in the image, as well as the gas purification system and the cooling bath (a mixture of liquid nitrogen and alcohol).

6.3.1 Silicon photomultiplier (SiPM)

Silicon photomultipliers (**SiPM**), also called Multi Pixel Photon Counters (**MPPC**), have been progressing from laboratory curiosities into detectors with some distinct advantages over other photon detectors. A single detector is made of 100-1500 tiny Avalanche Photo Diodes (APDs), arranged in a two-dimensional array. The whole array for the first devices was about $1 \times 1mm^2$ in size, but larger devices, of $3 \times 3mm^2$ are already available on the market. Each single cell (or APD) has its own current limiting resistor, and all cells in the array are interconnected. The APDs are reverse biased, and the voltage is high enough to operate in Geiger mode (i.e., an electron-hole pair created by a photon causes a breakdown in the cell limited by the resistor). The signal from each cell is independent from the number of initial pairs created by the photon. This leads to a rather unusual signal formation, where the signal amplitude is determined by the number of responding cells. This measurement is only linear if the probability of a single cell being hit by more than one photon is small. The response of a SiPM is thus ideal for photon counting.
The operation in Geiger mode produces a much higher signal in comparison to regular APDs. The gain in a SiPM is typically around 10^6. The signal can be observed directly on an oscilloscope, although a Charge Sensitive Amplifier (CSA) is normally used to filter noise and shape the signal. For timing purposes, however, a voltage amplifier is preferable to take advantage of the very fast signal rise time of the order of 100 psec. The SiPM is thus expected to be faster than regular photomultipliers.

Like APDs, SiPMs are not specifically processed for the detection of VUV light. Also, since standard windows are not made of UV-transmitting quartz, we used naked devices for the test, (i.e. without any cover or window). The main manufacturing parameters, for the MEPhI-PULSAR produced SiPMs tested in this study, are given in Table 6.2.

Size	1.1 x 1.1 mm^2
Number of Pixels	1156
Single Cell Size	32μm x 32 μm
Active Area of Cell	24 μm x 24 μm
Geometrical efficiency	56 %

Table 6.2: Main Parameters of the SiPM from MEPhI-PULSAR.

6.3.1.1 Experimental Setup

As shown in figure 6.9, two SiPMs were mounted side by side on a custom support made of Polytetrafluoroethylene (PTFE or Teflon), which reflects some of the stray light back on to the Si-PM and thus increases the light collection efficiency as reported by Yamashita *et al.* (2004). A ^{210}Po alpha emitting source with activity 0.1 σCi, was mounted opposite to the two SiPMs at a distance of 10 mm. The source position was movable by means of a motion feedthrough, so it could swing in or out to take also background data without direct light coming from the alpha source (see Fig.6.10). For test purposes, a blue (440 nm) emitting LED was also mounted in the chamber. Finally, a platinum resistor (RTD) measured the temperature of the Teflon plate (shown in Fig 6.9). This set was introduced inside a stainless steel vessel chamber of about 0.65 liters. Hermetic feedthroughs are used to bias the SiPMs and to power the LED. The setup is shown schematically in figure 6.11

Figure 6.9: Photo of two SiPMs mounted side by side on a PTFE Teflon plate. The platinum resistor (RTD) to measure the temperature of the Teflon plate is also shown on top.

The stainless steel vessel chamber was hermetically closed and suspended in a dewar with an alcohol and liquid nitrogen mixture as a thermal bath. For such a small chamber, this cooling is enough for liquefying xenon gas keeping it in liquid state for many hours, just by adding liquid nitrogen at regular intervals. About 800g of xenon were liquefied in the vessel, so source and SiPMs were completely covered. Before filling it with xenon, the

Figure 6.10: Photography of SiPMs detectors with the source device placed in front of the detector(right) and outside the detector(left).

chamber was emplied of air and kept under vacuum for at least 24 hours to outgas the materials. The vacuum levels obtained were typically of the order 10^{-6} torr.

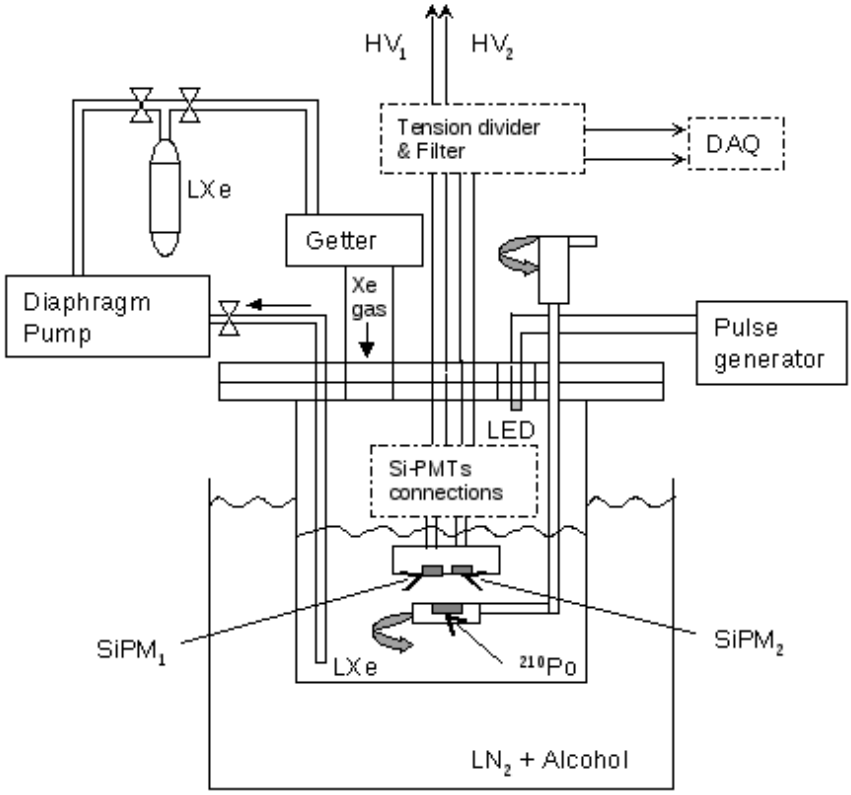

Figure 6.11: Schematic drawing of the chamber.

Alpha particles have a very short range in liquid xenon, of only a few σm, i.e. for all practical purposes the light source for the tests was point-like. The source was illuminating the two detectors simultaneously so that coincidences between the detector could be used

to trigger alpha events. The distance the light has to cross within the liquid (10mm) is too small to observe any attenuation in the VUV signal.

6.3.1.2 Electrical Connections and Read Out

A typical scheme proposed by the manufacturer to connect a SiPM is shown in figure 6.12(a). Due to the high gain of $10^5 - 10^6$ of the diode cells operated in Geiger mode the signal is in the tens of mV range, sufficient to be directly observed on an oscilloscope. For our tests, we modified the scheme to also read the signal on the anode contact (see modified scheme in figure 6.12(b)).

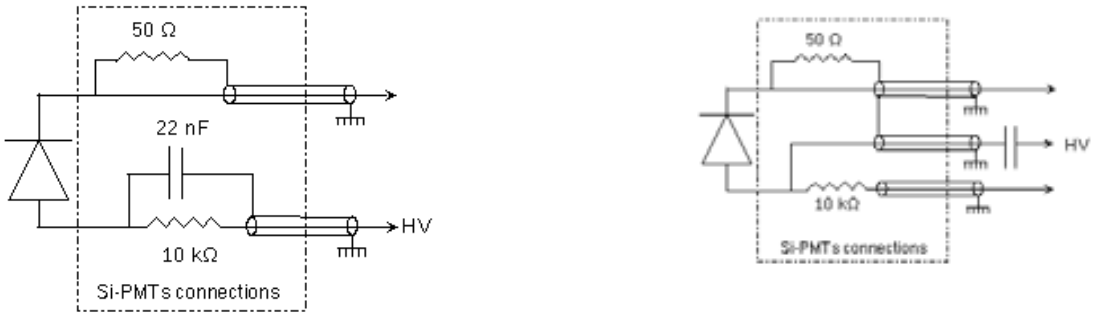

(a) Typical connections of SiPMs.

(b) Modified connection scheme.

Figure 6.12: SiPMs connections.

Although the signal formation is often described as collecting the charges from the multiplication process in the silicon, the observed signal in fact is the induced pulse from the moving charges. The signals on cathode and anode are therefore identical, but of inverted polarity. Figure 6.13 shows typical pulses for a single event on cathode and anode. The third trace shows the subtraction of both signals. We note that, in a high electrical noise environment, a differential read out would be possible as shown by the third trace in fig. 6.13.
For better noise immunity at high frequencies, the signals from the anode were routed through a Charge Sensitive Amplifier (Clear Pulse Model 5016 Dual CSA)[5]. The shaping time of the CSA was set to 100 nsec. The pulses were shaped and amplified in a spectroscopy amplifier (Ortec Amplifier Model 450)[6] for analysis with a Multi Channel Analyzer (MCA). Fig. 6.14 shows a typical anode pulse after the CSA.
The bias voltage for the SiPMs is within a 10V range, around 65V. At liquid xenon temperatures, the bias voltage is at the lower end of this range, whereas at room temperature higher voltages are required. Since the amplification in the SiPMs is based on operation in Geiger mode, no signal can be observed below 55V. Although not ideal for this application, a standard 4 channel PMT HV supply was used (model RPH-032, REPIC Co.). The

[5] www.clearpulse.co.jp
[6] www.ortec-online.com

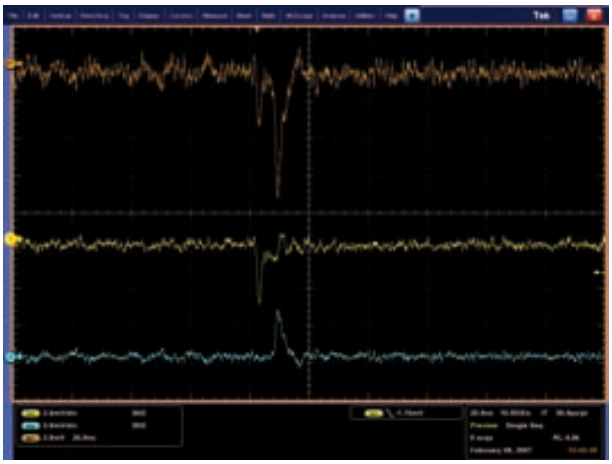

Figure 6.13: Alpha source signals detected by SiPM. Signal from cathode and anode pulse, as well as the substraction of both signals, are shown from top to bottom as seen on the screen of the oscilloscope.

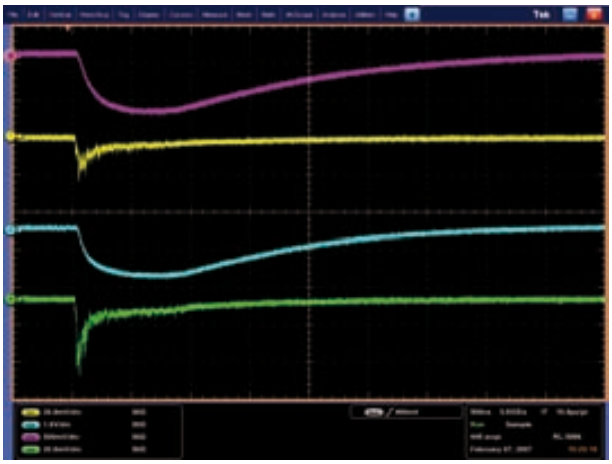

Figure 6.14: The two upper curves correspond to the signal detected from the anode of one SiPM, before and after Charge Sensitive Amplifier. The smoother curve correspond to the signal after the CSA. The two lower curves are from the second SiPM.

output voltage was reduced by resistive dividers. Added capacitors provided the necessary filtering of electrical noise. Figure 6.15 shows all the connections, signal and HV, used for the tests.

6.3.1.3 Measurements and results

Figure 6.16 shows a spectrum of one of the two SiPMs acquired with LED light pulses. It is typical for spectra of SiPMs to show distinct peaks corresponding to the number of hit cells. Since a single electron-hole pair can start the avalanche in a cell, the peaks correspond to the photoelectron peaks in a regular PMT (Hyman *et al.*, 1964). For small numbers of cells, the signal depends linearly on the number of original photons, while for large numbers, non-linearities show either neighboring cells firing, or a cell hit by several photons. In analogy to a PMT, the pulse height corresponding to a single cell is called P_e. The calibration of a SiPM is similar to a standard photomultiplier, but due to the single

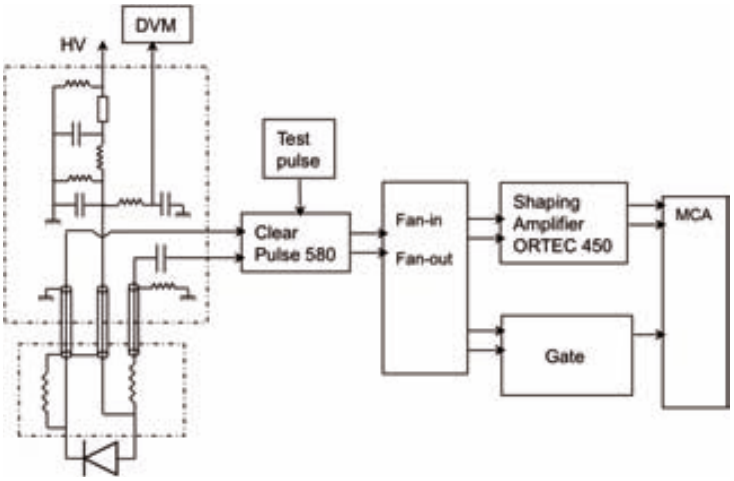

Figure 6.15: HV and signal connections.

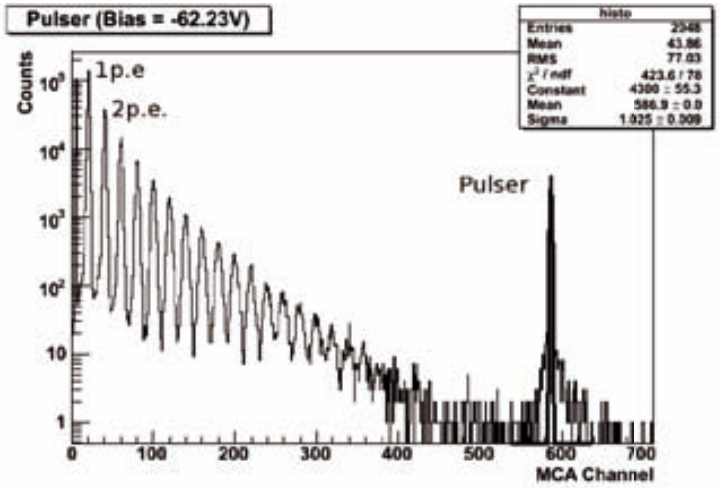

Figure 6.16: Amplitude distribution of a SiPM for a MCA calibration pulse.

photoelectron sensitivity, a SiPM is selfcalibrating. The single photoelectron peak (P_e), as well as the pedestal, is clearly defined in figure 6.16. Instead of the single P_e location, the average distance between successive peaks can be used. Since we can distinguish the peaks clearly up to about 20 P_e, we can accurately determine the single P_e equivalent, even without fitting a curve.
The *gain* of the SiPM was obtained by comparing the single P_e with a test pulse of known height. The test pulse injects a charge via a known capacitor to the input of the CSA, and thus we can easily determine the ADC conversion rate (electric charge per channel). The gain is expressed by the following equation:

$$Gain \ = \frac{(P_e[ch]) \ x \ (ADC \ conversion \ rate[C/ch])}{1 \ e^- \ charge[C]} \tag{6.1}$$

The gain of the SiPM is a function of the bias voltage, due to dependence on P_e on the bias (Figure 6.17 shows this dependence). Above 65V (see figure 6.17), the signal became very noisy. We attribute this to an unstable condition within the single cells causing them

to show a breakdown even without a photon hitting the cell. Below 60V the signal was too small to be measured. The gain of this SiPM was below 10^6.

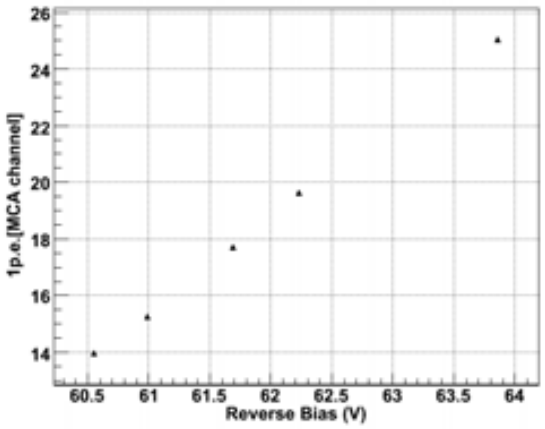

Figure 6.17: One photon equivalent versus reverse bias.

Another important parameter is the *quantum efficiency* Q_e, or the efficiency with which a photon hitting the active part of a cell causes an avalanche. To define a clear signal, we use the coincidence of the two SiPMs to gate the MCA. Figure 6.18 shows the spectrum of the ^{210}Po source. To ascertain that the discriminator setting does not cut into this distribution, figure 6.19 shows the spectrum under identical conditions but with the source removed. The noise contributions are still notorious down to a single P_e, but above $2P_e$ very few background remains.

Since the SiPM signal is calibrated in units of photoelectrons, the peak pulse height in figure 6.18 corresponds to the average number of 22 P_e. ^{210}Po emits 5.305 MeV alphas, which corresponds to 2 $7 \cdot 10^5$ photons using the energy value of 19.6 eV for alpha particles to produce a scintillation photon in liquid xenon (Doke *et al.*, 2002). The solid angle of a single SiPM for the point like light source in our setup is about 0 08%, i.e. for each alpha an average number of 216 photons are impinging on the SiPM. The photon detection efficiency of this particular type of SiPM is therefore 10%, nearly doubled from the value measured for earlier models in Aprile *et al.* (2006b). The improvement is due to a larger active area for each cell (0.56 instead of 0.254 of the total area) compared to the old model.
The quantum efficiency of the SiPM can be calculated from the efficiency as: $\epsilon = Q_e \times A$, where A is the active area ratio of the device. Assuming A=0.56, we infer a $Q_e = 18 \pm 4\%$. The error largely reflects uncertainties in the source location, since the moving mechanism for the source did not allow accurate positioning.
In order to confirm that the observed peak is due to alpha particles, the geometry was changed by moving the source closer to the two detectors. As expected, the number of detected photons increased with the solid angle. For the new geometry, the calculated Q_e value was 23%, and 19% for the other SiPM.

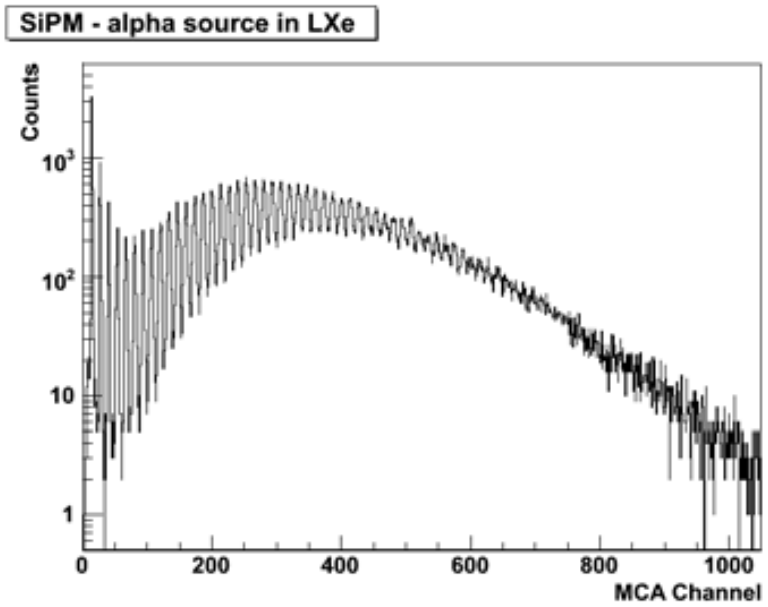

Figure 6.18: Amplitude distribution for ^{210}Po α particle scintillations with a gate on the MCA requiring the coincidence of the two SiPMs

The low temperature of the liquid xenon environment, of course, reduces the noise counts of the SiPMs. The background spectrum of figure 6.19 was acquired over a 300 sec life time and contains 7507 events above $0.5P_e$ corresponding to 25 cps. A significant portion of the noise is contained in the $1P_e$ peak. The noise count rate for SiPMs is therefore often quoted as $> 1\ 5P_e$. For this threshold we obtain 12.4 cps.

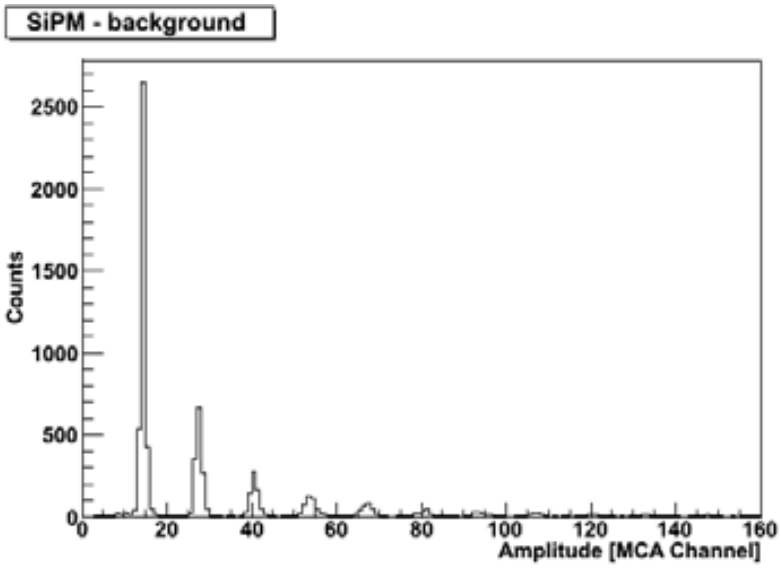

Figure 6.19: Amplitude distribution for background measured over 300sec life time with SiPM inmersed in LXe.

6.3.1.4 Data Read Out for 2-D Arrays

With the connection scheme shown in the right panel of figure 6.12, we observe two identical pulses on the cathode and the anode, but with opposite polarity (see figure 6.13). With a small number of SiPMs, this can be used to provide two electronics channels, one with a voltage amplifier for timing or triggering purposes, and one with a CSA to measure the amplitude. The benefit of this scheme appears when a two dimensional array of detectors has to be read out, as described in Giboni *et al.* (1998).

6.3.1.5 Conclusion

We have tested the feasibility of a silicon photomultiplier (SiPM) to detect LXe scintillation light. The SiPM was operated inside the liquid, at -95C, to detect the fast xenon scintillation light produced by an internal ^{210}Po source. The gain was estimated to be below 10^6 and we measured its variation with the applied bias voltage. The quantum efficiency was estimated to be 18% (10% is the photon detection efficiency) at $178nm$.
It must be pointed out here that this quantum efficiency should be considered as a lower limit for silicon photomultiplier, since the quantum efficiency for each APD (that constitute a SiPM) is expected to be much higher, as will be discussed in the next section. A higher quantum efficiency would be obtained if the device were optimized in the manufacturing process for a wave length of $178nm$.
The low noise, high single photon detection efficiency and low bias voltage of SiPM make these purely solid state devices a quite suitable solution for liquid xenon scintillation detection. Moreover, the easily realization of X-Y read out, allows large arrays of SiPMs for LXe detectors in many applications.

6.3.2 Large Area Avalanche Photodiodes(LAAPD)

In recent years, large area avalanche photodiodes (LAAPD) have been successfully applied as photodetectors for a variety of scintillators, including liquid xenon (Solovov *et al.*, 2002). Here we describe the results on the detection of LXe scintillation light produced by alpha particles, with a 16mm diameter LAAPD from Advanced Photonix Inc.(API) immersed in liquid xenon. This kind of LAAPD is UV sensitive and has been successfully operated in high-pressure scintillation detectors previously (Lopes *et al.*, 2001). The interest in LAAPDs for LXe is because of their high quantum efficiency (QE) at 178nm, as originally reported by Solovov *et al.* (2002). A lower value was reported by Ni *et al.* (2005) after the tests performed with the same LAAPD from API, also at the Nevis Laboratory (NY). Unlike our experiment, those measurements were made in a xenon ionization and scintillation chamber in order to confirm that using a LAAPD in LXe does not introduce impurities which may inhibit the drifting of free electrons. The test presented here was aimed at confirming the high QE for LXe scintillation reported in the literature, and at verifying the compatibility of LAAPDs immersed in the liquid.

6.3.2.1 Experimental Setup

The setup in this experiment is similar to that used in the previous test with the SiPM. A 16mm diameter windowless LAAPD (model API SD 630-70-75-500, see Fig.6.20) was mounted inside a chamber filled with high purity LXe.
The LAAPD, originally glued on a thin ceramic substrate, was mounted on a PTFE (or teflon) disk as shown in Fig. 6.21. To polarise the APD, the anode and cathode were pressed against the teflon holder with two layers of copper foil and then welded to two wires. As in the previous test, we used an open bath cooling apparatus with a liquid nitrogen and alcohol mixture to condense the xenon gas. The vessel enclosing the assembled detector was filled with high purity LXe, completely covering the LAAPD.
An alpha emitting source (^{210}Po with activity 0.1 σCi) was placed at a distance of 6mm facing the APD. The source could be moved with a motion feedthrough, thus it could swing in or out to also take background data without light from the alpha source (see fig. 6.21). For test purposes, a blue (440 nm) emitting LED was also mounted in the chamber. Hermetic feedthroughs are used to bias the LAAPD and to connect its output to a charge sensitive amplifier, as well as to power the LED.

Figure 6.20: Picture of the 16mm diameter windowless LAAPD (SD 630-70-75-500) from Advanced Photonix, Inc.

The scintillation light, which is created from alpha particles in the LXe, hits the LAAPD and produces photoelectrons which are amplified by the avalanche process. The avalanche electrons are collected by a pre-amplifier (model AmpTek A250) and the signal is fed into a low-noise shaping amplifier (model ORTEC 450). The shaping time of the amplifier was set at $0\ 25\sigma sec$. The amplified signals are further fed into a PC-based multi-channel analyser (MCA) for spectroscopy analysis.
Known test pulses are used to calibrate the DAQ system. The capacitance in the preamplifier was calibrated with a silicon detector, as described next.

Calibration of the input capacitance of the preamplifier The capacitance in the preamplifier was calibrated using a silicon detector. Taking $W_{Si} = 3\ 65eV$ as the energy required per electron-hole pair production in silicon, and $E_\beta = 976keV$ the energy of the β-particle from the ^{207}Bi source placed in the silicon detector, we can easily infer the charge produced in the silicon. Because energy needed for one pair production in silicon is rather small, one can get a very good signal for calibration purposes.

Figure 6.21: Picture of the LAAPD mounted on a PTFE disk with the alfa source device placed in front of the detector (right) and outside the detector (left).

The preamplifier used in this experiment was fed with the signal from the silicon detector, as well as a precision pulser connected to the test input of the preamplier. Figure 6.22 shows the output of the multi-channel analyser with the signals adjusted by a gaussian in both cases. From the fit, we can determine the charge introduced by the test pulse, and knowing the amplitude of the pulser ($V = 23.87mV$) we can calculate the capacity of the preamplifier: $C = 2.78pF$. Once the input capacitance of the preamplifier is calibrated, we can calculate the charge due to an applied voltage to the preamplifier.

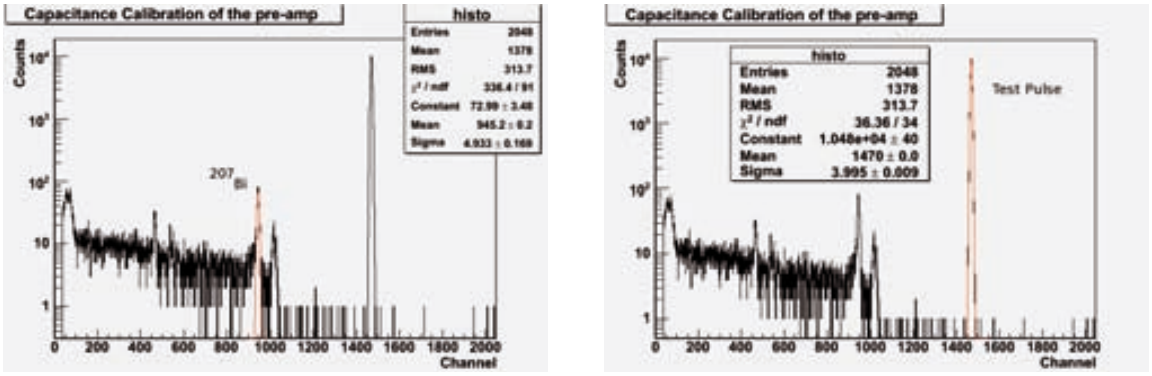

(a) Gaussian fit to the energy line from ^{207}Bi

(b) Gaussian fit to the test pulse with an amplitude of 23.87mV.

Figure 6.22: Calibration of the capacitance in the preamplifier

6.3.2.2 Measurements and results

LAAPD gain The gain of the LAAPD was measured by placing the LAAPD very close (about 3mm) to the source plate. The direct scintillation from a 5.305MeV alpha source (^{210}Po) was measured as a function of applied voltage on the LAAPD, up to about 1200V (see Figure 6.23). For higher voltages we observe a deformation at the peak of the spectrum, probably due to a manufacturing defect of the device. Unitary gain was determined from the average amplitude in the 300-500V range (Fernandes *et al.*, 2004). At low voltages, the LAAPD capacity varies with bias voltage. For gains above the uni-

tary gain and up to the highest values, the capacity changes less than 1-1.5% (Solovov *et al.*, 2002). In our setup, the dominant error for the gain measurement comes from the temperature variations (±1). Typical reduction in applied voltage when reducing temperature at a constant gain was observed, corresponding to an average voltage variation of approximately 2.4V/ , at a gain of 100.

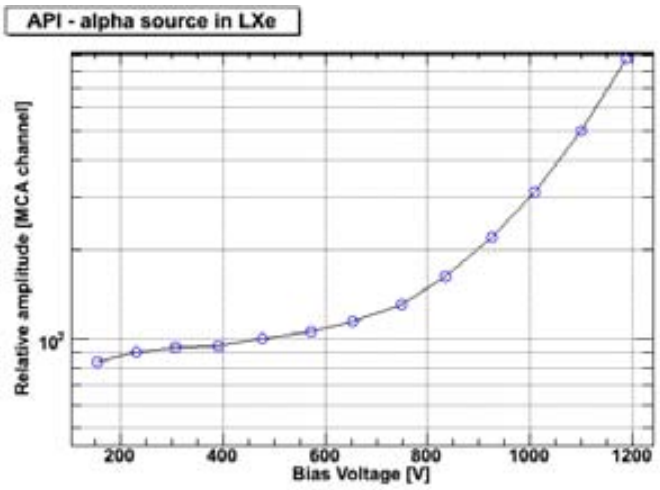

Figure 6.23: LAAPD pulse amplitude as a function of the reverse bias voltage for alpha source inmersed in LXe.

Quantum efficiency We calculate the quantum efficiency (η) of a LAAPD through the following equation:

$$\eta = \frac{N_0}{N_p} = \frac{N_d \ M}{\alpha N_{tot}} \tag{6.2}$$

Here N_0 is the number of photoelectrons from the LAAPD, N_p is the number of photons reaching the LAAPD surface, M is the LAAPD gain, N_d is the number of electron charges detected by the pre-amplifier and N_{tot} is the total number of scintillation photons produced by an event. N_{tot} is approximately equal to $E \ W_{ph}$, where E is the energy of the event, and W_{ph} is the average energy required to produce a scintillation photon in liquid xenon. The W_{ph} values is 19.6eV for alpha events (Doke & Masudab, 1999). α is the light collection efficiency, which is defined as the percentage of the total LXe light yield reaching the LAAPD surface. We have estimated the light collection efficiency, by geometrical approximation, to be about 17%. From these considerations, we estimated the quantum efficiency (QE) of the LAAPD to be ∼100%. The main error comes from the estimation of the light collection efficiency.

6.3.2.3 Conclusion

We have tested the operation of a LAAPD immersed in liquid xenon to detect scintillation light from alpha particles. The quantum efficiency was estimated to be 100% at $178nm$, in good agreement with previously reported experimental results (Solovov *et al.*,

2002). Further optimization on the manufacturing process for the wave length of $178nm$, especially the thickness of the protective oxide layers, could improve the response of these devices.
The LAAPD was operated at bias voltage between 400 and 1200 V corresponding to the gain range from 1 to 9. This gain is much lower than that of PMTs or SiPM, but at higher bias voltage (1700V) it can reach 1200 as reported by Solovov *et al.* (2002). On the other hand, properties of LAAPDs, such as their compact size, very high QE, and compatibility with low radioactive background and high LXe purity requirements, make them attractive for LXe detectors.

Chapter 7

Conclusions and future work

In this thesis, a test performed with the CLAIRE s gamma-ray lens was presented. Likewise, three detector concepts with different technologies were studied for the focal plane of a focusing telescope mission.

> In order to investigate the performance of a Laue lens, a ground test was carried out using a lens-source distance of 200m. This distance was long enough to test the Laue lens prototype of the CLAIRE project, with a quasi-parallel beam close to what is expected from a cosmic source. In preparation for the test, the lens was tuned at the optical bench in CESR(Toulouse).

This experiment was intended as a verification of the lens principle, since it permitted the testing of its pointing ability, by varying the relative position of the lens with respect to the gamma-ray beam (equivalent to a shift of the source off the optical axis). Furthermore, the test validated the relationship of energy-distance used for tuning the lens in the short distance available in the laboratory. A lens efficiency of about 10% was measured, in agreement with the CLAIRE balloon-borne experiment results. Regarding the focal plane detector, the imaging capabilities of a Laue lens telescope were studied. The computed point-spread-function showed that a position resolution on the millimetre range is needed to track the focal spot across the focal plane detector. In addition, off-axis detection becomes enabled, providing imaging capability to the lens in its field-of-view.

> In the framework of the GRI (Gamma-Ray Imager) mission study, a focal plane detector configuration based on CdTe/CZT detector, with fine spatial resolution, was proposed. In order to study the performance and understand the detector response, a single detector module was developed and tested.

A CdTe pixel detector (11x11 array) was developed. The pixel pitch and thickness were optimized through simulations in order to obtain the best spectral response and imaging capability in the MeV energy range. A prototype with 1mm picth and 2mm thickness was design and developed. Each pixel was stud bonded to a fanout board and routed to a front end ASIC to measure pulse-height and rise-time for each gamma-ray photon interaction. An energy resolution of 2.6% (FWHM) at 335keV was measured. This prototype

was intended as a basic module of our proposed focal plane detector configuration. The high segmentation of this detector would require a large number of channels, which is a major constraint in a space mission and might be a handicap of the proposed detector configuration. However, this detector configuration has successfully been registered under an European Patent and is being considered for medical detector applications.

Simulations of the expected space radiation environment at L2 and the resulting detector activation of the all-sky Compton telescope of the DUAL mission were performed in order to obtain the expected performance of the proposed mission.

One of the most critical aspects of the DUAL mission was the instrumental background and detection efficiency, which limits the sensitivity. An accurate mass model, which includes passive material in the detector and its surroundings, true energy thresholds and energy and position measurement accuracy, was implemented to obtain the expected performances. The results show that the all-sky Compton telescope of DUAL could achieve, after two years of operation, a continuum sensitivity one order of magnitude better than any past and current observatory in the MeV energy range. On the other hand, the Laue lens of DUAL achieves an improvement of sensitivity by a factor of 30, for 10^6s observation, of the ^{56}Co 847keV broad-line from SNIa.

A detector based on LXe was proposed with a readout system based on solid-state devices. Performances of two types of avalanche photosensors directly immersed into LXe were investigated.

We have tested the capability of SiPM and LAAPD immersed in liquid xenon in order to detect the fast xenon scintillation light at 178nm. The quantum efficiency was estimated to be 18% (SiPM) and 100% (LAAPD). The low noise of SiPM, along with its high single photon detection efficiency and low bias voltage, make these purely solid state devices a quite suitable solution for liquid xenon scintillation light detection. Large arrays of SiPMs offer a promising approach for reading out 3D position-sensitive LXe detectors. The proposed LXe detector would have a uniform detector volume with excellent stopping power and 3D position measurement capability with millimetric resolution.

Despite the strong effort carried out in the field of simulations of gamma-ray detectors and the build-up of prototypes, further research should be done in this direction to develop the next generation of gamma-ray telescopes in the MeV energy range. Currently, knowledge of Cd(Zn)Te detector technology is available and a realistic instrument concept based on this technology has been proposed. A possible pathway for future research is to develop and manufacture a reasonable prototype and experimentally verify all its capabilities, e.g. 3D positioning and polarization measurement. In fact, such a prototype is being considered as an option for a balloon-borne experiment with a CdTe polarimeter, currently under study. Concerning liquid Xenon detector technologies, laboratory measurements of performance (spectral response and fast timing) with a readout system based on solid state photosensors are ambitioned for the future, while the technology of vacuum

ultraviolet (VUV) photosensors continues with its spectacular progress.

In conclusion, it is clear that a new generation of high energy telescopes, incorporating novel high sensitivity detector designs is necessary in order to achieve the sensitivity required to answer several hot scientific topics of nuclear astrophysics.

Appendices

Appendix A

GRI and DUAL consortium

Jürgen Knödlseder, Peter von Ballmoos (CESR, France)
Filippo Frontera (UNIFE, Italy), Angela Bazzano (INAF/IASF-Rome, Italy)
Finn Christensen (DNSC, Denmark)
Margarida Hernanz (IEEC,CSIC, Spain)
Cornelia B. Wunderer (UCB, USA)

This proposal has been prepared by the GRI consortium, formed by about 100 scientists from the following countries (in alphabetical order): Belgium, China, Denmark, France, Germany, Ireland, Italy, Poland, Portugal, Russia, The Netherlands, Spain, Turkey, United Kingdom, and USA.
A complete list of consortium members can be found at: http://gri.iasf-roma.inaf.it/GRIMemberList.asp

Contents

We acknowledge the support of Thales Alenia Space and COSINE in the preparation of the technical part of this proposal. The proposal has also benefit from the results of the phase 0 study conducted by CNES in the context of the MAX project, and from the results of the Technical Reference Study conducted by ESA in the context of the GRL project. Technical developments in the context of GRI are financially supported by ASI (contract I/088/06/0), CNES (contract 02/0551/01-DPI120 and DCT/SA/AB N° 07-3202), ESA (ESTEC contract 20357/07/NL/NR) and the Spanish Ministry of Education and Science.

The GRI Consortium:

The Science Working Group (SWG): S. Basa (LAM), L. Bassani (IASF Bologna), A. Bazzano (IASF Rome), T. Belloni, (OA Brera), A. Bykov (IOFFE), P. Caraveo (IASF Milano), A. Chieffi (IASF Rome), S. Colafrancesco (OARM), A. De Rosa (IASF Roma), R. Diehl (MPE), F. Frontera (UNIFE), M. Hernanz (IEEC/CSIC), J. Isern (IEEC/CSIC), A. Iyudin (SINP), P. Jean (CESR), J. Knödlseder (CESR), L. Kuiper (SRON), J. Greiner (MPE), M. Limongi (OARM), N. Masetti (IASF Bologna), M. Orlandini (IASF Bologna), N. Prantzos (IAP), V. Tatischeff (CSNSM), D. F. Torres (ICE/IEEC), P. Ubertini (IASF Rome), S. Zane (Mullard), A. Zdziarski (Warsaw)

Instrument Working Group (IWG): J. Alvarez (IEEC/CSIC), K. Andersen (ILL), N. Barrière (CESR), P. Bastie (ILL), S. Boggs (SSL), C. Budtz-Jorgensen, (DNSC/DTU), E. J. Buis (Leiden), E. Cabruja (CNM-IMB), V. Carassiti (UNIFE), E. Caroli (IASF Bologna), M. Chmeissani (IFAE), F. E. Christensen (DNSC), D. Clark, (Southampton), P. Courtois (ILL), R. da Silva (Coimbra), A. Dean (Southampton), S. del Sordo (IASF Palermo), S. Di Cosimo (IASF Roma), F. Evangelisti (UNIFE), J. O. R. Grigorjan (SINP), G. Loffredo (UNIFE), M. Lozano (CNM-IMB), N. Lund (DSNC), L. Natalucci (Rome), A. Pacheco (IFAE), G. Pareschi (OA Brera), G. Pellegrini (CNM-IMB), R. Farinelli (UNIFE), A. Pisa (UNIFE), C. Puigdengoles (IFAE), E. M. Quadrini (IASF Milano), G. Roudil (CESR), B. Smither (USA), J. B. Stephen (IASF Bologna), S. I. Svertilov (SINP), L. Terés (CNM-IMB), J. Tueller (GSFC), M. Ullán (CNM-IMB), M. Uslenghi (Milano), P. von Ballmoos (CESR), C. Wunderer (SSL), A. Zappettini (IMEM), A. Zoglauer (SSL)

Data Analysis Working Group (DAWG): A. Bird (Southampton), H. Bloemen (SRON), V. Galkin (SINP), H. Halloin (APC), S. Sturner (GSFC), J. Vink (Utrecht), G. Weidenspointer (CESR), C. Wunderer (SSL), A. Zoglauer (SSL)

Supporting Scientists: L. Amati, M. Avillez, G. Di Cocco, R. Fusco Femiano, L. Hanlon, A. Hitschmann, J. Jose (IEEC/UPC), E. Kalemci, C. Kouveliotou, P. Leleux, K. Kruse Madsen, B. McBreen, A. Murphy, G. Skinner, L. Titarchuk, S. N. Zhang.


P. von Ballmoos (CESR)
P. Jean (CESR)
E. Hinglais (CNES)
J. Knödlseder (CESR)
B. Pirard (Canberra)
JP. Prost (TAS)
J. Alvarez (IEEC/CSIC)
JM. Del Cura Velayos (Sener)
M. Hernanz (IEEC/CSIC)
J. Isern (IEEC)
L. Hanlon (UCD)
F. Frontera (UNIFE)
T. Takahashi (ISAS)
R. da Silva (Coimbra)
A. Bykov (IOFFE)
R. Walter (ISDC)
L. Kuiper (SRON)
N. Barriere (SSL)
S. Boggs (SSL)
M. Leising (Clemson U)
J. Tomsick (SSL)
A. Zoglauer (SSL)
DUAL
TWO VIEWS OF THE EXTREME UNIVERSE
This proposal has been prepared by the DUAL consortium, formed by more than 100 scientists from : France, Spain, Ireland, Italy, Japan, Portugal, Russia, Switzerland, The Netherlands, USA, Belgium, Germany, India, Czech Republic, Sharjah UAE, Turkey, United Kingdom
A complete list of consortium members and institutions can be found at http://dual.cesr.fr

We acknowledge the support of THALES ALENIA Cannes, SENER Madrid, CANBERRA Lingolsheim in the preparation of the technical part of this proposal. The proposal has also benefit from the results of the phase 0 study conducted by CNES in the context of the MAX project, and from the results of the Technical Reference Study conducted by ESA in the context of the GRL project. Technical developments in the context of DUAL are financially supported by ASI (contract I/088/06/0), CNES (lens R&D contracts 02/0551/01-DPI120 and DCT/SA/AB No 07-3202, R-S06/- and R-S09/SU-0002-025, and R-S06/SU-0002-026), ESA (ESTEC contract 20357/07/NL/NR) and the Spanish Ministry of Education and Science.

DUAL
TWO VIEWS OF THE EXTREME UNIVERSE

The DUAL Consortium :

N. Abrosimov (IKZ), F. Aharonian (DIAS/MPIK), J. Alvarez (IEEC/CSIC), L. Amati (IASF Bologna), M. Amman (LBL), JL. Atteia (LATT), N. Auricchio (IASF Bologna), D. Barret (CESR), N. Barriere (SSL), S. Basa (OAMP), P. Bastie (LSP), A. Bird (Southampton), A. Bodaghee (SSL), S. Boggs (SSL), G. Bonnetto (TAS), Cristina Burgui (SENER), A. Bykov (IOFFE), Enric Cabruja (IMB-CNM/CSIC), T. Camus (CESR), E. Caux (CESR), E. Caroli (IASF Bologna), S. Chakrabarti, S. Chaty (CEA), A. Chieffi (IASF Roma), D. Clark (CESR), S. Colafrancesco (OA Roma), F. Cordero (Vega Group), P. Courtois (ILL), R. da Silva (Coimbra), F. Daigne (IAP), G. De Geronimo (BNL), T. Dean (Southampton), J.M. Del Cura Velayos (Sener), M. Del Santo (IASF Roma), JW. den Herder (SRON), R. Farinelli (UNIFE), F. Frontera (UNIFE), Joe Luis Galvez (IEEC/CSIC), D. Gangloff (CNES), D. Garcia-Senz (IEEC/UPC), J. Gayrard (CNES), N. Gehrels (NASA), PC. Gloster (Coimbra), E. Gogus (Sabanci), E. Grove (NRL), N. Guessoum(Sharjah), C. Guidorzi (UNIFE), D. Gutknecht (Canberra), H. Halloin (APC), L. Hanlon (UCD), M. Hernanz (IEEC/CSIC), W. Hermsen (SRON), E. Hinglais (CNES), R. Hudec, J. Isern (IEEC), P. Jean (CESR), M. Jentschel (ILL), N. Johnson (NRL), J. Jose (IEEC/UPC), E. Kalemci (Sabanci), J. Knoedlseder (CESR), M. Kocka (Masaryk U), M. Kokubun (ISAS), L. Kuiper (SRON), P. Laporte (GEPI), M. Leising (Clemson U), B. Lin (SSL) supporting scientist, Manuel Lozano (IMB-CNM/CSIC), P. Martin (MPE), A. Martin-Carillo (UCD), B. McBreen (UCD), A. Murphy (Edinburgh U), K. Nakazawa (Tokyo U), L. Natalucci (IASF Roma), L. Nicastro (IASF Bologna), U. Oberlack, M. Orlandini (IAS Bologna), Giulio Pellegrini (IMB-CNM/CSIC), B. Phlips (NRL), V. Pierrard (U Louvain), B. Pirard (Canberra), N. Prantzos (IAP), N. Produit, JP. Prost (TAS), N. Rea (IEEC/CSIC), H. Riemann (IKZ), E. Rivierre (CNES), DE Rou (UC Irvine), D. Rodriguez-Gomez (Sener), G. Roudil (CESR), J. Rousselle (CESR), R. Sanchez Maestro (Sener), Jesus Ignacio Santos (SENER), G. Skinner (GSFC), D. Smith, J. Stephen (IASF Bologna), B. Swinyard, H. Tajima (KIPAC), T. Takahashi (ISAS), T. Tanaka (KIPAC), V. Tatischeff (CSNSM), L. Titarchuk (UNIFE), J. Tomsick (SSL), D. Torres (IEEC/CSIC), J. Tueller (GSFC), P. Ubertini (IASF-Roma), Y. Uchiyama (KIPAC), Igone Urdampilleta (Sener) J. Vink (Utrech U), E. Virgilli (UNIFE), P. von Ballmoos (CESR), N. von Krusenstiern (Vega Group), R. Walter (ISDC), S. Watanabe (ISAS), G. Weidenspointner (HLL/MPE), EA. Wulf (NRL), S. Zane (MSSL), A. Zoglauer (SSL).

For a complete list of collaborating institutions please see http://dual.cesr.fr/M3/collaboration.

Appendix B

Simulation tools

B.1 Monte Carlo simulation toolkit

B.1.1 GEometry ANd Tracking: GEANT4

Geant4 is a Monte Carlo simulation toolkit based on C++ computer language, for the simulation of the passage of particles through matter (Agnostelli *et al.*, 2003). It has been developed by a world-wide collaboration of scientists and software engineers whose goal is to develop, maintain and provide support to the users of Geant4. Its application areas include high energy physics, nuclear physics, medical science and space physics studies. The source code is distributed by CERN and is accessible on the web page *http://geant4.cern.ch/*. Geant4 provides the option to use the GLECS/GLEPS package by Kippen (2004) to take into account the energy of bound electrons and photon polarization in Compton scattering.

B.1.2 MGGPOD

MGGPOD is a suite of five closely integrated Monte Carlo packages, namely MGEANT, GCALOR, PROMPT, ORIHET, and DECAY. The MGGPOD suite resulted from a combination of the NASA/GSFC MGEANT (Sturner et al., 2000) and the University of Southampton GGOD (Dean et al., 2003) Monte Carlo codes, which we supplemented with the newly developed PROMPT package. All these packages are based on the widely used GEANT Detector Description and Simulation Tool created and supported at CERN, which is designed to simulate the passage of elementary particles through an experimental set-up. In a nutshell, the capabilities and functionalities of the five packages that constitute the MGGPOD suite are as follows:

- MGEANT is a multi-purpose simulation package that was created at NASA/GSFC to increase the versatility of the GEANT simulation tool. A modular, object oriented approach was pursued, allowing for rapid proto-typing of detector systems and easy generation of most of the radiation fields relevant to γ-ray astronomy. Within the MGGPOD suite, MGEANT (i.e., GEANT) stores and transports all particles, and treats electromagnetic interactions from about 10keV to a few TeV.

- GCALOR, developed by C. Zeitnitz and T.A.Gabriel, simulates hadronic interactions down to 1 MeV for nucleons and charged pions and down to thermal energies (10^{-5} eV) for neutrons. Equally important, this package provides access to the energy deposits from all interactions as well as to isotope production anywhere in the simulated set-up.

- PROMPT simulates prompt photon emission associated with the deexcitation of excited nuclei produced by neutron capture, inelastic neutron scattering, and spallation.

- ORIHET, originally developed for the GGOD suite and improved for MGGPOD, calculates the build-up and decay of activity in any system for which the nuclide production rates are known. Hence ORIHET can be used to convert nuclide production rates, determined from simulations of cosmic-ray irradiation, to a decay rate, which is a necessary input for simulating the radioactive decays giving rise to the delayed background.

- DECAY, again originally developed for GGOD and improved, enables MGGPOD to simulate radioactive decays.

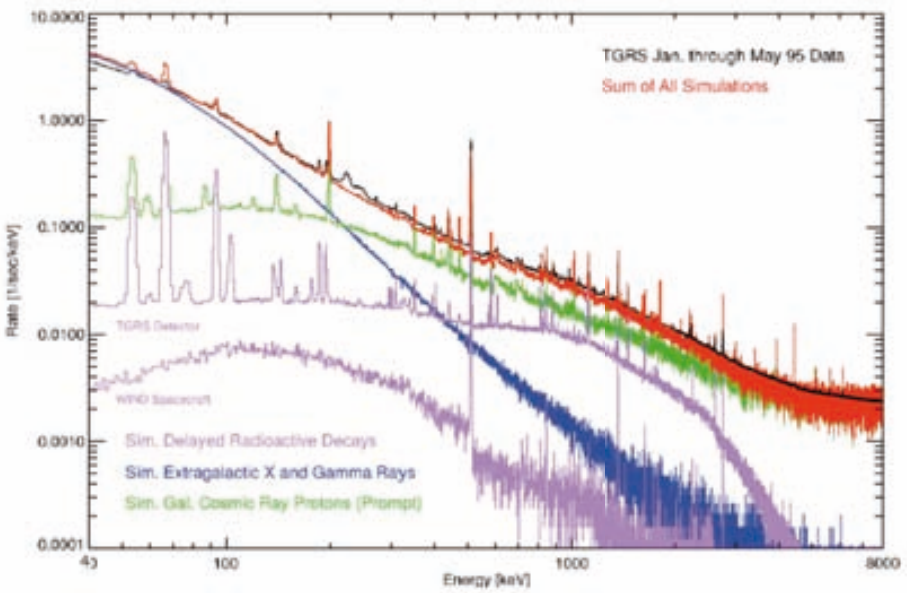

Figure B.1: The background spectra recorded by Wind/TGRS and simulated by MGGPOD (Weidenspointner *et al.*, 2005a).

MGGPOD, has demonstrated its capabilities for modelling instrumental backgrounds by applying it to Wind/TGRS and INTEGRAL/SPI. The background spectra recorded by TGRS and simulated with MGGPOD is shown in figure B.1, reprinted from Weidenspointner et al. (2005). MGGPOD, is very successful in modelling both the continuum and line backgrounds of the TGRS instrument, consisting of a $215cm^3$ Ge crystal.

B.2 Medium-Energy Gamma-ray Astronomy library: MEGAlib

This library, originally developed for the MEGA prototype (Kanbach *et al.*, 2004), was enhanced in the framework of the ACT study and it became a major set of software tools to analyze data for the next generation of Compton telescopes (Zoglauer *et al.*, 2006b). A detailed explanation of MEGAlib can be found in Zoglauer (2005). A brief overview over the main programs which are available in MEGAlib and the tasks which can be performed with them, is given in the following paragraphs:

- **Geomega** is the detector geometry package. It provides a uniform geometry and detector setup description for MEGAlib. Starting from a geometry file, which includes the description of all materials, volumes, detectors, trigger criteria, etc., the geometry is built and can be viewed with Geomega. The underlying geomega library is in turn used by all other programs of MEGAlib to access this geometry information. For example: 1) The simulation tool Cosima is using Geomega to import the geometry into its own Geant4 format. 2) When the simulation file is read by e.g. the event reconstruction tool Revan, then the ideal simulation data is noised according to the detector description of geomega. 3) Revan & Mimrec uses Geomega to calculate absorption probabilities, check where the hits occurred. 4) The geometry can be converted to formats which the GEANT3 simulation program GMega as well as MGeant/MGGPOD can process. 5) The Geant4 program Cosima directly loads Geomega s shared library to use the geometry package.

- **Sivan** is intended for the analysis of simulated data and explicitly using simulation information: the underlying library is mainly used to determine responses and determine the maximum possible efficiency of an event reconstruction algorithm.

- **Revan** provides the event reconstruction, i.e. it handles the transition of the events from pure hits into interaction processes (Compton, Pair, etc.). The algorithm is split into four subsections: clustering (blobbing adjacent hits into one larger hit), tracking (finding showers, muons, pair events and Compton electron tracks), Compton sequence reconstruction (identifying the sequence of Compton interactions) and finally decay detection (identifying events, which might originate from decays).

- **Mimrecs** main duty is list-mode likelihood image reconstruction. In addition it can handle other high-level data analysis, like compiling spectra, ARM-distributions, scatter-angle distribution, and more.

- **Cosima** Cosima is intended as a universal simulator for low-to-medium-energy gamma-ray telescopes, detecting gamma-rays via photo-effect, Compton scattering, and pair creation. This goal requires accurate simulation from a few keV up to hundreds of GeV, including particles ranging from gamma-ray to cascades triggered by cosmic high-energy particles. It has also been used for simulations for medical

imaging and nuclear surveillance applications. Cosima is full integrated into MEGAlib. For the simulations, one can use the same geometry file used with MEGAlib. The output of Cosima, the sim-file, can be used by MEGAlibs Revan and Sivan programs.

B.3 ACT simulation toolset

As illustrated in Fig. B.2, for simulating γ-ray instruments in a space environment four basic types of tools are required: (1) models to describe source and background environment in terms of particle distributions, (2) models to describe the detailed geometry and mass of the instrument and spacecraft, (3) Monte Carlo simulation tools to predict the response of the instrument to particle sources and backgrounds, and (4) tools to process and analyze the resulting data in a manner emulating anticipated operational capabilities. There was no single simulation solution that included all these required tools.

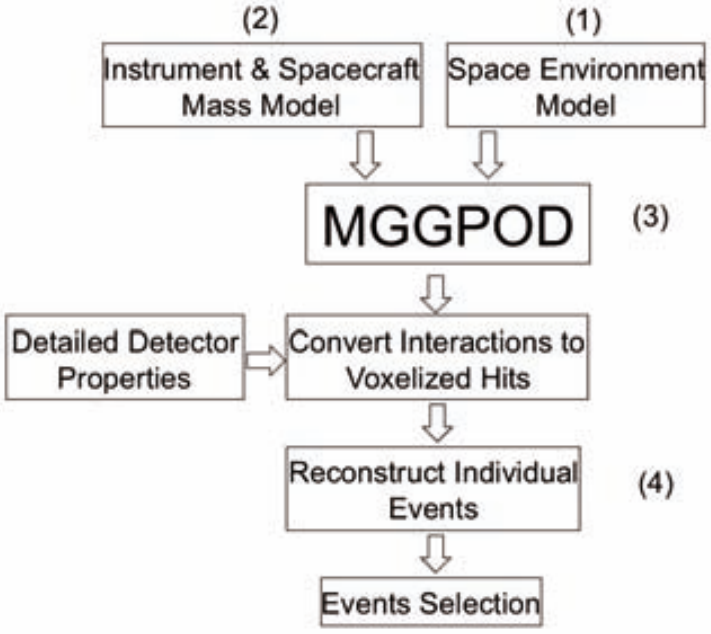

Figure B.2: Overview over the data analysis steps integrated in the ACT tool.

The development and application of computer simulations and models for estimating realistic instrument performance parameters was one of the major issues of the ACT concept study (Boggs *et al.*, 2006). Previously existing tools were combined into a complete, powerful package for γ-ray astronomy (ACTtool [1]).

Accurate space environment models are crucial inputs for reliable prediction of instrument performance (see section1.2.2.1). The primary resource used for background models is the CREME96 package (Tylka *et al.*, 1997) from the U.S. Naval Research Laboratory.

[1] http://public.lanl.gov/mkippen/actsim/act-study

The process of modeling detailed instrument geometry and mass distributions for use in realistic Monte Carlo simulations is often long and laborious. For the ACT study a mass model generation tool was developed in order to conveniently support different detector and structural materials and combine them with a reasonably detailed spacecraft model. The Monte Carlo package at the heart of the ACT simulation toolset is the above described MGGPOD package. Concerning the data analysis, the package MEGAlib (described above) comprises the complete data analysis chain for Compton telescopes -from discretizing simulation data and calibrating real measurements, to the reconstruction and selection of events, up to high-level data analysis, i.e. image reconstruction, background estimation, and polarization analysis. The most critical part in the data analysis is the reconstruction of photon energy and direction (and polarization) from raw measured quantities (interaction positions and energies). Event reconstruction is the key to differentiating source events from background. The capabilities of MEGAlib to correctly reconstruct incident directions of photons and to ultimately produce images was reported by Zoglauer *et al.* (2004).

Bibliography

Abrosimov, N. *et al.* (2005). Growth and properties of $\mathtt{G}e_{1-x}\mathtt{S}i_x$ mosaic single crystals for γ-ray lens application. *J. Crystal Growth*, *275*, 495 500.

Agnostelli, S. *et al.* (2003). Geant4 - a simulation toolkit. *Nucl. Instrum. Meth. Phys. Res. A*, *506*, 270 278.

Álvarez, J., Gálvez, J., Hernanz, M., Isern, J., Llopis, M., Lozano, M., Pellegrini, G., & Chmeissani, M. (2010a). Imaging detector development for nuclear astrophysics using pixelated CdTe. *Nucl. Instr. and Meth. in Phy. Res. A*, *623*(1), 434 436.

Álvarez, J., Gálvez, J., Hernanz, M., Isern, J., Lozano, M., Pellegrini, G., Chmeissani, M., Cabruja, E., & Ullán, M. (2010b). Research and development of a gamma-ray imaging spectrometer in the MeV range in Barcelona. In *Proceedings of the SPIE*. vol. 7732, 77324P 77324P 11.

Álvarez, J., Gálvez, J., *et al.* (2011). CdTe/CdZnTe pixel detector for gamma-ray spectrometry with imaging and polarimetry capability in astrophysics. *IEEE Nuclear Symposium Conf. Rec.* In press.

Álvarez, J., Halloin, H., Hernanz, M., von Ballmoos, P., *et al.* (2004a). Long distance test of the CLAIRE gamma-ray lens. In V. Schonfelder, G. Lichti, & C. Winkler (Eds.), *ESA SP-552: 5th INTEGRAL Workshop on the INTEGRAL Universe*. 757 759.

Álvarez, J. & Hernanz, M. (2006). Simulations of gamma-ray detectors for astrophysics with Geant4. In *VII reunion cientifica de la SEA (Barcelona)*.

Álvarez, J., Hernanz, M., & vonBallmoos, P. (2004b). Calibration of gamma-ray instruments for nuclear astrophysics. Tech. rep., Proposal for the Contruction of a Gamma-Ray Beam Line at the Spanish Synchrotron ALBA, Online available `http://www.cells.es/static/gamma_rays.pdf` .

Aprile, E. & Doke, T. (2010). Liquid xenon detectors for particle physics and astrophysics. *Rev. Mod. Phys.*, *82*(3), 2053 2097.

Aprile, E., Giboni, K., Majewski, P., Ni, K., & Yamashita, M. (2007). Observation of anticorrelation between scintillation and ionization for MeV gamma rays in liquid xenon. *Phys. Rev. B*, *76*(1), 014115.

Aprile, E., Mukerjiee, R., & Suzuki, M. (2006a). Performance of a liquid xenon ionization chamber irradiated with electrons and gamma-rays. *Nucl. Instr. and Meth. in Phy. Res. A*, *302*, 177.

Aprile, E. & Suzuki, M. (1989). Development of liquid xenon detectors for gamma-ray astronomy. *IEEE Trans. Nucl. Sci*, *36*, 311.

Aprile, E. *et al.* (2001). A liquid xenon time projection chamber for γ-ray imaging in astrophysics: present status and future directions. *Nucl. Instrum. Meth. Phys. Res. A*, *461*, 256 261.

Aprile, E. *et al.* (2002). Detection of gamma-rays with a 3.5l liquid xenon ionization chamber triggered by the primary scintillation light. *Nucl. Instr. and Meth. in Phy. Res. A*, *480*, 636.

Aprile, E. *et al.* (2004). Calibration and in-flight performance of the compton telescope prototype LXeGRIT. *New Astronomy Reviews*, *48*, 257 262.

Aprile, E. *et al.* (2006b). Detection of liquid xenon scintillation light with a silicon photomultiplier. *Nucl. Instr. and Meth. in Phy. Res. A*, *556*, 215 218.

Arutyunian, F. & Tumanian, V. (1963). The compton effect on relativistic electrons and the possibility of obtaining high energy beams. *Phys. Lett.*, *4*, 176.

Auricchio, N. *et al.* (1999). Investigation of response behavior in CdTe detectors versus inter-electrode charge formation position. *IEEE Trans. Nucl. Sci.*, *46*, 853 857.

Authier, A. & Malgrange, C. (1998). Diffraction physics. *Acta Cryst.*, *A54*, 806 819.

Barrett, H., Eskin, J., & Barber, H. (1995). Charge transport in arrays of semiconductor gamma-ray detector. *Phys. Rev. Lett*, *75*, 156 159.

Barriere, N., von Ballmoos, P., Halloin, H., Abrosimov, N., Álvarez, J., *et al.* (2005). MAX, a laue diffraction lens for nuclear astrophysics. *Experimental Astronomy*, *20*, 269 278.

Barriere, N., von Ballmoos, P., Skinner, G., Smither, B., Bastie, P., Hinglais, E., Abrosimov, N., Álvarez, J., *et al.* (2006). MAX: Development of a laue diffraction lens for nuclear astrophysics. *Nucl. Instr. and Meth. in Phy. Res. A*, *567*, 333 336.

Barriere, N. *et al.* (2007). R and D progress on second-generation crystals for Laue lens applications. In *Proceedings of the SPIE*. vol. 6688.

Berger, M., Hubbell, J., Seltzer, S., *et al.* (2009). Photon cross sections database (XCOM). National Institute of Standards and Technology Standard Reference,Online available http://physics.nist.gov/PhysRefData/Xcom/html/xcom1.html .

Bethe, H. & Heitler, W. (1934). On the stopping of fast particles and on the creation of positive electrons. *Proc. R. Soc. London*, *A146*, 83.

Bhattacharya, D. *et al.* (2004). Prototype TIGRE compton gamma-ray balloon-borne instrument. *New Astronomy Reviews*, *48*, 287 292.

Biggs, F. *et al.* (1975). Hartree-Fock Compton Profiles for the Elements. *Atomic Data and Nuclear Data Tables*, *16*.

Boggs, S. (2006). The advanced compton telescope mission. *New Astronomy Reviews.*, *50*(Issue 7-8), 604 607.

Boggs, S. *et al.* (2004). Overview of the nuclear compton telescope. *New Astronomy Reviews*, *48*, 251 255.

Boggs, S. E. & Jean, P. (2001). Performance characteristics of high resolution compton telescopes. *Astronomy and Astrophysics*, *376*, 1126 1134.

Boggs, S. E. *et al.* (2006). The Advanced Compton Telescope Mission. Astro-ph/0608532.

Boggs, S. E. *et al.* (2008). GRASP: Galactic radioactivity survey probe. *NASA SMEX A0, NNH07ZDA0030*, 1 28.

Brown, C. *et al.* (2005). GRL technology reference study final report. *ESA SCI-A/2005/058/GRL/CB*.

Caroli, E., Álvarez, J., *et al.* (2011). A balloon-borne 3D CZT scattering polarimeter for hard X-ray astrophysics. *IEEE Nuclear Symposium Conf. Rec.* In press.

Caroli, E. *et al.* (2005). A focal plane detector design for a wide-band laue-lens telescope. *Experimental Astronomy*, *20*, 341 351.

Caroli, E. *et al.* (2009). A polarimetric experiment with a laue lens and CZT pixel detector. *IEEE Trans. Nucl. Sci.*, *56*, 1848.

Caroli, E. *et al.* (2010). Development of a 3D CZT detector prototype for laue lens telescope. *Proceedings of the SPIE*, *7742*.

Caspi, A. *et al.* (2006). Measuring the temperature of hot flare plasma using RHESSI Fe and Fe/Ni line observations. *Astron. Astrophys.*, *38*, 253.

Chmeissani, M., Álvarez, J., & Sanchez, C. (2008). Device for detecting highly energetic photons. *European Patent Office*, *WO2010034619*.

Chmeissani, M. *et al.* (2009). Modeling and simulation of pet scanner based on pixelated solid-state detector. *IEEE Trans. Nucl. Sci.*, *1-5*, 3496 3502.

Coburn, W. & Boggs, S. (2003). Polarization of the prompt γ-ray emission from the γ-ray burst of 6 december 2002. *Nature*, *423*, 415.

da Silva, R. C. *et al.* (2008). Polarimetric performance of a laue lens gamma-ray CdZnTe focal plane prototype. *Journal of Appl. Phy.*, *104*, 084903.

Darwin, G. (1941). The theory of X-ray reflection. *Philos. Mag*, *27*, 315 333.

Davisson, C. (1966). *Alpha-, Beta-, and Gamma-Ray Spectroscopy*. North-Holland, Amsterdam.

Dean, A. J. *et al.* (2003). The modelling of background noise in astronomical gamma-ray telescopes. *Space Science Reviews*, *105*, 285 376.

Devanathan, R. *et al.* (2006). Signal variance in gamma-ray detectors - a review. *Nucl. Instrum. Methods Phys. Res. A*, *565*, 637 649.

Diehl, R. (2006). Radioactive ^{26}Al from massive stars in the galaxy. *Nature*, *439*, 45 47.

Diehl, R. (2011). *Introduction to Astronomy with Radioactivity*, Springer Berlin / Heidelberg, vol. 812. 3 23.

Diehl, R., Prantzos, N., & von Ballmoos, P. (2005). Astrophysical constraints from gamma-ray spectroscopy. *Nuclear Astrophysics, special volume of Nuclear Physics A, ed. F.-K. Thielemann et al.*.

Doke, T. & Masudab, K. (1999). Present status of liquid rare gas scintillation detectors and their new application to gamma-ray calorimeters. *Nucl. Instr. and Meth. in Phy. Res. A*, *420*, 62.

Doke, T. *et al.* (2002). Absolute scintillation yields in liquid argon and xenon for various particles. *J. Appl. Phys.*, *41*, 1538 1545.

Du, F. *et al.* (1999). Monte carlo investigation of the charge sharing effects in 3D position sensitive CdZnTe gamma ray spectrometers. *IEEE Trans. Nucl. Sci.*, *46*(4), 844 847.

Duchon, P. (2005). MAX: Formation flying for nuclear astrophysics. *Experimental Astronomy*, *20*, 483 495.

DuMond, J. (1929). Compton modified line structure and its relation to the electron theory of solid bodies. *Phys.Rev.*, *33*, 643.

Evans, R. (1955). *The Atomic Nucleus*. McGraw-Hill New York.

Fano, U. (1947). Ionization yield of radiations II. the fluctuation of the number of ions. *Phys. Rev.*, *72*, 26 29.

Fernandes, L. (2005). *Caracterization of Large Area Avalanche Photodiodes for detection of X-rays vacuum ultraviolet and visible light*. Ph.D. thesis, University of Coimbra.

Fernandes, L. *et al.* (2004). LAAPD low temperature performance in X-ray and visible-light detection. *IEEE Trans. Nucl. Sci.*, *NS-51*(4), 1575.

Ferreira, S. *et al.* (2002). The modulation of 4- to 16- mev electrons in the outer heliosphere: Implications of different local interstellar spectra. *Journal of Geophysical Research (Space Physics)*, *107*, 12.

Frisch, O. (1944). Unpublished report. *British Atomic Energy Report*, *BR-49*.

Gehrels, N. (1992). Instrument background in gamma ray spectrometers flown in low earth orbit. *Nuclear Instr. And Meth. In Phys. Res. Sect. A*, *313*, 513 528.

Gehrels, N. *et al.* (2004). The SWIFT Gamma-Ray Burst Mission. *The Astrophysical Journal*, *611*, 1005 1020.

Georgii, R. *et al.* (2002). Comptel upper limits for the ^{56}Co gamma-ray emission from SN1998bu. *Astron. Astrophys.*, *394*, 517 523.

Giboni, K., Aprile, E., & Rochwarger, I. (1998). Schottky CdTe detectors for imaging in nuclear medicine and astrophysics. *Proceedings of the SPIE*, *3446*, 228.

Giboni, K., Aprile, E., *et al.* (2005). Fast timing measurements of gamma-ray events in liquid xenon. *IEEE Trans. Nucl. Sc.*, *52*, 1800 1804.

Gómez-Gomar, J. *et al.* (1998a). Gamma-ray emission from individual classical novae. *Mon. Not. R. Astron. Soc.*, *296*, 913 920.

Gómez-Gomar, J. *et al.* (1998b). Prospects for Type iA supernova explosion mechanism identification with gamma-rays. *MNRAS*, *295*, 1 9.

Gruber, D. *et al.* (1999). The spectrum of diffuse cosmic hard X-rays measured with HEAO 1. *The Astrophysical Journal*, *520*, 124 129.

Halloin, H. (2003). ***CLAIRE**: Premiéres lumiéres d une lentille gamma*. Ph.D. thesis, Université Paul Sabatier, Toulouse.

Halloin, H. (2005a). Laue diffraction lenses for astrophysics: From theory to experiments. *Exp. Astron.*, *20*, 171 184.

Halloin, H. (2005b). Simulens v2.0. *GRI collaboration*.

Halloin, H. & Bastie, P. (2005). Laue diffraction lenses for astrophysics: Theoretical concepts. *Exp. Astron.*, *20*, 151 170.

Halloin, H., von Ballmoos, P., Evrard, J., Skinner, G., Hernanz, M., Abrosimov, N., Bastie, P., Hamelin, B., Lonjou, V., Álvarez, J., *et al.* (2004). CLAIRE gamma-ray lens: flight and long-distance test results. In O. Citterio & S. L. O Dell (Eds.), *Optics for EUV, X-Ray, and Gamma-Ray Astronomy. Edited by Citterio, Oberto; O Dell, Stephen L. Proceedings of the SPIE.*. vol. 5168, 471 481.

Harmon, B. (1992). The compton observatory science workshop. In C. Shrader, N. Gehrels, & B. Dennis (Eds.), *NASA CP-3137*. vol. 69.

Harris, M. J. *et al.* (2005). Detection of gamma-ray lines from interstellar 60Fe by the high resolution spectrometer SPI. *Astron. Astrophys.*, *433*, L49 L52.

He, Z. (2001). Review of the Shockley-Ramo theorem and its application in semiconductor gamma ray detectors. *Nucl. Instrum. Methods Phys. Res. A*, *463*, 250 267.

He, Z., Knoll, G., *et al.* (1996). 1D position sensitive single carrier semiconductor detectors. *Nucl. Instr. and Meth. in Phy. Res. A*, *380*, 228.

He, Z., Knoll, G., *et al.* (1997). Position-sensitive single carrier CdZnTe detectors. *Nucl. Instr. and Meth. in Phy. Res. A*, *388*, 180.

He, Z., Li, W., Knoll, G., *et al.* (1999). 3D position sensitive CdZnTe gamma-ray spectrometers. *Nucl. Instr. and Meth. in Phy. Res. A*, *422*, 173.

Hecht, K. (1932). Zum mechanismus des lichtelektrischen primrstromes in isolierenden kristallen. *Z.Phys.*, *77*, 235 245.

Hernanz, M. & José, J. (2004). γ-rays from classical novae: expectations from present and future missions. *New Astronomy Reviews*, *48*, 35 39.

Hernanz, M. *et al.* (1999). Gamma-ray emission from novae related to positron annihilation: Constraints on its observability posed by new experimental nuclear data. *Astrophysical Journal Letters*, *526*, L97 L100.

Hitachi, A. *et al.* (1983). Effect of ionization density on the time dependence of luminescence from liquid argon and xenon. *Phys. Rev. B*, *27*, 5279.

Hyman, L., Schwarz, R., & Schluter, R. (1964). Study of high speed photomultiplier systems. *Rev.Sci.Instr.*, *35*, 393.

Ichinose, H. *et al.* (1992). Energy resolution for gamma-rays and electrons from 207bi in liquid xe doped with tea. *Nucl. Instrum. Meth. Phys. Res. A*, *322*, 216 224.

Isern, J. *et al.* (2004). γ-ray emission from type ia supernovae. *New Astronomy Reviews*, *48*, 31 33.

Iyudin, A. *et al.* (1994). COMPTEL observations of ^{44}Ti gamma-ray line emission from Cas A. *Astron. Astrophys.*, *284*, L1 L4.

Jordanov, V., Pantazis, J., & Huber, A. (1996). A. compact circuit for pulse rise-time discrimination. *Nucl. Instrum. Meth. Phys. Res. A*, *380*, 353 357.

Kanbach, G. *et al.* (2004). The mega project. *New Astronomy Reviews*, *48*, 275 280.

Kippen, R. M. (2004). The geant low energy compton scattering (GLECS) package for use in simulating advanced compton telescopes. *New Astronomy Reviews*, *48*, 221 225.

Kittel, C. (2005). *Introduction to Solid State Physics*. Wiley.

Klein & Nishina (1929). Uber die streuung von strahlung durch freie elektronen nach neuen relativistichen quantendynamik von z. dirac. *Physik*, *52*, 853.

Knodlseder, J. (2007). GRI: The gamma-ray imager mission. *Advances in Space Research*, *40*(Issue 8), 1263 1267.

Knodlseder, J. *et al.* (2005). The all-sky distribution of 511 kev electron-positron annihilation emission. *Astronomy and Astrophysics*, *411*, 513 532.

Knodlseder, J. *et al.* (2009). GRI: focusing on the evolving violent universe. *Experimental Astronomy*.

Knoll, G. F. (1999). *Radiation detection and measurement*. John Wiley and Sons, 2Ed.

Kohnle, A. (1998). *A Gamma-ray lens for nuclear astrophysics*. Ph.D. thesis, Université Paul Sabatier, Toulouse.

Koren, B. & Szawlowski, M. (1998). Large-area avalanche photodiodes challenge PMTs. *Advances and applications in Optoelectronics, Laser Focus World*.

Kubo, H. *et al.* (2006). Balloon-borne sub-mev gamma-ray imager using electron tracking gaseous TPC and scintillation camera. *IEEE NSS Conference Record*, *N14*, 101.

Kubota, S. *et al.* (1978). Recombination luminescence in liquid argon and in liquid xenon. *Phys. Rev. B*, *17*, 27622765.

Kurfess, J. *et al.* (2000). Considerations for the next compton telescope mission. *AIP Conf. Proc.*, *510*, 789 793.

Kurfess, J. *et al.* (2004). An advanced compton telescope based on thick, position-sensitive solid-state detectors. *New Astronomy Reviews*, *48*, 293 298.

Lange, K. & Carson, R. (1984). EM reconstruction algorithms for emission and transmission tomography. *Journal of Computer Assisted Tomography*, *8(2)*, 306 316.

Lebrun, F. (2006). Semiconductor detectors for soft γ-ray astrophysics. *Nucl. Instrum. Meth. Phys. Res. A*, *563*, 200 204.

Lei, F. *et al.* (1997). Compton Polarimetry in Gamma-Ray Astronomy. *Space Science Reviews*, *82*, 309 388.

Leo, W. R. (1994). *Techniques for Nuclear and Particle Physics Experiments*. Springer-Verlag, 2Ed.

Leventhal, M. *et al.* (1978). Detection of 511 kev positron annihilation radiation from the galactic center direction. *Astrophysical Journal*, *225*, L1.

Limousin, O. *et al.* (2011). Polarisation performance of the CdTe/CZT caliste detector modules. *IEEE Nuclear Symposium Conf. Rec., in press*.

Lin, R. *et al.* (2002). The reuven-ramaty high-energy solar spectroscopic imager RHESSI. *Solar Physics*, *219*(3-32).

Loffrendo, G., Frontera, F., *et al.* (2005). The ferrara hard x-ray facility for testing/calibrating hard x-ray focusing telescopes. *Exp. Astron*, *20*, 415 422.

Lopes, J. *et al.* (2001). A xenon gas proportional scintillation counter with a UV-sensitive large-area avalanche photodiode. *IEEE Trans. Nucl. Sci.*, *NS-48*(3), 312.

Luke, P. (1995). Unipolar charge sensing with coplanar electrodes - application to semiconductor detectors. *IEEE Trans. Nucl. Sci.*, *42*, 207 213.

Lund, N. (1992). A study of focusing telescopes for soft gamma rays. *Experimental Astronomy*, *2*, 259 273.

Mahoney, W. A. *et al.* (1984). HEAO 3 discovery of ^{26}Al in the interstellar medium. *The Astrophysical Journal*, *286*, 578.

Matsumoto, C., Takahashi, T., *et al.* (1997). Performance of a new Schottky CdTe detector for hard X-ray spectroscopy. *Nuclear Science Symposium, IEEE*, *1*, 569 573.

McGregor, D. *et al.* (1998). Single charge carrier type sensing with a parallel strip pseudo-frisch-grid CdZnTe semiconductor radiation detector. *Appl.Phys.Lett.*, *12*, 192 194.

Mészáros, P. *et al.* (2006). Gamma-ray bursts. *Rep. Prog. Phys.*, *69*, 2259.

Mizuno, T. *et al.* (2004). Cosmic-ray background flux model based on a gamma-ray large area space telescope balloon flight engineering model. *The Astrophysical Journal*, *614*, 1113.

Morris, D. *et al.* (1995a). Evidence for ^{56}Co-lines from the Type Ia supernova 1991T using COMPTEL. *Ann. of New York Acad. of Sci.*, *759*, 397 400.

Morris, D. *et al.* (1995b). Neutron measurements in near-earth orbit with comptel. *Journal of Geophysical Research*, *100*, 12243.

Moskalenko, I. *et al.* (2002). Secondary antiprotons and propagation of cosmic rays in the galaxy and heliosphere. *The Astrophysical Journal*, *565*, 280 296.

Natalucci, L., Álvarez, J., *et al.* (2008). CdZnTe detector for hard x-ray and low energy gamma-ray focusing telescope. *Proceedings of the SPIE*, *7011*.

Naya, J. (1995). *Spectroscopie Gamma Fine et Haute Resolution Angulaire*. Ph.D. thesis, Université Paul Sabatier, Toulouse.

Naya, J. *et al.* (1996). Experimental results obtained with the positron annihilation radiation telescope of the Toulouse-Argonne collaboration. *Nuclear Instr. And Meth. In Phys. Res. Sect. A*, *373*, 159.

Ni, K., Aprile, E., *et al.* (2005). Performance of a large area avalanche photodiode in a liquid xenon ionization and scintillation chamber. *Nucl. Instr. and Meth. in Phy. Res. A*, *551*, 356363.

Owens, A. & Peacock, A. (2004). Compound semiconductor radiation detectors. *Nucl. Instr. and Meth. in Phy. Res. A*, *A531*, 18.

Owens, A. *et al.* (1995). A high-resolution Ge spectrometer for Gamma-Ray burst astronomy. *Space Sci. Rev.*, *71*, 273.

Paul, J., Mandrou, P., Ballet, J., *et al.* (1991). SIGMA: The hard x-ray and soft gamma-ray telescope on board the GRANAT space observatory. *Adv. Space Res.*, *11*(8), 289 302.

Perlmutter, S. *et al.* (1999). Measurements of omega and lambda from 42 high-redshift supernovae. *The Astrophysical Journal*, *517*, 565.

Phillips, M. (1993). The absolute magnitudes of Type iA supernovae. *Astronomical Journal Letters*, *413*, L105 L108.

Pluschke, S. *et al.* (2001). The COMPTEL 1.809 Mev survey. *ESA SP*, *459*, 55.

Poludniowski, G. *et al.* (2009). Spekcalc: a program to calculate photon spectra from tungsten anode x-ray tubes. *Phys Med Biol.*, *54(19)*, N433 8.

Prantzos, N. (2004). Radioactive ^{26}Al and ^{60}Fe in the milky way: Implications of the RHESSI detection of ^{60}Fe. *Astron. Astrophys.*, *420*, 1033.

Richter, M. & Siffert, P. (1992). High resolution gamma ray spectroscopy with CdTe detector systems. *Nucl. Instrum. Meth. Phys. Res. A*, *322*, 529 537.

Riess, A. *et al.* (1998). Observational evidence from supernovae for an accelerating universe and a cosmological constant. *Astronomical Journal*, *116*, 1009.

Saint, G. (2009). Brillance scintillators: Performance summary. Tech. rep., Saint Gobain Technical Note. Http://www.detectors.saint-gobain.com/.

Sato, G., Fujuyamma, T., Watanabe, S., *et al.* (2011). Study of polarization phenomena in schottky CdTe diodes using infrared light illumination. *Nucl. Instrum. Methods Phys. Res. A*, *in press*.

Schlickeiser, R. & Thielheim, K. (1977). Spatial distribution of high energy cosmic ray electrons perpendicular to the galactic plane. *Astrophysics and Space Science*, *47*, 415 421.

Schonfelder, V. (2003). Lessons learnt from COMPTEL for future telescopes. *New Astronomy Reviews*, *48*, 193 198.

Schonfelder, V., Hirner, A., Bennett, K., *et al.* (1993). Instrument description and performance of the imaging gamma-ray telescope COMPTEL aboard the NASA s compton gamma-ray observatory. *Ap. J. Suppl.*, *86*, 657 692.

Schonfelder, V., Hirner, A., & Schneider, K. (1973). A telescope for soft gamma ray astronomy. *Nucl. Instr. and Meth. in Phy. Res. A*, *107*, 385 394.

Seller, P. *et al.* (2006). NUCAM: a 128 channel integrated circuit with pulse-height and rise-time measurement on each channel including on-chip 12bit ADC for high-Z X-ray detectors. *IEEE Nuclear Symposium Conf. Rec.*, *6*, 3786 3789.

Shonfelder, V., Diehl, R., Lichti, G., Georgii, R., *et al.* (2001). *The Universe in Gamma Rays*. Springer-Verlag Berlin Heidelberg.

Siffert, P. (1994). Cadmium telluride and related materials as X- and gamma-ray detectors: A review of recent progress. *Proceedings of the SPIE*, *2305*, 98 109.

Skinner, G. (1984). Imaging with coded-aperture masks. *Nucl. Instrum. Meth. Phys. Res. A*, *221*, 33.

Skinner, G. (2001). Diffractive/refractive optics for high energy astronomy: I. gamma-ray phase fresnel lenses. *Astronomy and Astrophysics*, *375*, 691700.

Smith, D. *et al.* (2004). RHESSI results on gamma-ray lines from diffuse radioactivity. *New Ast. Rev.*, *48*, 87.

Solovov, V. *et al.* (2002). Detection of scintillation light of liquid xenon with a LAAPD. *Nucl. Instr. and Meth. in Phy. Res. A*, *488*, 572578.

Sordo, S. D. (2009). Progress in the development of CdTe and CdZnTe semiconductor radiation detectors for astrophysical and medical applications. *Sensors (ISSN 1424-8220)*, *9*, 3491 3526.

Tain, J. *et al.* (2004). Proposal for the construction of a gamma-ray beam line at the spanish synchrotron ALBA. Http://www.cells.es/static/gamma_rays.pdf.

Takahashi, T. & Watanabe, S. (2001). Recent progress in CdTe and CdZnTe detectors. *IEEE Trans. Nucl. Sci.*, *48*(4), 950 959.

Takahashi, T. *et al.* (2001). High resolution CdTe detector and applications to imaging devices. *IEEE Trans. Nucl. Sci.*, *48*, 287 291.

Tylka, A. *et al.* (1997). CREME96: A revision of the cosmic ray effects on microelectronics code. *IEEE Trans.Nucl.Sci.*, *44*(6), 2150 2160.

Vedrenne, G. *et al.* (2003). SPI: The spectrometer onboard INTEGRAL. *Astronomy and Astrophysics*, *411*, L63 L70.

von Ballmoos, P. (2005). *High-Energy Spectroscopic Astrophysics*. Springer.

von Ballmoos, P. (2006). *Focusing Telescopes in Nuclear Astrophysics*. Springer.

von Ballmoos, P., Álvarez, J., *et al.* (2011). The DUAL mission concept. *Proceedings of the SPIE*, *8145*, 81450E 81450E 15.

von Ballmoos, P., Halloin, H., Evrard, J., Skinner, G., Abrosimov, N., Álvarez, J., *et al.* (2004a). CLAIRE s first light. *New Astronomy Reviews*, *48*, 243 249.

von Ballmoos, P., Halloin, H., Evrard, J., Skinner, G., Álvarez, N. A. J., *et al.* (2005). CLAIRE: First light for a gamma-ray lens. *Experimental Astronomy*, *20*, 253 267.

von Ballmoos, P., Halloin, H., Skinner, G., Smither, R., Paul, J., Abrosimov, N., Álvarez, J., *et al.* (2004b). MAX: a gamma-ray lens for nuclear astrophysics. In O. Citterio & S. L. O Dell (Eds.), *Optics for EUV, X-Ray, and Gamma-Ray Astronomy. Edited by Citterio, Oberto; O Dell, Stephen L. Proceedings of the SPIE.*. vol. 5168, 482 491.

von Ballmoos, P. & Smither, R. K. (1994). A positron annihilation radiation telescope using laue diffraction in a crystal lens. *Astrophysical Journal Supplement Series*, *92*, 663 669.

von Ballmoos, P., Takahashi, T., & Boggs, S. (2010a). A DUAL mission for nuclear astrophysics. *Nucl. Instr. and Meth. in Phy. Res. A*, *623*, 431 433.

von Ballmoos, P. *et al.* (2004c). The MAX mission : focusing on high sensitivity gamma-ray spectroscopy. *Proceedings of the 5th INTEGRAL Workshop on The Integral Universe*, *ESA SP-552*, 747 753.

von Ballmoos, P. *et al.* (2010b). DUAL: two views of the extreme universe. *RN99*, 1 48.

Wang, W. *et al.* (2007). SPI observations of the diffuse ^{60}Fe emission in the galaxy. *Astron. Astrophys.*, *469*, 1005 1012.

Weidenspointner, G., Harris, M., Sturner, S., & Teegarden, B. (2005a). MGGPOD: A monte carlo suite for modeling instrumental line and continuum backgrounds in gamma-ray astronomy. *Astrophys. J., Suppl. Ser*, *156*, 69 91.

Weidenspointner, G. *et al.* (2004). MGGPOD: a monte carlo suite for modelling instrumenal backgrounds in γ-ray astronomy an its application to Wind/TGRS and INTEGRAL/SPI. *New Astronomy Reviews*, *48*, 227 230.

Weidenspointner, G. *et al.* (2005b). Monte carlo study of detector concepts for the MAX laue lens gamma-ray telescope. *Exp. Astron*, *20*, 375 386.

Wilderman, S. *et al.* (1998). List-mode maximum likelihood reconstruction of compton scatter camera images in nuclear medicine. *IEEE Trans. Nucl. Sci.*, *45*, 957.

Winkler, C. *et al.* (2003). The INTEGRAL mission. *Astronomy and Astrophysics*, *411*, L1 L6.

Wunderer, C. *et al.* (2005). Simulated performance of dedicated ge-strip compton telescopes as γ-lens focal plane instrumentation. *Experimental Astronomy*, *20*, 365 373.

Yamashita, M. *et al.* (2004). Scintillation response of liquid Xe surrounded by PTFE reflector for gamma rays. *Nucl. Instr. and Meth. in Phy. Res. A*, *535*, 692 698.

Zachariasen, W. (1945). *Theory of X-Ray Diffraction in Crystals*. New York: Dover Publications Inc.

Zoglauer, A. (2005). *First Light for the Next Generation of Compton and Pair Telescopes*. Ph.D. thesis, Technischen Universitat Munchen.

Zoglauer, A. & Kanbach, G. (2003). Doppler broadening as a lower limit to the angular resolution of next-generation compton telescopes. In J. Truemper & H. Tananbaum (Eds.), *X-Ray and Gamma-Ray Telescopes and Instruments for Astronomy*. vol. Proc. SPIE 4851, 1302.

Zoglauer, A. *et al.* (2004). Data analysis for the mega prototype. *New Astronomy Reviews*, *48*, 231.

Zoglauer, A. *et al.* (2006a). Simulated performance of CZT-based focal plane detectors for gamma-ray lenses. *IEEE, Conference Record*, 3742.

Zoglauer, A. *et al.* (2006b). MEGAlib the medium energy gamma-ray astronomy library. *New Astronomy Reviews*, *50*, 629 632.

Zoglauer, A. *et al.* (2009). Cosima - the cosmic simulator of MEGAlib. *IEEE, Conference Record*, *NSS09*.